Protein crystallization in droplet-based microsystems

Joana Ferreira

Examination committee:
Prof. Dr. D. Vandermeulen, chair (KU Leuven)
Prof. Dr. S. Kuhn, supervisor (KU Leuven)
Prof. Dr. F. Rocha, supervisor (University of Porto)
Dr. F. Castro, co-supervisor (University of Porto)
Prof. Dr. K. Bernaerts (KU Leuven)
Prof. Dr. J. Campos (University of Porto)
Prof. Dr. J. Degrève (KU Leuven)
Dr. P. Martins (University of Porto)
Prof. Dr. D. Maes (Vrije Universiteit Brussel)
Prof. Dr. J. Gavira (National Research Council, CSIC)

December 2020

Preface

"I have no special talent. I am only passionately curious."

<div align="right">– Albert Einstein (n.d.).</div>

Although protein crystallization has been known since 1840, most of the bottlenecks found over the last 180 years cannot be solved nowadays. This intriguing dilemma has attracted me since the beginning, as well as the fact that I knew almost nothing about crystallization processes! The original plan for my PhD was intended to mostly cover protein crystallization assays. However, I always tried to extend the study towards a deeper characterization of the fluid dynamics. Therefore, I wish to express my enormous gratitude to my promoter at KU Leuven, Simon Kuhn, for the academic freedom you gave me and for your continuous support in pursuing my research interests. In this context, I am thankful to Helene Van Ammel and Joren van Stee who trusted my scientific input for their projects. It is a pleasure to see that combined efforts and different scientific perspectives can result in a contribution to the research field. I am also grateful to my promoter, Professor Fernando Rocha, and co-promoter, Filipa Castro, at FEUP. Even before choosing this topic, you provided me the important answers I needed to make the important decision of tackling this topic.

My interest in fluid dynamics and transport phenomena started during my course of studies at FEUP, which continued until my master thesis. The main responsible is Professor João Campos. For this reason, I want to thank him and his research team, CEFT, for their personal support and friendship. In particular, I want to thank João Carneiro with whom I learned a lot about microfluidics and multiphase flow, as well as Tomás Rodrigues and Filipe Direito for their capacity to understand (sometimes based on high levels of patience) my peculiar scientific jokes!

Due to the joint nature of this project, there are plenty of people who helped me with all the bureaucratic aspects in which I stumbled during too much time. In particular, I am thankful to Graziella Del Savio at

To Tomás,
my first friend

Abstract

"It is sometimes easier to circumvent prevailing difficulties [in science] rather than to attack them."

– Jacobus Henricus van't Hoff (1878).

The development of the first microfluidic prototype appeared at the beginning of the 1980s. However, over the last decade, droplet-based microfluidics has emerged as a powerful tool with a broad range of applications in most science and engineering fields. The high surface-to-volume ratio associated with the small scale offers attractive advantages over the traditional macroscale instruments. This enables controlled and rapid mixing of fluids, which results in decreased reaction times as well as lower reagent and energy consumption. Due to the unique transport phenomena characteristics provided by droplet microfluidic platforms, it is possible to reach an enhanced control of molecular diffusion and crystal nucleation. This tool allows the fluidic manipulation of independent droplets surrounded by a carrier fluid at identical conditions.

Protein crystallization processes are stochastic and relatively poorly understood, especially the formation of nuclei. This is mainly attributed to the specific structure of these biomacromolecules, which influence their behaviour in solution. Thus, it is often a matter of trial-and-error to successfully crystallize a protein, and therefore demands time-consuming experimental work to test a large number of potential crystallization conditions. In this context, phase diagrams are used as a design of experiments tool. This is not a common strategy because phase diagrams are usually not available, and their construction is required. An early use of phase diagrams represents a rational approach to study protein crystallization as the optimal crystallization conditions are defined (*i.e.* protein phase behaviour as a function of certain parameters).

The aim of this dissertation is to combine a high-throughput microfluidic device with the knowledge of the protein phase behaviour. This intends to apply a more rational strategy to study protein crystallization. Firstly, a microfluidic platform is developed to attend to the needs of the targeted application, protein crystallization. The main requirements to attend to are temperature control strategy and microchannel wall stability over long crystallization times, as well as the optical access for further image analysis. The viability of the droplet microfluidic strategy is analysed based on a hydrodynamic study under the squeezing flow regime, where experimental and numerical approaches are combined. A wide range of droplet volumes was achieved, while ensuring sustainable droplet production with the desired frequency and monodispersity. Additionally, a VOF numerical approach coupled with the smoothing procedure based on a Laplacian function accurately predicts the droplet curvature and complex flow topology effects inside the droplets. This allows a significant reduction of the artificial velocities at the interface. The numerical study is further extended, and the transport phenomena are characterized through the integration of scalar transport equations, concentration and temperature. For the studied droplet volumes, the results do not indicate a major effect on the heat transfer distribution in the microchannel. However, additional test cases revealed the capabilities of this conjugate heat transfer solver to avoid challenging and time-consuming experimental work in the future.

After a detailed investigation of the transport phenomena, the phase behaviour of a model protein (lysozyme) is studied in microdroplets, including the influence of the droplet volume on kinetic (metastability) parameters. It was found that under fast supersaturation changes and small microdroplet volumes, enhanced lysozyme nucleation control is achieved. This results in growing large crystals with well-controlled size distribution. The droplet volume effect becomes predominant at lower supersaturation as the crystal number follows the droplet volume increase, while at higher supersaturation, the crystal number does not considerably vary with the droplet volume.

The obtained results indicate that droplet microfluidics allows a higher degree of control over the crystallization conditions than conventional methodologies. Therefore, different crystallization strategies are combined to simultaneously promote and control protein nucleation. The synergistic effect of low-frequency pulsed ultrasound on lysozyme crystallization in microdroplets is also investigated. Pulsed actuation allows control over

crystallization temperature, while the ultrasound effect significantly reduces induction time and crystal size. It was found that protein nucleation is enhanced by pulsed sonication without causing precipitation and resulting in crystal size uniformity. On the one hand, the initial supersaturation has a crucial contribution to crystal size for silent experiments. On the other hand, a threshold for induction time is observed in ultrasonic crystallization regardless of the applied ultrasound energy and initial supersaturation.

At a later stage, the crystallization study is extended towards another protein, insulin. Insulin presents considerable importance to the medical field, where the search for new drug formulations to replace the frequent injections is still an up to date problem. This preliminary study aims to provide insights into the structural and fundamental understanding of the crystallization process, particularly in the early stages of nucleation. The shear thinning behaviour of the crystallization solutions might result in the formation of supramolecular strands of intermediates (*i.e.* dense network of weakly-bound chains of protein molecules). Partial unfolding or even orientation of the secondary/tertiary configuration might occur at lower insulin concentrations (*i.e.* lower interfacial tension values), while a more stable insulin structure with a lower energy state might be characteristic of higher insulin concentrations (*i.e.* higher interfacial tension values). Moreover, contrary to what has been reported for different proteins (*e.g.* lysozyme), the temperature effect on crystal size is not observed during the insulin crystallization assays. Finally, the presence of cloudy aggregates is observed before the formation of insulin crystals. This suggests that nuclei might be formed within the mesoscopic protein clusters or even that the clusters act as heterogeneous nucleation sites. The nature of these intermediate clusters and how they influence the nucleation mechanism is still an open question. Nevertheless, initial observations might already support a non-classical nucleation hypothesis.

Beknopte samenvatting

"Het is soms gemakkelijker om hardnekkige moeilijkheden [in de wetenschap] te omzeilen dan ze proberen op te lossen."

– Jacobus Henricus van't Hoff (1878).

De ontwikkeling van de eerste microfluïdische prototypes stamt uit de jaren 80. In de laatste 10 jaar is microfluïdica op basis van druppels geëvolueerd tot een krachtig instrument met vele applicaties in verschillende wetenschaps- en ingenieursdisciplines. De hoge oppervlakte-volume verhouding als gevolg van de kleinschaligheid biedt aantrekkelijke voordelen ten opzichte van traditionele grootschalige technologieën. Werken op microschaal zorgt voor een snelle menging van de betreffende componenten hetgeen resulteert in een verlaagde reactietijd en een lager reagentia- en energieverbruik. Door de unieke transportverschijnselen in de kleine volumes die druppel gebaseerde microfluïdische platformen bezitten, is het mogelijk om de controle over moleculaire diffusie en kristalnucleatie te verhogen. Dit instrument laat de vloeistofmanipulatie toe van onafhankelijke druppels omgeven door een dragervloeistof, onder identieke omstandigheden.

Eiwitkristallisatie is een stochastisch proces waarvan het mechanisme relatief slecht begrepen is. Specifiek over de vorming van nuclei is veel onbekend. Dit komt hoofdzakelijk door de structuur van deze biomacromoleculen, die hun gedrag in oplossingen beïnvloedt. Trial-and-error is dan ook vaak de beste methode om een eiwit succesvol te kristalliseren. Deze strategie resulteert meestal in experimentele studies waarbij vele verschillende kristallisatiecondities moeten worden getest, hetgeen tijdrovend is. In deze context worden fasediagrammen gebruikt om de experimentele strategie te bepalen. Het gebruik van fasediagrammen is meestal niet de gevolgde strategie omdat ze doorgaans niet beschikbaar zijn, en ze dus zelf moeten worden opgesteld. Een vroeg gebruik van fasediagrammen is een rationele benadering om eiwitkristallisatie te

bestuderen, omdat de optimale kristallisatiecondities worden gedefinieerd (d.w.z. het gedrag van de eiwitfase als functie van bepaalde parameters).

Het hoofddoel van dit proefschrift is het combineren van een "high-throughput" microfluïdische reactor met de kennis over het gedrag van de eiwitfase en om vervolgens een rationelere strategie te introduceren om eiwitkristallisatie te bestuderen. Ten eerste is een microfluïdisch platform ontwikkeld specifiek voor het kristalliseren van eiwitten. Temperatuurcontrole, de stabiliteit van de microkanaalwand voor lange kristallisatietijden en de mogelijkheid om optische metingen uit te voeren voor verdere beeldanalyse zijn de belangrijkste vereisten voor het microfluïdisch platform. De haalbaarheid van de druppel microfluïdische strategie is geanalyseerd gebaseerd op een hydrodynamische studie onder het zogenaamde "squeezing flow" regime. Hierbij worden experimentele en numerieke experimenten gecombineerd. Een breed scala aan monodisperse druppelvolumes werd geproduceerd met de gewenste frequentie. Verder werd een VOF numerieke aanpak gekoppeld met een smoothing procedure gebaseerd op een Laplace functie om precies de kromming van de druppel en verscheidene topologische effecten gerelateerd met de stroming in de druppel te kunnen bepalen. Dit zorgt voor een significante vermindering van artificiële snelheidscomponenten aan de interface. De numerieke studie is verder uitgebreid en de verschillende transportverschijnselen zijn gekarakteriseerd door het integreren van de scalaire transportvergelijkingen met name de concentratie en de temperatuur. De bestudeerde druppelvolumes hebben geen groot effect op de warmteoverdrachtverdeling in het microkanaal. Echter, extra testen brachten de mogelijkheden van deze geconjugeerde warmteoverdrachtsolver aan het licht om in de toekomst uitdagend en tijdrovend experimenteel werk te vermijden.

Na gedetailleerde studies naar de transportverschijnselen, is het fasegedrag van een modeleiwit (lysozym) in microdruppels bestudeerd. Alsook de invloed van het druppelvolume op de kinetische (metastabiele) parameters. Wanneer de supersaturatie in microdruppels zeer snel verandert, verbetert de controle over het lysozym nucleatieproces. Dit resulteert in de groei van grote kristallen met een controleerbare grootteverdeling. Het druppelvolume effect overheerst bij lagere supersaturaties omdat het aantal kristallen de volumetoename van de druppel volgt, terwijl bij hogere supersaturaties het aantal kristallen niet aanzienlijk varieert met het druppelvolume.

De verkregen resultaten tonen aan dat het gebruik van druppel microfluidica meer controle geeft over de kristallisatiecondities in vergelijking met traditionele methoden. Daarom worden verschillende kristallisatiestrategieën gecombineerd om tegelijkertijd de vorming van eiwitten te bevorderen en te controleren. Het synergetische effect van laagfrequent gepulst ultrasoon geluid op lysozymkristallisatie in microdruppels is ook onderzocht. Gepulst ultrasoon geluid maakt controle over kristallisatie temperatuur mogelijk, terwijl het ultrasoon effect de inductietijd en de grootte van het kristal aanzienlijk reduceert. Het bleek dat de eiwitnucleatie wordt verbeterd door gepulseerde sonicatie zonder dat dit leidt tot neerslag en dat dit resulteert in uniformiteit in de grootte van het kristal. Aan de ene kant heeft de initiële supersaturatie een cruciale bijdrage aan de kristalgrootte voor stille experimenten. Aan de andere kant wordt bij ultrasone kristallisatie een drempelwaarde voor de inductietijd waargenomen, ongeacht de toegepaste ultrasone energie en initiële supersaturatie.

In een later stadium is de kristallisatiestudie uitgebreid naar een ander proteïne, insuline. Insuline is van groot belang in de medische wereld, waar het zoeken naar nieuwe medicijnformuleringen ter vervanging van de frequente injecties nog steeds een actueel probleem is. Deze preliminaire studie heeft tot doel inzicht te verschaffen in het structurele en fundamentele begrip van het kristallisatieproces, met name in de vroege stadia van de nucleatie. Het "shear thinning" gedrag van de kristallisatieoplossingen zou kunnen leiden tot de vorming van supramoleculaire strengen van tussenproducten (d.w.z. een dicht netwerk van zwak gebonden ketens van eiwitmoleculen). Gedeeltelijke ontvouwing of zelfs een oriëntatie van de secundaire/tertiaire configuratie kan optreden bij lagere insulineconcentraties (d.w.z. lagere interfaciale spanningswaarden), terwijl een stabielere insulinestructuur met een lagere energietoestand kenmerkend kan zijn voor hogere insulineconcentraties (d.w.z. hogere interfaciale spanningswaarden). Bovendien wordt, in tegenstelling tot wat voor verschillende proteïnes (bijv. lysozym) is gerapporteerd, het temperatuureffect op de kristalgrootte niet waargenomen tijdens de insulinekristallisatieanalyse. Ten slotte wordt de aanwezigheid van troebele aggregaten waargenomen vóór de vorming van insulinekristallen. Dit suggereert dat nuclei kunnen worden gevormd binnen de mesoscopische proteïneclusters of zelfs dat de clusters fungeren als heterogene nucleatieplaatsen. De aard van deze tussenliggende clusters en hoe ze het nucleatiemechanisme beïnvloeden is nog steeds een open vraag.

Toch kunnen deze eerste waarnemingen al een niet-klassieke nucleatiehypothese ondersteunen.

Resumo

"Às vezes é mais fácil contornar os problemas persistentes [na ciência] do que resolvê-los."

— Jacobus Henricus van't Hoff (1878).

O desenvolvimento do primeiro protótipo de dispositivo microfluídico data do início dos anos 80. No entanto, os dispositivos baseados na formação de gota têm emergido durante a última década como uma ferramenta poderosa numa gama alargada de aplicações, na maioria campos científicos e da engenharia. A razão elevada entre a superfície e o volume associada à escala pequena oferece, comparativamente aos instrumentos tradicionais à macroescala, vantagens atrativas. Isto permite uma mistura rápida e controlada dos fluidos, resultando numa redução de tempos reacionais, bem como menores consumos de reagentes e energéticos. Face às características únicas dos processos de transporte fornecidas pelos dispositivos baseados na formação de gota é possível atingir um controlo melhorado da difusão molecular e da nucleação de cristais. Esta ferramenta permite uma manipulação fluídica de gotas independentes, rodeadas por um fluido contínuo, a condições idênticas.

Os processos de cristalização de proteínas são estocásticos e relativamente mal compreendidos, especialmente a formação de núcleos. Isto é maioritariamente atribuído à estrutura específica destas macromoléculas biológicas, que influencia o seu comportamento em solução. Assim, é muitas vezes uma questão de tentativa-erro para cristalizar uma proteína com sucesso e, portanto, exige-se um trabalho experimental demorado para testar um número elevado de potenciais condições de cristalização. Neste contexto, os diagramas de fase são utilizados como uma ferramenta de design de experiências. Esta não é uma estratégia comum porque geralmente os diagramas de fase não estão disponíveis, e a sua construção é necessária. O uso inicial de diagramas de fase representa uma abordagem racional para estudar a cristalização de proteínas, uma vez que as condições

ideais de cristalização são definidas (isto é, o comportamento da proteína em função de determinados parâmetros).

O objetivo principal desta dissertação é combinar dispositivos microfluídicos de elevada capacidade com o conhecimento do comportamento da fase proteica e, consequentemente, aplicar uma estratégia mais racional para estudar a cristalização de proteínas. Em primeiro lugar, um dispositivo microfluídico é desenvolvido para atender às necessidades da aplicação alvo, cristalização de proteínas. Os principais requisitos a satisfazer são a estratégia para o controlo de temperatura e a estabilidade da parede do microcanal durante tempos longos de cristalização, bem como o acesso ótico para posteriores análises de imagem. A viabilidade da estratégia microfluidica de gotas é analisada de acordo com o estudo hidrodinâmico em regime de "squeezing flow", onde são combinadas as abordagens experimental e numérica. Obteve-se uma gama ampla de volumes de gota, garantindo uma produção de gotas sustentável com a frequência e dispersividade desejadas. Além disso, uma abordagem numérica VOF juntamente com o procedimento de "smoothing" baseado numa função de Laplace prevê com precisão a curvatura da gota e os efeitos complexos da topologia de fluxo dentro das gotas. Isto permite uma redução significativa das velocidades artificiais na interface. O estudo numérico é posteriormente ampliado e os fenómenos de transporte são caracterizados através da integração de equações escalares de concentração e temperatura. Para os volumes de gota estudados, os resultados não sugerem um efeito claro na distribuição da transferência de calor ao longo do microcanal. No entanto, casos de estudo adicionais revelam as capacidades deste "solver" de transferência de calor, de forma a evitar trabalho experimental desafiador e demorado no futuro.

Após uma investigação detalhada dos fenómenos de transporte, o comportamento da fase proteica (lisozima) em microgotas é estudado, incluindo a influência do volume de gota nos parâmetros cinéticos (metaestabilidade). Verificou-se que para mudanças de sobressaturação rápidas e microgotas de volume pequeno, um controlo melhorado da nucleação de lisozima é alcançado. Isto resulta no crescimento de cristais maiores com uma distribuição de tamanho bem controlada. A sobressaturações mais baixas, o efeito do volume de gota torna-se predominante, pois o número de cristais segue a tendência do aumento de volume da gota, enquanto que para sobressaturações mais elevadas, o número de cristais não varia consideravelmente com o volume da gota.

Os resultados obtidos indicam que a microfluidica de gotas permite um maior grau de controlo sobre as condições de cristalização comparativamente às metodologias convencionais. Deste modo, estratégias de cristalização diferentes são combinadas de forma a, simultaneamente, promover e controlar a nucleação de proteínas. O efeito sinergético do ultrassom pulsado de baixa intensidade também é investigado para a cristalização da lisozima em microgotas. A atuação pulsada permite o controlo da temperatura de cristalização, enquanto que o efeito do ultrassom reduz significativamente o tempo de indução e o tamanho do cristal. Verificou-se que a nucleação de proteínas é promovida devido à sonicação pulsada, sem causar precipitação, resultando numa uniformidade do tamanho do cristal. Por um lado, a sobressaturação inicial tem uma contribuição essencial para o tamanho do cristal em experiências sem a aplicação de ultrassons. Por outro lado, observa-se um limite para o tempo de indução na cristalização com ultrassons, que é independente da energia aplicada e da sobressaturação.

Numa fase posterior, o estudo da cristalização é alargado à insulina. A insulina apresenta uma importância considerável para a área médica, onde a procura por novas formulações de medicamentos para substituir as injeções frequentes é ainda um problema atual. Este estudo preliminar visa fornecer perspetivas sobre a compreensão estrutural e fundamental do processo de cristalização, particularmente nos estágios iniciais de nucleação. O comportamento "shear thinning" das soluções de cristalização poderá resultar na formação de filamentos supramoleculares de intermediários (isto é, uma rede densa de moléculas de proteína ligadas através de cadeias fracas). O desdobramento parcial ou mesmo até uma orientação da configuração secundária/terciária poderá ocorrer a concentrações de insulina mais baixas (isto é, valores de tensão interfacial mais baixos), enquanto que uma estrutura de insulina mais estável com um nível de energia mais baixo poderá ser característica de concentrações de insulina mais elevadas (isto é, valores de tensão interfacial mais altos). Além disso, ao contrário do que tem sido reportado para outras proteínas (por exemplo, lisozima), durante os ensaios de cristalização da insulina não é observado um efeito da temperatura no tamanho do cristal. Finalmente, observa-se a presença de agregados turvos antes da formação dos cristais de insulina. Isto sugere que os núcleos se poderão formar a partir dos "clusters" mesoscópicos de proteína ou até que os "clusters" atuam como promotores de nucleação heterogénea. A natureza destes "clusters" intermediários e como influenciam o mecanismo de nucleação é ainda uma

questão em aberto. No entanto, estas observações iniciais poderão apoiar a hipótese de nucleação não clássica.

List of abbreviations

CAD	Computer-Aided Design
CFD	Computational Fluid Dynamics
CFL	Courant-Friedrichs-Lewy
CLSM	Confocal Laser Scanning Microscopy
CNT	Classical Nucleation Theory
CP	Continuous phase
CSF	Continuum Surface Force
DLS	Dynamic Light Scattering
DOE	Design of Experiments
DP	Dispersed phase
ID	Inside diameter
LOC	Lab-on-a-Chip
LS	Level-Set
LU	Lower/Upper (triangular)
MULES	Multidimensional Universal Limiter with Explicit Solution
MZ	Metastable zone
MZW	Metastable zone with
NGSP	Nucleation-growth separation principle
NZ	Nucleation zone
OD	Outside diameter
OpenFOAM	Open-source Field Operation and Manipulation
PDMS	Polydimethylsiloxane
PEEK	Polyether ether ketone
PFA	Perfluoroalkoxy alkane
PIMPLE	Pressure Implicit Method for Pressure Linked Equations
SLA	Stereolithography
VOF	Volume-of-Fluid

List of symbols

Latin scripts (continues)

A	[# of nuclei·m^{-3}·s^{-1}]	Kinetic nucleation parameter (Chapter 1)
A', A''	[mol·m^{-3}]	Optimization parameters (Chapter 4)
B', B''	[K]	Optimization parameters (Chapter 4)
c_p	[J·kg^{-1}·K^{-1}]	Heat capacity
C	[mol·m^{-3}]	Concentration
C', C''	[-]	Optimization parameters (Chapter 4)
d	[m]	Diameter
D, D_T	[m^2·s^{-1}]	Molecular diffusion coefficient, molecular diffusion coefficient at a certain temperature
D_{T_0}	[m^2·s^{-1}]	Pre-exponential coefficient (Chapter 3)
D', D''	[mol·m^{-3}]	Optimization parameters (Chapter 4)
E_0	[J·mol^{-1}]	Activation energy (Chapter 3)
E_{tot}	[J]	Total ultrasound energy
f	[s^{-1}]	Frequency
f_c	[-]	Fraction of total droplets
$\mathbf{f}_\sigma$	[N]	Surface tension forces
$\mathbf{g}$, g	[m·s^{-2}]	Gravitational acceleration
G	[J·mol^{-1}]	Gibbs free energy
H	[J·mol^{-1}]	Enthalpy
J_{nucl}	[# of nuclei·m^{-3}·s^{-1}]	Nucleation rate
k	[W·m^{-1}·K^{-1}]	Thermal conductivity
k_1, k_2, k_3, k_4	[-]	Geometric parameters (Chapter 2)

Latin scripts (continues)

k_B	[J·K^{-1}]	Boltzmann constant
k_{cg}	[m·s^{-1}]	Growth rate constant (Chapter 5)
k_{nc}	[s^{-1}]	Proportionality constant (Chapter 5)
k_{t}	[-]	Fitting parameter (Chapter 5)
k_{v}	[-]	Shape factor
K	[m^2·s^{-1}]	Diffusion coefficient (D), thermal diffusivity ($k/\rho c_p$) (Chapter 1)
K'	[Pa·s$^{\eta}$]	Fluid consistency index (Chapter 6)
K_{eq}	[-]	Equilibrium constant (Chapter 4)
m	[kg]	Mass
M	[N·m]	Torque
n	[-]	Power law index (Chapter 6)
n_{m}	[mol]	Molecules number in the cluster (Chapter 1)
$\mathbf{n}$	[-]	Interface-normal vector
N_0	[-]	Number of droplets
N_{c}	[-]	Number of crystals
N_{tot}	[-]	Total number of droplets
P	[Pa]	Pressure
P_{e}	[W]	Electric power
P_{nucl}	[-]	Nucleation probability
Q	[m^3·s^{-1}]	Flow rate
Q_{h}	[W·m^{-2}]	Local heat flux density
r	[m]	Radius, radial coordinate
R	[m]	Radii of curvature (Chapter 1)
R_{g}	[J·mol^{-1}·K^{-1}]	Ideal gas constant (Chapter 4)
S	[J·mol^{-1}]	Entropy
S_A	[m^2]	Interfacial area (Chapter 1)
S_f	[m^2]	Surface area of a cell (Chapter 2)
t, t_{conv}	[s]	Time, convection time
t_{g}	[s]	Growing period of a nuclei
t_{r}	[s]	Residence time (of each droplet)
t_{ss}	[s]	Time to reach a quasi-steady-state
T	[K]	Absolute temperature
$\mathbf{v}, u$	[m·s^{-1}]	Velocity field, axial component

Latin scripts (continued)

u_r	[m·s⁻¹]	Compression velocity (Chapter 2)
V	[m³]	Volume
V_m	[m³·mol⁻¹]	Molar volume
w_c	[m]	Depletion zone width
x_c	[m]	Cell size
z	[m]	Position of each crystal

Greek scripts (continues)

α	[-]	Phase indicator (VOF) function, volume fraction $[Q_\mathrm{i}/(Q_\mathrm{c} + Q_\mathrm{d})]$
β	[K⁻¹]	Coefficient of volume expansion
β_1	[kg·m⁻³·K⁻¹]	Coefficients for a 1st-order
β_2	[kg·m⁻³]	approximation of the density (Chapter 3)
β_3	[Pa·s·K⁻²]	Coefficients for a 2nd-order
β_4	[Pa·s·K⁻¹]	approximation of the dynamic
β_5	[Pa·s]	viscosity (Chapter 3)
β_6	[N·m⁻¹·K⁻¹]	Coefficients for a 1st-order
β_7	[N·m⁻¹]	approximation of the interfacial tension (Chapter 3)
$\dot{\gamma}$	[s⁻¹]	Shear rate
ε	[m]	Film thickness
η	[Pa·s]	Shear viscosity
θ	[rad]	Contact angle
κ	[-]	Interface curvature
μ	[Pa·s]	Dynamic viscosity
ν	[m²·s⁻¹]	Kinematic viscosity
ρ, ρ_0	[kg·m⁻³]	Density, density at standard temperature
σ	[N·m⁻¹] or [J·m⁻²]	Specific surface energy (Chapter 1), interfacial tension (Chapters 2, 3, 6)

Greek scripts (continued)

τ	[Pa]	Shear stress
Υ	[N·m⁻¹] or [J·m⁻²]	Surface tension
ϕ	[rad]	Cone angle (rheometer)
Ω	[rad·s⁻¹]	Angular velocity

Dimensionless numbers

Ca	$[\mu u/\sigma]$	Capillary number
Co	$[\mathbf{v}\Delta t/\Delta x]$	Courant number
Fo	$[KL/(d^2 u)]$	Fourier number
Re	$[\rho d u/\mu]$	Reynolds number
Pe	$[Lu/K]$	Péclet number
Pr	$[\mu c_p/k]$	Prandtl number
S	$[C^0/C^s]$	Supersaturation ratio
We	$[\rho d u^2/\sigma]$	Weber number

Subscripts (continues)

∞	Infinite time
analyt	Analytical
c	Cluster (Chapter 1), Crystal (Chapters 4–6)
cg	Crystal growth
d	Droplet (dispersed phase)
ent	Inlet (Chapter 2)
exp	Experimental
f	Final
f	Face indices (Chapter 2)
het	Heterogeneous nucleation
hom	Homogeneous nucleation

Subscripts (continued)

i	Phase ($i = d$, dispersed and $i = c$, continuous) (Chapter 1), species (protein, NaCl) (Chapter 3)
ij	Binary mixture
ins	Insulin
ind	Induction
k	Cell indices (Chapter 2)
lys	Lysozyme
mix	Mixing
nucl	Nucleation
p	Protein
PS	Salt solution
sil	Silent
t	Teflon tube
US	Ultrasound

Superscripts

$*$	Critical
$\circ$	Standard conditions
∞	Infinite time
0	Initial time
b	Bulk
c	Crystal
met	Metastability
s	Solubility

Graphemes

$\tilde{\alpha}$	Smoothed indicator fraction
$\lvert \nabla \alpha \rvert$	Absolute value of the indicator fraction
$\overline{N_c}$	Average number of crystals per droplet
∇T_h	Temperature gradient
$\lVert \mathbf{v} \rVert$	Velocity magnitude

Contents

1. Introduction

"The important thing in science is not so much to obtain new facts as to discover new ways of thinking about them."

– William Lawrence Bragg (n.d.).

Throughout its history, since the attribution of the first Nobel Prize award in 1901, 32 awards and 58 laureates have been assigned for scientific achievements directly related to, or involving the use of, crystallographic methods and techniques [1]. Among those scientific breakthroughs, some of them are still reflected in the investigation carried out nowadays. Max von Laue was awarded with the Nobel Prize in Physics 1914 for the discovery of the diffraction of X-rays by crystals and, consequently, the determination of crystals' structures. One year later, the Nobel Prize in Physics 1915 was awarded jointly to Sirs William Henry Bragg and William Lawrence Bragg for their contribution to the analysis of crystal structure through X-rays.

More than 30 years later, James Batcheller Sumner was awarded with the Nobel Prize in Chemistry 1946 for the discovery that enzymes can be crystallized. Almost 2 decades later, Dorothy Crowfoot Hodgkin was awarded with the Nobel Prize in Chemistry 1964 for the determination by X-ray techniques of the structures of important biochemical substances, which includes the first X-ray photograph of an insulin crystal. More recently, as an alternative to crystallography, in 1990, Richard Henderson succeeded in using an electron microscope to generate a 3D image of a protein at atomic resolution. Jacques Dubochet, Joachim Frank and Richard Henderson were jointly awarded with the Nobel Prize in Chemistry 2017 for the development of cryo-electron microscopy for the high-resolution structure determination of biomolecules in solution.

Nevertheless, the major bottleneck in X-ray crystallography of biomacromolecules is the lack of generalized methods for producing high-

quality crystals due to the highly stochastic nature of the entire crystallization process [2]. Therefore, the reported literature over the last 3 decades still highlights this probabilistic aspect of crystallization as observed in the following articles' titles: ''2D crystallization: From art to science'' (1992) [3], ''Turning protein crystallization from an art into a science'' (2004) [4], and ''Chemical crystallography – Science, technology or a black art'' (2010) [5].

The main theoretical aspects of protein crystallization and droplet microfluidics are presented along this introductory chapter. The remainder of this chapter further delineates the challenges (section 1.3), our motivation to tackle this specific research field (section 1.4), the main objectives (section 1.5), and concludes with a brief outline (section 1.6) by clarifying the structure of this dissertation. Therefore, the chapter division consists of two main parts: (i) Protein crystallization (section 1.1) and (ii) Droplet microfluidics (section 1.2).

1.1   Protein crystallization

A protein is a biological macromolecule with a complex 3D structure, involving, at least, one polypeptide chain. The existence of thousands of atoms results in a large number of degrees of freedom, due to the several molecular interactions, such as dipole-dipole interactions, covalent bonds and salt bridges. Proteins are the building blocks of all cells in all living creatures and given the fact that all their functions are dependent on their structure, one can easily understand the importance of determining their 3D structure [6]. Protein crystallization requires that, besides the fact that the protein under study must be crystallizable, thermodynamic (concept of supersaturation and phase diagram overview) and kinetic (mostly nucleation and crystal growth) features are fulfilled, which are explained along the current section.

Protein crystallization appeared for the first time in the first half of the 19th century [7]. The production of a protein crystal is complex due to the highly variable nature of the process, which commonly depends on thermodynamic and kinetic parameters. Protein crystals present unique characteristics, such as [8], [9]:

- Structural complexity, but chemically well-defined;
- Limited in size (commonly the volume is smaller than 10 mm^3);
- Very soft, fragile, brittle and crush easily;
- Exhibit weak optical properties and diffract X-rays poorly.

Thermodynamics

The experimental conditions to crystallize a protein are difficult to accomplish and require knowledge about the thermodynamic properties of the protein solution. The first requirement is to create a supersaturated protein solution [8], [10], [11], so insight into the protein phase diagram is fundamental to design crystallization experiments.

Supersaturation

Crystallization of a macromolecule depends upon the creation of a supersaturated state, which is thermodynamically unstable. In other words, this unstable (non-equilibrium) state may develop in an ordered (crystalline) or disordered (amorphous) phase until the return to the equilibrium state. Supersaturation is the driving force of crystallization and can be expressed by the ratio between the protein concentration in solution (C_{p}^{0}) [mol·m^{-3}] and the protein solubility, *i.e.* the protein concentration $(C_{\mathrm{p}}^{\mathrm{s}})$ [mol·m^{-3}] remaining in solution in equilibrium with the crystals, as represented by

$$S = \frac{C_{\mathrm{p}}^{0}}{C_{\mathrm{p}}^{\mathrm{s}}}. \tag{1.1}$$

The degree of supersaturation depends on the protein solubility that is affected by many factors (*e.g.* pH, temperature, ionic strength, buffer types, additives, and precipitating agents). These variables can be used to change the supersaturation and thus to enable protein crystallization. The methods commonly used to generate supersaturation when designing protein crystallization experiments are presented in Table 1.1. Typically, microbatch is the crystallization technique applied during the crystallization experiments conducted in this thesis (Chapters 4–6). However, complementary crystallization techniques are carried out alongside

microbatch, including ultrasound irradiation in microdroplets (Chapter 5) and vapour diffusion (Chapter 6).

Table 1.1. Overview of the main methods used to generate supersaturation in protein crystallization [11].

Method	General description
(Micro)batch	Mixing the protein solution with the precipitating agent until supersaturation is reached by preventing evaporation and uncontrolled concentration changes of the components in microdroplets.
Dialysis	There are available different types of systems, but all follow the same general principle; a semipermeable membrane allows the passage of small molecules but prevents it for proteins.
Vapour diffusion	A droplet containing the protein to be crystallized, buffer and precipitating agent are equilibrated against a reservoir containing a solution of the precipitant at a higher concentration. Equilibrium proceeds due to the diffusion until the vapour pressure of the droplet equals the one in the reservoir.
Interfacial diffusion	Assays are performed in capillaries, avoiding fast mixing and convection. Equilibrium occurs only by diffusion of precipitant into the protein solution.
Crystallization in gelled media	Convection-free environment, where the precipitating agent solution is diffused into the protein solution, with the consequent establishment of a supersaturation gradient.
Miscellaneous crystallization methods	Changes in the physical environment, which might include *e.g.* pressure or even external stimuli (*e.g.* magnetic and electric fields, ultrasound and light irradiation).

Phase diagram

A phase diagram indicates which state (liquid, crystalline, or amorphous precipitate) is stable when varying crystallization parameters (*e.g.* protein concentration, precipitant identity and concentration, pH, temperature). The construction of a phase diagram allows to place the crystallization experiment relative to the solubility curve of the solute. Depending on the location in the phase diagram, a certain crystallization step, nucleation or

crystal growth, occurs spontaneously. Crystal nucleation is favoured in the nucleation zone, above the metastability curve (labile zone in Figure 1.1), while crystal growth is optimized in the metastable zone, above the solubility curve and below the metastability curve (metastable zone in Figure 1.1 [12]. A simple phase diagram for the crystallization of macromolecules is represented in Figure 1.1, where the conditions for crystallization are described by the protein concentration in function of an adjustable parameter (*e.g.* precipitating agent concentration). Further investigation on the protein phase behaviour through the use of phase diagrams is carried out in Chapter 4, where a complete overview of thermodynamics and kinetics aspects is proposed.
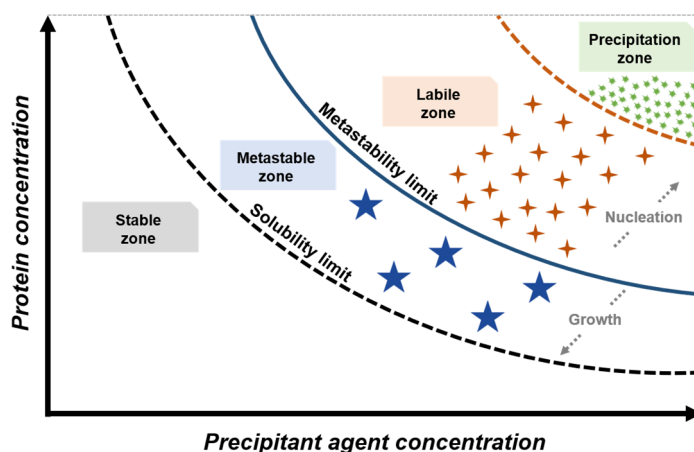
Figure 1.1. Schematic representation of the phase diagram for the crystallization of a macromolecule in function of the protein concentration and precipitating agent concentration, including the different zones and limits.

Kinetics

Crystallization is a physical two-step process, where supersaturation is the driving force. The first step is the formation of nuclei (nucleation), followed by the growth of these nuclei (crystal growth) until reaching a detectable size. Compared to crystal growth, nucleation is more difficult to address theoretically and experimentally due to its highly stochastic nature [13]–[19].

Nucleation

Nucleation represents a first-order phase transition by which molecules pass from a wholly disordered state to an ordered one [20]. Protein nucleation requires extremely high levels of supersaturation to overcome the critical free energy barrier. Classical nucleation theory (CNT) introduced by Volmer and Weber in 1926 is the most consensual theory to explain the protein nucleation mechanism [21]. One of the suppositions of this classical approach is that all the clusters exhibit the same degree of crystallinity regardless of their size [22]. However, the validity of some assumptions in this classical theory has recently been questioned and drastically contradicted [23]–[25]. The non-classical approaches designate nucleation as a multistep process, where metastable intermediate states (*i.e.* pre-critical clusters) are involved in a multistep nucleation theory [23]. One of these theories was proposed by Galkin and Vekilov in 2000, where the protein nucleation phenomenon is defined as a two-step mechanism [26]. Sleutel & Van Driessche (2014) [23] showed evidence that clusters are liquid-like and metastable with respect to the emerging crystalline phase. Ferreira *et al.* (2017) [27] demonstrated the existence of clusters that remain, and clusters which do not give rise to protein crystals. A schematic representation of the protein crystallization process involving the classical *versus* non-classical views of the nucleation mechanism is shown in Figure 1.2.
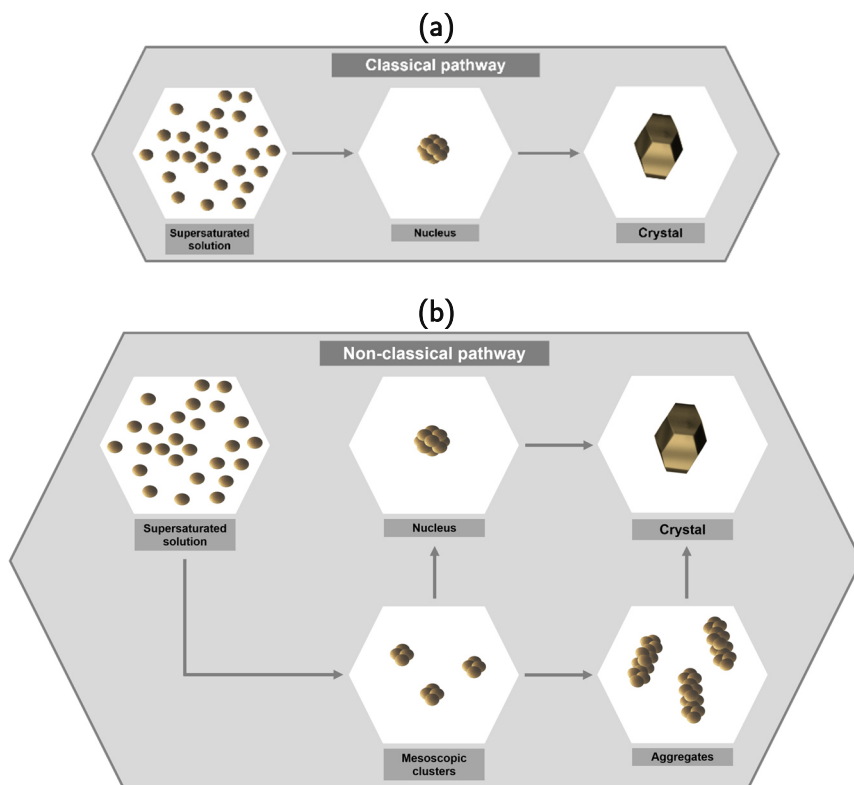
Figure 1.2. Schematic representation of the protein crystallization process: **(a)** Classical (single-step nucleation pathway as each nucleus results in a crystal) *versus* **(b)** non-classical (multistep nucleation pathway as the formation of intermediate states occurs before the crystalline phase) views of the nucleation mechanism.

The nucleation process is commonly divided into primary and secondary nucleation, based on the mechanisms generating crystal nuclei. The first can either be homogeneous or heterogeneous (Figure 1.3). During homogeneous nucleation [Figure 1.3-(a-1)], nuclei are spontaneously generated through clusters, which will originate the crystals. If the nucleus is formed with the aid of foreign particles, the nucleation mechanism is called heterogeneous [Figure 1.3-(a-2)]. These foreign particles act as a catalyst, lowering the energy barrier to transforming clusters into nuclei. Thus, these nuclei are formed at lower supersaturation ratios. Contrarily to primary nucleation, which happens in the absence of its crystalline matter, secondary nucleation [Figure 1.3-(a-3)] typically occurs when the formation of new nuclei is induced by the presence of crystals of the material being crystallized. This nucleation can occur at lower

supersaturation ratios compared to primary nucleation by requiring a lower energy value [10]. All these considerations can be done by assuming the validity of the Classical Nucleation Theory (CNT). Further perspectives on protein nucleation are provided along Chapter 5. Additionally, experimental evidence about the non-validity of the CNT will be highlighted, while an alternative nucleation mechanism is proposed along Chapter 6.
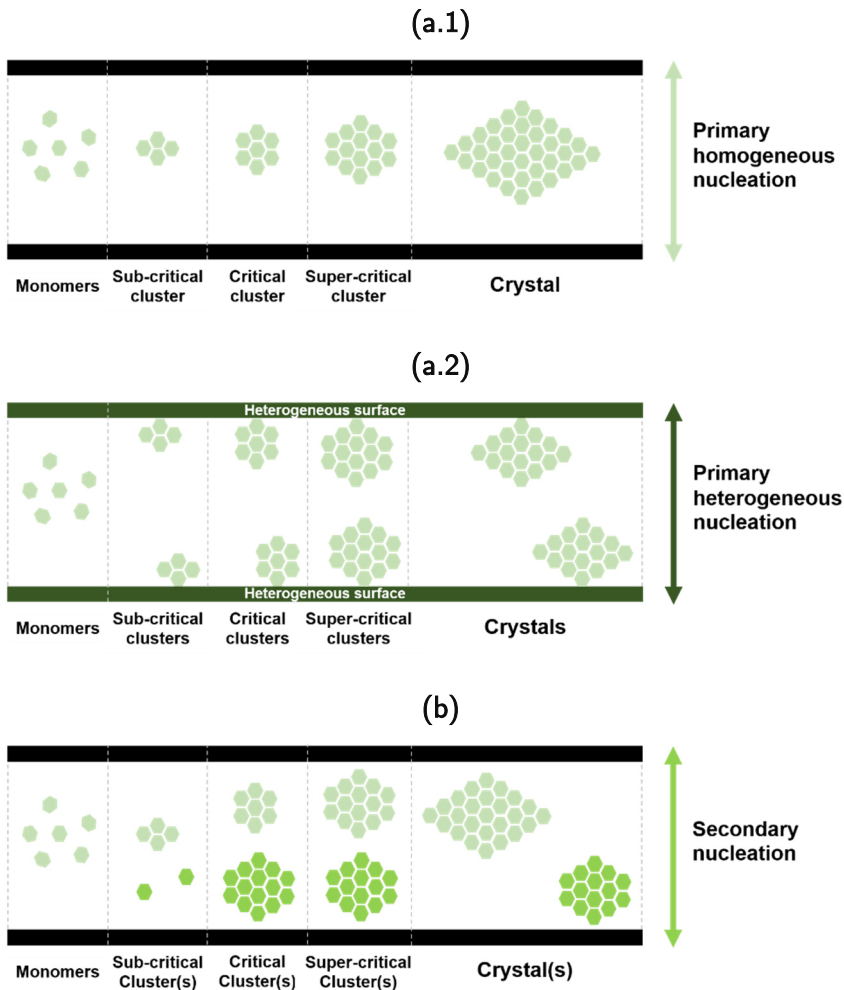
Figure 1.3. Schematic representation of the nucleation process: **(a)** Primary [**(1)** homogeneous *versus* **(2)** heterogeneous] and **(b)** Secondary nucleation.

The formation of a stable nucleus from a spherical cluster involves the creation of a volume (ΔG_{bulk}) and a surface (ΔG_{surf}) (Figure 1.4) in a

system that is thermodynamically away from equilibrium. This nucleus grows until reaching a critical size, which will evolve to a crystal. Gibbs free energy for the occurrence of homogeneous nucleation $(\Delta G_{\mathrm{hom}})$ [J] is described by [8]

$$\Delta G_{\mathrm{hom}} = \underbrace{-\left(\frac{4\pi r_{\mathrm{c}}^3}{3n_{\mathrm{m}}V_{\mathrm{m}}}\right)k_B T \ln \mathrm{S}}_{\Delta G_{\mathrm{bulk}}} + \underbrace{(4\pi r_{\mathrm{c}}^2)\sigma}_{\Delta G_{\mathrm{surf}}}, \tag{1.2}$$

where r_{c} [m] is the cluster radius, n_{m} [mol] the molecules number in the cluster, V_{m} [m³·mol⁻¹] the molar volume occupied by a protein unit in the crystal, k_B [J·K⁻¹] the Boltzmann constant, T [K] the absolute temperature, and σ [N·m⁻¹] the specific surface energy (at the cluster-solution interface). At equilibrium $(\partial \Delta G_{\mathrm{hom}}/\partial r_{\mathrm{c}} = 0)$, the critical cluster size $(r_{\mathrm{c,hom}}^*)$ [m] at which a crystal starts growing can be estimated by Equation (1.3.1). At this stage, a sufficient supersaturation ratio is reached, and homogeneous nucleation occurs spontaneously since the critical free energy $(\Delta G_{\mathrm{hom}}^*)$ [J·mol⁻¹] is overcome [Equation (1.3.2)] [8].

$$r_{\mathrm{c,hom}}^* = 2\frac{V_{\mathrm{m}}\sigma}{k_B T \ln \mathrm{S}}, \tag{1.3.1}$$

and

$$\Delta G_{\mathrm{hom}}^* = \frac{16\pi}{3}\frac{V_{\mathrm{m}}^2\sigma^3}{(k_B T \ln \mathrm{S})^2}. \tag{1.3.2}$$

When heterogeneous nucleation occurs, the solute molecules have an affinity for the substrate, resulting in a reduction of the free energy barrier and, consequently, a lower supersaturation ratio compared to homogeneous nucleation [8]. Gibbs free energy for the occurrence of heterogeneous nucleation $(\Delta G_{\mathrm{het}})$ [J·mol⁻¹] is described by [8]

$$\Delta G_{\mathrm{het}} = -\left(\frac{4\pi r_{\mathrm{c}}^3}{3V_{\mathrm{m}}}\right)\left(\frac{2 - 3\cos\theta + \cos^3\theta}{4}\right)k_B T \ln \mathrm{S} \tag{1.4}$$
$$+ (4\pi r_{\mathrm{c}}^2)\left(\frac{1-\cos\theta}{2} - \frac{1-\cos^2\theta}{4}\cos\theta\right)\sigma,$$

where θ [rad] is the contact angle at the triple point substrate-nucleus-solution.

Analogously to homogeneous nucleation, at equilibrium $(\partial\Delta G_\text{het}/\partial r_\text{c} = 0)$, the critical cluster size $(r^*_\text{c,het})$ [m] at which a crystal starts growing can be estimated by Equation (1.5.1). Finally, a generalized relationship between the critical free energy (activation energy) for the occurrence of homogeneous (ΔG^*_hom) and heterogeneous (ΔG^*_het) [J·mol^{-1}] nucleation in function of the contact angle is obtained by Equation (1.5.2) [8]

$$r^*_\text{c,het} = 2\,\frac{V_\text{m}\sigma}{k_B T \ln S}\,\frac{\left(\frac{1 - \cos\theta}{2} - \frac{1 - \cos^2\theta}{4}\cos\theta\right)}{\left(\frac{2 - 3\cos\theta + \cos^3\theta}{4}\right)}, \qquad (1.5.1)$$

and

$$\Delta G^*_\text{het} = \Delta G^*_\text{hom}\left(\frac{1}{2} - \frac{3}{4}\cos\theta + \frac{1}{4}\cos^3\theta\right). \qquad (1.5.2)$$

The nucleation rate (J_nucl) [# of nuclei·m^{-3}·s^{-1}] is defined as the number of nuclei per unit volume per unit time that exceeds the critical size $(r^*_\text{c,hom})$ [8], [21] and can be determined through an Arrhenius reaction velocity relationship by [10]

$$J_\text{nucl} = A\,\exp\left(-\frac{\Delta G^*_\text{hom}}{k_B T}\right), \qquad (1.6)$$

where A [# of nuclei·m^{-3}·s^{-1}] is the kinetic nucleation parameter. Finally, the induction time (t_ind) [s] is the time that elapses between the achievement of supersaturation and the detection of crystals. As a matter of simplification, the induction time can be estimated by [10], [21]

$$t_\text{ind} = \frac{A}{V}\,\exp\left(\frac{\Delta G^*_\text{hom}}{k_B T}\right), \qquad (1.7)$$

where V [m^3] is the crystallization volume.

Crystal growth

Crystal growth consists of a multistage process involving several mechanisms, such as bulk diffusion, interfacial adsorption, and incorporation of the growth unit. When a stable nucleus is formed in a supersaturated solution, it immediately begins to grow into a macroscopic crystal by the incorporation of growth units [10], [21].
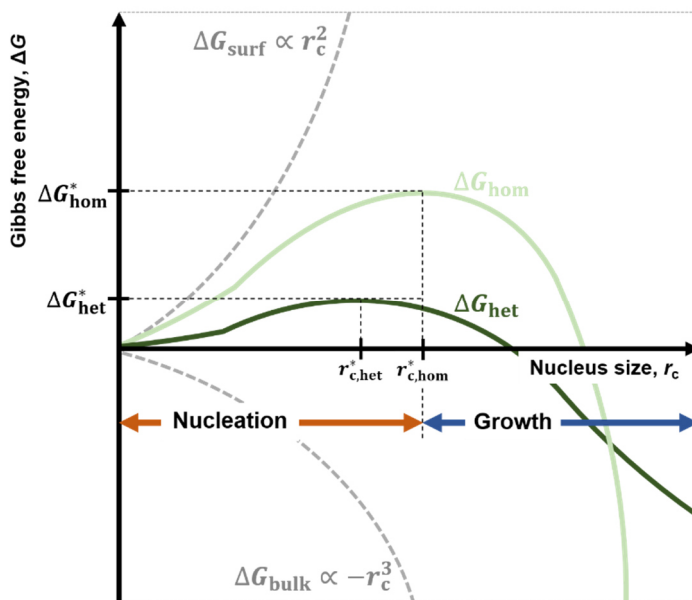
Figure 1.4. Variation of the Gibbs free energy (ΔG) in function of the cluster size (r_c) during the nucleation (homogeneous and heterogeneous) and growth stages.

As the important aspects involved in protein crystallization have been presented along section 1.1, section 1.2 further elucidates about the underlying physics involved in droplet microfluidics as well as application range of this research area.

1.2   Droplet microfluidics

Microfluidics is the science and technology of systems that manipulate fluids on the microscale through networks of channels with characteristic dimensions in the range of 1 µm–1 mm [14], [28]–[36]. Microfluidics allows

to carry out complex protocols on a single chip – Lab-on-a-chip (LOC) devices –, for fluid-handling and processing, which can cover a broad range of fields and practical applications (Table 1.2) [15], [28], [29], [33], [34], [37]–[39]. Droplet flow microfluidics is a promising research field in both academic and industry by offering flexibility and a unique fluid flow behaviour at the microscale [16], [17], [40]. LOC devices offer attractive advantages over conventional macroscale instruments, including faster reactions and operation times, lower cost, lower reagent consumption, lower energy consumption, and ease-of-use (portability and sensitivity). Thus, these devices allow conducting a higher number of tests with a small amount of sample [15], [17], [19], [28], [30], [38], [41]–[43]. The characteristic small volumes allow a minimal surface fouling [44], safer handling of hazardous materials, and reduced waste and risk [32], [45], [46].

Table 1.2. Overview of the main research fields and subfields where microfluidic platforms are applied and the corresponding applications.

Research fields	Applications	References
	- Chemical synthesis (*e.g.* molecules, nanoparticles, colloidal assemblies)	[28], [38], [43], [47], [48]
Chemistry	- Crystallization or precipitation (*e.g.* macromolecules)	[14], [29], [33], [38], [43], [49], [50]
	- Analytical chemistry	[41]
	- Biochemistry	[15]
		[15], [17], [54], [30], [34], [37], [43], [47], [51]–[53]
	- Analytical Biology Biological and molecular analysis (*e.g.* biomolecules, including proteins, nucleic acids, enzymes, DNA)	[14], [28], [33], [47], [55]
Biology	Separation and manipulation (*e.g.* cells, molecules, microparticles)	[56]
		[15], [17], [53], [57], [58], [19], [30], [33], [34], [37], [43], [47], [52]
	- Clinical diagnosis	[41], [55], [59], [60]
Medicine	- Biomedicine	[54]
		[33], [34], [37], [54], [57]
	- Engineering Biomedical Chemical Electrical Aerospace	[19], [34], [54], [60], [61] [33], [62] [19], [33] [63]
Technology	- Biotechnology	[41], [64]
	- Microsystems & Microelectronics	[28], [41]
Others	- Pharmaceutics and food - Textile industry	[48], [62] [62]

Liquid-liquid segmented flow

Multiphase flow is characterized by, at least, two partially or completely immiscible fluids that are brought into contact [34], [36], [65]. In

comparison to single-phase flow, multiphase flow involves several physicochemical phenomena (*i.e.* fluid hydrodynamics, transport phenomena and interfacial characteristics) that allow the coexistence and confinement of multiple phases in one system [36], and are commonly classified into two categories: (i) segmented flow and (ii) stratified flow. In segmented flows, the fluids are distributed along the flow direction and generate discrete fluid segments. The discrete fluid constitutes the dispersed phase, while the carrier fluid surrounding that phase is the continuous phase. The fluids are structured along the direction normal to the flow in stratified flow by introducing stable interfaces [66].

Due to the high surface-to-volume ratio characterizing microscale systems, surface phenomena become dominant over volume phenomena [35], [43]. Surface effects appear at the interface between the microchannel wall and the liquid (S-L) or between the two immiscible fluids (L-L) [38]. Hydrophobic microchannels favour the creation of dispersed-in-continuous emulsions, while continuous-in-dispersed emulsions are generated in hydrophilic microchannels [17], [34], [57], [67].

Fluid dynamics

Depending on the length and time scales, some forces are less important or even negligible, while others are increasingly dominant. At the microscale, the fundamental fluid physics is complex and changes dramatically [30], [35]. Buoyancy and gravitational forces are negligible, and viscous and interfacial forces become more important [29], [31], [33], [34], [36], [45]. Hence, dimensionless numbers express the competition between the various phenomena and their relative importance for the system [35]. Besides the volume fraction of the continuous phase $[\alpha_c = Q_c/(Q_c + Q_d)]$ and viscosity ratio (μ_c/μ_d), the main dimensionless numbers related to transport phenomena in multiphase microfluidic flows at the microscale are the Capillary (Ca), Weber (We), Fourier (Fo), Péclet (Pe), and Prandtl (Pr) numbers, which are given by [68]

$$\mathrm{Ca_i} = \frac{\mu_i u_i}{\sigma}, \qquad (1.8.1)$$

$$\mathrm{We}_{\mathrm{i}} = \frac{\rho_{\mathrm{i}} d_{\mathrm{d}} u_{\mathrm{i}}^2}{\sigma}, \tag{1.8.2}$$

$$\mathrm{Fo} = \frac{K L_{\mathrm{d}}}{d_{\mathrm{d}}^2 u_{\mathrm{d}}}, \tag{1.8.3}$$

$$\mathrm{Pe} = \frac{L_{\mathrm{d}} u_{\mathrm{d}}}{K}, \tag{1.8.4}$$

$$\mathrm{Pr}_{\mathrm{i}} = \frac{\mu_{\mathrm{i}} c_{p_{\mathrm{i}}}}{k_{\mathrm{i}}}, \tag{1.8.5}$$

where i denotes the phase (i $=$ c for continuous phase and i $=$ d for dispersed phase); μ [Pa·s^{-1}] is the dynamic viscosity, u [m·s^{-1}] the superficial velocity, ρ [kg·m^{-3}] the density, c_p [J·kg^{-1}·K^{-1}] the heat capacity, and k [W·m^{-1}·K^{-1}] the thermal conductivity; d_{d} [m] and L_{d} [m] are the droplet diameter and system length, respectively, and R_{d} [m] the droplet radii of curvature; g [m·s^{-2}] is the gravitational acceleration, and σ [N·m^{-1}] the interfacial tension; K [m^2·s^{-1}] simultaneously defines the diffusion coefficient D (species transport) and thermal diffusivity $k_{\mathrm{i}}/\rho_{\mathrm{i}} c_{p_{\mathrm{i}}}$ (heat transport). $L_{\mathrm{d}}/u_{\mathrm{d}}$ [s] is the average residence time of each droplet, d_{d}^2/D [s] the characteristic timescale for radial diffusion, and $d_{\mathrm{d}}^2 \rho_{\mathrm{i}} c_{p_{\mathrm{i}}}/k_{\mathrm{i}}$ [s] the characteristic timescale for thermal conduction [68].

The interfacial tension (σ) controls the evolution of the interface of the two phases when the droplets are shaping [37], [69]. At the interface, an additional amount of energy remains, described by the different states experienced by the molecules from either bulk state, which is expressed by

$$\sigma = \left(\frac{\partial G}{\partial S_A} \right)_{T,P}, \tag{1.9}$$

where G [J·mol^{-1}] is the Gibbs free energy of the entire system and S_A [m^2] the interfacial area. When the two immiscible phases contact with each other, they tend to maintain an interface that is as small as possible to attain a lower amount of energy [37]. The capillary pressure difference across the interface between the two phases ($P_{\mathrm{d}} - P_{\mathrm{c}}$) [Pa], dispersed (d) and continuous (c) can be calculated using the *Young-Laplace equation* by

$$P_{\mathrm{d}} - P_{\mathrm{c}} = \sigma \left(\frac{1}{R_{\mathrm{d}}} + \frac{1}{R_{\mathrm{c}}} \right), \qquad (1.10)$$

where R_{d} [m] and R_{c} [m] are the principal radii of curvature. A schematic representation of the droplet formation in a microchannel and the main involved forces and variables is shown in Figure 1.5.
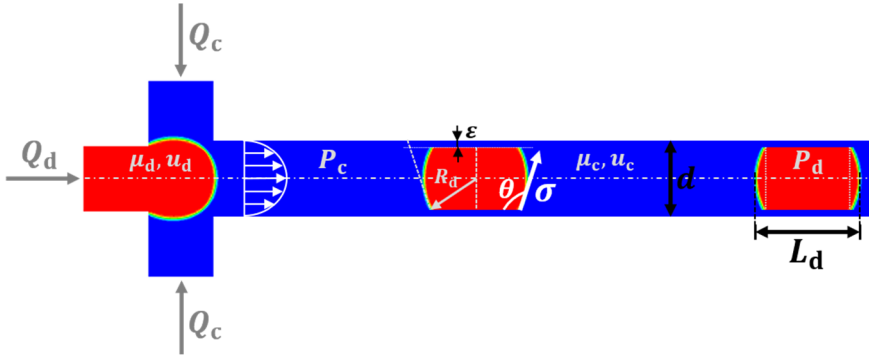

Figure 1.5. Sketch of immiscible droplets in a microchannel and involved forces and variables. [Q_{d} and Q_{c} define the flow rate of the dispersed (red) phase and continuous (blue) phases, respectively; μ_{c} is the dynamic viscosity, u_{c} the superficial velocity, and P_{c} the pressure of the continuous phase; μ_{d} is the dynamic viscosity, u_{d} the superficial velocity, and P_{d} the pressure of the dispersed phase, R_{d} is the radii of curvature, σ the interfacial tension, and θ the contact angle; L_{d} is the droplet length, d the microchannel diameter, and ε the film thickness].

Flow regime and droplet generation

The droplet formation at the entrance of a microchannel results from the interaction between two stresses – fluid shear force and surface tension –, at an unstable interface [57], which implies that the imposed force is large enough to disturb the interfacial tension [67]. The droplet length results from the balance between these two stresses [35]. The breakup process is exclusively governed by the fluid flow, consisting of two stages: the blocking stage [Figure 1.6-(a)] and the squeezing stage [Figure 1.6-(b)] [44]. When the neck breaks up, part of the liquid is injected into the droplet, and the remaining liquid in the head of the bulk liquid is used to form the next droplet. The composition of the neck will significantly influence the volume fraction of the new droplet [70]. Further

perspectives on droplet generation and flow regime are provided in Chapter 2 since a detailed hydrodynamics study is carried out there using experimental and numerical approaches.
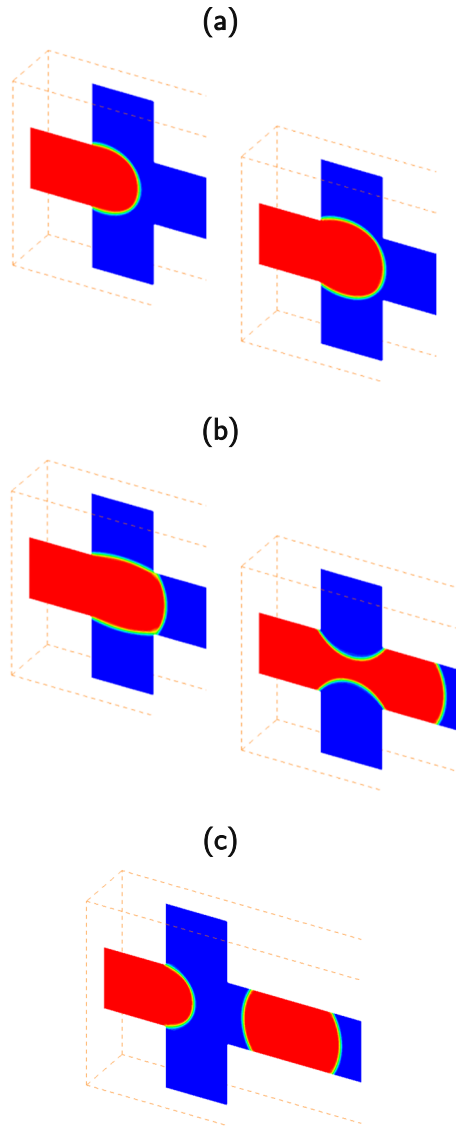
(a)

(b)

(c)

Figure 1.6. Schematic representation of the sequential droplet stages before the breakup in a microfluidic flow-focusing geometry: **(a)** Blocking and **(b)** squeezing stages, and **(c)** droplet generation. [Dispersed and continuous phases represented in red and blue, respectively].

Commonly, the possible hydrodynamic configurations for the droplet generation in two-phase immiscible flows are cross-flow (*T*-junction), flow-focusing, and co-flow. Figure 1.7 displays schematic representations of the droplet generation in different geometries at the squeezing regime.
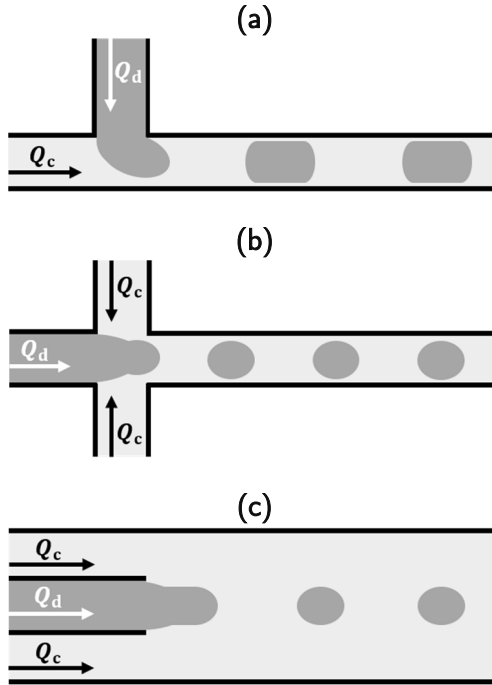
Figure 1.7. Schematic representation of the droplet generation in different microfluidic junctions at squeezing regime: **(a)** Cross-flow, **(b)** flow-focusing, and **(c)** co-flow [Q_d and Q_c define the flow rate of the dispersed (dark grey) and continuous (light grey) phases].

A fluid flow map can be divided into squeezing, dripping and jetting regimes. In the *squeezing* regime (low Ca values), the interfacial tension dominates and, consequently, the generated droplet tends to assume a spherical shape. On the opposite side, when Ca values are high (*jetting* regime), the viscosity controls the droplet formation. At this point, the droplets are easily deformed in the continuous phase by assuming an asymmetric shape [44], [67], [71].

Transport phenomena

At the microscale, one of the main problems is to promote efficient mixing between two fluid streams. Mixing is achieved by taking advantage of the relevant small length/liquid volumes [65]. Although the small diffusion distance is characteristic of the microscale, long mixing time scales are still observed since diffusion constitutes the main contribution [34]. Typically, the micromixers are categorized based on the energy source in passive systems (hydrodynamic principles, *e.g.* device geometry) and active (external perturbations, *e.g.* pressure field, ultrasound irradiation) ones [29], [34], [42], [44], [47], [51], [72]–[74]. During the design of a micromixer, the main goal is to increase the specific interfacial area between the phases [30], [51], [52], [65] by minimizing the diffusional distances and increasing the contact time to induce fast mixing between fluid phases [72], [75], [76]. Thus, the contact line, shape and size of the interface can be precisely controlled [34], [52], [57], [72]. Further aspects of the characterization of transport phenomena in droplet microfluidics are highlighted in Chapter 3.

1.3   Challenges

Protein crystallization is an interdisciplinary research field where the process fundamentals are still not completely well-known and characterized, particularly nucleation (Chapters 5 and 6). Due to the stochastic nature of the entire process and the multiplicity of variables involved, protein crystallization is a challenging scientific topic. Therefore, the validation of the experimental conditions at which a certain protein crystallizes requires the performance of a large number of assays. Droplet microfluidics seems to emerge as a reliable answer to address the current limitations by enabling experimental conditions that are difficult to attain at the macroscale (Chapter 4).

Droplet-based microfluidics integrates soft-matter physics, biochemistry, and microsystems engineering [41], [50], [77]. This tool allows an independent control of each droplet, which behaves as an individual and isolated microreactor with unique physical and chemical properties [19], [52]. This constitutes one of the driving forces for the applicability of these devices for protein crystallization applications. However, the production of

droplets with a certain volume under a well-controlled generation frequency is still a challenge (Chapters 2 and 3).

In summary, stable and uniform droplets with a precise volume are a consequence of the unique features at the microscale. An important question to be addressed is the construction of new devices (*i.e.* development of new materials and fabrication techniques, and surface patterning), as well as control of the fluid pattern (*i.e.* integration and automation of microfluidic platforms) [38].

1.4   Motivation

The main focus of protein crystallization has been in the production of high-quality crystals for three dimensional (3D) structure determination by X-ray crystallography [13]–[19]. The insight gained from a 3D protein structure has a crucial impact on fundamental research in *e.g.* biochemistry and biology, which has led to considerable progress in molecular biology. But it is also of formidable value in the pharmaceutical industry, from rational drug design for the creation and discovery of new drugs and pharmaceutical products to genetic engineering of proteins. However, protein crystallization is still a complex and multiparametric process, involving thermodynamic and kinetic features, as well as the optimization of several variables (see Table 1.3), where there is not yet an accurate theory to substitute for empirical approaches [14], [17]. A schematic representation of the main features and variables involved in protein crystallization is displayed in Figure 1.8. Protein crystallization is a highly stochastic process in which certain conditions must be met for the process to take place [78], such as:

1. Protein: The protein itself is the main variable of the process. A protein must be inherently crystallisable;

2. Thermodynamics: Establish the necessary but not the sufficient conditions for crystallization;

3. Kinetics: Determine whether the thermodynamics outcome will be accomplished.
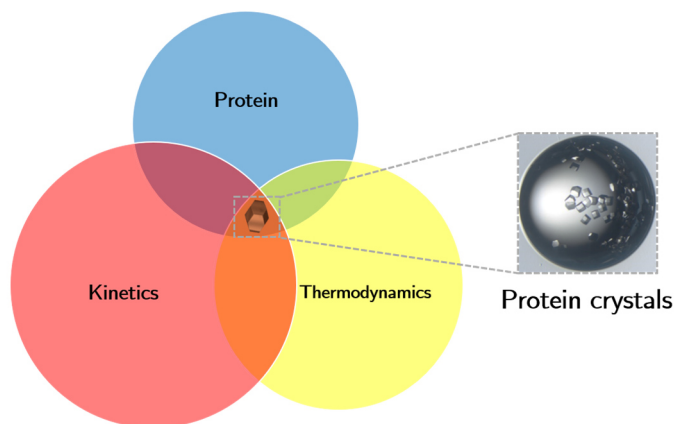
Figure 1.8. Schematic representation of the main features involved in protein crystallization, where the working window is highlighted. At this point, all the conditions are gathered, and a protein crystal is produced.

Table 1.3. Summary of the main protein, thermodynamic, and kinetic features involved in crystallization [14].

Protein	Thermodynamics	Kinetics
- Protein structure - Protein purity and homogeneity	- Solubility line (*e.g.* temperature, pH, precipitating agent, buffer solution) - Presence of metastable phases - Presence of polymorphs - Liquid-liquid separation	- Nucleation and crystal growth (*e.g.* crystallizer geometry and dimensions, transport phenomena mechanisms, heterogeneous interfaces)

Due to the highly variable nature of protein crystallization, especially associated with the highly probabilistic nature of nucleation, it is often a matter of trial-and-error to successfully crystallize a protein. Currently, this methodology relies on testing a large number of potential crystallization conditions, while consuming large amounts of protein, without any theoretical background as guidance. Since proteins are usually available in low quantities, high-throughput experimental methodologies for the acquisition of relevant thermodynamic and kinetic data, as well as a more systematic crystallization strategy are needed. In this context, droplet-based microfluidic devices represent an attractive tool for high-throughput screening experimentation [16], [19], [28], [35], [49], since each droplet is defined as an independent microreactor, allowing to carry out a large

number of experiments under identical conditions. Thus, this offers more flexibility, while requiring minimal material consumption [79]. Furthermore, droplet microfluidics provides unique transport phenomena characteristics when compared to larger-scale systems, such as precise control of molecular diffusion and crystal nucleation due to the confined volume [80]. Droplet-based microfluidics has emerged considerably over the past decade with the development of liquid-liquid flows for a wide range of fields and applications [32], where protein crystallization in micro- to nanodroplets is among the examples [17], [28], [41], [81].

1.5   Aim

This thesis aims to improve the current understanding of protein crystallization processes, with a focus on the nucleation step, in droplet microfluidic devices. Therefore, this study intends to result in a combined approach involving a more complete characterization of the transport phenomena (momentum, mass, and energy) occurring in droplet flow, and in better control of protein nucleation. In particular, the specific objectives are to:

1. Design and characterize a droplet-based microreactor through a complete investigation of the hydrodynamics and transport phenomena involved by combining experimental and numerical approaches;

2. Develop more rational screening methodologies to crystallize proteins by using phase diagrams;

3. Investigate experimental strategies to promote and control protein nucleation by, simultaneously, decreasing the energetic barrier for nuclei formation and avoiding the occurrence of precipitation;

4. Provide a preliminary fundamental and structural understanding of a protein crystallization process, particularly the early stages of nucleation.

1.6   Outline

This dissertation is divided in seven chapters, which correspond to the main developed tasks during the time frame of this study. An introductive perspective to the scientific topic is presented in Chapter 1. The initial chapters are dedicated to droplet microfluidics (cause), while the last chapters focus on protein crystallization (consequence).

Chapter 2 introduces general concepts for the design and construction of a droplet-based microreactor to fully fulfil the demands of a protein crystallization application. Additionally, a hydrodynamics study is conducted by combining experimental and numerical simulation results. Further on, the transport phenomena characterization is presented in Chapter 3. This includes the implementation of scalar transport equations on the customized solver developed in Chapter 2.

Chapter 4 is dedicated to phase diagrams as a design of experiments (DOE) tool for the study of protein phase behaviour, where thermodynamic and kinetic contributions are estimated. Based on the insight gained from this chapter, Chapter 5 describes crystallization strategies to overcome the challenge of, simultaneously, promote and control protein nucleation, including the application of external stimuli. This extensive investigation is carried out for a model protein, lysozyme. The protein crystallization study proceeds until Chapter 6, with a more complex protein, insulin. This chapter intends to outline fundamental and structural perspectives of a protein crystallization process, with the main focus on the early stages of nucleation. Finally, Chapter 7 concludes with the summary of the main findings and highlights open questions the dissertation does not (or could not yet) address.

In summary, the applicability focus of this work is to highlight the performance of a droplet-based microreactor to study protein crystallization kinetics, namely nucleation, and to provide insight into the crystallization mechanism. This is mostly achieved through a combination between: (i) experimental (screening of crystallization conditions and construction of phase diagrams) and (ii) numerical perspectives (microreactor design and transport phenomena characterization).

2. Design of a droplet-based microreactor

"Can you measure it? Can you express it in figures? Can you make a model of it? If not, your theory is apt to be based more upon imagination than upon knowledge."

– William Thomson, *The Lord Kelvin* (n.d.).

Section 2.3 is published in:

J. Ferreira, F. Castro, F. Rocha, S. Kuhn. Protein crystallization in a droplet-based microfluidic device: Hydrodynamics analysis and study of the phase behaviour. *Chemical Engineering Science*, **191**(14): 232–244. 2018;

as part of the methodology and results discussion on the hydrodynamics study. The numerical analysis is extended, and the coalescence mechanism is analysed.

Author contributions

J. Ferreira conceived the research, conducted the experiments and numerical simulations, and wrote the article.

This chapter introduces the design of a droplet-based microreactor to be further explored for protein crystallization applications. Along this Chapter 2, a detailed hydrodynamics study is conducted by combining experimental results, numerical simulations and empirical correlations. Afterwards, the transport phenomena characterization is conducted in

Chapter 3. Finally, along Chapters 4–6, protein crystallization experiments are performed in the developed microreactor.

2.1   Introduction

Protein crystallization in droplets has become a popular topic during the last decade and represents an attractive tool for high-throughput screening experimentation [16], [19], [28], [35], [49]. Each droplet acts as an independent microreactor, thus enabling to perform a significant number of assays under identical conditions [79]. This segmented flow system creates discrete volumes using immiscible phases, where the droplets (dispersed phase) are generated within a second immiscible carrier fluid (continuous phase) along the microchannels [65] as displayed in Figure 2.1.
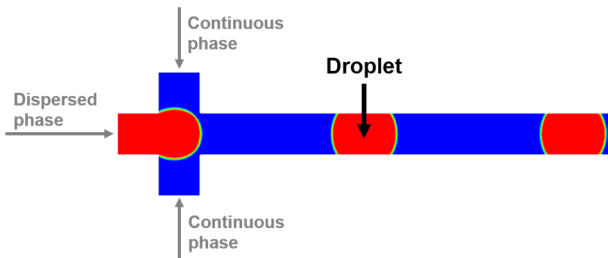
Figure 2.1. Schematic representation the droplet generation in a microfluidic flow-focusing geometry with the indication of the phase entrances. [Dispersed and continuous phases represented in red and blue, respectively].

2.2   Reactor design considerations

The reactor design comprises the first step before its experimental application. For the current application – protein crystallization in microdroplets – the main requisites are temperature control and microchannel wall stability over long crystallization times as well as visualization capabilities for further image analysis. This implies that the reactor consists of several parts, which need to be assembled in a single device. Compared to the traditional fabrication strategies, 3D-printing technology offers the versatile aspect of generating separate CAD files, which can be printed using several polymers under the necessary resolution. Preliminary drawing tests were conducted using *AutoCAD* [82] and 3D-printed by *Antleron* [83] by testing different transparent polymers and coating strategies. Although stereolithography (SLA) (direct micromachining) has been reported as a feasible option [84], this iterative process revealed diverse limitations in terms of the printing resolution/precision and surface varnishing.

A schematic representation of the full crystallization platform is shown in Figure 2.2. As soon as the temperature in the crystallization platform reaches steady-state, each experiment starts by filling the two independent parts of the reactor [PFA tubing enters in (1) and leaves in (2), Figure 2.2-(a.1) and section (5) – Figure 2.2-(a.2) with the continuous and dispersed phases]. The PFA tubing is fixed in section (5) and assembled between the upper (3) and lower (4) plates. Temperature control is enabled by counter-current fluid recirculation between upper/lower plates and section (5). Preliminary experiments were carried out to ensure that a uniform temperature profile along the platform is achieved and the heat conduction due to the thickness of the different layers' walls does not compromise the heat transfer. This is further explored and characterized in Chapter 3. This procedure ensures that the crystallization assays are performed at a constant initial supersaturation ratio.
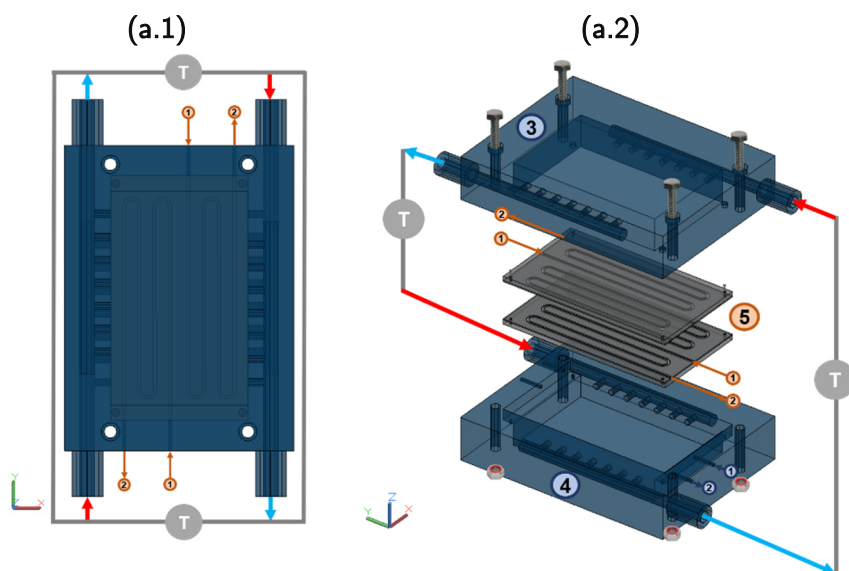
Figure 2.2. Schematic representation of the crystallization platform used during the crystallization assays: **(a.1)** Top and **(a.2)** side views. [(1) Inlet and (2) outlet for the PFA tubing connection, (3) top and (4) bottom plates of the platform used for the integration of temperature control with fluid recirculation, and (5) covers to fix the PFA tubing].

The different assembled parts are 3D-printed using normal resolution stereolithography (*Protolabs* Ltd [85]) and WaterShed XC 11122 as the material and an additional varnishing step to improve transparency. However, a distinct crystallization platform is presented in more detail along Chapter 4. The crystallization process takes place in a tubular crystallizer (PFA tubing). Although different materials and designs of microfluidic devices have emerged for protein crystallization experiments over the last decade [14], [15], [93]–[98], [16], [86]–[92], PFA is still a valuable option due to the flexibility, low price, no detectable evaporation over time, and solvent compatibility. These requisites are not fulfilled by other materials, such as PDMS, where the material swelling over time constitutes a limitation for long time range experiments. Additionally, the continuous phase fluids used along this work (silicon oil and fluorinert FC-70) present a good wettability with PFA [92]–[95], which is a requirement for the current droplet-based crystallization experiments.

2.3   Droplet formation

The droplet breakup and size are determined by the hydrodynamic conditions (*i.e.* cross-flow, co-flow or flow-focusing) and the flow rates of the two fluids. These combined effects will determine the regime of droplet formation (*i.e.* size and frequency of the droplets) [19], [35], [99]. Furthermore, droplet-based microfluidics provides unique experimental approaches when compared to larger-scale systems, such as enhanced control over molecular diffusion and protein crystal nucleation [80]. Controlling the droplet volume is important to achieve a better understanding of the nucleation phenomenon [98], [100], which has not yet been explored in detail. Only the works reported by Zhang *et al.* (2017, 2015) [93],   [101],   Hammadi *et al.* (2013) [98], Roberts *et al.* (2010) [102],   and   Akella *et al.* (2014) [103]   present contributions to justify the crucial influence of the droplet volume on protein crystallization.

Experimental procedure

The initial droplet-based microfluidic platform consisted of a Teflon tube (PFA tubing 1/16'' OD × 0.040'' ID × 5 ft, *IDEX Health & Science*) fixed by an acrylic plate and then jacketed to control the temperature through a water bath (*Huber – Ministat 125*, accuracy $\pm$ 0.02 °C). Syringe pumps (*NE-4000, New Era, USA*) were used to control the flow rates of both phases. Glass syringes (*Fortuna Optima$^{\circledR}$ Ganzglasspritze, Poulten & Graf GmbH*) were used to improve flow rate control and avoiding pulsation [104].

The microfluidic platform was placed under an optical microscope (*Nikon SMZ1500 Stereoscopic Zoom Microscope* with a *Nikon DS-2M digital camera*) to monitor the droplets. Time-lapse images were post-processed for further analysis (including the determination of the static contact angle) using the *NIS-Elements Basic Research Imaging software* [105]. The characterization of the droplet length distribution was done using an image analysis methodology reported by Ferreira *et al.* (2011, 2012) [106], [107]. The experimental set-up involves three main sections (I–IV) as shown in Figure 2.3.
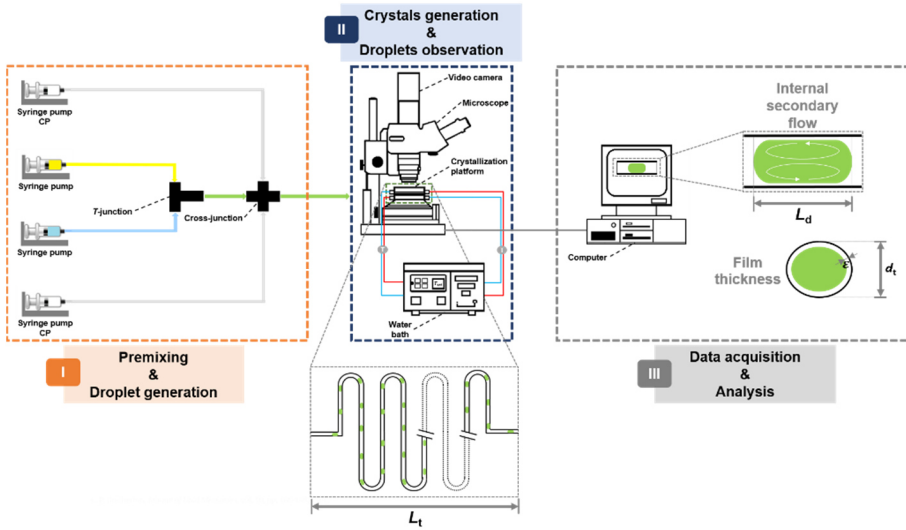
Figure 2.3. Schematic overview of the experimental set-up: **(I)** Solutions mixing and droplet formation: Injection of dispersed (*T*-junction) and continuous (flow-focusing junction) phases using syringe pumps; **(II)** Droplet incubation and analysis: Microfluidic platform with an integrated temperature controller [L_t defines the Teflon tube length]. Experiments are monitored by optical microscopy; **(III)** Data acquisition and analysis: Droplet length measurement by image analysis techniques [L_d defines the droplet length, d_t the Teflon tube diameter (1 mm), and ε the film thickness].

The fluid connections consist of a *T*-junction (Tee Tefzel 1/16'' 0.020'' thru-hole) for the mixing of the aqueous solutions (protein and NaCl solutions), and a flow-focusing junction (Cross PEEK 1/16'' 0.020'' thru-hole), where the dispersed (aqueous solution) and continuous phase (silicon oil, *Hampton Research*^{TM}) (organic solution) meet, thus forming droplets. A preliminary numerical study is also conducted for choosing the contacting geometry. The flow-focusing junction was connected to a serpentine Teflon tube and the generated droplets were distributed continuously along its entire length (1.2 m).

Fluid flow segmentation

Experiments are performed in a tubular microreactor at low Ca numbers (4.1×10^{-5}–2.3×10^{-4}), resulting in a broad range of droplet lengths. The physical properties of the studied liquids are listed in Table 2.1. Silicon oil (purchased from *Hampton Research*^{TM}) is commonly used as a continuous

phase, due to its good wettability of Teflon surfaces. Therefore, it is possible to generate aqueous droplets avoiding contact with the Teflon wall, preventing possible protein adsorption by the microchannel surface and, at the same time, increasing the frequency of droplet generation. It is assumed that the protein and precipitating agent aqueous solutions are sufficiently diluted to neglect a concentration effect on the physical properties of the fluids. Shear viscosity and interfacial tension are measured using a rotational rheometer (*Physica MCR301, Anton Paar*) and a Du Nuöy ring tensiometer (*Biolin Scientific Sigma 701*), respectively. The rheometer, a cone and plate geometry, is coupled to a Peltier temperature control system set at 20 °C. For both measurements, at least, three repetitions are done.

Table 2.1. Physical properties of the fluids (continuous and dispersed phases) at $T = 20$ °C.

Fluid	Density, ρ [kg·m^{-3}]	Dynamic viscosity, μ [mPa·s]	Interfacial tension, σ [mN·m^{-1}]	Contact angle, θ [°]
Water (dispersed phase)	1000	1.0		
			38.7	120
Silicon oil (continuous phase)	827	0.95		

Numerical simulations

The droplet formation in a flow-focusing geometry is also numerically studied using Computational Fluid Dynamics (CFD). Numerical simulations can facilitate the design of microfluidic devices for protein crystallization experiments, as reported by Zhang *et al.* (2015) [94], Wang *et al.* (2013) [108], Ngo *et al.* (2015) [109], Li *et al.* (2014) [110], and Wang *et al.* (2015) [111]. Furthermore, simulations of the droplet formation can be used to reduce the number of costly and time-consuming experiments. Different models have been proposed following Lagrangian (*i.e.* Moving Mesh and Front-Tracking) and Eulerian (*i.e.* Volume-of-Fluid, Level-Set and Phase Field) approaches with commercial and open-source software [33].

At a preliminary stage, the Eulerian Level-Set (LS) approach was adopted to predict the droplet formation in 2D microfluidic junctions. Besides the

apparent accuracy associated with LS, this methodology suffers from the lack of mass conservation, while the simulations are computationally demanding [33]. In the end, Volume-of-Fluid (VOF) interface capturing approach was selected to predict the droplet formation in the flow-focusing geometry. The particular challenge of the numerical study is related to the low Capillary numbers (see Table 2.2), as this dominance of surface tension is known to introduce spurious currents in the solution [112]. For computations, we used OpenFOAM-5.x [113] and the *interFoam* solver with the extension of the "interfaceProperties" library [114], which was initially reported by Hoang *et al.* (2013) [115]. In the following, we briefly summarize the governing equations and the solution schemes [69], [84]. Assuming incompressible flow and Newtonian behaviour, the two-phase flow is governed by the conservation of mass (continuity equation) as

$$\nabla \cdot \mathbf{v} = 0, \tag{2.1}$$

where $\mathbf{v}$ [m·s^{-1}] is the velocity field, and the conservation of momentum (Navier-Stokes equations)

$$\rho \left(\frac{\partial \mathbf{v}}{\partial t} + \mathbf{v} \cdot \nabla \mathbf{v} \right) = -\nabla P + \mu \, \nabla^2 \mathbf{v} + \rho \mathbf{g} + \mathbf{f}_\sigma, \tag{2.2}$$

where ρ [kg·m^{-3}] is the fluid density, t [s] the time, μ [Pa·s] is the dynamic viscosity and $\mathbf{g}$ [m·s^{-2}] the gravitational acceleration; ∇P [N·m^{-3}] represents the pressure forces, and $\mathbf{f}_\sigma$ [N·m^{-3}] the surface tension forces. The surface tension force is modelled as a volumetric force by the Continuum Surface Force (CSF) method [116] as

$$\mathbf{f}_\sigma = \sigma \kappa \mathbf{n}, \tag{2.3}$$

where σ [N·m^{-1}] is the interfacial tension, κ [m^{-1}] the interface curvature $\left(\kappa = \nabla \cdot \mathbf{n} \right)$, and $\mathbf{n}$ [-] the interface-normal vector $\left(\mathbf{n} = \frac{\nabla \alpha}{|\nabla \alpha|} \right)$. In addition to the continuity and Navier-Stokes equations, the VOF method solves an advection equation for the phase indicator function (α) by

$$\frac{\partial \alpha}{\partial t} + \nabla \cdot (\alpha \mathbf{v}) = 0, \tag{2.4}$$

where α [-] varies from 0 to 1, with $\alpha = 1$ representing the dispersed phase, $\alpha = 0$ the continuous phase, and grid cells that contain the interface have a value situated between 0 and 1 (Figure 2.4), depending on the volume fraction of each phase. The fluid properties are calculated according to Equations (2.5.1) and (2.5.2) by

$$\rho = \alpha\rho_{\mathrm{d}} + (1 - \alpha)\rho_{\mathrm{c}}, \tag{2.5.1}$$

and

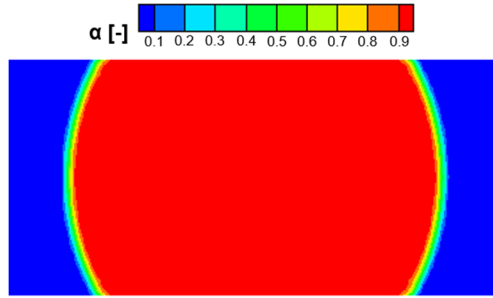$$\mu = \alpha\mu_{\mathrm{d}} + (1 - \alpha)\mu_{\mathrm{c}} \tag{2.5.2}$$

Figure 2.4. Representation of the phase indicator function (α): $\alpha = 0$ (carrier fluid, represented in blue), $\alpha = 1$ (dispersed phase, represented in red), and $\alpha \in \,]0 - 1[$ (interface).

Due to the large gradients in the α field, the phase-fraction equation is penalized by numerical diffusion [117]. To counteract, Equation (2.4) is extended with an interface compression term [3rd term in Equation (2.6)], which is only active in the interface region [118] by

$$\frac{\partial\alpha}{\partial t} + \nabla \cdot (\alpha\mathbf{v}) + \nabla \cdot [u_r\alpha(1 - \alpha)] = 0, \tag{2.6}$$

where u_r [m·s^{-1}] is the relative (compression) velocity.

Since the fluid interface is implicitly represented by the VOF function, the phase fraction variable is discrete, and abrupt changes in its value lead to errors in the calculation of the interface curvature and normal vectors. These errors can induce the appearance of artificial velocity magnitude values where the calculation of the interface forces is more difficult

(*e.g.* regions near the droplet interface and in the recirculation zones inside the droplet). Hoang and co-workers [115] proposed that if the curvature (κ) is computed from a smoothed VOF function ($\tilde{\alpha}$) over a finite region around the fluid interface by

$$\kappa = \nabla \cdot \left(\frac{\nabla \tilde{\alpha}}{|\nabla \tilde{\alpha}|} \right) \tag{2.7}$$

the appearance of non-physical spurious currents could be suppressed. A Laplacian filter was proposed by Lafaurie *et al.* (1994) [112] and the transformation from the VOF function α to a smoother function $\tilde{\alpha}_k$ is done according to Equation (2.8)

$$\tilde{\alpha}_k = \frac{\sum_{f=1}^{n} \alpha_f S_f}{\sum_{f=1}^{n} S_f}, \tag{2.8}$$

where the subscripts k [-] and f [-] represent the cell and face indexes, respectively, and S [m²] is the surface area. This smoothing procedure transforms the indicator function by interpolating it from cell centres to face centres back to the cell centres, which is repeated twice. This is qualitatively represented in Figure 2.5.
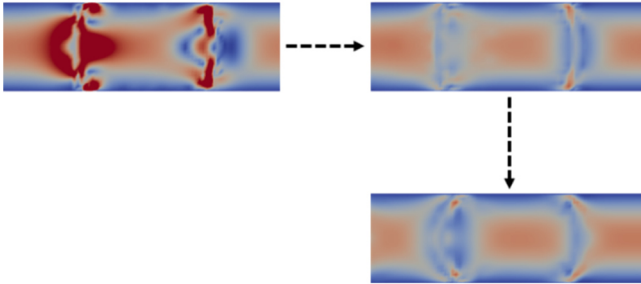

Figure 2.5. Qualitative representation of the smoothing procedure outcome based on the velocity magnitude field with the suppression of the parasitic currents and improvement of the droplet curvature [Red and blue correspond to high and low values of the velocity magnitude, respectively].

The equations are solved using standard numerical schemes (Gauss linear), except for the velocity component advection term and flux of the compression velocity. Furthermore, the advection equation for the volume fraction is solved using an explicit temporal solver with a first-order spatial

discretization scheme. The transient terms are discretized using a first-order explicit Euler scheme and the *MULES* (Multidimensional Universal Limiter with Explicit Solution) explicit solver is used to ensure the boundedness of the phase fraction function. The *PIMPLE* (Pressure Implicit Method for Pressure Linked Equations) algorithm with 2 corrector loops and interface compression is applied for the pressure-velocity coupling to obtain a sharp interface together with a divergence-free velocity field for incompressible flow. In summary, a flowchart of the numerical methodology implemented in the *interFoam* solver is displayed in Figure 2.6.
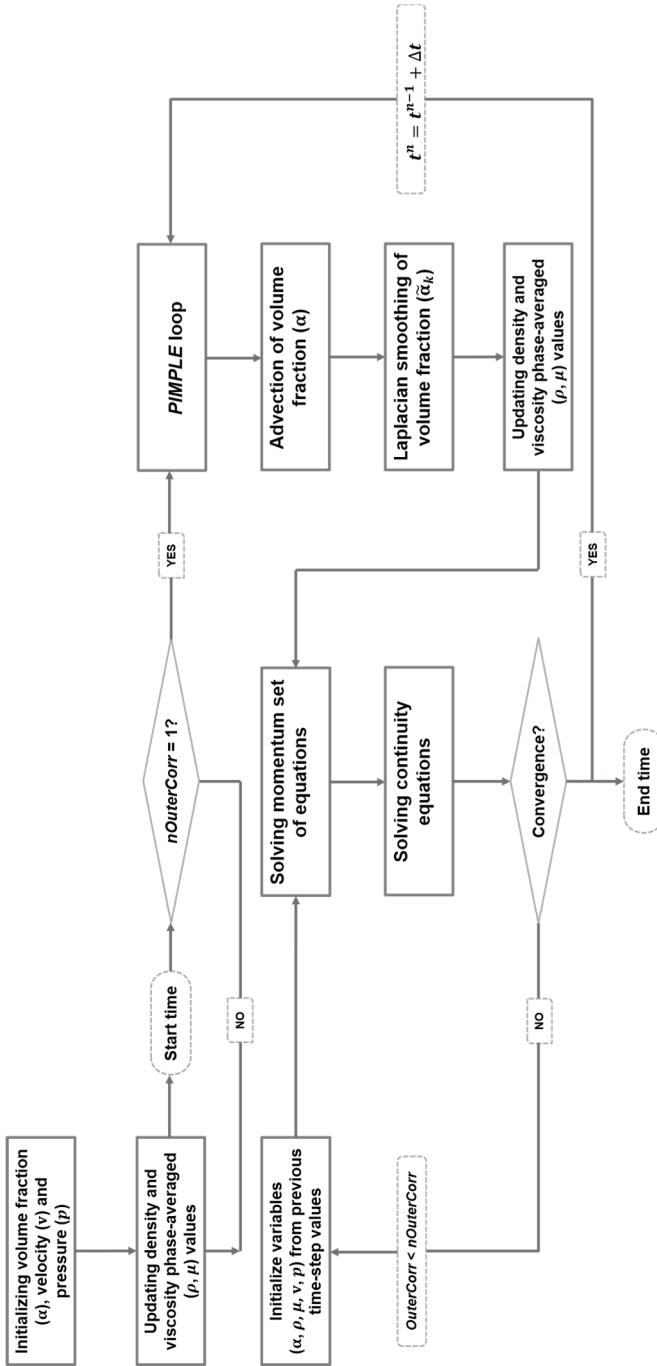
Figure 2.6. Flowchart of the numerical methodology implemented in the *interFoam* solver.

The Courant-Friedrichs-Lewy (CFL) condition was used to limit the time step, which is based on the maximum Courant number (Co) [-] by

$$\mathrm{Co} = \frac{\|\mathbf{v}\|\Delta t}{\Delta x},$$

(2.9)

where $\|\mathbf{v}\|$ [m·s^{-1}] is the velocity magnitude in the cell, Δt [s] is the time-step, and Δx [m] is the cell size in the flow direction. For all considered cases, Co number is limited to 0.5 in the bulk of the phases, and to 0.25 in the interfacial region.

The flow-focusing geometry is reconstructed using *SALOME-8.3.0* [119] and the numerical mesh was generated with the *snappyHexMesh* utility. The entrance lengths (L_{ent}) are calculated to ensure fully developed flow, $L_{\mathrm{ent}} = 0.379\mathrm{e}^{-0.148\mathrm{Re}} + 0.055\mathrm{Re} + 0.26,$ as proposed by Dombrowski *et al.* (1993) [120]. A mesh independency study to achieve stable droplet length was performed, and the final mesh element sizes are $\Delta x_{c,x} = \Delta x_{c,y} = \Delta x_{c,z} = 25$ μm (*blockMesh* utility), with refinement layers near the walls. The mesh convergence occurs for a cell size of 25 μm since an identical droplet length is achieved for cell sizes of 30 μm and 35 μm. The final mesh consists of a total of 538 910 cells. Figure 2.7 illustrates different planes of the discretized solution domain.
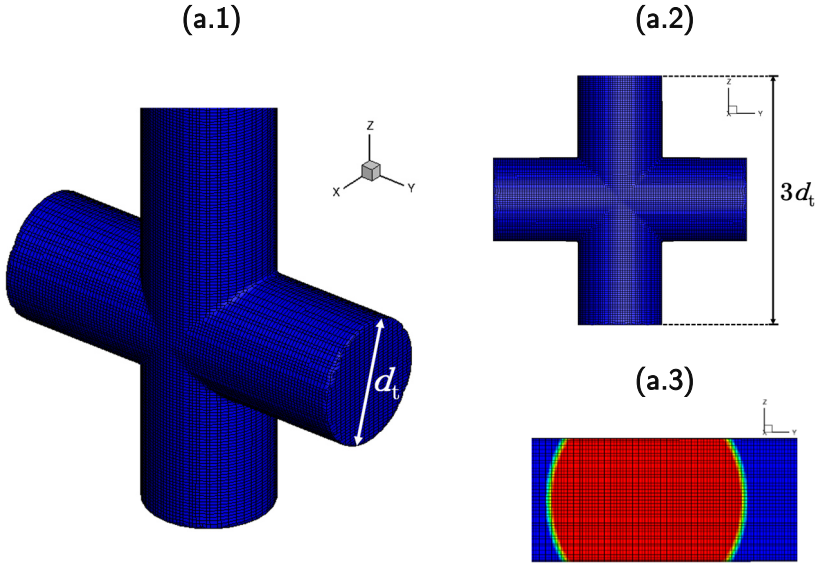
(a.1)   (a.2)

(a.3)

Figure 2.7. Discretized solution domain: **(a.1)** 3D view, **(a.2)** side view (*y-z* plane) of the microchannel entrances [microchannel entrance lengths of 1 mm], and **(a.3)** computed droplet curvature by the VOF method in a 2D plane (*y-z*) [d_t, microchannel (Teflon tube) diameter, 1 mm].

The thickness of the film developing between the droplet interface and Teflon wall (ε [m]) can be estimated using *Bretherton's law* [121], which is expressed in Equation (2.10) for circular sections and low Capillary number values (Ca$_d$ < 0.01) [79], [122].

$$\varepsilon = 1.34 \frac{d_t}{2}\left(\frac{u_d \mu_c}{\sigma}\right)^{2/3} \tag{2.10}$$

For the studied cases, the film thickness is situated in the range of 1.2 −1.7 μm. Thus, the computational mesh is not able to resolve the film. The film capture requires expensive computational capabilities and, consequently, most of the works reported in the literature assume the absence of a liquid film. Simulations performed by Raj *et al.* (2010) [32] showed that for Ca$_c$ < 0.01 there is no film. However, the disappearance of the film only occurs when the flow is stopped (Appendix A − A1).

Although this numerical methodology is introduced in the context of droplet formation in microfluidic junctions, its applicability range is wide within the field of multiphase flow. One of these examples is the simulation of droplets subjected to simple shear flow. The particle-free droplet-matrix

system is numerically simulated to identify streamline profiles, velocity, shear rate and vorticity magnitudes under high viscosity ratios and low interfacial tension values. The observed steady-state particle distributions can partially be explained by shear-induced migration towards zones of low shear rates and/or lower streamline curvature.

Hydrodynamics study

A hydrodynamics study in the squeezing flow regime, which allows a wide range of droplet lengths, is conducted for a range of low values of the Ca number (Ca < 10^{-4}), using experimental and numerical approaches. A Capillary number-based flow map within the squeezing regime for the studied hydrodynamic conditions is depicted in Figure 2.8. The squeezing regime in a flow-focusing geometry is characterized by $Ca_c < 0.1$ and $Ca_d < 0.01$ [123]. These ranges indicate that interfacial tension dominates over the viscous forces during the droplet breakup and formation, controlling the evolution of the interface [79]. In the VOF method, this effect is responsible for the generation of spurious currents (parasitic currents) that tend to appear near the interface and in the recirculation zones of the droplet. This is further explored in Chapter 3, including the implication on the transport phenomena simulations.

The results of the coalescence analysis are shown in Figures 2.9 and 2.10. Droplet generation in the squeezing regime resulted in uniform droplets in an extended range of droplet lengths with good frequency and monodispersity (Figures 2.11 and Table 2.2). Table 2.2 lists the experimental conditions of the studied hydrodynamic conditions.

Table 2.2. Overview of the hydrodynamic points for the studied segmented flow regimes.

Regime	Droplet	Irregular segmented		Plug	
Case	#1	#2	#3	#4	#5
Q_c [ml·min^{-1}]	0.200	0.250	0.200	0.150	0.150
Q_d [ml·min^{-1}]	0.080	0.200	0.300	0.315	0.435
α_c [-]	0.714	0.556	0.400	0.323	0.256
V_d [µl]	0.9	2.1	3.7	8.8	18.3
t_r [min]	11.4	4.6	3.0	2.9	2.1
f_d [s^{-1}]	1.4	2.4	2.9	2.0	1.9

[**Note 1:** Droplet frequency, f_d [Hz]: $f_d = u_d/L_d$].

[**Note 2:** Reactor residence time, t_r [s]: $t_r = L_t/u_d$, where L_t and u_d define, respectively, the length of Teflon tube and velocity of dispersed phase].

[**Note 3:** Droplet volume, V_d [m^3] [124]: $V_d = \pi/12 \left[2L_d^3 - (L_d - d_d)^2(2L_d + d_d)\right]$, where L_d and d_d represent the droplet length and droplet diameter, respectively].
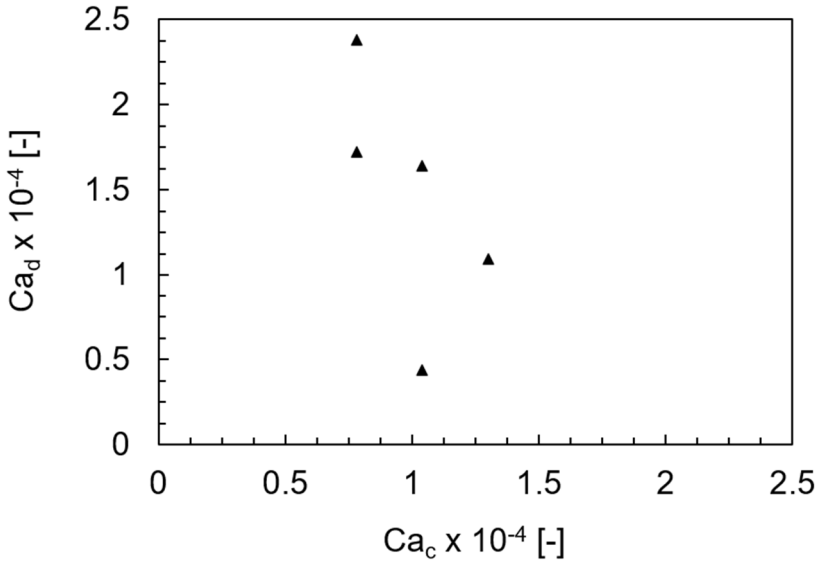

Figure 2.8. Capillary (Ca) number-based flow map in the squeezing regime (see Table 2.2).

During the hydrodynamics study, the droplet length is numerically predicted and experimentally measured. Figure 2.11 depicts a qualitative comparison of the droplet images obtained from experiments and the corresponding simulation results, while in Figure 2.12 the normalized droplet length by the Teflon tube diameter is presented. The numerical results are averaged for the first 5 generated droplets, and the experimental results represent the average of around 750 droplets per experiment.

A very good agreement between the experimental and numerical results is observed, which proves that the applied VOF model is capable to predict the droplet generation in the flow-focusing geometry at low Capillary numbers. The only significant deviation is observed for the experimental point #5 in the plug flow regime that corresponds to the highest Q_d, which also corresponds to the lowest Ca_c (Table 2.2). However, the experimentally observed droplet size distribution (Figure 2.13) for this case is broader compared to the other conditions. Furthermore, for this fluid flow condition, the smallest distance between droplets is observed (Figure 2.11). This effect might explain the shift to larger sizes compared to the numerically predicted droplet length for this fluid flow condition. The critical volume fraction of the dispersed phase (α_d^*) before the occurrence of coalescence can be calculated by

$$\alpha_d^* = \frac{1}{3} \frac{3L_d - d_t}{L_d},$$

(2.11)

where a schematic representation with the geometrical variables is displayed in Figure 2.9.
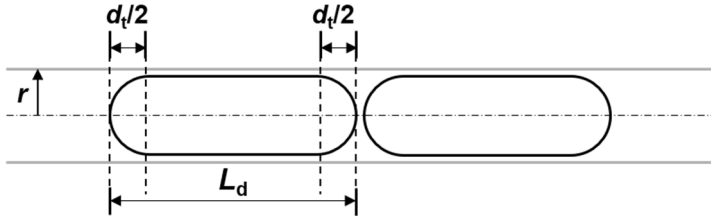

Figure 2.9. Schematic representation of the moment before the occurrence of coalescence and involved geometrical variables. [L_d defines the droplet length, and d_t the Teflon tube diameter (1 mm)].

However, for the studied hydrodynamic conditions, the analytical equation predicts that the experimentally measured droplet lengths still belong to the stable region, even for the highest Q_d (Figure 2.10).
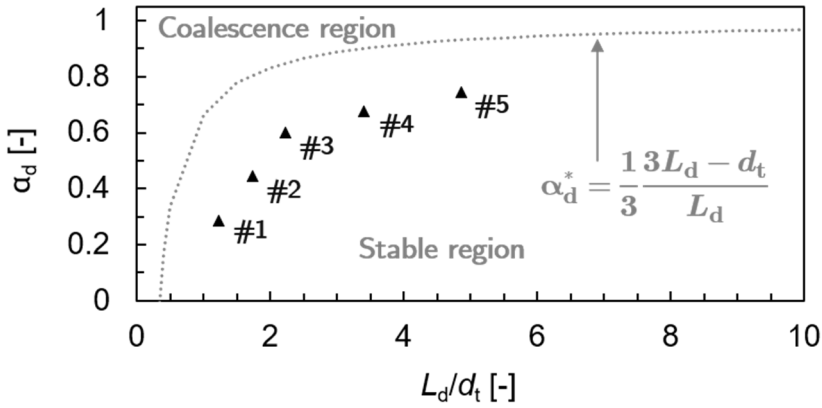
Figure 2.10. Coalescence map regime (defined by stable and coalescence regions) based on the volume fraction of the dispersed phase (α_{d}) in function of the normalized droplet length ($L_{\mathrm{d}}/d_{\mathrm{t}}$) [see Equation (2.11)].
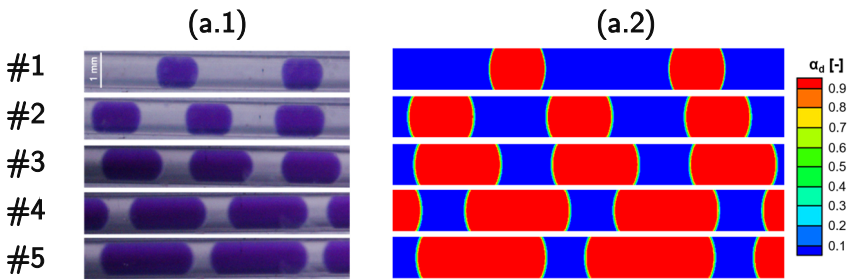
Figure 2.11. Comparison between **(a.1)** experimental and **(a.2)** numerical (volume fraction of the dispersed phase, α_{d}) results obtained in a flow-focusing cylindrical geometry. [A diluted dye solution was used as the dispersed phase to help with the visualization]. [Teflon tube diameter of 1 mm].
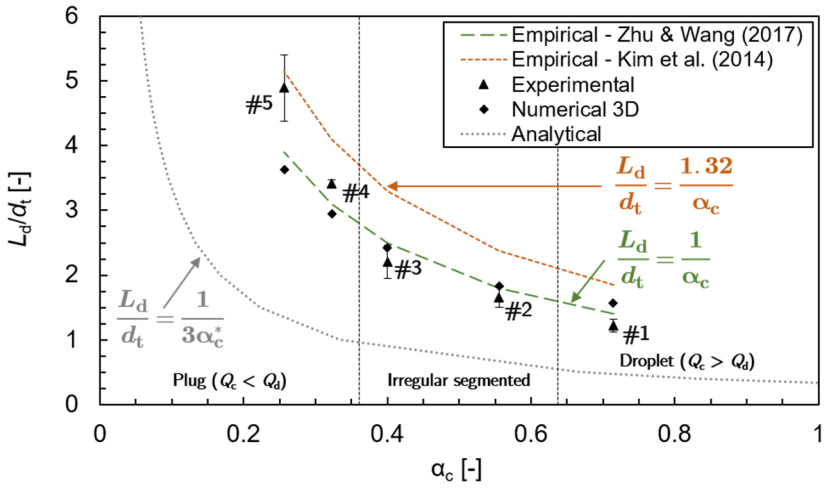
Figure 2.12. Droplet length (L_d) normalized with the Teflon tube diameter (d_t) as a function of the volume fraction of the continuous phase (α_c) in a flow-focusing geometry. Empirical scaling laws: $L_d/d_t = 1/\alpha_c$ [125] and $L_d/d_t = 1.32/\alpha_c$ [126] and analytical equation [see Equation (2.11) ($\alpha_c^* = 1 - \alpha_d^*$)]. [The error bars are standard deviations from, at least, three independent experiments].
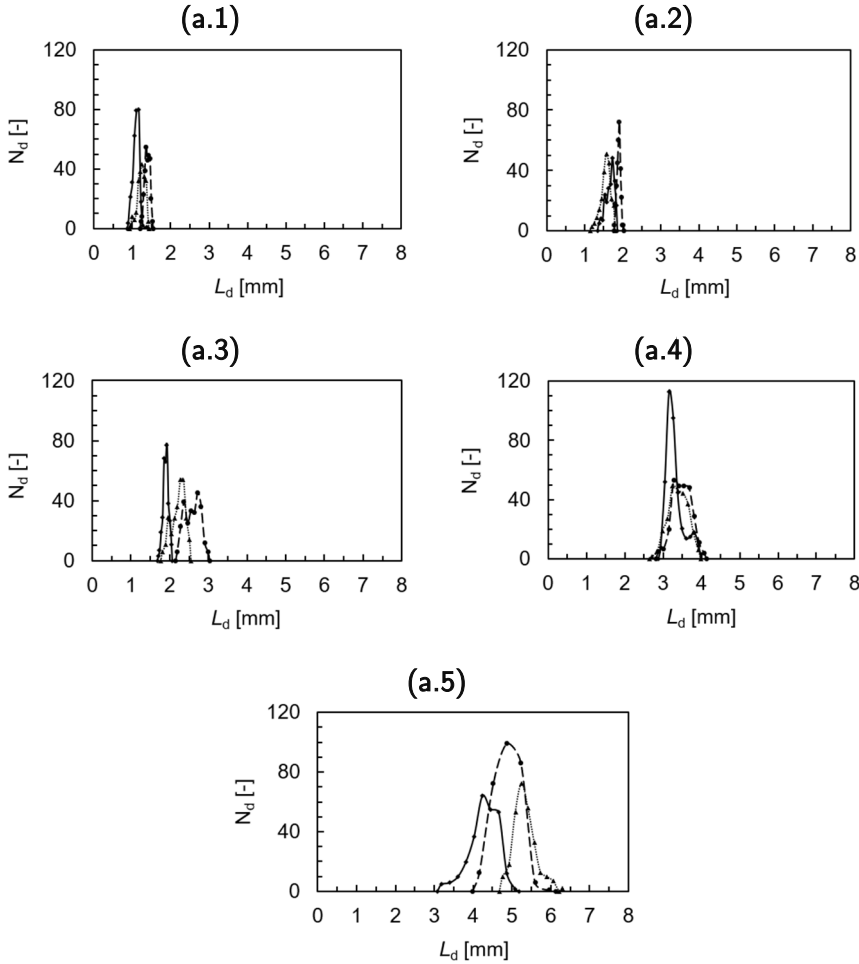
Figure 2.13. Droplet size (L_d) distribution: **(a.1)** Case #1, **(a.2)** Case #2, **(a.3)** Case #3, **(a.4)** Case #4, and **(a.5)** Case #5 (see Table 2.2). [Three independent assays (A) were performed, N_d is the number of droplets].

A comparison of the experimentally and numerically obtained droplet lengths with empirical correlations from literature reveals a good agreement with the correlation reported by Zhu & Wang (2017) [125], represented by Figure 2.12

$$L_d/d_t = 1 + Q_d/Q_c = 1/\alpha_c. \qquad (2.12)$$

Garstecki *et al.* (2006) [127] reported that this correlation is limited to *T*-junction geometries. However, in the squeezing regime and at similar phase

viscosities (Table 2.1), the mechanisms involved during the droplet generation could be considered identical for both hydrodynamic configurations. Furthermore, the empirical correlations are usually obtained for geometries with cross-sections, which can limit the applicability of the power laws [79], [128] (Figure 2.12). The typical form of a correlation to predict the droplet length in a *T*-junction is $L_{\mathrm{d}}/d_{\mathrm{t}} = k_1 + k_2 Q_{\mathrm{d}}/Q_{\mathrm{c}}$ [127].

A proposed correlation to predict the droplet length in a flow-focusing geometry is of the form $L_{\mathrm{d}}/d_{\mathrm{t}} = k_3/\alpha_{\mathrm{c}}$, *e.g.* with $k_3 = 1.32$ as suggested by Kim *et al.* (2014) [126] (Figure 2.14). As one of the empirical correlations overpredicts the experimental droplet length, different power laws $(L_{\mathrm{d}}/d_{\mathrm{t}} = k_1 + k_2 \alpha_{\mathrm{c}}^{-k_3})$ were used to fit the experimental results, which are shown in Figure 2.14. These power laws are able to predict the droplet lengths for all considered values of the continuous and dispersed phase flow rates.
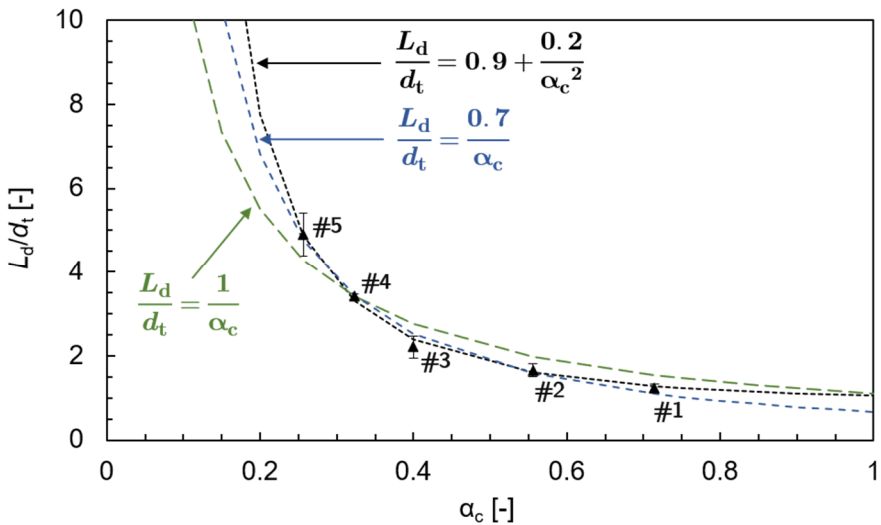
Figure 2.14. Droplet length (L_{d}) normalized with the Teflon tube diameter (d_{t}) as a function of the volume fraction of the continuous phase (α_{c}) in a flow-focusing geometry. The different lines, in the form $L_{\mathrm{d}}/d_{\mathrm{t}} = k_1 + k_2 \alpha_{\mathrm{c}}^{-k_3}$, represent power laws to fit to the experimental results. [The error bars are standard deviations from, at least, three independent experiments].

2.4   Conclusions

Droplet-based microfluidic devices constitute a rational and systematic strategy to address protein crystallization as hundreds of independent microbatch reactors are produced, which introduces a high-throughput methodology. The developed droplet-based microfluidic platform enables the production of uniform and stable droplets with a very good frequency (up to 250 droplets per assay). It also allows large flexibility regarding the generated droplet volume (range of 0.9–18 µl).

The numerical simulations are validated by the experimental measurements and empirical correlations. Furthermore, the VOF numerical approach accurately predicts the droplet curvature and the complex flow topology effects inside the droplets, with significant suppression of the artificial spurious velocities at the interface. However, the impact of the artificial velocities on the simulations increases for low Capillary numbers. Approaches for further suppression should be explored in more detail, especially for simulations of coupled interfacial heat and mass transfer.

3. Characterization of a droplet-based microreactor

"The equations of motion so formed are very complicated, but yet they admit of solution in some instances, especially in the cases of small oscillations."

– George Gabriel Stokes, *1st Baronet* (1880).

Due to the laminar flow in microscale reactors, reagents are expected to mix primarily by molecular diffusion. This is the main premise for the transport phenomena analysis conducted in Chapter 3. The hydrodynamics study was previously discussed in Chapter 2.

3.1   Problem statement

To our best knowledge, although multiphase flow in microfluidics has been extensively studied during the last two decades [19], [28], only four papers have reported numerical approaches to simulate heat transfer in droplet flow. This absence is the driving force for this chapter. A preliminary conjugate solver for heat transfer in droplet flow is developed. Besides the heat transfer analysis of different case studies, this study aims to obtain a general simulation tool for design and optimization purposes.

Urbant *et al.* (2008) [129] explored the influence of the droplet shape on convective heat transfer in a microchannel. Fischer *et al.* (2010) [130] observed that the interfacial tension has a major effect on radial heat transfer. Che *et al.* (2015) [131] concluded that the droplet length does not play a significant role on the heat transfer distribution. More recently, Khater *et al.* (2019) [132] investigated the influence of heat transfer on droplet length based on experimental data. Khater and co-workers found that the droplet length increases when the droplet is heated, and the

droplet velocity increases as witnessed experimentally [132]. Although limited work has been conducted in this field, it seems that the outcomes are not in agreement.

Numerical simulations

The customized *interFoam* solver used in Chapter 2 was updated to the latest OpenFOAM version available at the time, OpenFOAM-7.x. Afterwards, scalar transport equations were coupled to the customized *interFoam* solver by adding the convection-diffusion equation and energy equation, respectively. A schematic representation of the numerical scheme is displayed in Figure 3.1.
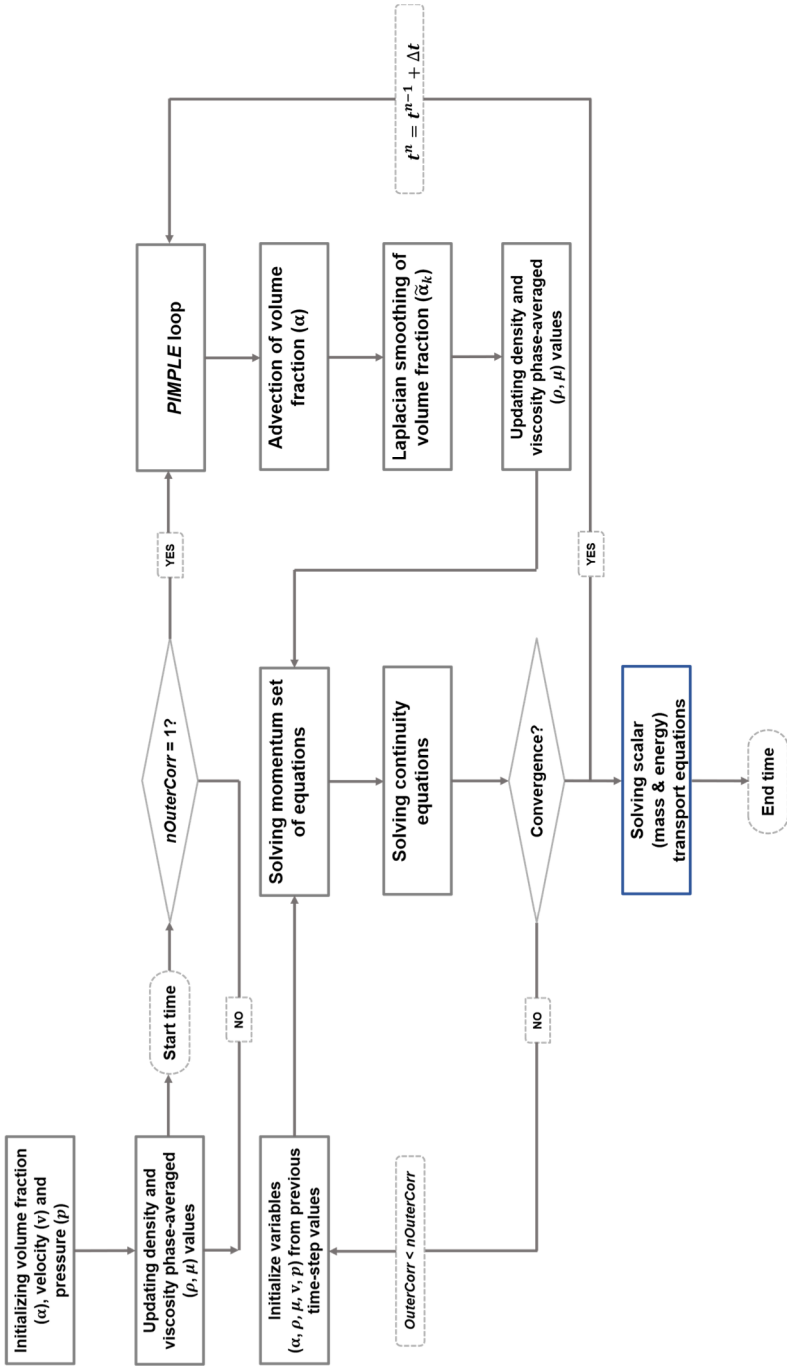
Figure 3.1. Flowchart of the numerical methodology implemented in the *interFoam* solver with the coupling of scalar transport equations.

As highlighted in Chapter 2, the spurious currents tend to appear near the liquid-liquid interface and in the recirculation zones of the droplet, where the calculation of the interface normal vectors [Equation (2.3)] and curvature [Equation (2.7)] are more difficult for low interfacial tension. Figure 3.2 depicts the velocity field streamlines inside and in the vicinity of the droplet interface in a reference frame moving with the droplet. The moving reference frame allows to visualize the secondary flow and resulting recirculation motions. At the lowest Capillary number, Ca_d, recirculation zones also appear outside the droplet, which are non-physical and are caused by the aforementioned spurious currents.
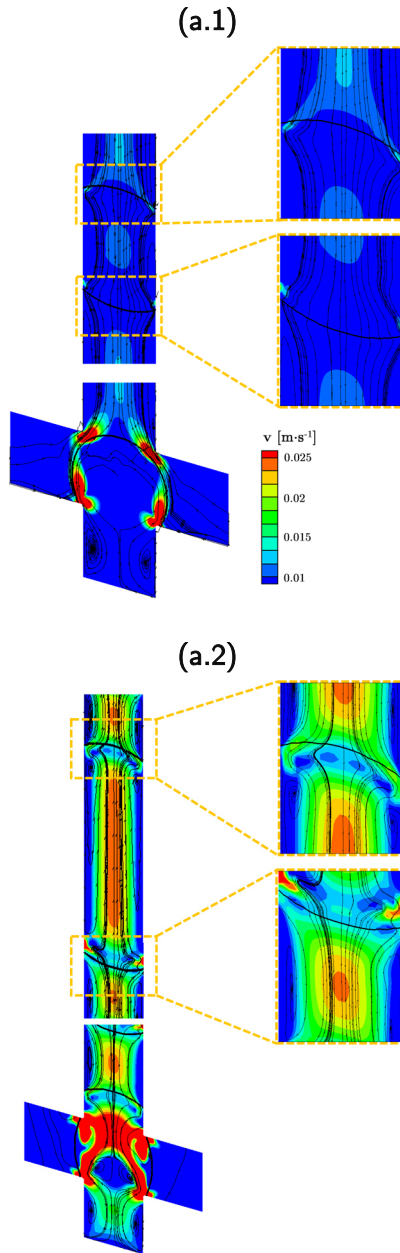
Figure 3.2. Velocity magnitude field [**v**] and streamlines (moving droplet reference frame) (*y-z* plane) (including a close-up of the droplet front/tail) for: **(a.1)** $Ca_d = 4.1 \times 10^{-5}$, and **(a.2)** $Ca_d = 2.3 \times 10^{-4}$. [Recirculation motions outside the droplet and artificial velocity magnitude are caused by non-physical velocities].

These unphysical velocity values are exclusively due to numerical inadequacies during the calculation of the interface curvature and normal vectors. This has a direct effect on the momentum equation for the calculation of the surface tension term [Equation (2.2)]. However, for all the cases, the droplet topology and curvature are apparently not affected by the spurious currents (see Chapter 2, Figure 2.11). The magnitude of the spurious currents increases with decreasing Capillary number, which is also observed in Figure 3.2.

In Chapter 2, a brief discussion about the mesh refinement to resolve liquid-liquid flow hydrodynamic problems was done. However, the mesh refinement level might not be suitable to overcome transport phenomena (*i.e.* mass and heat transfer) problems. Based on a unitary local Péclet number (Pe), a scaling analysis reveals the minimum cell size by considering the convection $[\nabla(\mathbf{v}C_{\mathrm{i}})]$ and diffusion $[\nabla(D_{\mathrm{i}}\nabla C_{\mathrm{i}})]$ contributions

$$\nabla(\mathbf{v}C_{\mathrm{i}}) = \frac{u_0 C_0}{\Delta x_{\mathrm{c}}} \tag{3.1.1}$$

and

$$\nabla(D_{\mathrm{i}}\nabla C_{\mathrm{i}}) = \frac{D C_0}{\Delta x_{\mathrm{c}}^2}, \tag{3.1.2}$$

where u_0 [m·s^{-1}] and C_0 [mol·m^{-3}] are the initial velocity and concentration values, respectively; D [m^2·s^{-1}] is the diffusion coefficient. Thus, since the grid cell Péclet number ($\mathrm{Pe_{local}}$) should remain bounded, the required cell size (Δx_{c}) can be estimated by

$$\mathrm{Pe_{local}} = \frac{u_0 \Delta x_{\mathrm{c}}}{D} \leq 1 \Rightarrow \Delta x_{\mathrm{c}} \leq \frac{D}{u_0} \tag{3.2}$$

Brune & Kim (1993) [133] developed a numerical method to predict the diffusion coefficient for a wide range of proteins in water. The obtained values for *e.g.* lysozyme (a model protein) are very similar to the ones obtained both experimentally and through the application of the Stokes-Einstein equation (modeling the molecule as a simple sphere). This value lies in the order of magnitude of 10^{-11} m^2·s^{-1} [133]. For the studied hydrodynamic cases (Chapter 2), the minimum initial velocity

(corresponding to the velocity of the dispersed phase) is around 10^{-3} m·s^{-1}. Thus, the cell size (Δx_c) is estimated to be on the same order of magnitude as the film thickness (ε). This mesh refinement is computationally demanding, and the potential simulation times go beyond the scope of this work. During the hydrodynamics simulations in Chapter 2, a flow-focusing geometry with circular section was used. Due to this circular section, the uniformity of the mesh refinement is not achieved, even removing any refinement gradient or boundary layers. These uniformities on the cell size distribution seem to disturb the transport phenomena simulation. Therefore, the simulations performed in this chapter were done in a cross-section to ensure equally sized cells. The channel width corresponds to the tube diameter (1 mm) (Chapter 2). The mesh element sizes are $\Delta x_{c,x} = \Delta x_{c,y} = \Delta x_{c,z} = 50$ µm, which corresponds to a final mesh consisting of 321 416 cells. For the studied hydrodynamic conditions, the theoretical film thickness is around 1 µm (10^{-3} mm).

Among the hydrodynamic cases studied in Chapter 2, three cases were selected to extend the transport phenomena analysis conducted in this chapter by representing each of the regimes, droplet, irregular segmented, and plug (see Table 2.2, Chapter 2). The flow rates were kept constant, but the superficial velocities were recalculated to account for the different cross area. Firstly, species transport is investigated in section 3.2. The studied species, protein (lysozyme) and precipitating agent (NaCl) correspond to a replicate of a crystallization experiment (see Chapters 4 and 5). Secondly, the developed conjugate heat transfer solver is tested in section 3.3.

3.2   Micromixing in droplet flow

At the microscale, one of the main concerns is to promote efficient mixing between the liquid streams. Although the main contribution for the mixing efficiency relies on diffusion due to the small diffusion distances, the convective flow during the droplet breakup is still important. As no reactions take place, the scalar transport equation representing the mass conservation of species can be expressed by

$$\frac{\partial C_{\mathrm{i}}}{\partial t} = -\nabla \cdot [-D_{\mathrm{i}} \, \nabla C_{\mathrm{i}} + \mathbf{v} C_{\mathrm{i}}], \tag{3.3}$$

where i defines the species (lysozyme, NaCl), C [mol·m^{-3}] the concentration, D [m^2·s^{-1}] the diffusion coefficient of the species in a certain solvent (water). The initial concentration of lysozyme and NaCl (before the mixing takes place) are 80 mg·ml^{-1} and 60 mg·ml^{-1}, respectively. The first term $(\partial C_{\mathrm{i}}/\partial t)$ represents the variation of species concentration in function of time, the second term $(D_{\mathrm{i}} \, \nabla^2 C_{\mathrm{i}})$ (diffusion contribution) corresponds to the species transport according to its gradient, and the last term $(-\mathbf{v} \cdot \nabla C_{\mathrm{i}})$ (convection contribution) represents the species quantity moving across the boundaries due to fluid flow. In OpenFOAM-7.x, a built in *functionObject* named *phaseScalarTransport* can be added to the customized multiphase solver (Chapter 2). When added to Equation (3.3), it implies a zero-flux condition on the fluid-fluid interface by avoiding the transport of species across the interface. Therefore, this *functionObject* is only valid if the species are soluble in one phase (dispersed phase), but immiscible in the other phase (continuous phase). A modified version of *phaseScalarTransport* with a custom added term is used for the temperature variable diffusion coefficient of the species. The Arrhenius-type equation is used to describe this temperature dependency by

$$D_{T,\mathrm{i}}\,(T) = D_{T_0,\mathrm{i}} \, \exp\left(-\frac{E_{a,\mathrm{i}}}{R_{\mathrm{g}}T}\right) \tag{3.4}$$

where D_{T_0} [m^2·s^{-1}] is the pre-exponential coefficient, E_a [J·mol^{-1}] the activation energy, R_{g} [J·mol^{-1}·K^{-1}] the ideal gas constant, and T [K] the absolute temperature. From the reported literature, $D_{T_0,\mathrm{NaCl}} = 1.1 \times 10^{-9}$ m^2·s^{-1}, $E_{a,\mathrm{NaCl}} = 2070$ J·mol^{-1} [134], and $D_{T_0,\mathrm{lys}} = 7.6 \times 10^{-11}$ m^2·s^{-1}, $E_{a,\mathrm{NaCl}} = 5941$ J·mol^{-1} [135]. Finally, the diffusion coefficient (D_{ij}) [m^2·s^{-1}] of the diluted binary mixture (lysozyme, NaCl) is estimated by [136]

$$D_{T,\mathrm{ij}} = \frac{C_{\mathrm{i}}^0}{C_{\mathrm{i}}^0 + C_{\mathrm{j}}^0} D_{T,\mathrm{j}} + \frac{C_{\mathrm{j}}^0}{C_{\mathrm{i}}^0 + C_{\mathrm{j}}^0} D_{T,\mathrm{i}} \tag{3.5}$$

where C^0 [mol·m^{-3}] is the initial concentration ($C_i^0 = 80$ mg·ml^{-1} and $C_j^0 = 60$ mg·ml^{-1}).

During the droplet formation, besides molecular diffusion there is also the convection contribution. The convection ($u_d L_d$) contribution is in order of 1×10^{-7} m^2·s^{-1}, while the diffusion ($D_{T,ij}$) contribution is in the order of 1×10^{-10} m^2·s^{-1} [57], [65], [74]. Because of the high surface-to-volume ratio characteristic of the microscale, a homogeneous distribution of the species concentration is expected [15], [17], [19], [32], [36], [40], [76]. When the flow is stopped, mixing inside the droplets occurs exclusively by diffusion of molecules across the miscible interface and fluids do not mix convectively [28]. However, due to the laminar flow in small-scale reactors, diffusion may not be enough to ensure the mixing of liquid phases [30]. In protein crystallization, the transport exclusively due to diffusion promotes homogeneous nucleation by increasing the probability of the formation of a single crystal. Therefore, the droplets with a length close to the characteristic dimension of the microchannel should exhibit a higher probability for the occurrence of a single nucleation event, while for larger volumes, polynuclear nucleation may occur [103], [137], [138]. Table 3.1 indicates the values of the different characteristic times for the studied hydrodynamic conditions and the main results are displayed in Figures 3.3 to 3.6.

Table 3.1. Overview of the hydrodynamic conditions for the studied segmented flow regimes (see Table 2.2), main variables and dimensionless numbers.

Regime	Droplet	Irregular segmented	Plug
Case	#1	#3	#5
Q_c [ml·min^{-1}]	0.200	0.200	0.150
Q_d [ml·min^{-1}]	0.080	0.300	0.435
α_c [-]	0.714	0.4	0.256
Ca_c [-]	8.2×10^{-5}	8.2×10^{-5}	6.1×10^{-5}
Ca_d [-]	3.4×10^{-5}	1.3×10^{-4}	1.9×10^{-4}
We_c [-]	2.4×10^{-4}	2.4×10^{-4}	1.3×10^{-4}
We_d [-]	4.6×10^{-5}	6.5×10^{-4}	1.4×10^{-3}
Pe_d [-]	7.5×10^{3}	3.8×10^{4}	7.3×10^{4}
Fo_d [-]	3.1×10^{-4}	1.1×10^{-4}	1.0×10^{-4}
L_d [mm]	1.5	2.1	2.7
V_d [µl]	1.6	3.1	5.6
t_r [s]	1.2	0.4	0.4
t_{conv} [s]	0.7	0.5	0.6

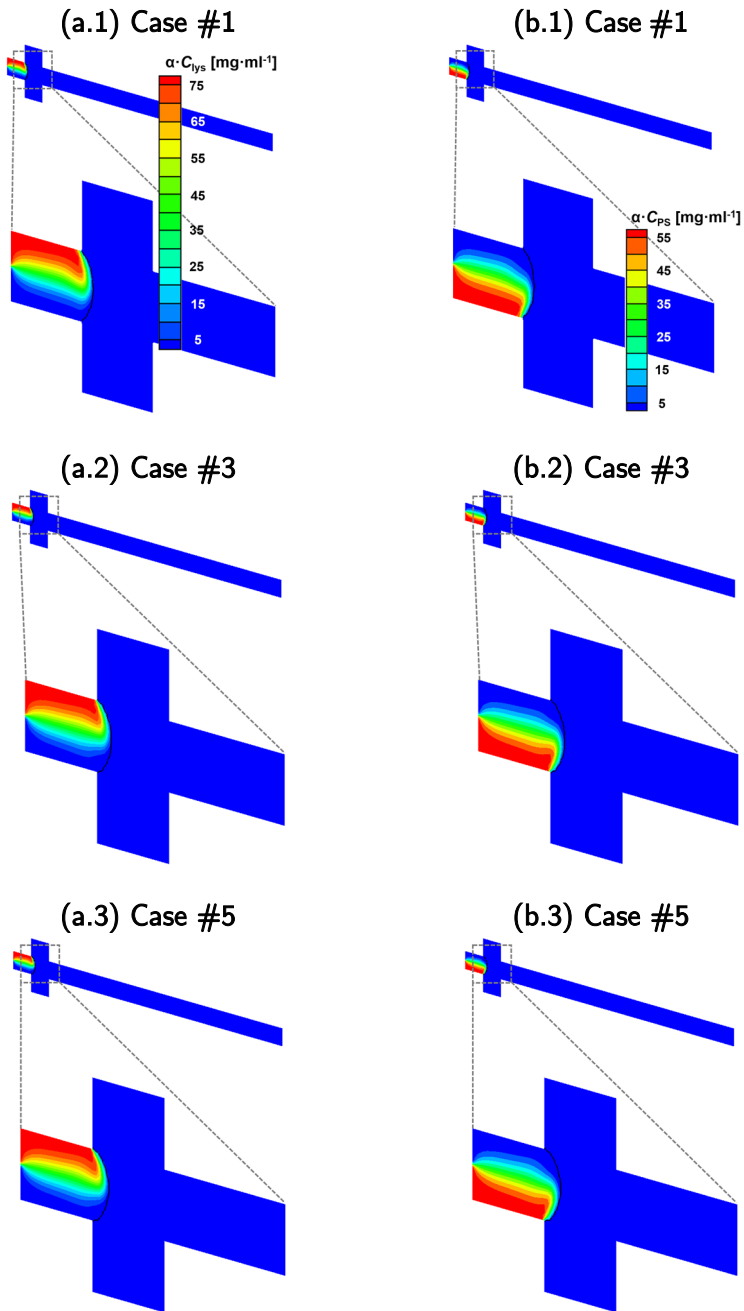[**Note:** t_r [s] – residence time of each droplet, t_{conv} [s] – convection time].

Figure 3.3. Concentration distribution [C_{lys} and C_{PS} correspond to the protein and precipitating agent concentration, respectively] (*y-z* middle plane) of **(a)** Lysozyme and **(b)** precipitating agent for the **(1)–(3)** hydrodynamic conditions (see Table 3.1) after 0.02 s (including a close-up).
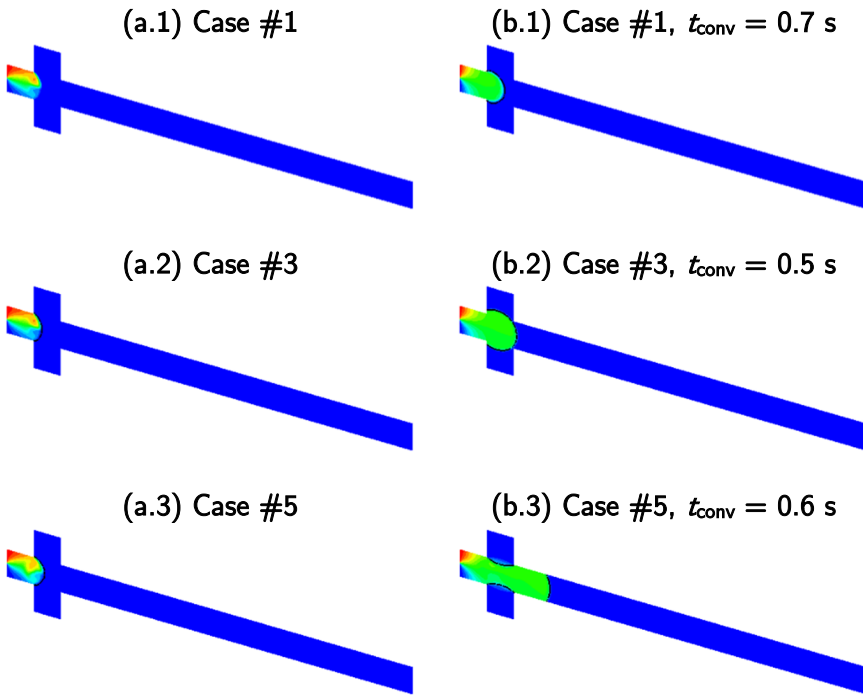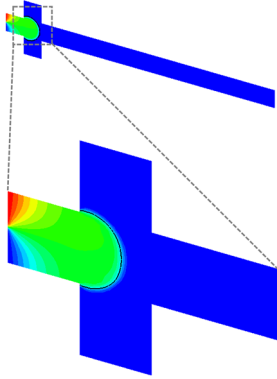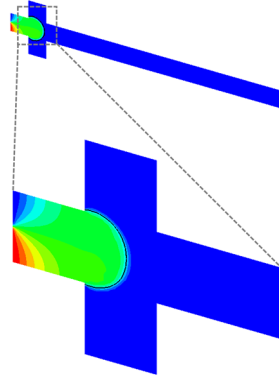
Figure 3.4. Concentration distribution (y-z middle plane) of lysozyme for the **(1)**–**(3)** hydrodynamic conditions (see Table 3.1) after: **(a)** 0.05 s and **(b)** reaching the convection time. [Color legend in Figure 3.3].
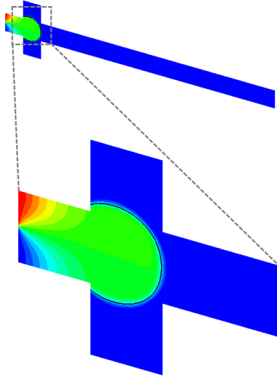
(a.1) Case #1, $t_r = 1.2$ s

(b.1) Case #1, $t_r = 1.2$ s

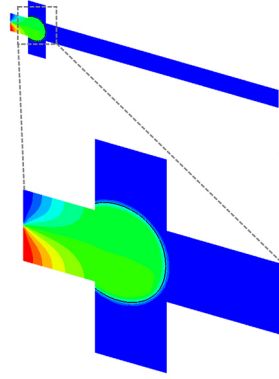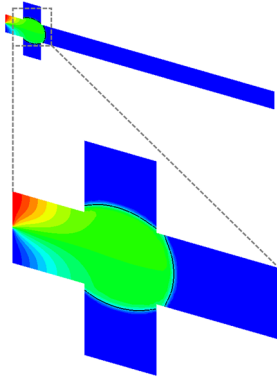(a.2) Case #3, $t_r = 0.4$ s

(b.2) Case #3, $t_r = 0.4$ s

(a.3) Case #5, $t_r = 0.4$ s

(b.3) Case #5, $t_r = 0.4$ s
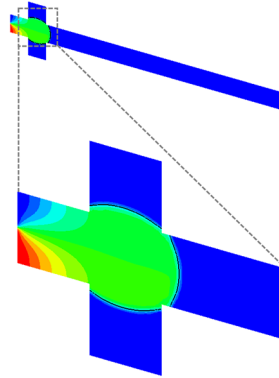
Figure 3.5. Concentration distribution (y-z middle plane) of **(a)** Lysozyme and **(b)** Precipitating agent for the **(1)**–**(3)** hydrodynamic conditions (see Table 3.1) after reaching the residence time of each droplet (including a close-up). [Color legend in Figure 3.3].
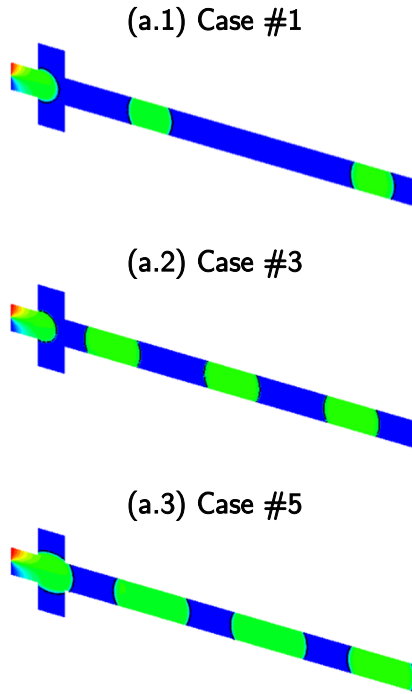
(a.1) Case #1

(a.2) Case #3

(a.3) Case #5

Figure 3.6. Concentration distribution (y-z middle plane) of lysozyme for the **(1)–(3)** hydrodynamic conditions (see Table 3.1) after **(a)** 2.5 s. [Color legend in Figure 3.3].

Inside the droplet, the mixing is improved by a recirculating secondary flow [Figure 3.4-(a)], which is induced by the contact between the droplet surface and the carrier fluid surrounding the microchannel wall. After a sufficient time, the fluid vortices are expected to be symmetrically distributed in the two halves of the droplet through the moving direction, thus enhancing the mixing [38]. Within each half of the droplet, provided by the difference of the fluid velocity from different positions inside the droplet, convection is enhanced due to the higher flow rate in the central region [108]. However, for the studied hydrodynamic conditions, the fast mixing does not allow the observation of the symmetrical vortices as the front part of the droplet is already uniformly mixed (Figure 3.7), while the convection times are very similar (see Table 3.1). At lower Ca numbers, the streamlines are disrupted due to the existence of artificial velocity values [Figure 3.7-(a.1)].
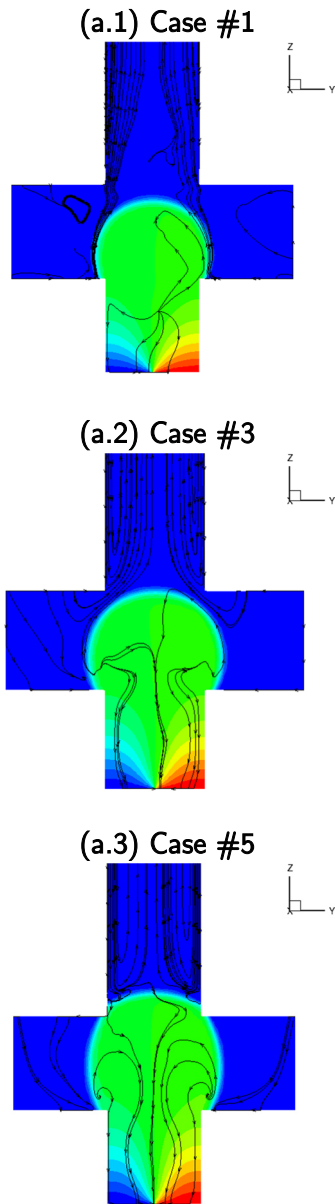
Figure 3.7. Concentration distribution of lysozyme and streamlines (*y-z* middle plane, moving droplet reference frame) for the **(1)**–**(3)** hydrodynamic conditions (see Table 3.1) after **(a)** reaching the residence time of each droplet. [Color legend in Figure 3.3].

3.3   Heat transfer in droplet flow

Temperature control is one of the most important requisites during the design of a microfluidic platform, especially for protein crystallization applications. A uniform heat distribution along the microchannel ensures that no supersaturation gradients are encountered, thus ensuring a reproducible crystallization assay. Moreover, proteins are extremely sensitive to temperature. The first part of this analysis comprises an experimental perspective. However, the focus of this section is the development of a conjugate heat transfer solver.

Thermal analysis of the crystallization platform

Preliminary tests were carried out by measuring the temperature values at the inlet and outlet of the Teflon tubes. Although those two temperature values were similar, thermal images were captured to confirm that no temperature gradients are observed in the entire platform. The thermal profile along the crystallization platform was qualitatively investigated (Figure 3.8) by pointing the thermal camera to the different reactor views to ensure a uniform temperature distribution and, consequently, a uniform distribution of supersaturation. According to Figure 3.8, temperature control is efficient by counter-current fluid recirculation.

(a.1) Early stage (a.2) Early stage

(b.1) Before steady-state (b.2) Before steady-state

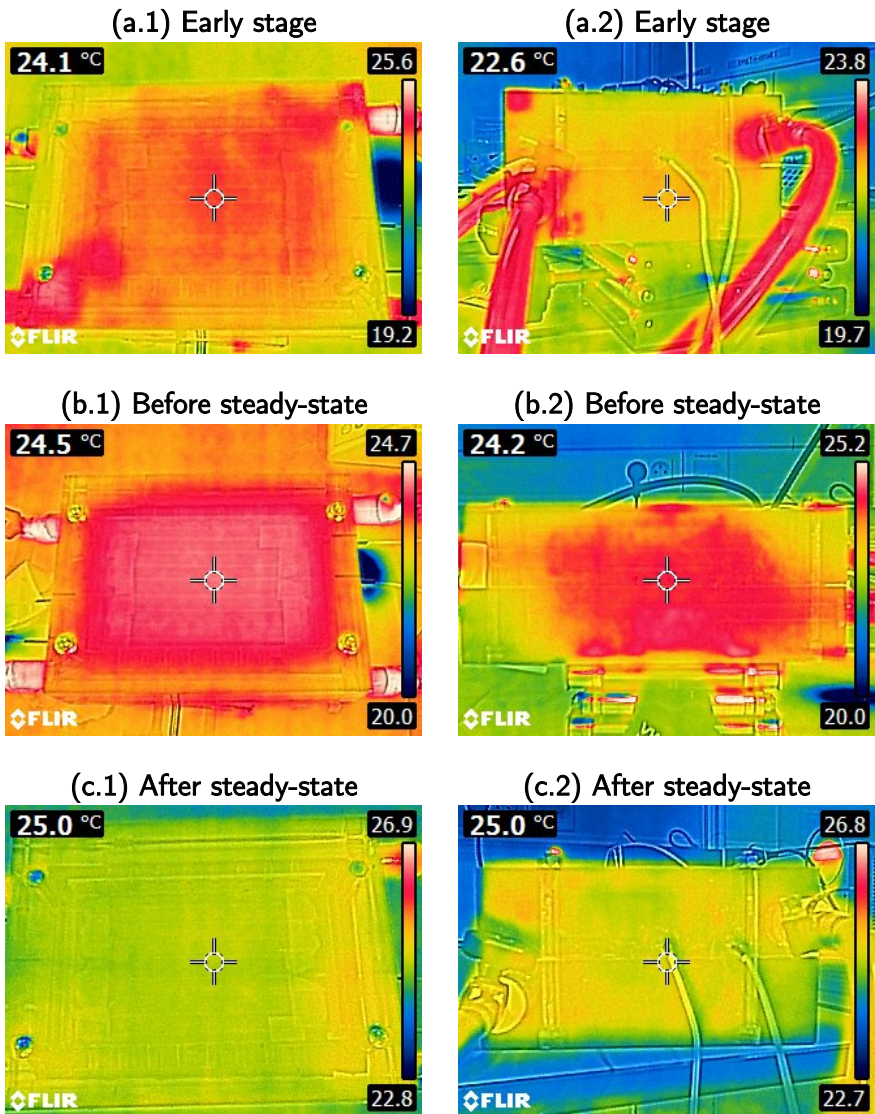(c.1) After steady-state (c.2) After steady-state

Figure 3.8. Thermal images of the crystallization platform: **(1)** Top view and **(2)** side view; **(a)** early stage of the heating step, **(b)** before reaching steady-state, and **(c)** after reaching steady-state ($T = 25$ °C).

Adding the energy equation

Analogously to the concentration of species, the temperature is another scalar field. The scalar transport equation can similarly be expressed as a balance of energy, where no radiation or external energy sources are considered. The heat transfer balance can be expressed by

$$\rho c_p \left(\frac{\partial T}{\partial t} + \mathbf{v} \cdot \nabla T \right) = \nabla \cdot (k \, \nabla T), \tag{3.6}$$

where T [K] is the absolute temperature, c_p [J·kg^{-1}·K^{-1}] the heat capacity of the mixture, and k [W·m^{-1}·K^{-1}] the mixture heat conductivity. The first term $[\partial(\rho c_p T)/\partial t]$ represents the variation of energy in function of time, the second term $(\rho c_p \mathbf{v} \cdot \nabla T)$ corresponds to the convection of energy through fluid flow, and the last term $(k \nabla^2 T)$ represents the conduction, which is the transportation of heat energy according to its thermal gradient. c_p and k are assumed to be constant fluid properties, which can be read in the *transportProperties* library in *incompressibleTwoPhaseMixture*. The definition of heat conductivity is described by *Fourier's law* by [68]

$$Q_{\mathrm{h}} = -k \, \nabla T_{\mathrm{h}}, \tag{3.7}$$

where Q_{h} [W·m^{-2}] is the local heat flux density and ∇T_{h} [K·m^{-1}] the temperature gradient. Heat conduction occurs at the interface between the two fluids, which implies that k needs to be interpolated at the interface. Equivalently to the dynamic viscosity and density values, the thermal conductivity and heat capacity for the mixture can be calculated as constant fluid properties by

$$k = \alpha \rho_{\mathrm{d}} \frac{c_{p_{\mathrm{c}}}}{\mathrm{Pr}_{\mathrm{c}}} + (1 - \alpha) \rho_{\mathrm{c}} \frac{c_{p_{\mathrm{d}}}}{\mathrm{Pr}_{\mathrm{d}}}, \tag{3.8.1}$$

and

$$c_p = \alpha c_{p_{\mathrm{d}}} + (1 - \alpha) c_{p_{\mathrm{c}}}. \tag{3.8.2}$$

By dividing both sides of Equation (3.4) with c_p, the sudden jump of the fluid properties from one phase to the other at the liquid-liquid interface is avoided, and an additional heat transfer expression is resulting

$$\rho \left(\frac{\partial T}{\partial t} + \mathbf{v} \cdot \nabla T \right) = \nabla \cdot \left(\frac{k}{c_p} \nabla T \right). \tag{3.9}$$

From the reported literature, $c_{p_c} = 1510$ J·kg^{-1}·K^{-1} and $k_c = 0.15$ W·m^{-1}·K^{-1}, and $c_{p_d} = 4186$ J·kg^{-1}·K^{-1} and $k_d = 0.6$ W·m^{-1}·K^{-1}. Additionally, the remaining fluid physical properties (density, dynamic viscosity, and interfacial tension) are also translated into temperature-dependent properties by [139], [140]

$$\rho = \rho_0 [1 - \beta(T - T_0)], \tag{3.10.1}$$

$$\nu = \frac{\mu}{\rho} = \frac{\beta_3 T^2 + \beta_4 T + \beta_5}{\beta_1 T + \beta_2}, \tag{3.10.2}$$

and

$$\sigma = \beta_6 T + \beta_7 \tag{3.10.3}$$

where ρ_0 [kg·m^{-3}] is the density at a standard temperature T_0 [K], and β [K^{-1}] the coefficient of volume expansion. Thus, ρ_0 and β are added to the list of physical properties being read in the *transportProperties* library, as well as the new variables added to the viscosity model. Due to the existence of a buoyancy-dominated flow, a temperature-dependent density can be added to Boussinesq's approximation. ν [m^2·s^{-1}] is the kinematic viscosity, β_1 [kg·m^{-3}·K^{-1}] and β_2 [kg·m^{-3}] the coefficients for a first-order approximation of the density; β_3 [Pa·s·K^{-2}], β_4 [Pa·s·K^{-1}] and β_5 [Pa·s] the coefficients for a second-order approximation of the dynamic viscosity; and β_6 [N·m^{-1}·K^{-1}] and β_7 [N·m^{-1}] the coefficients for a first-order approximation of the interfacial tension. Besides the solvers mentioned in Chapter 2, transient terms of the transport equations (concentration and temperature) are discretized using a Euler scheme. The diffusive terms of the transport equations are solved through a Gauss linear corrected

scheme, while the convective terms are solved by applying Gauss upwind schemes. Finally, the momentum, advection and energy equations are solved using a smooth solver with symmetric Gauss-Seidel, and the scalar concentration equation using a stabilized preconditioned conjugate gradient method for both symmetric and asymmetric matrices with incomplete LU preconditioner.

Heat distribution in droplet flow

For testing the capabilities of the developed solver with conjugate heat transfer, besides the hydrodynamic cases explored in section 3.2 under isothermal conditions (20 °C) [Case (A)], additional cases are considered. The first case assumes a temperature in the domain of 25 °C, while the temperature at the microchannel wall is 15 °C [Case (B)]. The second case is similar, but the temperature values are 20 °C and 10 °C instead [Case (C)]. The main results are shown in Figures 3.9–3.14.

(a.1) Case (B), #1

(b.1) Case (C), #1

(a.2) Case (B), #3

(b.2) Case (C), #3

(a.3) Case (B), #5

(b.3) Case (C), #5

Figure 3.9. Temperature distribution (*y-z* middle plane) for **(a)** Case (B) and **(b)** Case (C) for the **(1)–(3)** hydrodynamic conditions (see Table 3.1) after 0.02 s. [Color legend in Figure 3.10].

Figure 3.10. Temperature (T) distribution (y-z middle plane) for **(a)** Case (B) and **(b)** Case (C) for the **(1)**–**(3)** hydrodynamic conditions (see Table 3.1) after 0.2 s (including a close-up).

(a.1) Case (B), #1

(b.1) Case (C), #1

(a.2) Case (B), #3

(b.2) Case (C), #3

(a.3) Case (B), #5

(b.3) Case (C), #5

Figure 3.11. Temperature distribution (y-z middle plane) for **(a)** Case (B) and **(b)** Case (C) for the **(1)–(3)** hydrodynamic conditions (see Table 3.1) after 0.5 s. [Color legend in Figure 3.10].

(a.1) Case (B), #1, $t = 2$ s

(b.1) Case (C), #1, $t = 2$ s

(a.2) Case (B), #3, $t = 1$ s

(b.2) Case (C), #3, $t = 1$ s

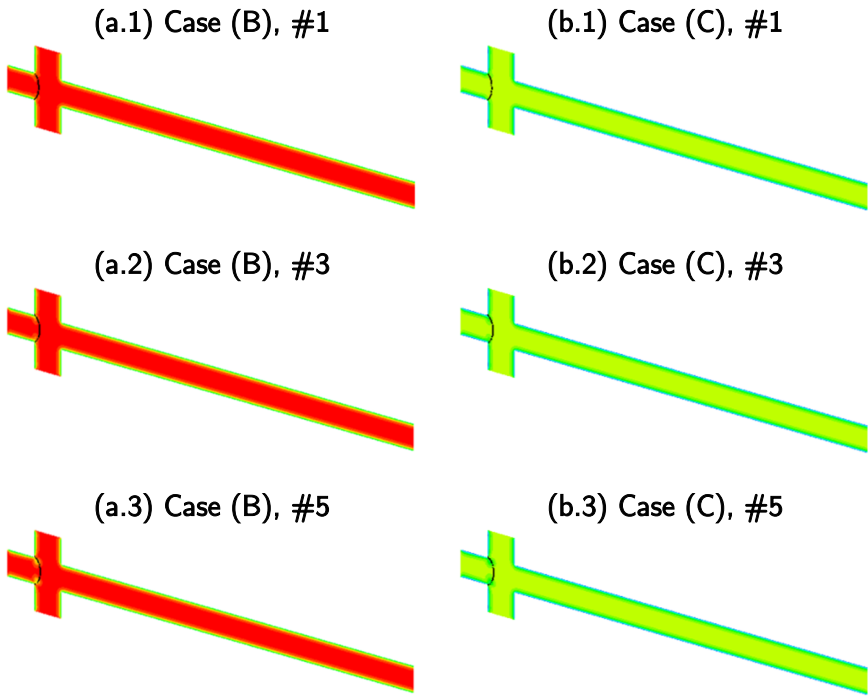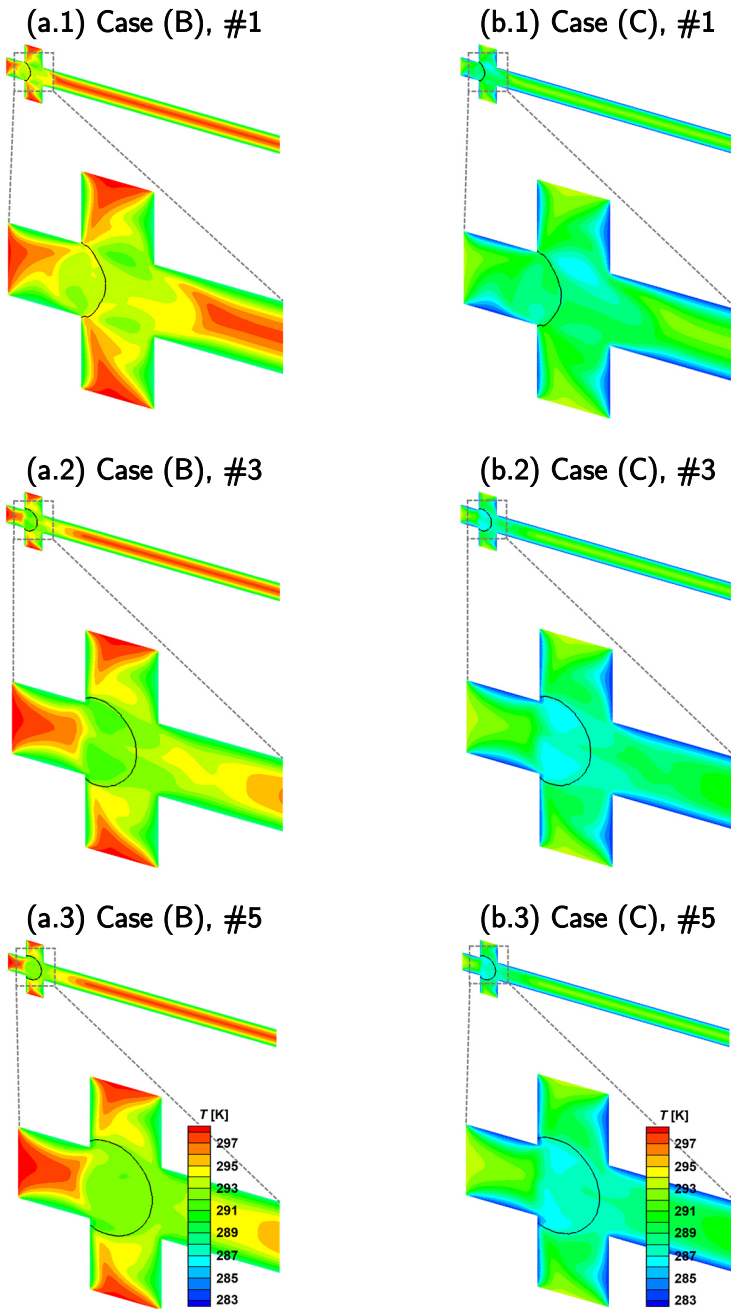(a.3) Case (B), #5, $t = 1$ s

(b.3) Case (C), #5, $t = 1$ s

Figure 3.12. Temperature distribution (y-z middle plane) for **(a)** Case (B) and **(b)** Case (C) for the **(1)**–**(3)** hydrodynamic conditions (see Table 3.1): **(1)** After 2 s, **(2)** and **(3)** after 1 s. [Color legend in Figure 3.10].

(a.1) Case (B), #1, $t = 2.25$ s

(b.1) Case (C), #1, $t = 2.25$ s

(a.2) Case (B), #3, $t = 1.5$ s

(b.2) Case (C), #3, $t = 1.5$ s

(a.3) Case (B), #5, $t = 1.5$ s

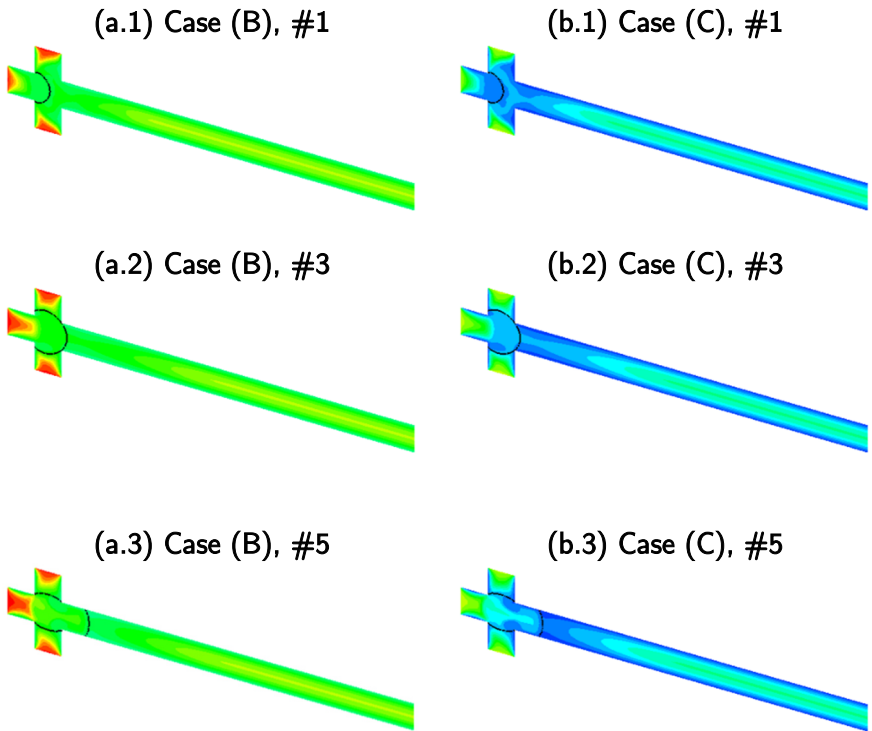(b.3) Case (C), #5, $t = 1.5$ s

Figure 3.13. Temperature distribution (y-z middle plane) for **(a)** Case (B) and **(b)** Case (C) for the **(1)**–**(3)** hydrodynamic conditions (see Table 3.1): **(1)** After 2.25 s, **(2)** and **(3)** after 1.5 s. [Color legend in Figure 3.10].

(a.1) Case (B), #1, $t = 5$ s

(b.1) Case (C), #1, $t = 5$ s

(a.2) Case (B), #3, $t = 2.5$ s

(b.2) Case (C), #3, $t = 2.5$ s

(a.3) Case (B), #5, $t = 2.5$ s

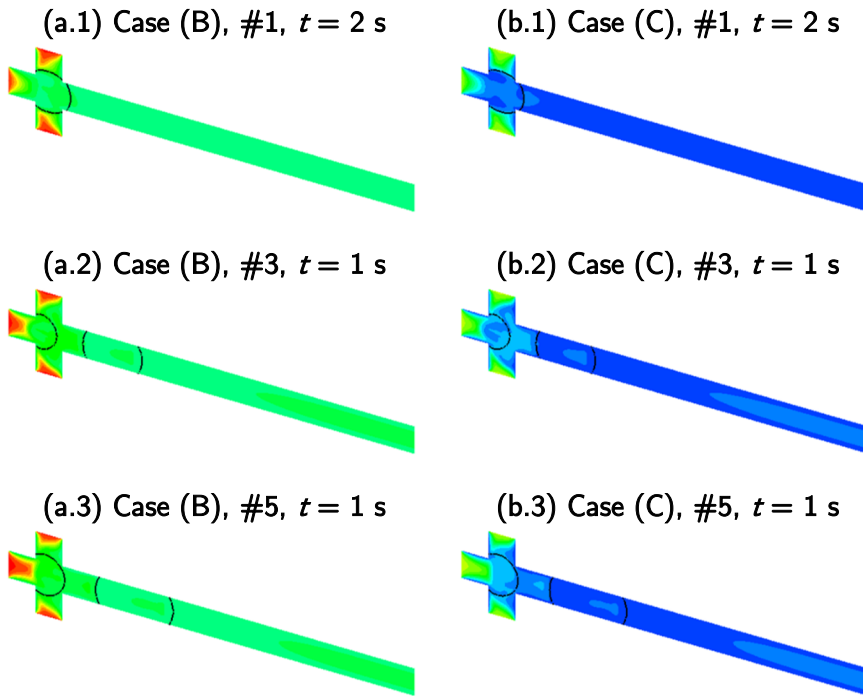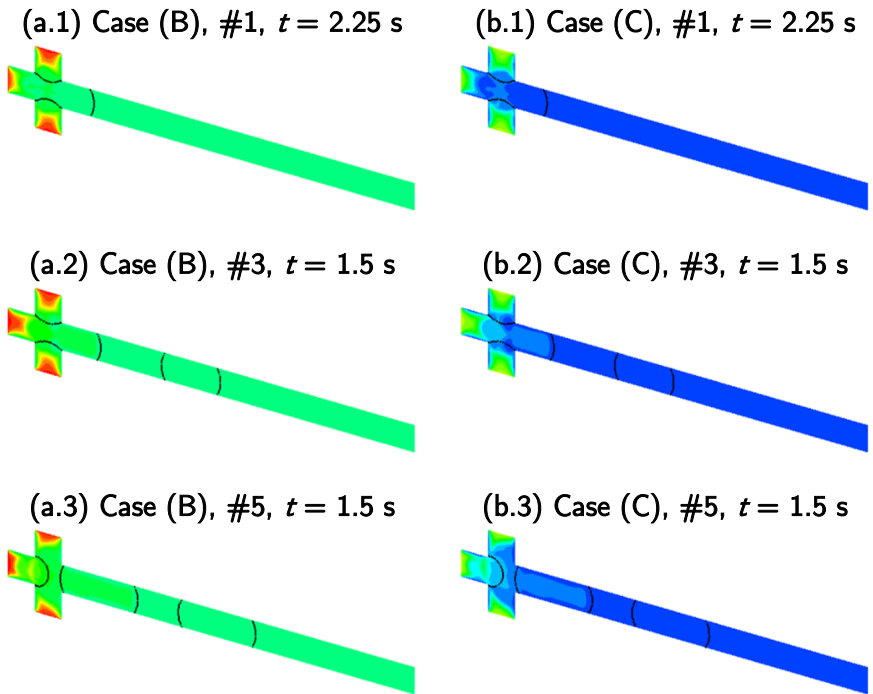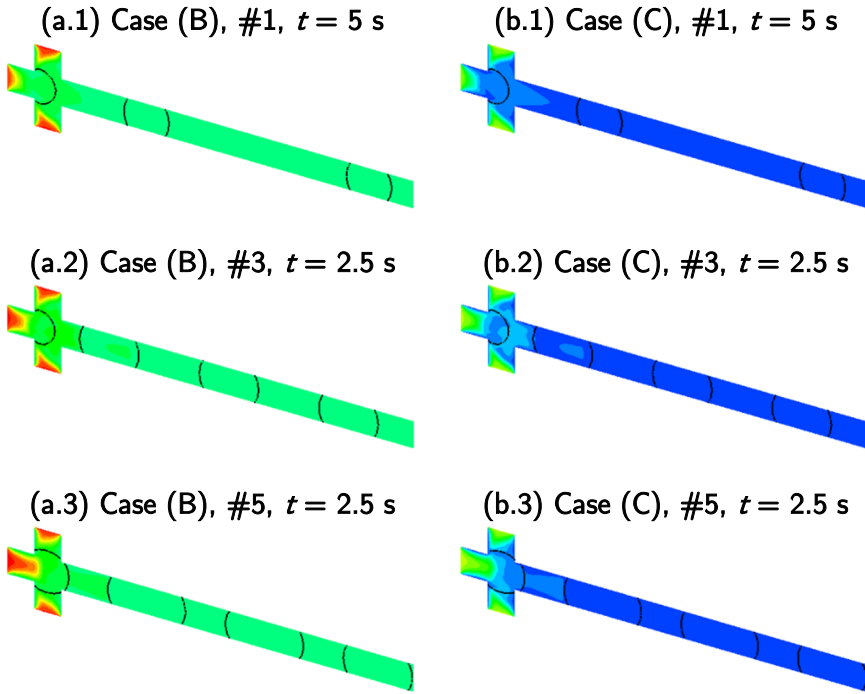(b.3) Case (C), #5, $t = 2.5$ s

Figure 3.14. Temperature distribution (y-z middle plane) for **(a)** Case (B) and **(b)** Case (C) for the **(1)**–**(3)** hydrodynamic conditions (see Table 3.1): **(1)** After 5 s, **(2)** and **(3)** after 2.5 s. [Color legend in Figure 3.10].

Urbant and co-workers [129] reported that a homogeneous distribution of the heat field is easily obtained in larger droplets, mainly attributed to the enhanced mixing due to the internal recirculation within the droplets. A similar trend is observed based on the obtained results (Figure 3.14). However, a uniform temperature distribution is immediately achieved after the droplet breakup (Figures 3.12 and 3.13) for small droplet volumes, while for larger volumes, the droplet needs to travel a certain distance. At an early stage, for the hydrodynamic conditions under Case (B), almost no differences in the heat distribution can be observed [Figures 3.10-(a) and 3.11-(a)] and, consequently, the generated droplets exhibit a uniform temperature despite the distance travelled in the microreactor [Figures 3.12-(a) and 3.14-(a)]. For the hydrodynamic conditions under Case (C), the main differences in the heat distribution are observed before the droplet breakup, especially during the blocking (Figures 3.12 and 3.14) and squeezing [Figures 3.11-(b.3), and 3.12-(b.1) and 3.13-(b.2)] stages. This might be attributed to a distinct recirculation time. A non-dimensional

recirculation time is used to quantify the importance of the vortices for the mixing/heat transfer and can be defined as the time for the liquid to move from tail of the droplet to the front $[V_\mathrm{d}/Q_\mathrm{d} \cdot u_\mathrm{d}/L_\mathrm{d}]$ [141]. Therefore, for larger droplet volumes (higher Ca_d number values) (see Table 3.1), higher values are obtained, which might indicate a lower mixing/heat transfer efficiency. This aspect is especially clear in the close-ups of the junction intersection [Figure 3.10-(b)] and during the evolution of the blocking stage [Figure 3.11-(b)]. Non-uniform heat distribution is observed for the larger droplet volume, while for the smaller droplet volume, the heat distribution is uniform at the front part of the droplet. At a later stage and with the outlet channel filled with droplets (Figure 3.14), no considerable changes in the heat distribution can be found for the different droplet lengths. Contrarily to the results reported by Khater *et al.* (2019) [132], the droplet length does not considerably change with variable temperature as the heat transfer distribution rapidly reaches a homogeneous distribution (Figure 3.14).

Finally, two additional case studies are considered for the intermediate hydrodynamic condition (#3, see Table 3.1), where the inlet temperatures differ. The temperature at the microchannel walls corresponds to the inlet temperature of the continuous stream. The dispersed phase is introduced at 20 °C and the continuous phase at 10 °C [Case (D)], while a pre-cooled dispersed phase is introduced at 10 °C and the continuous phase at 20 °C in Case (E). The temperature distributions before and after the droplet breakup are displayed in Figure 3.15.
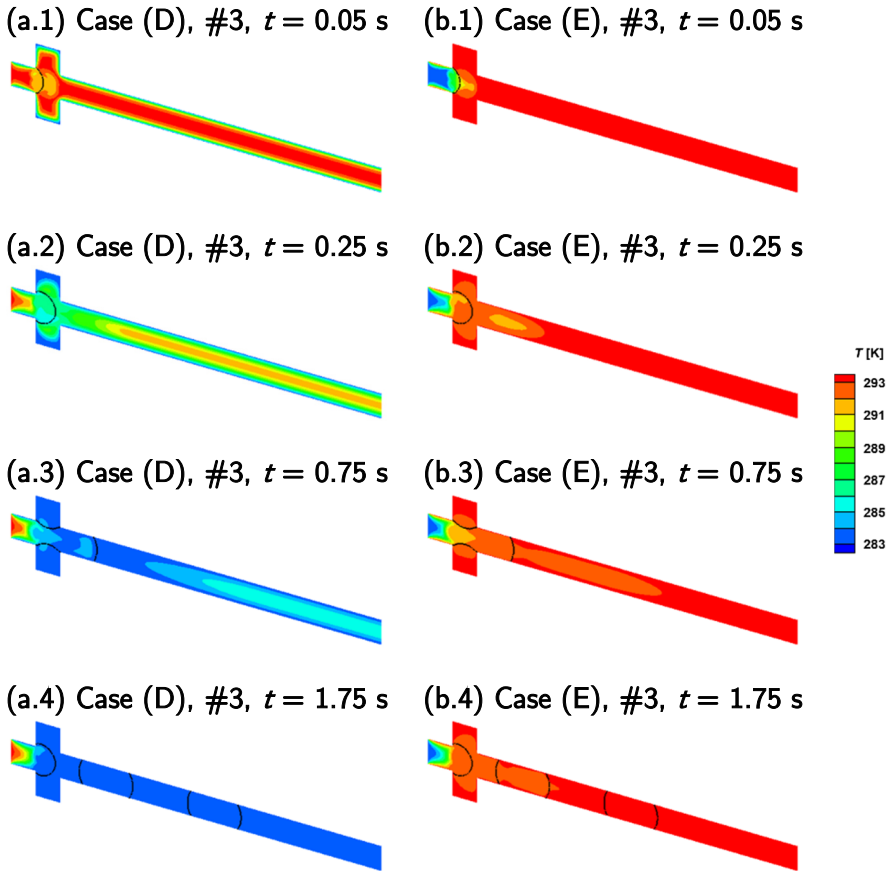
(a.1) Case (D), #3, $t = 0.05$ s   (b.1) Case (E), #3, $t = 0.05$ s

(a.2) Case (D), #3, $t = 0.25$ s   (b.2) Case (E), #3, $t = 0.25$ s

(a.3) Case (D), #3, $t = 0.75$ s   (b.3) Case (E), #3, $t = 0.75$ s

(a.4) Case (D), #3, $t = 1.75$ s   (b.4) Case (E), #3, $t = 1.75$ s

Figure 3.15. Temperature (T) distribution (y-z middle plane) for **(a)** Case (D) and **(b)** Case (E): After **(1)** 0.05 s, **(2)** 0.25 s, **(3)** 0.75 s, and **(4)** 1.75 s.

At similar initial time value [*e.g.* 0.05 s, Figure 3.15-(2)], during the blocking stage of the droplet formation, the pre-cooled dispersed phase is close to reaching the temperature of the continuous phase, and almost uniform temperature distribution along the radial direction is observed. However, at a later stage, [1.75 s, Figure 3.15-(b.4)], the droplet needs to travel a certain distance before reaching its maximum temperature. A clear temperature gradient is recognized for Case (D) due to a slower heat transfer rate (the entrances of the reactor are not pre-heated or pre-cooled) [Figure 3.15-(a.2)]. Due to a contribution of the higher velocity of the dispersed phase, the temperature distribution on the first droplet is already uniform [Figure 3.15-(a.4)].

The Fourier number (Chapter 1) compares the timescale for heat conduction in the radial direction with the timescale of the fluid to travel a certain distance. For the studied cases, laminar flow and constant microchannel wall temperature, the Fo numbers indicate two limiting cases: (i) a thermally fully developed flow [Fo >> 1] and (ii) a thermal entrance region [Fo << 1] [68]. The values for the studied hydrodynamic conditions are indicated in Table 3.2.

Table 3.2. Overview of the hydrodynamic conditions for the studied segmented flow regimes (see Tables 2.2 and 3.1), main variables and dimensionless numbers.

Regime	Droplet	Irregular segmented	Plug
Case	#1	#3	#5
α_c [-]	0.714	0.4	0.256
L_d [mm]	1.5	2.1	2.7
Pe_c [-]	1.7×10^1	8.6×10^1	1.7×10^2
Pe_d [-]	1.4×10^1	7.2×10^1	1.4×10^2
Fo_c [-]	0.14	0.05	0.05
Fo_d [-]	0.17	0.06	0.05

However, for the investigated cases, the heat transfer lies in between the two critical boundaries (Table 3.2). As Fo > 0.01, no significant effect of the heat conduction in the radial direction is observed. Therefore, the heat fluxes due to conduction are not critical for the temperature distribution, especially for the cases under lower droplet volume (see Table 3.2).

3.4   Conclusions

The mass transfer in small-scale reactors is mainly limited by the absence of active mixing in single-phase laminar flow. It is shown in the current chapter that this limitation is overcome by two-phase flow. The formation of dispersed droplets surrounded by an immiscible carrier fluid creates individual microreactors, where the mixing efficiency is high due to the mechanisms involved during the droplet formation, fluid shear force and surface tension stresses (see section 1.2 for further details). Molecular diffusion is an extremely slow transport mechanism in opposition to convection as defined by the Péclet number. Therefore, larger droplet volumes, characterized by higher Péclet number, exhibit higher non-dimensional circulation times. Although, mixing and heat transfer can be

presented as analogous, they are distinct transport processes, among others, due to the characteristic timescales for radial diffusion (around 1 h) and thermal conduction (around 10 s). In summary, although the analysis of the transport phenomena involved in this chapter might not seem exhaustive, the conjugate heat transfer solver might show good perspectives for other droplet-based applications in lab-on-a-chip devices. However, for a more extended discussion, the case studies should involve, at least, differences in the Ca numbers of two orders of magnitude. At this point, a clear effect of the residence time on the mixing and heat transfer efficiencies would be observed.

4. Study of the lysozyme phase behaviour

"We may hence say that life has borrowed from inanimate processes the same basic mechanism used in producing those striking structures that are crystals, with their beautiful plane faces, their unfailingly constant interfacial angles, and their wonderfully complex geometrical forms."

– Linus Pauling, *World Scientific Series in 20th Century Chemistry*, *Selected Scientific Papers*, *Volume II – Biomolecular Sciences* (2001).

Author contributions

J. Ferreira conceived the research, conducted the experiments, and wrote the article.

Although an overview on the main concepts involved in protein crystallization is presented in Chapter 1, the current chapter intends to highlight the importance of a phase diagram as a DOE tool to perform protein crystallization experiments. This is conducted for a broad supersaturation ratio range and involves a multiparametric study, where the influence of lysozyme and precipitating agent concentration, temperature, and droplet volume are studied. Based on the different regions of the phase diagram, thermodynamics and kinetics contributions are estimated. Additionally, two different approaches to predict the lysozyme concentration decay during the crystallization experiments are introduced in this chapter, mass balance (empirical prediction) and protein self-assembly theory (analytical prediction). The conclusions drawn will be applied in Chapter 5.

4.1   Introduction

Since the pioneering work of Friedrich Hünefeld in 1840, who accidentally discovered protein crystals in blood samples [7], researchers from different scientific fields are trying to produce high-quality protein crystals for three dimensional (3D) structure determination by X-ray crystallography [13]–

[19]. This is a crucial insight for fundamental research in biochemistry for the identification and design of new drugs and pharmaceutical products, and to understand biological systems at a molecular level [6].

Typically, crystallization is a two-step physical process in which the supersaturation is the driving force. The first step (nucleation) is the formation of nuclei, followed by the growth of these nuclei to a macroscopic scale (crystal growth). Compared to crystal growth, nucleation is more difficult to address theoretically and experimentally due to its stochastic nature and the high supersaturation levels required to overcome the critical free energy barrier [13]–[19]. The highly stochastic nature of protein nucleation implies to test a large number of potential crystallization conditions with large amounts of the protein of interest. However, proteins are usually only available in low quantities.

4.2   Phase diagram construction

The complexity of crystallizing biological macromolecules stands out compared to other molecules (*i.e.* organic and inorganic compounds), not only due to the stochastic nature of nucleation (where high supersaturation ratios are required [21]), but mainly due to the dynamic behavior of proteins [20]. Crystallization conditions can be derived from a phase diagram that indicates which state (liquid, crystalline, or amorphous precipitate) is stable under certain experimental parameters. Figure 4.1 depicts the protein concentration as a function of an adjustable parameter (*e.g.* temperature). In the labile zone (nucleation zone) the spontaneous formation of new nuclei is occurring, whereas in the metastable zone crystal growth is favoured, with a low probability for the formation of new nuclei. In addition, there is a stable zone (below the solubility curve), where the protein is soluble, and a precipitation zone, where the formation of an amorphous solid phase is observed [12].
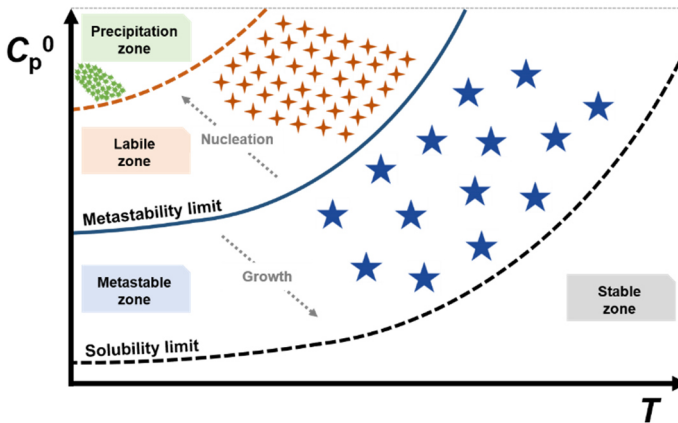
Figure 4.1. Schematic representation of the phase behaviour of a biological macromolecule as the initial protein concentration (C_{p}^{0}) in function of the crystallization temperature (T): Stable, metastable (above the solubility limit), labile (above the metastability limit), and precipitation zones.

The information on protein phase behaviour is fundamental for a systematic design of crystallization experiments, which contributes to a more accurate prediction of protein crystallization conditions. However, most of the studies so far were focused on the solubility instead of the metastability data [142], [143]. The effect of different parameters on the metastability limit was reported in a few number of publications. For example, the effect of salt concentration was studied by Crespo *et al.* (2010) [144] and Castro *et al.* (2016) [145], the temperature effect by Maosoongnern *et al.* (2012) [146] and Ildefonso *et al.* (2012) [96], and the ultrasound effect also by Crespo and co-workers [144].

Initially, a two-dimensional (2D) protein phase diagram with the lysozyme phase behaviour in function of the protein concentration and temperature is derived at 3% (w/v) sodium chloride and pH 4.7. This is done for a single droplet volume within the range explored in Chapters 2 and 3. Furthermore, the lysozyme phase behaviour is extended in function of the protein and salt concentration for a certain droplet volume range.

Experimental procedure

The initially developed droplet-based microfluidic platform (Chapter 2) was placed under an optical microscope to monitor the nucleation events. The experimental set-up involves three main sections (I–III) as shown in Figure 4.2. Premixing of the protein and NaCl aqueous solutions at the *T*-junction, using equal flow rates, was conducted to avoid nucleation in the glass syringes before starting the temperature control.
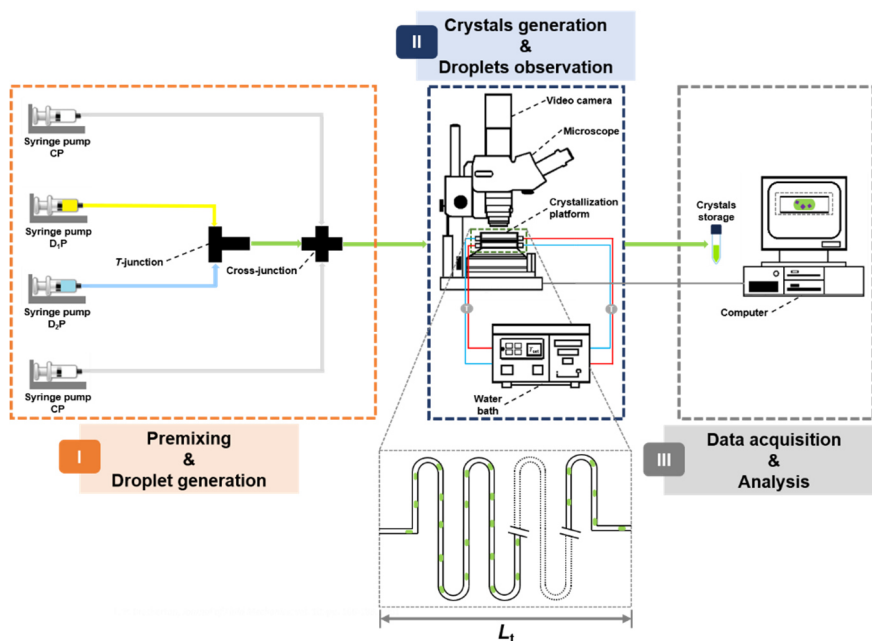

Figure 4.2. Schematic overview of the experimental set-up: (**I**) Solutions mixing and droplet production; (**II**) Droplet incubation and crystal production [L_t, Teflon tube length]; and (**III**) Data acquisition and analysis (crystals are measured and counted after 20 h). Crystals are collected and at the end of the experiment.

During the crystallization experiments, chicken egg-white lysozyme (purchased from *Merck* CAS-No. 9001-63-2) was used without further purification. The lysozyme used in this work is commercially supplied as a lyophilized powder. The lysozyme preparation is ensured by the supplier, which involves an initial purification, followed by a crystallization step performed three times, and dialysis. All lysozyme solutions are freshly prepared, without any external agitation and waiting 6 h before starting

the experiment to ensure lysozyme dissolution. Lysozyme and precipitating agent aqueous solutions [sodium chloride 6% (w/v), obtained from *Panreac AppliChem* (99.5%, Germany)] were both prepared in a 0.2 M sodium acetate buffer stock solution [sodium acetate trihydrate from *Sigma-Aldrich* (99.5%, Germany)], whose pH was adjusted to 4.7 with glacial acetic acid [*Merck* (100%, Germany)]. Sodium chloride aqueous solution pH was posteriorly adjusted with a 1 M hydroxide sodium (*Pronolab*, Portugal) solution. All the solutions were prepared with ultrapure water (Milli Q water, resistivity of 18.3 MΩ·cm^{-1} at 20 °C) and filtered using syringe filters (Puradisc FP 30 mm, cellulose acetate, 0.2 μm [*Sigma-Aldrich*, *Whatman*, Germany]).

Microbatch lysozyme crystallization trials were then carried out by mixing the lysozyme and sodium chloride aqueous solutions in a *T*-junction before the intersection between the continuous and the dispersed phases. The estimation of the timescale for mixing between the protein and salt solutions requires the assumption of a diffusion dominated process, for which the mixing time ($t_{\mathrm{mix,diff}}$) is calculated by

$$t_{\mathrm{mix,diff}} \sim \frac{d_{\mathrm{t}}^2}{D_{\mathrm{ij}}}, \tag{4.1}$$

where D_{ij} [m^2·s^{-1}] is the molecular diffusion coefficient of the diluted binary mixture (lysozyme, sodium chloride) and d_{t} is the Teflon tube diameter (1 mm). Several correlations with different applicability restrictions have been published to predict the diffusion coefficients in mixtures [136]. As an example, at 20 °C and initial concentration (80 mg·ml^{-1} and 60 mg·ml^{-1} for lysozyme and NaCl, respectively), using the diffusion coefficients reported in [147], we obtain $D_{\mathrm{ij}} = 1 \times 10^{-9}$ m^2·s^{-1} (which is reasonable for a liquid mixture, especially for large molecules such as proteins). The obtained mixing time is in the order of 14 min. However, it is possible to establish an analogy between this work and the experiments conducted by Garcia-Ruiz and co-workers in wells [148]. Since in our crystallization experiments the protein and salt solutions immediately contact, it can be expected that for the conditions indicated above, we are either (i) under a Rayleigh-Taylor instability regime, due to a small difference in the density of the solutions, and then the solution is homogeneous in less than 1 min or (ii) under the double-diffusive salt fingering instability regime, due to a

difference of one order of magnitude in the diffusion coefficients, in which case it is expected to have a homogeneous solution in 2–3 min. The latter effect is dominant. Therefore, it can be concluded that the actual mixing time is in the order of 2–3 min, which is the same order as the residence time in the mixing section of the reactor. Finally, it is necessary to reiterate that both nucleation and growth are slow processes, with an involved timescale in the order of hours and, consequently, complete mixing before the onset of crystallization can be assumed.

It was necessary to wait a certain time to ensure droplet stability and monodispersity. An extended hydrodynamics study was conducted in Chapter 2. At this moment, the syringe pumps were stopped, after which each generated droplet can be considered as an independent microreactor. After approximately 20 h, the droplets were observed using optical microscopy. The droplets were classified as belonging to the metastable, labile or precipitation zones and the crystals were counted. Afterwards, three independent microbatch trials were conducted for the hydrodynamic condition that allows the generation of microdroplets with a volume of 0.9 µl.

Nucleation probability

Different methods to assess nucleation experiments by microscopy techniques are available [21]. At this stage, the applied method was based on the probability of nucleation events in a certain droplet. Crystal nucleation is a stochastic mechanism and can be considered an independent event from one droplet to another. At this point, the nucleation probability in a certain droplet is defined as the probability of finding at least a single crystal [149]–[151] by

$$P_{\text{nucl}} = 1 - \frac{N_0}{N_{\text{tot}}},$$
(4.2)

where N_0 [-] is the number of droplets that do not contain any crystal, and N_{tot} [-] the total number of droplets. It was assumed that an event is included on the metastable zone if the nucleation probability was less than

10% $(P_{nucl} < 0.1)$, which means a low nucleation probability. The obtained data led to the construction of a lysozyme phase diagram for static droplets generated in a single hydrodynamic condition, droplet volume of 0.9 µl. The values of initial supersaturation ratio (S_0) and nucleation probability (P_{nucl}) are represented in Figure 4.3.
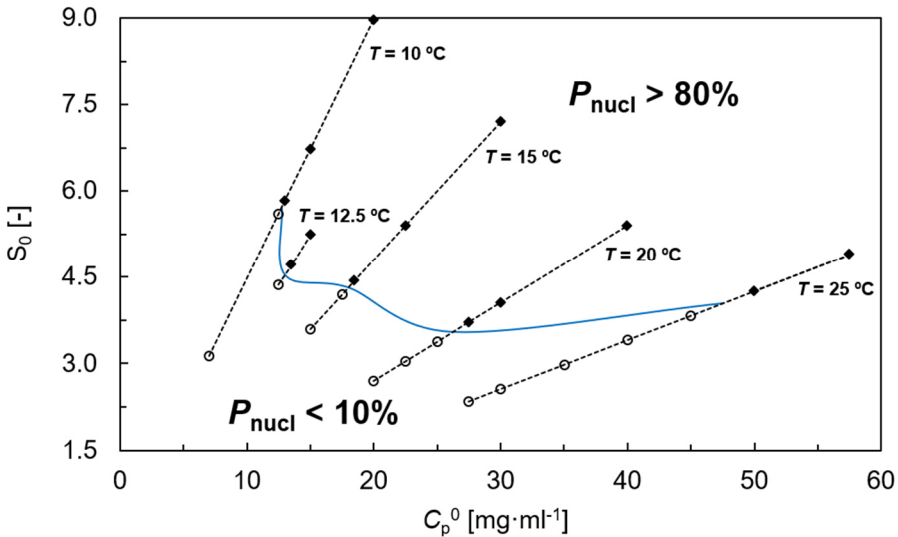

Figure 4.3. Initial supersaturation ratio (S_0) in function of the initial protein concentration (C_p^0) and nucleation probability (P_{nucl}) values for the crystallization trials at different crystallization temperatures in droplet volumes of 0.9 µl. [Clear markers correspond to clear droplets $(P_{nucl} < 10\%)$ and filled markers to droplets with tetragonal lysozyme crystals $(P_{nucl} > 80\%)$].

With this set of experiments, it is possible to clearly define the nucleation and metastable regions based on the nucleation probability (Figure 4.3). In the metastable region, as explained above, the limit of nucleation probability was initially fixed at 10% (low nucleation probability), but for the studied conditions this probability value was always below 10%. In the labile region, where nucleation is spontaneous, the nucleation probability was higher than 80% for all the cases.

Phase diagram construction

For building the 2D phase diagram representing the protein concentration in function of temperature, microbatch crystallization assays were performed at several initial supersaturation ratios by changing the initial lysozyme concentration (C_{lys}^0 ∈ [12.5–57.5] mg·ml^{-1}) and the temperature (T ∈ [10–25] °C). For all experiments, the droplet-based platform was filled with the silicon oil and both lysozyme and salt solutions as soon as the temperature in the droplet incubation zone reached steady-state. This ensures that the crystallization trials were conducted at a constant initial supersaturation ratio.

To obtain a reliable phase diagram, the generated droplets need to be monodispersed and stable as the droplet volume plays an important role in the nucleation mechanism. This effect has not currently been sufficiently well understood in the scientific community [98], thus it is explored in this chapter. Small droplet volumes can lead to lower nucleation probability, as the number of available spots where nucleation can take place is lower and, consequently, the width of the metastable region could be larger. Thereby, this metastable region may include the metastability limits for the other droplet flow conditions since the droplet volume is higher for the other hydrodynamic conditions. Figure 4.4 represents all the experimental points, with the presence or absence (clear droplets) of crystals inside the droplets.
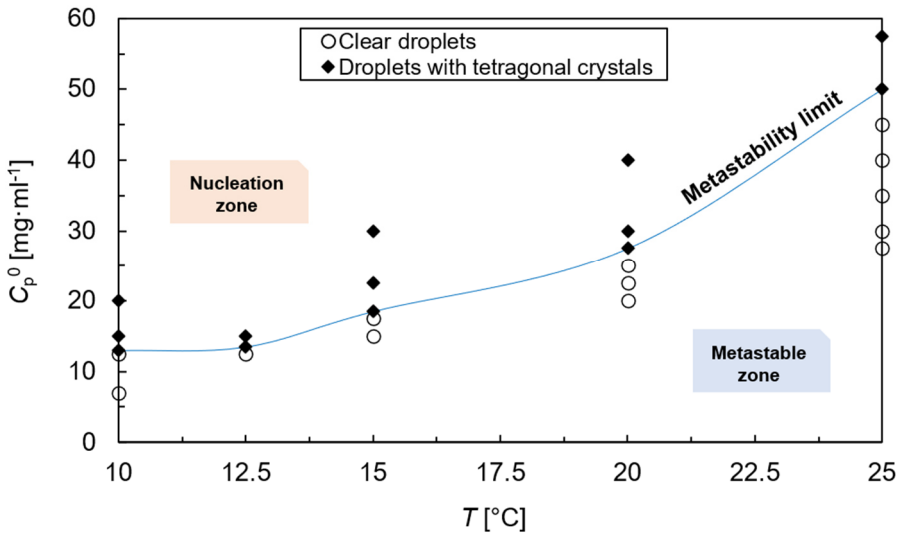
Figure 4.4. Lysozyme metastability limit at sodium chloride 3% (w/v) and pH 4.7 in droplet volumes of 0.9 μl as the initial protein concentration (C_p^0) in function of the crystallization temperature (T). [Clear markers correspond to clear droplets and filled markers to droplets with tetragonal lysozyme crystals].

Below the metastability limit, the solution is supersaturated but the critical supersaturation was not yet reached, and clear droplets are obtained. Nucleation should not occur (not spontaneously) and crystal growth is promoted. Otherwise, above the metastability limit, depending on the initial lysozyme concentration and temperature conditions (maintaining the initial NaCl concentration and pH value), tetragonal crystals were obtained varying in terms of number and size. The lysozyme phase diagram in the droplet-based microfluidic platform, representing the lysozyme concentration as a function of the temperature is plotted in Figure 4.5.
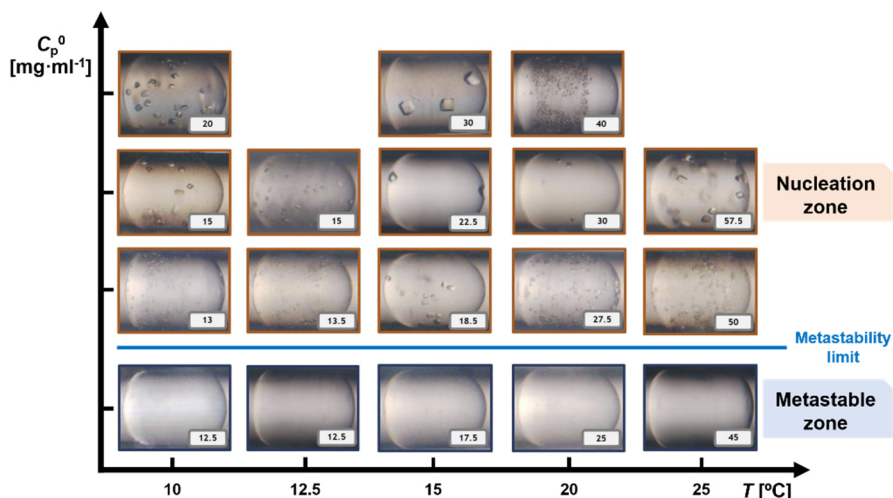
Figure 4.5. Lysozyme phase behaviour represented by the initial protein concentration (C_p^0) in function of the crystallization temperature (T): Lysozyme crystals obtained in droplet volumes of 0.9 µl at sodium chloride 3% (w/v) and pH 4.7 with the indication of the metastable and nucleation zones separated by the metastability limit. [Lysozyme concentrations in mg·ml^{-1} are indicated in each picture, increasing along both abscissa and ordinates axes].

For all temperatures, a large number of small crystals was observed at the lowest investigated concentration level (Figure 4.5). At the same temperature, for a sequential increase in the supersaturation ratio, an increase in crystal size was observed. In principle, this observation is not expected, since the formation of many small crystals is usually observed at higher supersaturation ratios (higher nucleation rate). A possible explanation for this observation could be increased crystal growth rates for larger crystal sizes, due to the increased supersaturation levels. Furthermore, for higher supersaturation values, it was also possible to identify a preferential crystal formation at the droplet interface (heterogeneous nucleation). For the studied range of Capillary numbers, besides the dominance of the interfacial forces during the droplet formation, these observations can also indicate heterogeneous nucleation.

For the same supersaturation ratio ($S_0 = 5.4$) (22.5 mg·ml^{-1} at 15 °C and 40 mg·ml^{-1} at 20 °C) (Figure 4.5), the number of crystals is higher for the droplets with higher initial lysozyme concentration (Figure 4.5). For identical initial lysozyme concentrations (15 mg·ml^{-1} at 10 °C and 12.5 °C,

and 30 mg·ml^{-1} at 15 °C and 20 °C in Figure 4.5), decreasing the temperature increases the crystal size, which is also observed when the temperature is maintained, and the concentration is gradually increased. For the latter, despite the increase in supersaturation level (enhancing nucleation), the crystal size increases. However, there is an extreme value at 20 °C (40 mg·ml^{-1}), where small crystals with a well-defined tetragonal shape are present in large number. A possible explanation is the proximity to the precipitation zone (high supersaturation levels) in the phase diagram.

Due to the volume range (microliter), it is expected that the nucleation probability is low, and the formation of a lower number of crystals could be expected for the entire range of temperatures and lysozyme concentrations, and not only for higher supersaturation ratios [98], [100]. A possible explanation for this unpredictable behaviour could be the presence of different states of lysozyme aggregation (oligomer formation) in solution and their implications on the occurrence of nucleation. Ferreira *et al.* (2017) [27] reported the effect of lysozyme concentration on the oligomer concentrations for a specified range of experimental conditions ($T \in$ [12.5–20] °C and $C_{\mathrm{lyz}} \in$ [25–50] mg·ml^{-1}), which includes the labile zone for the studied case at $T = 20$ °C. At $T = 15$ °C, Ferreira and co-workers observed a gradual increase in the oligomer concentration with the lysozyme concentration, but a decrease in monomer concentration was observed for the highest lysozyme concentration. This observation emphasizes the complex behaviour of lysozyme in solution and the possible implications on nucleation and crystal growth since nucleation will be difficult to achieve due to the lower availability of monomers. The results could be explained as a competition between cluster growth (oligomers can act as heterogeneous nucleation sites) and crystal growth [27], [152]. For the entire temperature range, the oligomer presence could explain the formation of a few large crystals at higher supersaturation ratios. However, the final crystal size is different at similar supersaturation ratios (but different temperatures). On the one hand, there is the concentration effect, where higher supersaturation ratios should result in smaller crystals. On the other hand, there is the behaviour of the oligomeric solution, which changes depending on temperature.

The images shown in Figure 4.5 were taken at the end of the experiments, thus intermediate stages during nucleation and crystals growth were not

assessed. The crystal size distribution appears to be uniform, which could be explained by Ostwald ripening [153] or simply by the fact that all the crystals may have formed at the same time. This mass transport process is responsible for an increase in the mean crystals radius over time due to lysozyme diffusion from smaller to larger crystals [154].

Another observation is the absence of crystals in the droplet caps at 20 °C and 40 mg·ml⁻¹. This could be explained by asymmetrical mixing patterns due to heterogeneous local concentration differences inside the droplet. This was further elaborated in Chapter 2. During the droplet formation, besides diffusion there is also convection contributing to mixing. The convection contribution $(u_{d}L_{d})$ is 1.7 × 10⁻⁷ m²·s⁻¹, while the diffusion coefficients of lysozyme and sodium chloride at 20 °C are 1.4 × 10⁻¹⁰ m²·s⁻¹ and 2.0 × 10⁻⁹ m²·s⁻¹, respectively [148]. However, when the droplets are stopped (microbatch experiments), mixing may predominantly occur by molecular diffusion.

4.3   Phase diagram limits and droplet volume

The solubility line is entirely defined by thermodynamics, and can be described by the van't Hoff equation [10]

$$\Delta G° = -R_{g}T \ln \mathrm{K_{eq}}, \qquad (4.3)$$

where $\Delta G°$ [J·mol⁻¹] is the Gibbs free energy, $\mathrm{K_{eq}}$ [-] the equilibrium constant, R_{g} [J·mol⁻¹·K⁻¹] the ideal gas constant, and T [K] the absolute temperature. After substituting the Gibbs free energy with its enthalpic $(\Delta H°)$ [J·mol⁻¹] and entropic $(\Delta S°)$ [J·mol⁻¹·K⁻¹] contributions, Equation (4.3) results in

$$\ln \mathrm{K_{eq}} = -\frac{\Delta H°}{R_{g}T} + \frac{\Delta S°}{R}. \qquad (4.4)$$

In this way, a theoretical equation to describe the solubility concentration (C_{p}^{s}) [mol·m⁻³] in function of temperature can be obtained by

$$C_p^s(T) = A' \exp\left(\frac{B'}{T} + C'\right) + D', \qquad (4.5)$$

where the parameters A' [mol·m⁻³], B' [K], C' [-], and D' [mol·m⁻³] are determined through the minimization of the sum of quadratic errors between the theoretically calculated and experimentally obtained concentration. The parameters B' $(-\Delta H°/R_g)$ and C' $(\Delta S°/R_g)$ allow the calculation of the system's enthalpy and entropy changes, respectively (Table 4.1).

The metastability line is a virtual limit, which results from a combination of thermodynamics and kinetics, and the most important, the type of the crystallizer. Contrarily to the definition of nucleation probability (in a droplet) presented before (see section 4.3), the Gibbs-type definition of nucleation probability (per unit volume) is defined by

$$P_{\mathrm{nucl}} = \exp\left(-\frac{\Delta G^*}{k_B T}\right), \qquad (4.6)$$

where ΔG^* is the critical Gibbs free energy and k_B [J·K⁻¹] the Boltzmann constant. Analogously to the solubility limit, based on the Markov approximation, a theoretical equation to describe the metastability concentration (C_p^{met}) [mol·m⁻³] in function of temperature is obtained by

$$C_p^{\mathrm{met}}(T) = A'' \exp\left(\frac{B''}{T} + C''\right) + D'', \qquad (4.7)$$

where the parameters A'' [mol·m⁻³], B'' [K], C'' [-], and D'' [mol·m⁻³] are again determined through the minimization of the sum of quadratic errors. The parameter B'' $(-\Delta G^*/k_B)$ allows the calculation of the critical Gibbs free energy (Table 4.2).

As previously mentioned, the solubility limit is well-defined and supported by a large number of published data for different conditions and system

configurations. In this study, the solubility line was constructed based on data reported by Forsythe *et al.* (1999) [142]. The obtained parameters for both solubility and metastability limits are indicated in Tables 4.1 and 4.2, respectively.

Table 4.1. Parameter values to predict the solubility limit in different case studies [see Equation (4.5)].

Variables values	Studied case	Ildefonso *et al.* (2012) [96]	Maosoongnern *et al.* (2012) [146]	
pH	4.7	4.5	4.4	5
C_{NaCl} [% (w/v)]	3	4	3	3
V_d	0.9 µl	0.25 µl	4 ml	
A' [mg·ml^{-1}]	1	1	1	1
B' [°C]	-88.1	-129.7	-166.2	-168.3
C' [-]	4.6	6.1	8.7	8.6
D' [mg·ml^{-1}]	1.7	1.9	1.7	1.5
$\Delta H°$ [kJ·mol^{-1}]	-129	-295	-379	-383
$\Delta S°$ [kJ·mol^{-1}·K^{-1}]	-10	-14	-20	-20

Based on the obtained values, it can be concluded that for different pH values [data reported by Maosoongnern *et al.* (2012) [146]], the enthalpic and entropic values are in the same order of magnitude. It is also worth noting that the change in entropy is similar for different set-up configurations, and operation at different flow rates, pH value and salt concentration. However, the enthalpic values depend on the used methodology and even under the same conditions different values could be obtained.

Table 4.2. Parameter values to predict the metastability limit in different case studies [see Equation (4.7)].

Variables values	Studied case	Ildefonso *et al.* (2012) [96]	Maosoongnern *et al.* (2012) [146]	
pH	4.7	4.5	4.4	5
C_{NaCl} [% (w/v)]	3	4	3	3
V_d	0.9 µl	0.25 µl	4 ml	
A'' [mg·ml^{-1}]	1	1	1	1
B'' [K]	-88.1	-416.6	-18.0	-15.2
C'' [-]	7.1	15.2	4.5	4.3
D'' [mg·ml^{-1}]	13.2	13.9	24.6	25.8
ΔG^* [kJ·mol^{-1}]	0.73	3.5	0.14	0.12

The higher Gibbs free energy values for the cases where the droplet volume is smaller could be explained considering the nucleation barrier. For these cases, the higher critical activation free energy barrier highlights the difficulty to nucleate in microliter droplets [21], where the nucleation probability decreases. The lysozyme phase diagram in droplet volumes of 0.9 µl representing the initial lysozyme concentration as a function of the temperature is plotted in Figure 4.6.
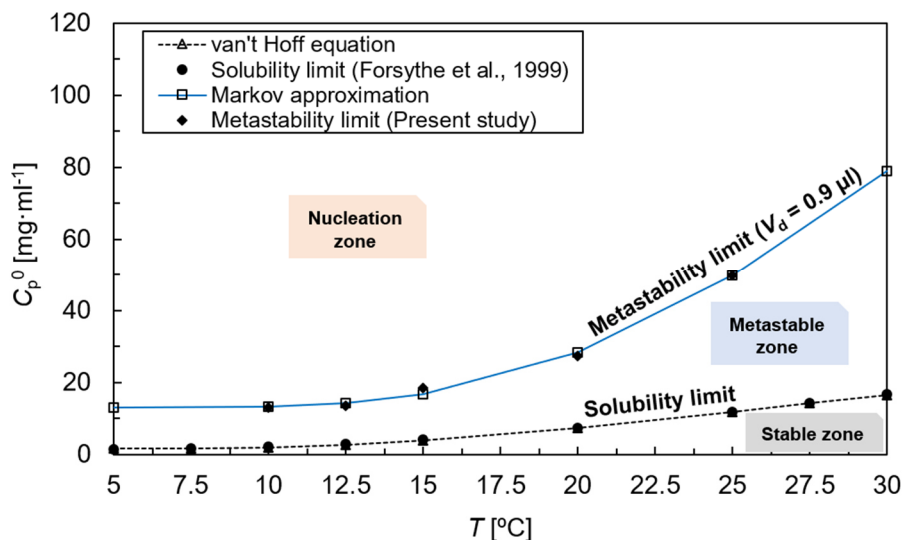
Figure 4.6. Lysozyme phase behaviour represented by the initial protein concentration (C_p^0) in function of the crystallization temperature (T) in droplet volumes of 0.9 µl at sodium chloride 3% (w/v) and pH 4.7, where the indicated exponential fits were obtained using van't Hoff equation (solubility limit) and Markov approximation (metastability limit).

As earlier mentioned, the metastability line is a virtual limit resulting from a combination of thermodynamics and kinetics. A higher nucleation probability (based on the definition of nucleation probability presented in section 4.2) is typically expected for larger droplet volumes as there are more available spots where nucleation can happen [155]. Crespo *et al.* (2010) [144] and Castro *et al.* (2016) [145] reported studies with the same nature and concentration of precipitating agent and buffer, and pH value at 20 °C, but for different geometries and mixing behaviour. In the present work, the lysozyme concentration in the metastability limit is 27.5 mg·ml^{-1}, and as previously mentioned each droplet has a volume of 0.9 µl. Crespo and co-workers performed batch lysozyme trials in microwells under static conditions in droplets with a volume of 8 µl. For this reported study, the lysozyme concentration in the metastability limit is 29.5 mg·ml^{-1}. The small reduction of the lysozyme concentration in the metastable zone for the studied case compared to the one conducted by Crespo and co-workers can be explained by the influence of convection during droplet generation, or even due to an interfacial effect (lower surface-to-volume ratio). However, due to the result uncertainty, this difference is not statistically significant. Castro and co-workers conducted

batch lysozyme trials under dynamic conditions using an oscillatory flow reactor with an approximate volume of 4 ml. In this case, the lysozyme concentration in the metastability limit is 23.1 mg·ml^{-1}. It is possible to observe nucleation at a lower lysozyme concentration, and the metastability zone width apparently decreases, which was expected as besides molecular diffusion, (oscillatory) convection also significantly contributes to mixing. Apparently, the crystal morphology is identical in all the cases (tetragonal crystals), but their number and size differ. Additionally, it was reported by Wang *et. al.* [156] that for temperatures lower than 25 °C, lysozyme crystals are tetragonal.

Finally, the effect of the precipitating agent concentration on the crystal size and number was also studied for two different droplet volumes. The experimental procedure is similar to the one presented along this chapter. With the purpose of reducing the nucleation probability by decreasing the droplet volume, the Teflon tube diameter was reduced from 1 mm to 500 µm. From the hydrodynamics study presented in Chapter 2, as the correlation to predict the droplet length was normalized by the Teflon tube diameter, it was possible to have an initial estimation for the current trials. Further investigation on the effect of the droplet length on the crystallization outcome can be found in Chapter 5.

For the initial case (droplet volume of 0.1 µl), the total flow rates of the dispersed and continuous were set to 0.2 ml·min^{-1} and 1.8 ml·min^{-1}, respectively, while 0.3 ml·min^{-1} and 0.2 ml·min^{-1} for the other case (droplet volume of 0.6 µl). All the experiments were performed at 25 °C and initial concentration (before the premixing) of 140 mg·ml^{-1} and 6% (w/v) for the lysozyme and NaCl, respectively. By changing the ratio between the flow rates of the protein and salt solutions (always an identical total flow rate of the phase), it was possible to vary two concentrations at once, protein and salt concentration. The obtained crystals for the studied cases are shown in Figure 4.7, as well as the initial supersaturation ratios.
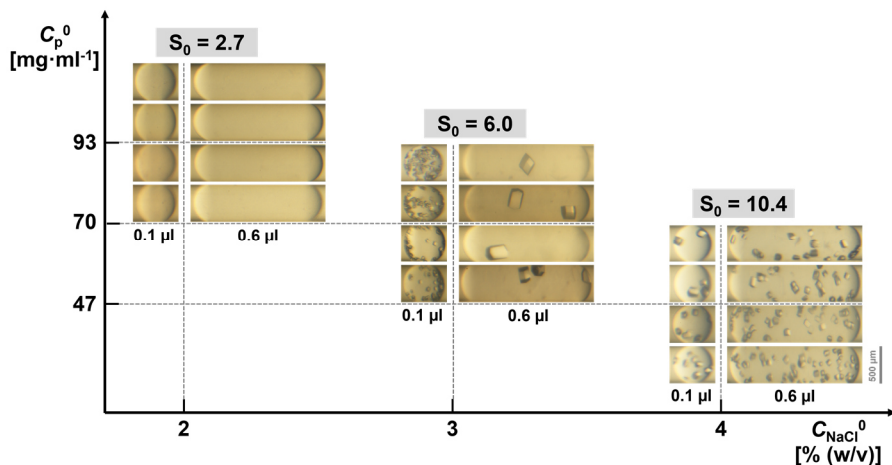
Figure 4.7. Lysozyme phase behaviour represented by the initial protein concentration (C_{p}^{0}) in function of the initial precipitating agent concentration (C_{NaCl}^{0}): Tetragonal crystals obtained in droplet volumes of 0.1 µl and 0.6 µl at 25 °C and pH 4.7.

For the case under the lowest initial supersaturation ratio ($S_0 = 2.7$), it is possible to observe that the droplets are clear, and no crystals were produced (Figure 4.7). From the previous discussion, this might indicate that, at these conditions, the point belongs to the metastable region and no nucleation events occurred. Unexpectedly, the intermediate supersaturation ratio ($S_0 = 6.0$) reveals a higher number of small crystals for the smaller droplet volume, while only a few large crystals are obtained for the larger droplet volume. This perhaps reveals the dominant effect of heterogeneous nucleation due to the higher surface-to-volume ratio for the smaller droplet volume. For the case under the highest initial supersaturation ratio ($S_0 = 10.4$), the number of crystals follows the droplet volume trend as there are, for larger droplets, more active spots where nucleation can take place, and, consequently, more crystals are produced on the larger droplet volume. It seems evident that the expected higher number of crystals at higher supersaturation ratios only occurs for the larger droplet volume (0.6 µl). For the smaller droplet volume, the opposite occurs, as the number of crystals decreases along the supersaturation ratio (Figure 4.7). For clarifying these initial predictions, a phase diagram with reported data for the solubility [142] and metastability [157] limits was drawn (Figure 4.8). For this, a fitting procedure was applied by following Equations (4.8) and (4.9) for the solubility and metastability limits, respectively.

$$C_{\mathrm{p}}^{\mathrm{s}}(C_{\mathrm{NaCl}}) = A' \, \exp\left(\frac{B'}{C_{\mathrm{NaCl}}}\right), \tag{4.8}$$

and

$$C_{\mathrm{p}}^{\mathrm{met}}(C_{\mathrm{NaCl}}) = A'' \, \exp\left(\frac{B''}{C_{\mathrm{NaCl}}}\right). \tag{4.9}$$
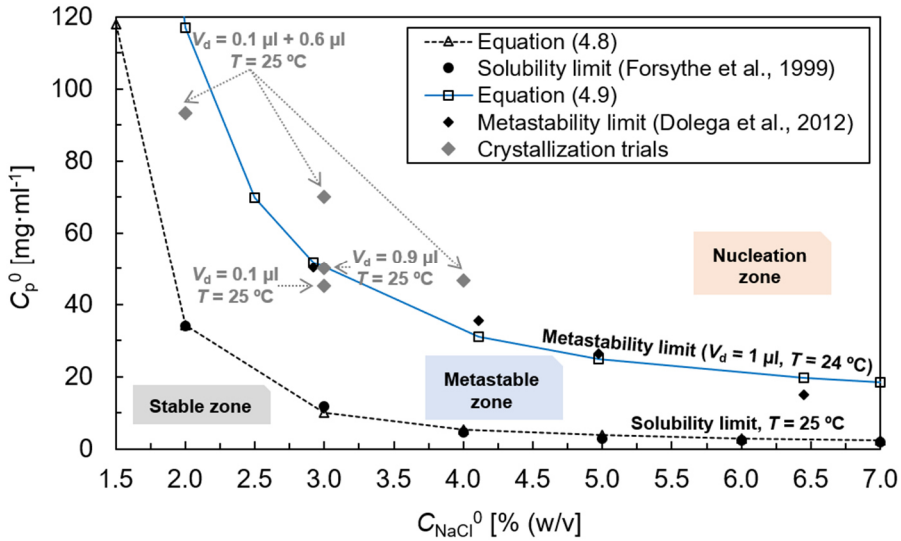

Figure 4.8. Lysozyme phase behaviour represented by the initial protein concentration (C_{p}^0) in function of the initial precipitating agent concentration (C_{NaCl}^0) at pH 4.7, where the indicated exponential fits were obtained using Equations (4.8) (solubility limit obtained at 25 °C) and (4.9) (metastability limit obtained at 24 °C and a droplet volume of 1 µl) [The grey markers indicate the different crystallization assays].

Although the metastability line is a virtual limit dependent on the droplet volume, as the droplet volume used to derive the metastability limit (1 µl) is in the middle of the studied values, it becomes clear that there is an absence of crystals for the lowest initial supersaturation ratio (Figure 4.8). Additionally, the quantitative results in terms of average crystal size and number are displayed in Figure 4.9. The procedure for measuring the crystal size is explained in Chapter 5.

(a.1) 3% NaCl, $S_0 = 6.0$

(a.2) 4% NaCl, $S_0 = 10.4$
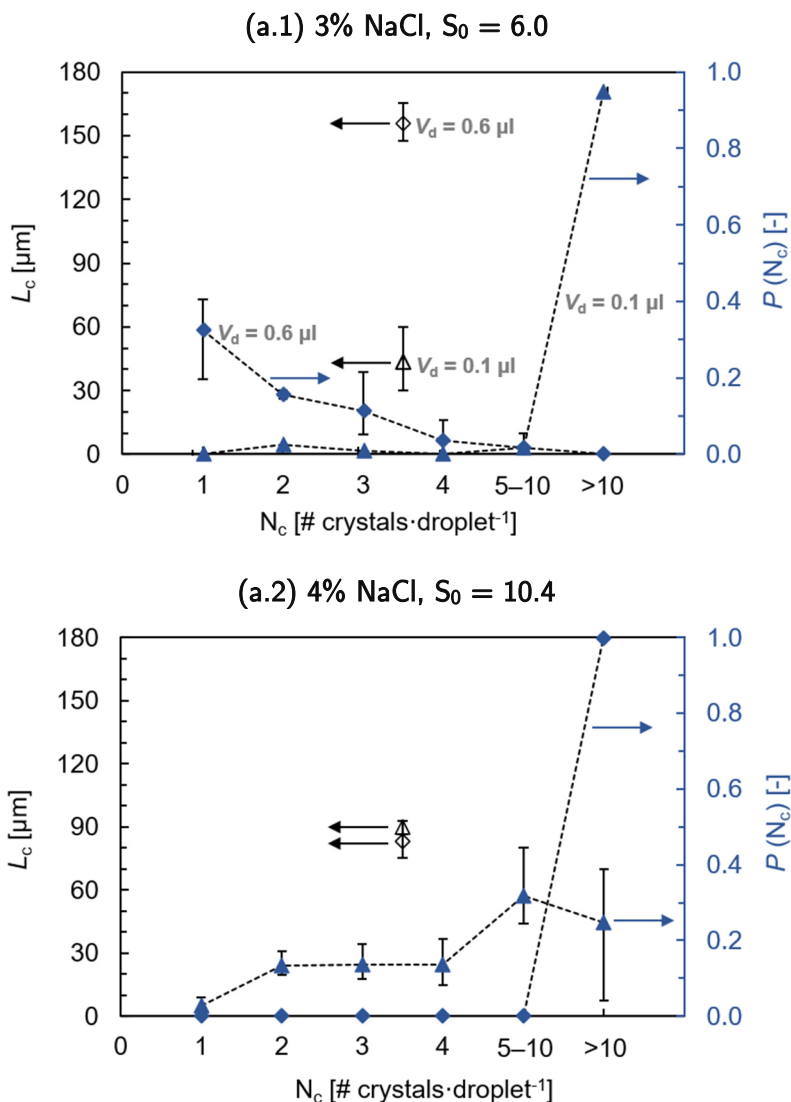
Figure 4.9. Average crystal size (L_c) and probability $[P(N_c)]$ to obtain a certain number of crystals per droplet (N_c) at 25 °C and pH 4.7, and sodium chloride concentrations of (a.1) 3% (w/v) $(S_0 = 6.0)$ and (a.2) 4% (w/v) $(S_0 = 10.4)$ for two different droplet volumes (0.1 μl and 0.6 μl). [The scale bars are standard deviations from, at least, three independent experiments].

The stochastic nature of the nucleation mechanism has an important contribution and, consequently, the number of produced crystals per droplet presents a high deviation. This is a common trend for both large

and small droplet volumes (Figure 4.9). Additionally, Figure 4.9 also shows that for excessive nucleation (Figure 4.7), the stochastic behaviour becomes less important as a high number of crystals is produced. At higher supersaturation ratios ($S_0 = 10.4$), the probability of obtaining a higher number of crystals increases [Figure 4.9-(a.2)]. This seems to indicate a low probability for the occurrence of a limited number of nucleation events possibly due to the studied high droplet volumes. Even for the higher droplet volume at $S_0 = 6.0$, where the probability for the occurrence of a single nucleation event reaches values around 30 %, the number of produced crystals is still broad.

4.4   Lysozyme concentration decay

The protein concentration decay can be estimated during the crystallization assay following the two different approaches presented below. This is further explored in Chapter 5.

Mass balance

The amount of protein in solution that is transported from the bulk phase to the crystal, at a certain time t [s], can be obtained by

$$V \Delta C_{\mathrm{p}}(t) = \Delta V_{\mathrm{c}} \rho_{\mathrm{c}} \Delta \mathrm{N}_{\mathrm{c}}(t), \qquad (4.10)$$

where V [m³] is the volume of the bulk phase, $\Delta C_{\mathrm{p}}(t)$ [kg·m⁻³] the changes in protein solute concentration between time $(t - \Delta t)$ [s] and time t [s], ΔV_{c} [m³] the changes in crystal volume, respectively; ρ_{c} [kg·m⁻³] the crystal density, and $\Delta \mathrm{N}_{\mathrm{c}}(t)$ [-] the changes in crystal number at time t [s] [158], [159]. Based on the mass balance, it is possible to establish that the initial state without crystals (m_{p}^{0}) [kg] must, at a later time, be equal to the mass of protein in single crystals $(m_{\mathrm{p}}^{\mathrm{c}})$ [kg] and mass of the protein remaining in the bulk phase $(m_{\mathrm{p}}^{\mathrm{b}})$ [kg], or as expressed by

$$V_{\mathrm{d}}C_{\mathrm{p}}^{0} = \underbrace{\rho_{\mathrm{c}}k_{\mathrm{v}}L_{\mathrm{c}}^{3}\mathrm{N}_{\mathrm{c}}}_{m_{\mathrm{p}}^{\mathrm{c}}} + \underbrace{V_{\mathrm{d}}C_{\mathrm{p}}^{\mathrm{b}}}_{m_{\mathrm{p}}^{\mathrm{b}}}, \qquad (4.11)$$

where V_{d} [m³] is the droplet volume, C_{p}^{0} [kg·m⁻³] the initial protein concentration, $C_{\mathrm{p}}^{\mathrm{b}}$ [kg·m⁻³] the protein concentration in the bulk phase, k_{v} [-] the volumetric shape factor, L_{c} [m] the crystal size, and N_{c} the total number of crystals. For the studied temperature range, the lysozyme crystals present a tetragonal shape [156]. Due to this morphology, the volumetric shape factor assumes a value of 0.54 [160], while the crystal density is the specific protein density for lysozyme (1.4 x 10³ mg·cm⁻³ [158]). The main purpose is to predict the remaining protein concentration in the bulk phase. For that reason, it is required to isolate the variable $C_{\mathrm{p}}^{\mathrm{b}}$ in the first term of the Equation (4.12) [160]–[162], which results in

$$C_{\mathrm{p}}^{\mathrm{b}} = \frac{V_{\mathrm{d}}C_{\mathrm{p}}^{0} - \rho_{\mathrm{c}}k_{\mathrm{v}}L_{\mathrm{c}}^{3}\mathrm{N}_{\mathrm{c}}}{V_{\mathrm{d}}}. \qquad (4.12)$$

This strategy is applied for the studied range of droplet volumes and initial supersaturation ratios in Chapter 5.

4.5   Conclusions

The use of phase diagrams constitutes a rational and systematic strategy to address the highly variable nature of protein crystallization. Furthermore, this enabled to acquire thermodynamic and kinetic data and make further comparisons with reported systems in literature. It was possible to conclude that the droplet volume has a major contribution to the nucleation probability (based on the definition of nucleation probability presented in section 4.2). It was theoretically expected that in droplet-based microfluidics, the nucleation probability decreases. Based on this, the formation of a lower number of crystals could be expected for the entire range of temperature and lysozyme concentration. This was however not observed due to the complex and stochastic mechanism of nucleation, including a possible competition between monomers and oligomers in

solution. This final remark highlights the stochastic behaviour of the nucleation mechanism, which becomes dominant for the cases where a lower number of crystals per droplet are produced.

5. Study of the lysozyme nucleation

"Every description of natural processes must be based on ideas which have been introduced and defined by the classical theory."

– Niels Bohr (n.d.).

Section 5.2 is published in:

J. Ferreira, J. Opsteyn, F. Rocha, F. Castro, S. Kuhn. Ultrasonic protein crystallization: Promoting nucleation in microdroplets through pulsed sonication. *Chemical Engineering Research & Design*, **162**: 249–257. 2020;

as part of the introduction, methodology, and results discussion.

Author contributions

J. Ferreira conceived the research and wrote the article.

Section 5.3 is published in:

J. Ferreira, F. Castro, S. Kuhn, F. Rocha. Controlled protein crystal nucleation in microreactors: The effect of the droplet volume *versus* high supersaturation ratios. *CrystEngComm*, **22**(28): 4692–4701. 2020;

as part of the introduction, methodology, and results discussion. The analysis is extended to the effect of precipitating agent concentration at a distinct droplet volume range and double-pulse temperature values.

Author contributions

J. Ferreira conceived the research, conducted the experiments, and wrote the article.

In Chapter 4, 2D phase diagrams with the lysozyme phase behaviour in function of the concentration and temperature were derived. This chapter intends to tackle one of the important issues in protein crystallization, the difficulty to simultaneously promote and control nucleation by avoiding the formation of many small crystals and/or precipitation occurrence. The crystallization strategies explored in this chapter aim to decrease this energy barrier for nuclei formation. This is carried out following three distinct strategies: In section 5.2, the application of low-frequency pulsed ultrasound in microdroplets is explored, while the influence of the microdroplet volume range and double-pulse temperature are assessed in section 5.3. A combined analysis of the droplet volume and double-pulse temperature is conducted takes place in this chapter.

5.1   Introduction

Biomacromolecular crystallization is difficult to address mainly due to the specific structure of these molecules [20]. Classical nucleation theory (CNT) introduced by Volmer and Weber in 1926 is a well-known theory to explain the protein nucleation mechanism [21]. An alternative theory was proposed by Galkin and Vekilov in 2000, which conceives the protein nucleation phenomenon as a two-step mechanism [26]. However, in practice, there is a poor control over the nucleation dynamics and, consequently, the crystallization outcome. Therefore, high-throughput crystallization methodologies are required, since it is often a matter of trial-and-error to successfully nucleate proteins [11]. Nucleation is a stochastic and thermally activated process with a certain activation energy [21]. Additionally, protein crystallization in microdroplets results in growing high-quality crystals with a well-controlled size distribution due to the small

volumes [91]. However, nucleation still occurs on unknown active centres present in the confined volume [163].

Protein crystallization is highly affected by external fields, *e.g.* electric and magnetic fields, and light and ultrasound irradiation [164], potentially acting as nucleation promoters. Electric fields tend to narrow the spatial location of the nucleation events through the alignment of the molecules. This results in an increase in crystal quality and yield, with the combined reduction of induction time and crystal number [164]–[167]. Additionally, Rodríguez-Romero and co-workers [168] reported that high-quality single protein crystals are obtained under an electric pulse-wave mode. Magnetic fields do not show a clear effect on nucleation, only on the crystal orientation [164], [169], [170] and quality [171], while light irradiation induces nucleation by forming radicals [164], [172], [173]. Finally, ultrasound irradiation increases the nucleation rate [174] by reducing the induction time and metastable zone width [144], [164], [175]–[177]. Moreover, the production of uniform tiny crystals might result in these dispersed crystals acting as seeds for industrial macromolecular crystallization processes [177]. Zhang and co-workers (2015) [178], Ruecroft and co-workers (2015) [179] and Ratsimba and co-workers (1999) [180] reviewed the new perspectives and developments in terms of the industrial application of sonocrystallization. However, the crystallization of macromolecules requires accurate control of process parameters (*i.e.* pH and temperature) to avoid protein denaturation or precipitation [10].

Kakinouchi and co-workers (2006) [175] performed microbatch crystallization experiments in microwells with a volume of 70 µl by applying two short pulses (10 s and 1 min) of 100 kHz and 100 W. The results point out a clear increase of the nucleation rate already after the first pulse, while long-term irradiation results in cluster damage without the generation of any nuclei [175]. Crespo and co-workers [144] validated the theoretical prediction of ultrasound acting as a nucleation promoter via reducing the metastable zone width. This study was conducted through vapour diffusion experiments with droplet volumes of 8 µl. An ultrasound signal of 37 kHz and 80 W within pulses of continuously alternated sonication periods (3 s) was established, followed by silent periods of 3 min. The results indicate that ultrasound leads to crystal formation at lower supersaturation ratios and, consequently, crystals with better diffraction properties. Cao and co-

workers [181] were able to generate large protein crystals in acoustically levitated droplets (frequency of 20 kHz and maximum forward power of 30.5 W) up to volumes of around 100 μl. Due to the absence of inertial effects, the obtained crystals exhibit better diffraction quality and fewer lattice imperfections.

Within a larger crystallization volume, Kitayama and co-workers [176] performed batch experiments in a volume of 2 ml at a frequency of 18 kHz. With a continuous cycle of alternated sonication and silent conditions (sonication for 1 min followed by a silent time of 2 min), the acceleration of nucleation kinetics was verified. Furthermore, in the unsonicated condition the formation of larger crystals occurs due to the suppression of new nucleation events [176]. More recently, Mao and co-workers [177] conducted an extended study of the influence of pulsed sonication during nucleation and crystal growth on the induction time, metastable zone width, crystal size, morphology, and process yield. The batch (under magnetic stirring) experiments performed in a volume of 30 ml showed that ultrasound irradiation leads to shorter induction times. Pulsed sonication during the crystal growth stage results in smaller crystal size. Additionally, ultrasonic crystallization in segmented flow has been only explored for organic molecules, which includes the works of Rossi and co-workers (2015) [182] on the continuous sonocrystallization of adipic acid in droplet flow, Jiang and co-workers (2015) [183] on the continuous sonocrystallization of L-asparagine monohydrate in gas-slurry flow, and Eder and co-workers (2012) [184] on the continuous sonocrystallization of acetylsalicylic acid in gas-slurry flow.

5.2   Pulsed sonication

Ultrasound is hypothesized to be a nucleation promoter [178] because of a theoretical decrease in the energy barrier for nuclei formation, due to cavitation and microstreaming [185]. Crystallization of macromolecules requires accurate control of process parameters (*e.g.* temperature, pH, among others) to avoid denaturation and/or precipitation. In particular, the nucleation step requires high supersaturation ratios [21]. Kakinouchi and co-workers [175] reported that long-term irradiation results in cluster damage without the generation of any nuclei, while Mao and co-workers

(2020) [177] observed the generation of very small and/or aggregated crystals during the continuous sonication experiments. In summary, the limitations of continuous sonication for protein crystallization applications are already established and reported in literature. These macromolecules are sensitive to high temperatures caused by continuous energy input [177], which might indicate changes in the cluster formation [175]. Revalor and co-workers (2010) [164] demonstrated that long-term ultrasound irradiation results in damages in the protein crystals due to the occurrence of secondary nucleation. Previously formed crystals can break and might act as seed crystals [164]. Nanev & Penkova (2001) [174] revealed that crystal breakage occurs and can be attributed to a higher energy of ultrasonic field than the one of intermolecular binding.

Thus, the influence of the ultrasonic power and sonication pulse time on protein crystals confined in microdroplets has not been investigated. Initially, the effect of the forward power on the experimentally measured parameters (crystals size and number, and induction time) is investigated. Based on this, the nucleation rate after 20 h at several forward powers is estimated. Furthermore, the sonication pulse time is increased, and the crystallization outcome is analysed. Finally, a comparative study with the reported literature is conducted. The influence of the total ultrasound energy on the induction time at different initial supersaturation ratios is analysed.

Experimental procedure

The experimental set-up to achieve ultrasound activated protein crystallization is displayed in Figure 5.1, while the experimental methodology is described in Chapter 2. The microbatch crystallization experiments were conducted in microdroplets with a volume equal to 0.1 µl (droplet length, L_d), generated in a microchannel with a characteristic dimension (d_t) of 500 µm (stable squeezing regime), and flow rates of the continuous (CP) and the dispersed (DP) phases equal to 0.4 ml·min^{-1} and 0.3 ml·min^{-1}, respectively.

In Section (A), the crystallization solutions (lysozyme and NaCl solutions) are premixed, while the droplets are generated after adding the continuous

phase (silicon oil) to the system [186]. The crystallization platform in Section (B) includes a coiled PFA tubing, which is sonicated during the ultrasound experiments (*Ultrasonic crystallization section*) as well as temperature control by fluid circulation through a thermostatic bath (*Huber Ministat 230*). The inlet and outlet temperatures are measured by thermocouple elements (*Omega HH374*). This coiled PFA tubing (tube-in-tube heat exchanger) is glued to a Langevin-type transducer, which is operated at its resonance frequency of 40.1 kHz, supplied by a waveform generator (*Keysight 33500B, series waveform*), and amplified by a power amplifier (*EI, RF* 2100 L, 100 W). The output signal is checked by an oscilloscope (*Keysight DS0X112A, Digital Storage Oscilloscope,* 70 MHz–2 GSa·s^{-1}) [187]–[189]. Normally, a uniform distribution of the pulse intensity for the droplets in the *Ultrasonic crystallization section* is observed without any preferential distribution. Besides the coiled PFA tubing, Section (B) also includes a microreactor device [*Silent crystallization section* in Figure 5.1-(a)], which is also temperature controlled.
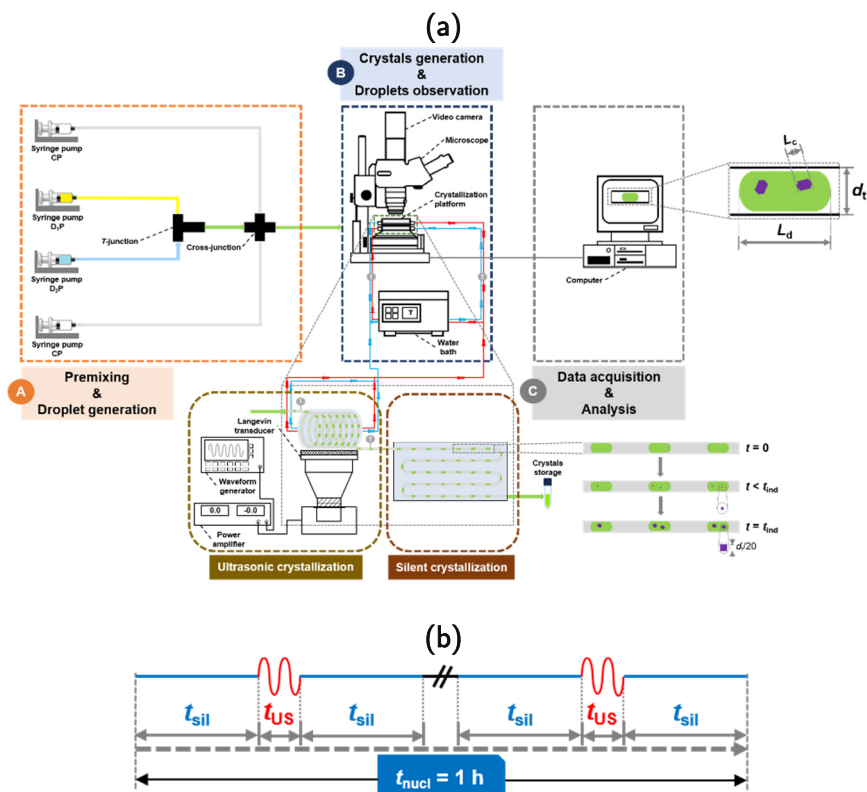
Figure 5.1. (a) Schematic representation of the experimental set-up: (A) Injection of the fluid phases using syringe pumps at room temperature; (B) Crystallization platform with an integrated temperature controller, which includes ultrasonic and silent crystallizations. Optical microscopy is used to monitor the experiments and the crystals are collected at the end of the platform; and (C) Crystal counting, and droplet length and crystal size measurements by image analysis techniques [L_d defines the droplet length, L_c the crystal size, d_t the Teflon tube diameter (500 μm), and t_{ind} the induction time]. (b) Schematic representation of pulsed sonication cycles [t_{sil} and t_{sil} define the silent and sonication times, respectively, and t_{ind} the induction time].

After the generation of stable droplets, flow is stopped, and the sonication starts up to a forward power value of 53 W·cycle^{-1}. The term forward power refers to the difference between the applied and reflected electric power of the amplifier. This is done following a burst sonication (pulsed ultrasound) profile as represented in Figure 5.1-(b). During 1 h (imposed nucleation time, t_{nucl}), generated droplets in the *Ultrasonic crystallization* section were exposed to ultrasonic radiation (duration time of 3 s·cycle^{-1} or 10 s·cycle^{-1})

(t_{US}), followed by an interval of 3 min without radiation (t_{sil}). This cycle is repeated until the imposed nucleation time is reached. The total ultrasound energy (E_{tot}) during the irradiation time reaches values up to 10.6 kJ. All the droplets and crystals are analysed in Section (C) after a crystallization time of 20 h. Furthermore, isothermal experiments were conducted under three different initial supersaturation ratios (S_0), defined as the ratio between the initial protein concentration in solution (C_0) [kg·m^{-3}] and the protein solubility (C_s) [kg·m^{-3}] [8], at pH 4.7 by changing the initial lysozyme concentration and temperature, as shown in Figure 5.2 and Table 5.1 [142]. The initial sodium chloride concentration was 3% (w/v). These values were selected based on a previous derived phase diagram in Chapter 4.

Table 5.1. Initial supersaturation ratios (S_0) and crystallization conditions (temperature, T, and initial lysozyme concentration, C_{lys}^0) for the performed sonocrystallization experiments [142] at sodium chloride 3% (w/v) and pH 4.7.

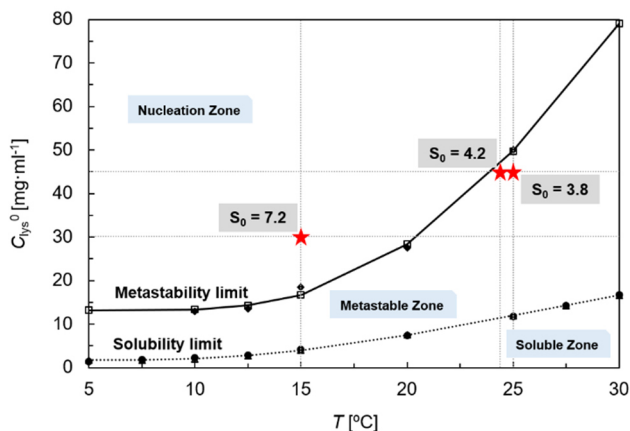| Initial supersaturation ratio S_0 [-]	Crystallization temperature T [°C]	Initial lysozyme concentration C_{lys}^0 [mg·ml^{-1}]
7.2	15	30
4.2	24	45
3.8	25	45

Figure 5.2. Lysozyme phase behaviour as the initial lysozyme concentration (C_{lys}^0) in function of the crystallization temperature (T) for a droplet volume of 0.9 μl (metastability limit from Chapter 4) at sodium chloride 3% (w/v) and pH 4.7 with the indication of the three studied initial supersaturation ratios (S_0). [The exponential fits were obtained using van't Hoff equation (solubility limit) and Markov approximation (metastability limit), and the experimental points are reported by [186]].

Induction time and nucleation rate measurements

The droplet analysis is done using *NIS-Elements Advanced Research* [190] and *ImageJ software* [191]. The crystal number is counted, while the size is determined by the equivalent diameter of a circle with an equal surface area as the projected crystal surface area. On average, 250 droplets per experiment are analysed, and three independent experiments are conducted. The induction time is determined as the first moment an observable crystal appears in a single droplet, using time-lapse capturing. For this, the crystallization platform is placed under the microscope and a picture is taken every minute (Figure 5.1). A threshold corresponding to the area of a square with width equal to $d_t/20$ is chosen, which corresponds to a circle with identical area and a diameter of $d_t/\sqrt{100\pi}$ ($d_t = 500$ μm). This threshold value ensures that the first moment of an observable crystal is detected with the current visualization setup. Once the crystal exceeds this threshold value, the measured time is set as the induction time. Following this, the induction time (t_{ind}) [s] corresponds to the time

between the moment of supersaturation and the first detection of crystals [155]. As an initial approximation, it can be calculated by [155]

$$t_{\mathrm{ind}} = t_{\mathrm{ss}} + t_{\mathrm{nucl}} + t_{\mathrm{g}}, \tag{5.1}$$

where t_{ss} [s] is the time to reach a quasi-steady-state distribution of clusters, t_{nucl} [s] the time required to form a nucleus of critical size (nucleation time), and t_{g} [s] the growing period of a nucleus until it reaches a detectable size. As $t_{\mathrm{ss}} \ll (t_{\mathrm{nucl}}, t_{\mathrm{g}})$, the theoretical induction time takes only into account two contributions from Equation (5.1) and the new empirical correlation is [192]

$$t_{\mathrm{ind}} = \frac{k_{\mathrm{t}}}{J_{\mathrm{nucl}} V_{\mathrm{d}}} + t_{\mathrm{g}}, \tag{5.2}$$

where J_{nucl} [# of nuclei·m⁻³.s⁻¹] is the homogeneous nucleation rate (number of nuclei per unit volume and per unit time that exceeds the critical size), V_{d} [m³] the droplet volume, and k_{t} [-] a fitting parameter. With the nucleation rate values estimated experimentally, k_{t} and t_{g} can be obtained from the fitting of Equation (5.2) through the minimization of the sum of quadratic errors between the theoretically calculated and experimentally obtained induction times $[\sum(t_{\mathrm{ind,exp}} - t_{\mathrm{ind,analyt}})^2]$. This quadratic error for $S_0 = 7.2$ results in 0.032 h². The values of k_{t} and t_{g} are 150.1 and 1.7 h, respectively.

The homogeneous nucleation rate can be calculated based on the average number of crystals per droplet $(\overline{N_{\mathrm{c}}})$ [-], where this last one is determined by [159], [193]

$$\overline{N_{\mathrm{c}}} = N_{\mathrm{c}}^{\infty}(1 - e^{-k_{\mathrm{nc}}t}), \tag{5.3}$$

where N_{c}^{∞} [-] is the number of crystals after infinite time (at the end of the crystallization experiment), and k_{nc} [s⁻¹] a proportionality constant. Finally, based on the definition of nucleation rate, the final number of crystals is estimated by [159], [193]

$$N_c^\infty = V_d \left(\frac{J_{\text{nucl}}}{D_p} \right)^{3/5}, \tag{5.4}$$

where D_p [m²·s⁻¹] is the diffusion coefficient of the protein [1.4 x 10⁻¹⁰ m²·s⁻¹ for lysozyme at 20 °C [148]].

Effect of the forward ultrasound power on the crystallization outcome

The influence of the forward power on the crystallization experiments performed at $S_0 = 7.2$ is shown in Figures 5.3 and 5.4, and Table 5.2. Figure 5.3 presents the lysozyme crystals generated in the confined microdroplets for silent conditions and by applying ultrasonic pulses at different forward powers, while Figure 5.4 displays the quantitative results in terms of crystal number and size. The experimentally measured induction time and the theoretically predicted homogeneous nucleation rate are shown in Table 5.2. This prediction allows the estimation of the required time for growing a nucleus to an observable size (1.7 h).
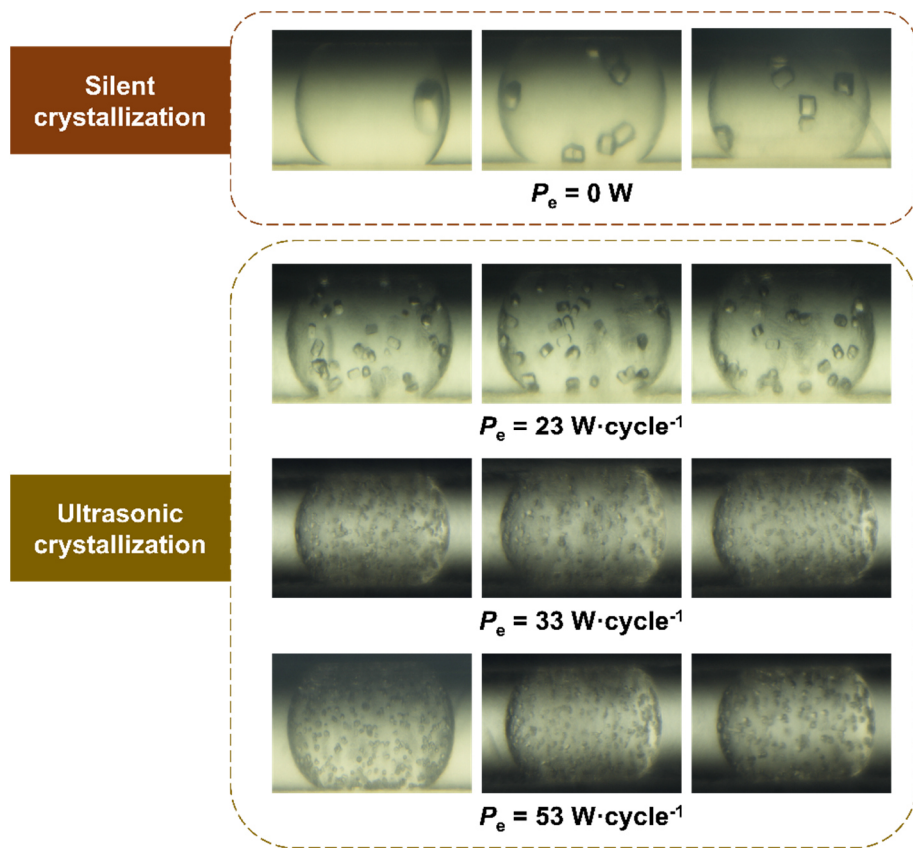
Figure 5.3. Overview of the lysozyme crystals confined in microdroplets for $S_0 = 7.2$: Silent conditions and subjected to pulsed ultrasonic radiation at the indicated forward power (P_e) and a pulse time duration of 3 s·cycle^{-1}. [All the pictures were taken 20 h after the start of each experiment and are representative results from three independent experiments after that time].
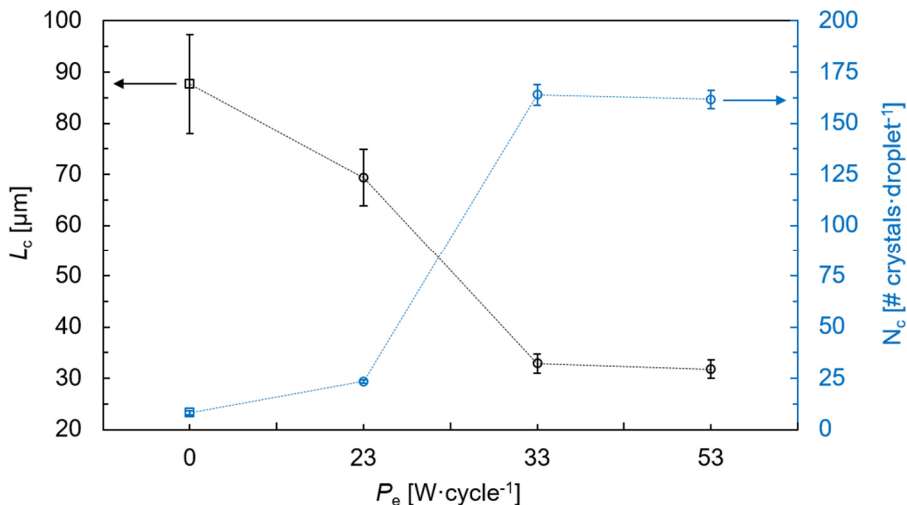
Figure 5.4. Overview of the sonocrystallization experiments for $S_0 = 7.2$: Crystal size (L_c) and number (N_c) in a single droplet for the applied range of forward power (P_e) and a pulse time duration of 3 s·cycle[-1]. [The scale bars are standard deviations from three independent experiments. The dashed lines are indicated to guide the eye].

Table 5.2. Overview of the sonocrystallization experiments for $S_0 = 7.2$ and a pulse time duration of 3 s·cycle[-1]: Experimentally measured and predicted [empirical correlation, Equation (5.2)] induction times (t_{ind}) and nucleation rate (J_{nucl}) for the applied forward power (P_e) range.

P_e [W·cycle[-1]]	t_{ind} [h]		J_{nucl} [# crystals·µl^{-1}·s^{-1}]
	Experimental	Predicted	
0	3.3 ± 0.6	3.4	0.29
23	2.0 ± 0.4	1.9	1.65
33	1.7 ± 0.4	1.7	42.00
53	1.5 ± 0.3	1.7	41.01

A few number of large crystals are obtained in silent conditions, while the number of crystals increases during the ultrasonic crystallization experiments with the forward power (Figures 5.3 and 5.4). However, the results suggest the existence of a critical forward power: Increasing the forward power results in an increase of the nucleation rate until 33 W·cycle[-1], while further increase of the forward power no longer leads to any extra increase of the nucleation rate (Table 5.2). A possible

113

explanation is that until reaching a certain forward power, the aggregation of protein molecules in solution is favoured, while for further increase there is a competition between aggregate (cluster) formation and breakage. Another possible explanation is based on the depletion zone theory proposed by Heymann and co-workers [193], initially applied to nanolitre-sized droplets. This theory states that when a nucleus is generated, a depletion zone corresponding to the region bordering the growing crystal is formed. The width of this depletion zone (w_c) defines the number of nucleation events taking place at approximately the same time. Therefore, the width of the depletion zone is a function of the induction time $(w_c \propto \sqrt{t_{ind}})$ [193]. The critical width corresponds to the instant of the last nucleation event. If a cubic shape for this volume is assumed, the number of depletion volumes fitting in the total crystallization volume is 148 $(w_c = \sqrt{t_{ind} D_p})$. At this point, the critical condition is reached, slightly lower than the number of crystals for the forward powers of 33 W·cycle⁻¹ and 53 W·cycle⁻¹ (approximately 160, as read for Figure 5.4). This might indicate that the critical forward power has been achieved.

No observable crystals were formed during the imposed nucleation time, and similar observations were reported by Kakinouchi and co-workers [175]. For the detection method used in this study, the measured induction time (Table 5.2) is higher than 1 h (imposed nucleation time). Additionally, Mao and co-workers [177] reported that ultrasound actuation during the crystal growth stage results in smaller crystals, which is possibly due to the simultaneous occurrence of secondary nucleation (and/or breakage) and crystal growth based on the combination between ultrasonic radiation and stirring. The induction time has three contributions: time to reach a quasi-steady-state distribution of clusters, nucleation time, and growth time of a nucleus until it reaches a detectable size. From the fitting of the induction time along the nucleation rate, it is concluded that it takes around 1.7 h (Table 5.2) for a nucleus to grow to an observable size. This might explain the reason for not observing any crystal after reaching the imposed nucleation time of 1 h. Additionally, Mao and co-workers [177] reported that sonication actuation during the crystal growth stage results in smaller crystals. This is possibly due to the simultaneous occurrence of secondary nucleation (and/or breakage) and crystal growth based on the combination between ultrasonic radiation and stirring. The induction time drastically decreases when applying ultrasound radiation. The effect is

already clear for the lowest forward power (Table 5.2). However, for a clear effect of the ultrasound radiation on the nucleation rate, a higher forward power is required.

On the one hand, the increase of the forward power contributes to an increase on the nucleation probability, and hence a decrease of the time required to form a nucleus (nucleation time). On the other hand, enhanced nucleation contributes to a faster decay of the lysozyme concentration in the bulk phase. This seems to suggest an intensified effect on the induction time for a forward power of 23 W·cycle^{-1} in comparison to the crystal number.

Effect of the sonication pulse time on the crystallization outcome

Without compromising the temperature control, the sonication pulse time was increased from 3 s·cycle^{-1} to 10 s·cycle^{-1}. Figure 5.5 and Table 5.3 display the obtained results for $S_0 = 4.2$ in silent conditions and at a forward power of 53 W·cycle^{-1}.
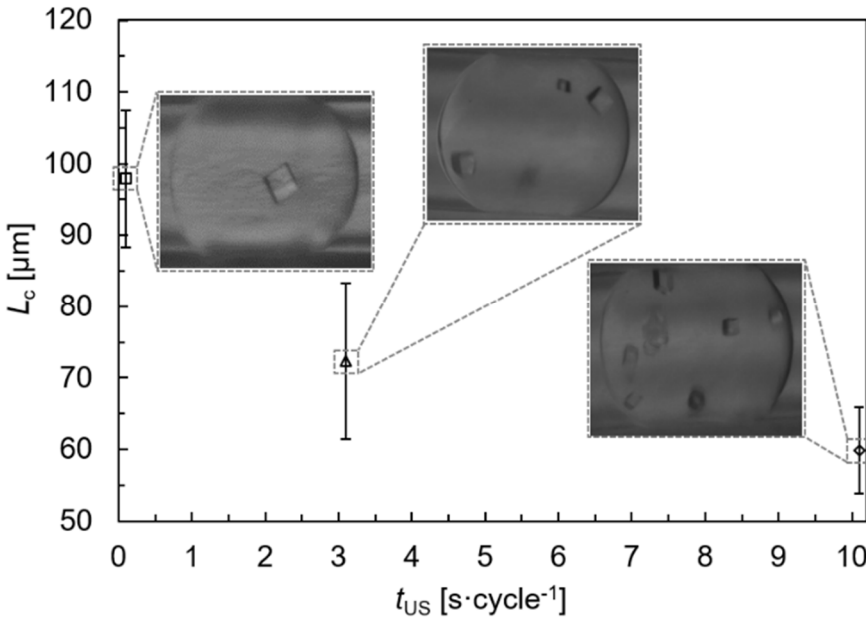
Figure 5.5. Crystal size (L_c) (including pictures of the lysozyme crystals confined in the microdroplets) for the crystallization experiments at $S_0 = 4.2$ in silent conditions and for a forward power of 53 W·cycle^{-1} and the applied sonication times (t_{US}). [The scale bars are standard deviations from three independent experiments]. [All the pictures were taken 20 h after the start of each experiment and are representative results from three independent experiments after that time].

Table 5.3. Overview of the sonocrystallization experiments at $S_0 = 4.2$: Crystal number in a single droplet (N_c) and predicted nucleation rate (J_{nucl}) for the silent case and different sonication pulse times (t_{US}) at 53 W·cycle^{-1}.

t_{US} [s·cycle^{-1}]	N_c [# crystals·droplet^{-1}]	J_{nucl} [# crystals·μl^{-1}·s^{-1}]
0	0.3 ± 0.02	0.0014
3	2.7 ± 0.7	0.046
10	5.6 ± 1.1	0.15

The droplets subjected to a longer sonication pulse time (10 s·cycle^{-1}) generated smaller crystals (from 60 μm to 72 μm) (Figure 5.5). However, the main effect comes from the supersaturation as shown in Figure 5.4 ($S_0 = 7.2$) and Figure 5.5 ($S_0 = 4.2$). At identical forward power (53 W·cycle^{-1}) and sonication pulse time (3 s·cycle^{-1}), the crystal size is

reduced by half with the increased initial supersaturation ratio (from 32 μm to 72 μm). This crystal size is further reduced for the droplets exposed to a longer sonication pulse time.

On the contrary, Mao *et al.* (2020) [177] reported that crystals obtained at a higher initial supersaturation ratio have a larger size, while the crystal number seems to be similar. The authors' proposal highlights the fact that higher protein concentrations can provide more solute for the nucleated crystals to grow into a larger size. This might be a contradiction as higher supersaturation ratios favour nucleation, many nuclei would be formed, which would consume much of the available protein in solution. The possible explanation is a higher protein concentration decay for higher initial supersaturation ratios, which increases the probability of crystal growth in the metastable zone. For lower protein concentration decays (crystallization points above the metastable zone), there is a higher probability for the occurrence of secondary nucleation. The study reported by Mao and co-workers [177] indicates that sonication improves the mixing process, where the crystals obtained under silent conditions seem to aggregate, while the number of crystals is four orders of magnitude lower compared to the one for continuous sonication. Also, Crespo *et al.* (2010) [144] showed a similar tendency of larger crystals for higher supersaturation ratios until a maximum crystal size is achieved. After this stage, the crystal size decreases as the supersaturation ratio increases.

Effect of the initial supersaturation ratio on the induction time

The induction time as a function of the total ultrasound energy for several initial supersaturation ratios, including data from reported cases in the literature, as well as the studied cases, is depicted in Figure 5.6. It must be noted that the applied nucleation detection strategy for defining the induction time differs between the studies. Mao and co-workers [177] identified the first moment of nucleation by measuring the turbidity. Kakinouchi and co-workers [175] used regular microscopic visualization to observe potential nucleation events at different irradiation points. The indicated values were obtained experimentally and do not result from any prediction. The only exception is the studied case at $S_0 = 4.2$, where the

growing period of a nucleus to reach a detectable size [Equation (5.2)] is assumed to be identical to the value achieved at $S_0 = 7.2$.
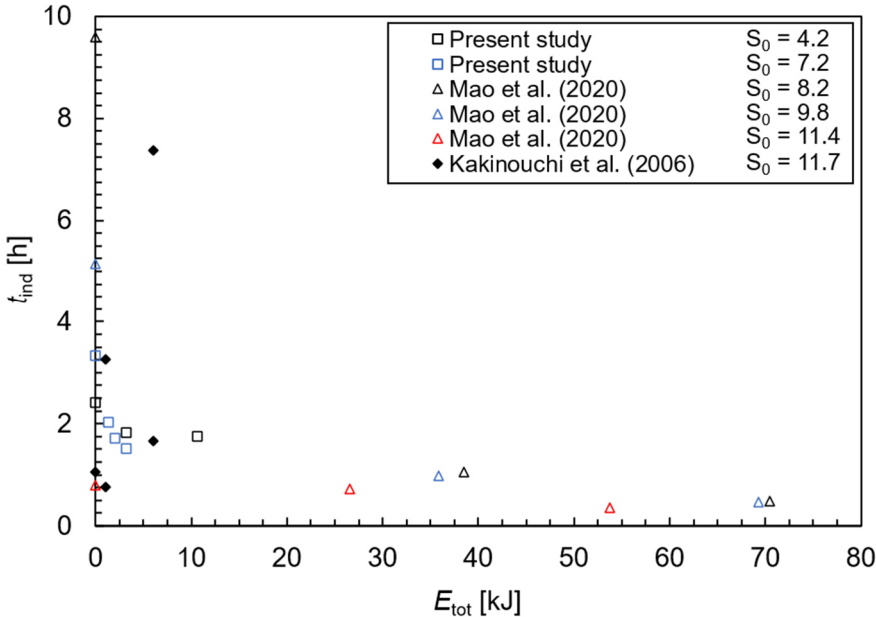

Figure 5.6. Induction time (t_{ind}) as a function of the total ultrasound energy (E_{tot}) for the reported [175], [177] and studied cases [$P_e = 271.2 \mid 389.2 \mid 625.0$ W·µl^{-1}] at the indicated initial supersaturation ratios. Kakinouchi and co-workers (2006) have exposed crystallization volumes of 70 µl during distinct irradiation times [$P_e = 1.4$ W·µl^{-1}] at different irradiation points, while Mao and co-workers (2020) simultaneously stirred and sonicated volumes of 30 ml [$P_e = 0.7 \mid 2.7$ W·ml^{-1}].

Despite the multiparametric nature of the process (*e.g.* forward power, frequency, and sonication pulse time), it is possible to observe a decreasing tendency of the induction time for higher energy inputs (Figure 5.6). As suggested by the results, there might exist a critical energy level from which further increase no longer introduces any effect on the induction time. Moreover, from a certain energy level, similar induction times are reached, regardless of the initial supersaturation ratio.

Although $S_0 = 7.2$ has 100% nucleation probability (this point belongs to the nucleation zone), $S_0 = 4.2$ only has 34%, which is a small margin below the metastability limit (Figure 5.2). Due to the supersaturation ratios close to the metastability limit, slight changes in the crystallization conditions,

can lead to the absence of any nucleation event. This is the case for $S_0 = 3.8$, where the nucleation probability is zero at both silent and ultrasonic conditions after the crystallization time (20 h). Crespo and co-workers [144] conducted crystallization experiments in a volume approximately two orders of magnitude larger than the studied cases. The results point out a shift in the metastability limit when applying ultrasonic radiation. This seems to indicate that the influence of ultrasound is limited for micro-sized droplets. Thereby, the effect of the ultrasonic radiation on droplet volume still needs further research. To our best knowledge, there are no parametric studies able to predict the minimum requirements of ultrasonic energy per droplet volume to accelerate the production of the first nucleation centres.

Crystal size distribution

Nucleation rate is controlled by means of alternating the supersaturation ratio and sonication pulse time. Besides this, the crystal size distribution is analysed. Figure 5.7 depicts the lysozyme crystal size distribution for silent and ultrasonic crystallization experiments at the studied initial supersaturation ratios and forwards powers.
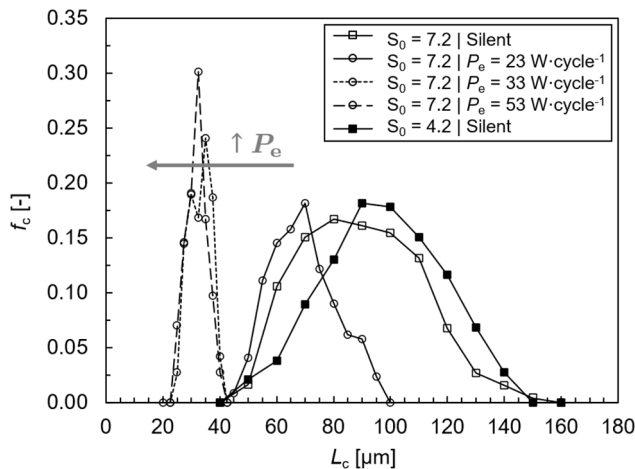

Figure 5.7. Protein crystal size (L_c) distribution for silent and ultrasonic crystallization experiments at different initial supersaturation rations (S_0). [f_c is the fraction of total droplets].

The obtained crystals under ultrasonic radiation result in a narrow size distribution, especially for higher forward powers (Figure 5.7). It seems that aggregation did not occur for both silent and ultrasonic crystallization experiments (Figures 5.3 and 5.5). The crystal size uniformity is due to the cavitation effect. Micromixing increase leads to a homogeneous local distribution of supersaturation in the droplets. Thereby, the crystals might have nucleated at the same time, which results in the formation of crystals with similar size. Finally, besides narrower size distribution, crystals are also smaller (Figure 5.7). The crystals formed at 33 W·cycle^{-1} and 53 W·cycle^{-1} present a similar size distribution, which corresponds to reaching the critical region. The distribution becomes broader for the cases under silent conditions.

Ultrasonic crystallization mechanisms

From the reported mechanisms of ultrasonic crystallization, besides cavitation, heterogeneous nucleation and cooling effect might be the ones contributing to the induction time and crystal size decrease [194]–[196]. The forward power increase promotes both mechanisms until a maximum nucleation rate is reached. The resonant cavitation bubble size of 82 µm results in a temperature difference on the cavitation bubble surface of 10 °C [197]. The point corresponding to $S_0 = 3.8$ ($T = 25$ °C) belongs to the metastable zone (Figure 5.2). For a decrease of 10 °C, this point ($S_0 = 10.8$, $T = 15$ °C) could be shifted to the nucleation zone, which would normally trigger nucleation under continuous ultrasound irradiation. Nevertheless, for the studied conditions, it is not possible to decide which mechanism is dominant as the proposed ones activate the interface of the cavitation bubbles. Furthermore, a possible competition between homogeneous and heterogeneous nucleation should not be discarded. Cavitation bubbles might directly act as nucleation sites (gas-liquid interface). Also, the liquid-liquid interface might promote nucleation. In this hypothetic scenario, the crystals could still be uniform, but nucleation would be defined as heterogeneous nucleation. At this stage, it is still reasonable to assume that the droplet interface is macroscopically homogeneous, so the nuclei formation is spontaneous. Therefore, it is expected an absence of preferential crystallization active spots (Figure 5.3).

For this last scenario, nucleation would be defined as homogeneous nucleation [198].

5.3   Microdroplet volume and double-pulse temperature

Typically, nucleation probability (based on the definition of nucleation probability presented in section 4.2) increases when the droplet volume increases since the number of available spots where nucleation can take place is increased [199]. However, the reported works conducted protein crystallization studies for a droplet volume below 1 µl [Figure 5.8-(a.1)] and mostly at low precipitant concentrations [Figure 5.8-(a.2)] [92], [96]–[98], [101], [103], [186], [200]–[202]. For this reason, there is a gap in the literature concerning the effect of the droplet volume on nucleation process. Figure 5.8 gives an overview of the crystallization conditions reported by different groups for studying protein crystallization in droplet microfluidic devices.
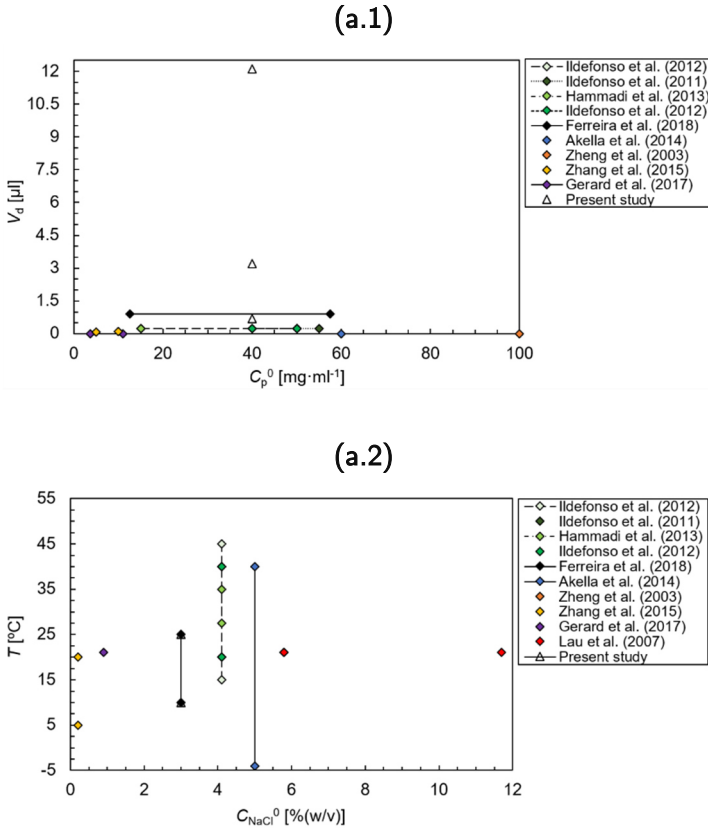
Figure 5.8. Summary of the crystallization conditions for studying protein crystallization using droplet microfluidics: **(a.1)** Droplet volume (V_d) and initial protein concentration (C_p^0) ranges and **(a.2)** crystallization temperature (T) and initial sodium chloride concentration (C_{NaCl}^0) ranges from the literature [92], [96]–[98], [101], [103], [186], [200]–[202].

Protein crystallization requires extremely high supersaturation ratios. An efficient way to easily achieve supersaturation ratio changes is by using the double-pulse method developed by Galkin & Velikov (1999) [20]. This method aims to study nucleation and relies on double-pulse temperature. The conditions promoting nuclei formation [nucleation zone, (2)] and growth [metastable zone, (1 and 3)] were selected based on the 2D phase diagram derived in Chapter 4 [Figure 5.9-(a)]. Based on this approach, supersaturation ratio and temperature profiles are created over time as shown in Figure 5.9-(b).
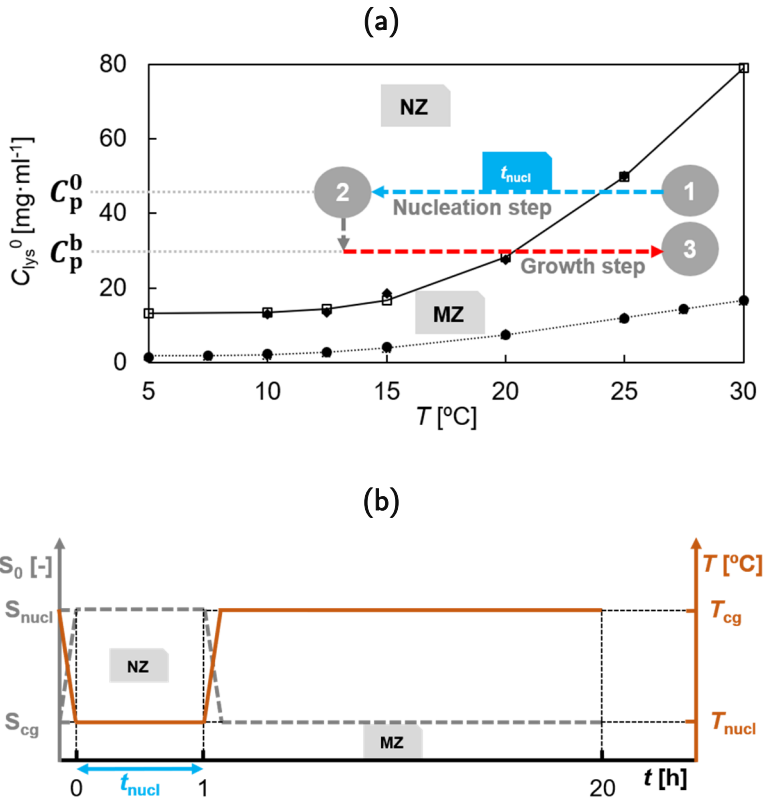
Figure 5.9. (a) Lysozyme phase behaviour as the initial lysozyme concentration (C_{lys}^0) in function of the crystallization temperature (T) at sodium chloride 3% (w/v) and pH 4.7 in the crystallization platform for a droplet volume of 0.9 μl. The indicated exponential fits were obtained using van't Hoff equation (solubility limit) and Markov approximation (metastability limit), and the experimental points are reported in [186]. [p – protein, b – bulk, and t_{nucl} – Imposed nucleation time]. **(b)** Initial supersaturation ratio (S_0) and crystallization temperature (T) profiles over time during the nucleation and crystal growth steps. [nucl – nucleation, cg – crystal growth, NZ – Nucleation zone, and MZ – Metastable zone].

As illustrated in Figure 5.9-(b), the droplets are initially generated at a certain supersaturation ratio (S_{cg}) and temperature T_{cg} situated in the metastable region (MZ) [(1)]. Subsequently, the temperature is reduced to value T_{nucl} to reach the nucleation region (NZ) [from (1) to (2) in Figure 5.9-(a)], where spontaneous nuclei formation occurs, until the imposed nucleation time is achieved. Finally, the temperature is again increased to T_{cg} to reach the metastable region [from (2) to (3)]. This further promotes

the macroscopic growth of the crystals formed in (2) and avoids the formation of new nuclei.

Experimental procedure

The experimental set-up involves three main sections (I–III) (Figure 5.10). Further details about the crystallization platform and fluid flow segmentation strategy are addressed in Chapter 2. The hydrodynamic data used for the study of the droplet volume effect on the nucleation mechanism are included in Table 5.4. Besides the distinct temperature range within a difference of 10 °C, the selected operating conditions also allow an extended droplet volume range. Therefore, these results are extending the analysis conducted in section 5.3.
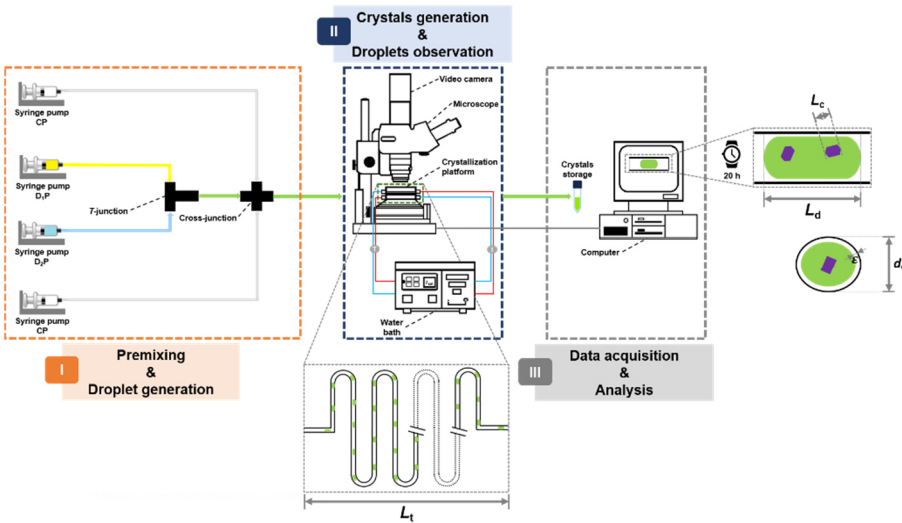

Figure 5.10. Schematic overview of the experimental set-up: **(I)** Injection of the fluid phases using syringe pumps at room temperature; **(II)** Microfluidic platform with an integrated temperature controller. Optical microscopy is used to monitor the experiments and the crystals are collected at the end of the platform; and **(III)** Crystal(s) counting and droplet length and crystal size measurements by image analysis techniques. [CP – Continuous phase (silicon oil), DP – Dispersed phase (1 – Lysozyme solution, 2 – NaCl solution); [L_t defines the Teflon tube length, L_d the droplet length, L_c the crystal size, d_t the Teflon tube diameter (1 mm), and ε the film thickness].

Table 5.4. Overview of the hydrodynamic conditions for the conducted study.

Hydrodynamic condition	#1	#2	#3
Q_{CP} [ml·min^{-1}]	0.6	0.6	0.4
Q_{DP} [ml·min^{-1}]	0.2	0.7	1.0
α_{CP} [-]	0.75	0.5	0.3
L_d [mm]	1.1	2.1	4.0
V_d [µl]	0.7	3.2	12.1

[**Note**: Q_{CP} – Flow rate of the continuous phase, Q_{DP} – flow rate of the dispersed phase, α_{CP} – volume fraction of the continuous phase [$\alpha_{\mathrm{CP}} = Q_{\mathrm{CP}}/Q_{\mathrm{CP}} + Q_{\mathrm{DP}}$], L_{d} – droplet length, V_{d} – droplet volume].

Similarly, to the experimental procedure adopted in Chapter 4, lysozyme is used without further purification. The assays are conducted in microdroplets with three different droplet volumes (Table 5.4). The initial lysozyme and NaCl concentration are 80 mg·ml^{-1} and 6% (w/v), respectively. The total duration of each experiment is 20 h. Preliminary trials are conducted to define the operating crystallization (nucleation and crystal growth) temperatures. No crystals are observed for a nucleation temperature of 20 °C ($S_{nucl} = 5.4$) and only very small crystals for 17.5 °C ($S_{nucl} = 7.7$) (25 °C as the crystal growth temperature, $S_{cg} = 3.4$). However, for a crystallization temperature of 10 °C ($S_{nucl} = 17.9$), there is not a clear effect of the droplet volume as many nuclei are formed for all the studied hydrodynamic conditions. This study reports three different set of experiments (Table 5.5), including isothermal and double-pulse temperature experiments. The isothermal experiments [Scenario (A)] were conducted at 20 °C, while for the double-pulse temperature experiments [Scenarios (B) and (C)] the temperature difference was 10 °C with an imposed nucleation time of 1 h (Figure 5.9). This corresponds to the following initial supersaturation ratios: $S_0 = 5.4$ [Scenarios (A) and (C)], and $S_0 = 3.4$ [Scenario (B)]. Figure 5.11 shows the temperature range and theoretical protein concentration decay along the crystallization experiments (Table 5.5).
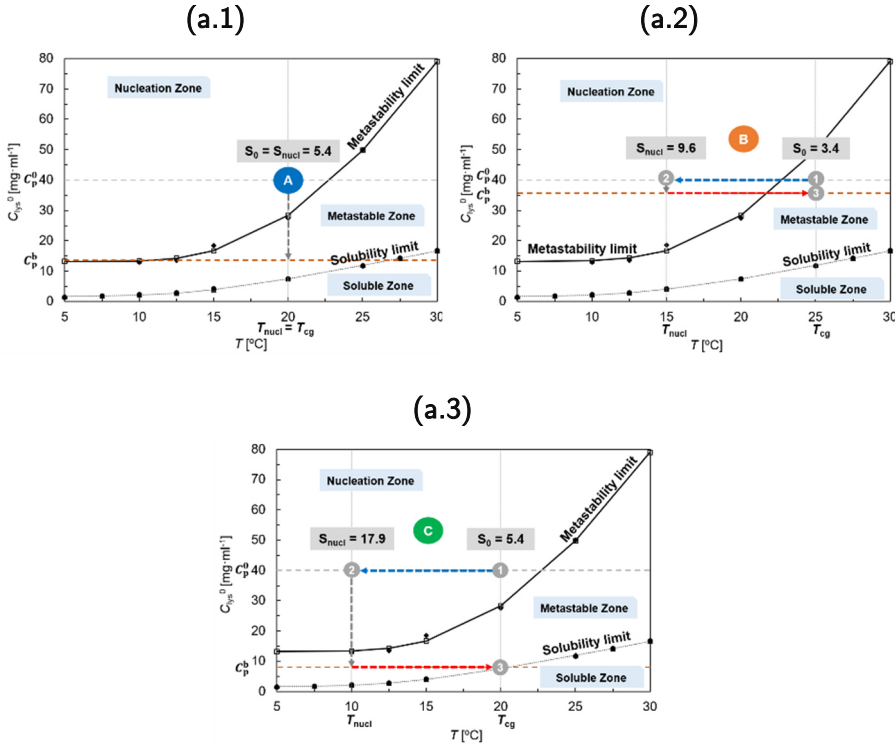
(a.1)

(a.2)

(a.3)

Figure 5.11. Lysozyme phase behaviour as the initial lysozyme concentration (C_{lys}^0) in function of the crystallization temperature (T) for a droplet volume of 0.9 µl with the representation of the nucleation [(2), T_{nucl}] and crystal growth [(3), T_{cg}] temperatures and the protein concentration decay for: **(a.1)** Scenario (A), **(a.2)** Scenario (B), and **(a.3)** Scenario (C). [The blue and red arrows indicate the cooling and heating steps, respectively]. [The supersaturation ratios (S_0 and S_{nucl}) correspond to the calculated values at a certain temperature using the initial protein concentration, 40 mg·ml^{-1}]. [The indicated concentration decays were obtained for the droplet volume $V_1 = 0.7$ µl].

Table 5.5. Overview of the crystallization experiments conditions during the nucleation (nucl) and growth (cg) stages (see Figure 5.11).

Scenario	Nucleation temperature (2), T_{nucl} [°C]	Crystal growth temperature (3), T_{cg} [°C]	Imposed nucleation time, t_{nucl} [h]
(A) Isothermal	20	20	20
(B) Double-pulse	15	25	1
(C) Double-pulse	10	20	1

126

Isothermal versus double-pulse temperature experiments

The experimental outcome is the production of crystals with different size and number for the three studied set of experiments following Scenarios (A)–(C) (Figure 5.12). Although nucleation is a stochastic mechanism, no nuclei formation should occur before the complete mixing between the protein and salt solutions. As explained in Chapter 4, by assuming a diffusion dominated process, it is expected a mixing time in the order of 2–3 min [148]. Nucleation and crystal growth are slow processes, with an involved time scale in the order of hours. Therefore, it can be assumed complete mixing before the onset of crystallization.

Figure 5.12. Droplets with different volume (V_d) $(V_1 = 0.7\ \mu l$, $V_2 = 3.2\ \mu l$, and $V_3 = 12.1\ \mu l)$ (see Table 5.4) and the produced crystals for the experiments at different initial supersaturation values (S_{nucl}) for Scenarios (A)–(C) (see Table 5.5): (A) Isothermal, (B) and (C) Double-pulse.

Without considering any heterogeneous nucleation event, a higher nucleation probability (based on the definition of nucleation probability presented in section 4.2) is typically expected for larger droplet volumes as there are more available spots where nucleation can happen [155]. For isothermal experiments [Scenario (A)], a clear influence of the droplet volume on crystal size and number is observed, while for double-pulse temperature experiments [Scenarios (B) and (C)], the results do not evidence a significant influence of the droplet volume. From the different studied scenarios, crystals seem to be larger for Scenario (C). Finally, there is a tendency for the formation of many small crystals in larger volumes. This observation is less clear for Scenario (B) since small crystals are obtained within the entire droplet volume range (Figure 5.12).

The supersaturation ratio reached during the imposed nucleation time for Scenario (C) is much higher ($S_{nucl} = 17.9$) compared to the other scenarios. Nucleation at different supersaturation ratios or even secondary nucleation might result in the formation of crystals with different size, which seems to be the case for the largest volume [Figure 5.12 – Scenarios (A) and (B)]. Following this observation, the influence of the droplet volume on nucleation (translated by the crystal size and number) seems to become more important for lower supersaturation ratios (Figure 5.12). At higher supersaturation ratios ($S_{nucl} = 17.9$), the results seem to indicate that the supersaturation effect dominates.

There are a few works in the literature reporting that temperature oscillations promote protein nucleation, while still contributing to the formation of larger crystals. Ferreira *et al.* (2011) [203] showed that lysozyme crystals generated under temperature oscillations of ± 1 °C in a supersaturation ratio range [3.4–17.6] are larger than the crystals obtained under identical isothermal conditions (hanging-drop experiments, 8 μl). This tendency is no longer valid for supersaturation ratios higher than 26.1. The reported study even reveals that for certain supersaturation ratios closer to the upper limit of the indicated range, no crystals are formed without temperature oscillation cycling. This controlled nucleation seems to promote the formation of larger crystals in Scenario (C) ($S_{nucl} = 17.9$). The tendency revealed by the reported work might indicate that extremely high supersaturation ratios ($S > 26.1$) accelerate the crystallization speed with excessive nucleation [204]. Liu *et al.* (2016) [205] reported that slight

temperature changes (control temperature of 20 °C) as small as 0.4 °C already have an effect on the lysozyme crystallization success rate (hanging-drop experiments, 2 μl). From the main findings of the reported study, it is possible to make an analogy with the studied cases. Scenarios (A) and (C) have a similar control temperature (20 °C), but while for Scenario (A) the temperature during the entire experiment is 20 °C, the temperature during the imposed nucleation time for Scenario (C) is 10 °C. Liu and co-workers showed that crystallization success rates by varying the temperature during the crystallization trial were always higher than those at constant temperature (20 °C). Wang *et al.* (2010) [206] reported that linear temperature programmes for a moderate time period (up to 48 h) and a large temperature range is beneficial for improving the screening efficiency of lysozyme crystallization (hanging-drop experiments, 1.5 μl). Since vapour diffusion experiments were conducted in the reported study, the volume reduction was indicated as possible explanation, due to a possible formation of a highly localised protein concentration at the surface of the crystallization droplet [206]. This might not be the case for the studied scenarios because no droplet volume changes were observed during the experiments. Overall, while controlled nucleation is promoted at high supersaturation ratios ($S < 26.1$), the double-pulse temperature procedure reveals a certain control because larger crystals are obtained.

Lysozyme concentration decay

As previously explained in Chapter 4, there are two different procedures for predicting the protein concentration decay. Figure 5.13-(a.1) displays the normalized lysozyme final concentration for different droplet volumes based on the crystal size and final number of crystals, while Figure 5.13-(a.2) shows a prediction of the normalized lysozyme concentration over time (protein self-assembly theory) for Scenario (A) (isothermal conditions).
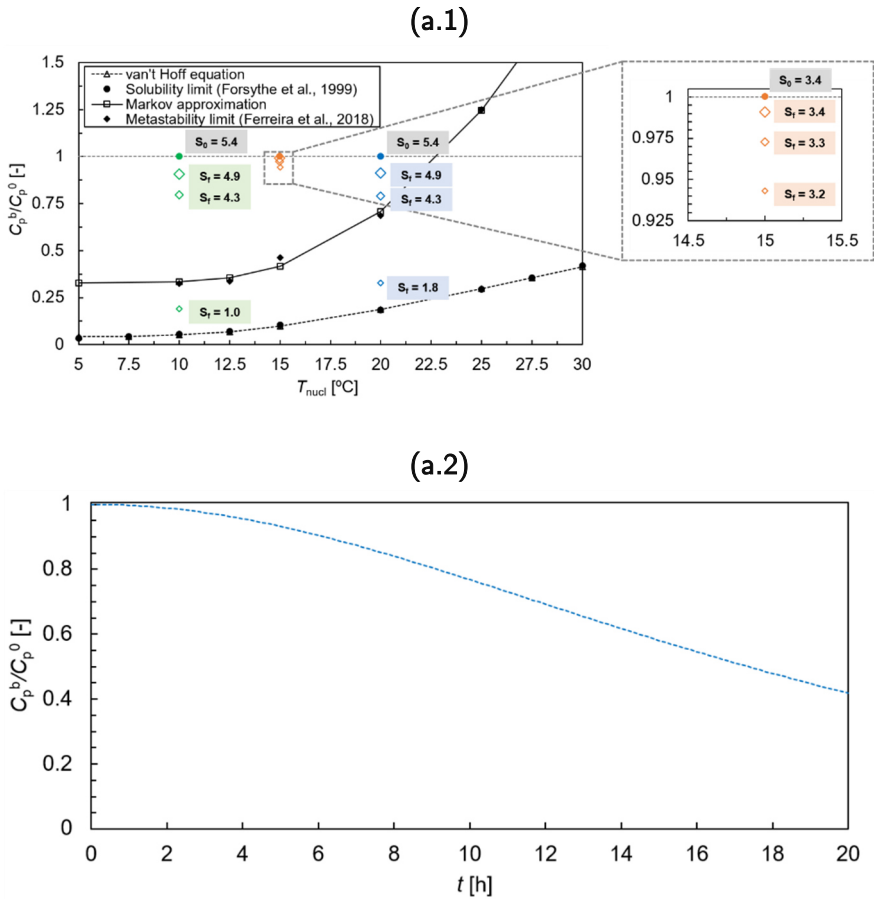
(a.1)

(a.2)

Figure 5.13. Normalized final lysozyme concentration (C_p^b) with the initial lysozyme concentration (C_p^0) **(a.1)** in function of the nucleation temperature (T_{nucl}) (initial supersaturation ratios, S_0, and final supersaturation ratios, S_f, were calculated at the temperatures in (1) and (3), see Figure 5.11 and Table 5.5) for Scenarios (A) (blue markers), (B) (orange markers), and (C) (green markers) and different droplet volumes, and **(a.2)** over time (t) for Scenario (A) (isothermal experiment) predicted by the protein self-assembly theory. [The larger marker area indicates larger droplet volume]. [The indicated exponential fits were obtained using van't Hoff equation (solubility limit) and Markov approximation (metastability limit), and the experimental points are reported in [186]].

Due to the high protein consumption expected for the smallest droplet volume in Scenarios (A) and (C), crystal growth within the metastable zone is promoted since the supersaturation ratio reaches values close to unity (solubility limit) at the end of the experiment [Figure 5.13-(a.1)]. For

larger volumes [Scenarios (A) and (C)] and as confirmed by the estimated final supersaturation ratios ($S_f > 4$), many small crystals are observed (Figure 5.12). For Scenario (A), the results shown in Figure 5.13-(a.2) predict a protein concentration decay around 60% after 20 h, which is estimated based on the protein self-assembly theory [isothermal experiments conducted at 20 °C, Scenario (A)]. Following this theory, the droplet volume is not considered for the crystallization outcome.

As a result of the high protein consumption in the bulk phase, crystal growth is expected to occur inside the metastable region [Scenario (C), see Figure 5.13-(a.3)]. For isothermal conditions [Scenario (A)], the protein concentration decay is more gradual. This results in a slower protein consumption [Figure 5.13-(a.1)]. Therefore, the protein concentration decay might be low. For this reason, other nucleation events might happen (at lower supersaturation ratios) until the critical protein concentration is achieved (metastability concentration). After this stage, crystal growth is favoured as there is available protein concentration to support crystal growth [Figure 5.13-(a.1)].

For experiments conducted under double-pulse temperature, Galkin & Vekilov (1999) [20] observed larger crystals than under isothermal conditions (microbatch experiments, 0.7 µl). Based on this work, Dombrowski and co-workers (2010) [159] applied Monte Carlo methods to model nucleation and crystal growth. From these reported studies, it is also possible to observe a steep supersaturation ratio decay for smaller droplet volumes (droplet length of 150 µm) (above 90%) compared to a larger droplet volume (droplet length of 1.1 mm) under isothermal conditions, which is in agreement with our results.

Crystal size and number measurements

The droplet analysis is done using *NIS-Elements Advanced Research* [190] and *ImageJ software* [191]. The crystals are counted, and the crystal size is determined by the equivalent diameter of a circle with an equal surface area as the projected crystal surface area. On average, at least, 100 droplets (at least 500 crystals) per experimental condition were analysed. As observed in Figure 5.12, for Scenario (B) and for the largest

droplet volume of Scenario (A), the presence of very small crystals makes the measurement of crystal size more difficult. Instead of counting the crystals, the number of crystals can be estimated based on the depletion zone width. The depletion zone corresponds to the region bordering the growing crystal, where the protein concentration is being depleted. The crystals stop growing as soon as this concentration decays significantly and any nucleation event cannot take place in this zone [193]. For the studied droplet range, if a similar value for the ratio between the number of crystals (N_c) and droplet volume (V_d) is found, the depletion zone width (w_c) [m] is, consequently, identical, which is the case for Scenario (A). This value calculated for a certain droplet volume can be used to estimate the number of crystals for another droplet volume. The depletion zone width (w_c) can be estimated by [193]

$$w_c = \left(\frac{V_d}{N_c}\right)^{1/3}. \tag{5.5}$$

For Scenarios (B) and (C), the same assumption is not valid because the droplets experience a double-pulse temperature during the experiment. The presence of many small crystals results in similar crystal size and number across the studied droplet volume range [Scenario (B)]. For the studied droplet volume range [Scenario (C)], there is only a slight difference in terms of the crystal number [Figure 5.14-(b)], which results in similar crystal size [Figure 5.14-(a)]. The imposed short time under an extremely high supersaturation ratio is translated in a high protein concentration decay until reaching values in the vicinity of the metastability limit (larger volumes) or even inside the metastable zone (smallest volume) [see Figure 5.13-(a.1)]. Therefore, together with the smallest droplet volume from Scenario (A), the largest crystals are produced [Figure 5.12-(a)]. For isothermal experiments [Scenario (A)], the ratio between the number of crystals for consecutive droplet volumes ($N_{c,V_2}/N_{c,V_1}$ and $N_{c,V_3}/N_{c,V_2}$) presents a higher value on the range of lower volumes, which perfectly fits the droplet volume ratio.
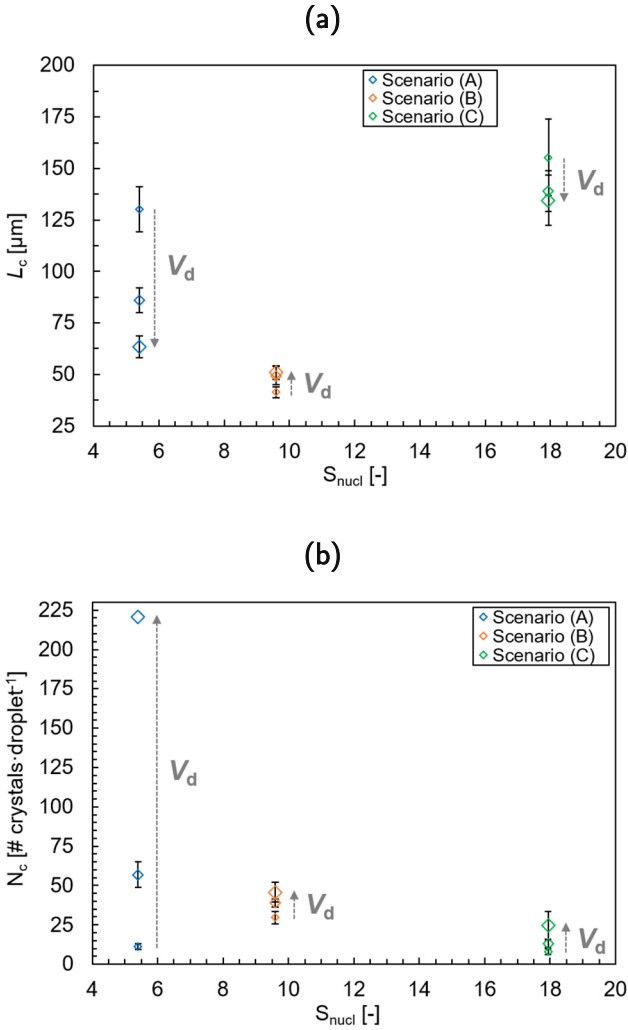
(a)

(b)

Figure 5.14. (a) Crystal size (L_c) and **(b)** Number of crystals per droplet (N_c) as a function of the initial supersaturation ratio during the imposed nucleation time (S_{nucl}) for the studied droplet volume (V_d) range in Scenarios (A)–(C). [The larger marker area indicates larger droplet volume]. [The scale bars are standard deviations from, at least, three independent experiments].

Ataka & Tanaka (1986) [207] performed millibatch lysozyme crystallization experiments at low supersaturation ratios (S < 6) and temperature differences around 3 °C. The crystallization outcome does not seem to indicate a clear trend in the crystal number with an increase in supersaturation ratio. This might validate the results shown in

Figure 5.14-(b). The reported study seems to indicate a tendency of larger crystals obtained under a temperature difference [207], which is in agreement with the results presented in Figure 5.14-(a). The crystallization outcome from the study reported by Judge *et al.* (1999) [208] (microbatch lysozyme experiments) indicates that the crystal number increases along with the supersaturation ratio, contrary to the observed in Figure 5.14-(a.1). As these experiments were conducted under isothermal conditions, no further comparisons to the studied cases can be done.

Nucleation and crystal growth rates measurements

Due to the existence of confined microvolumes, independent nucleation events take place in each droplet. For that reason, a Poisson distribution represents the number of crystals nucleated in droplets at constant temperature. The time evolution of the probability $[P_0(t)]$ that a droplet does not contain any crystal (clear droplet) is described by [58]

$$P_0(t) = \frac{N_0}{N_{tot}} = e^{-J_{nucl}V_d t}, \qquad (5.6)$$

Due to the small crystallization droplet volumes, the nucleation rate can be estimated by [150], [159], [193], [209]

$$J_{nucl} = \left(\frac{N_c^\infty}{V_d}\right)^{5/3} D_p, \qquad (5.7)$$

The calculated nucleation rate is an estimation without considering the supersaturation ratio changes during the experiment. The crystal growth rate (J_{cg}) [m·s^{-1}] assuming a diffusion-controlled growth can be estimated by [210]

$$J_{\mathrm{cg}} = k_{\mathrm{cg}} \left(\frac{C_{\mathrm{p}}^{\mathrm{b}}}{C_{\mathrm{p}}^{\mathrm{s}}} - 1 \right)^2 , \qquad\qquad (5.8)$$

where k_{cg} [m·s^{-1}] is a growth rate constant obtained empirically (in this case, $k_{\mathrm{cg}} = 0.15$ nm·s^{-1} [210]). The predicted values for nucleation and crystal growth rates are displayed in Figures 5.15-(a) and 5.15-(b), respectively.
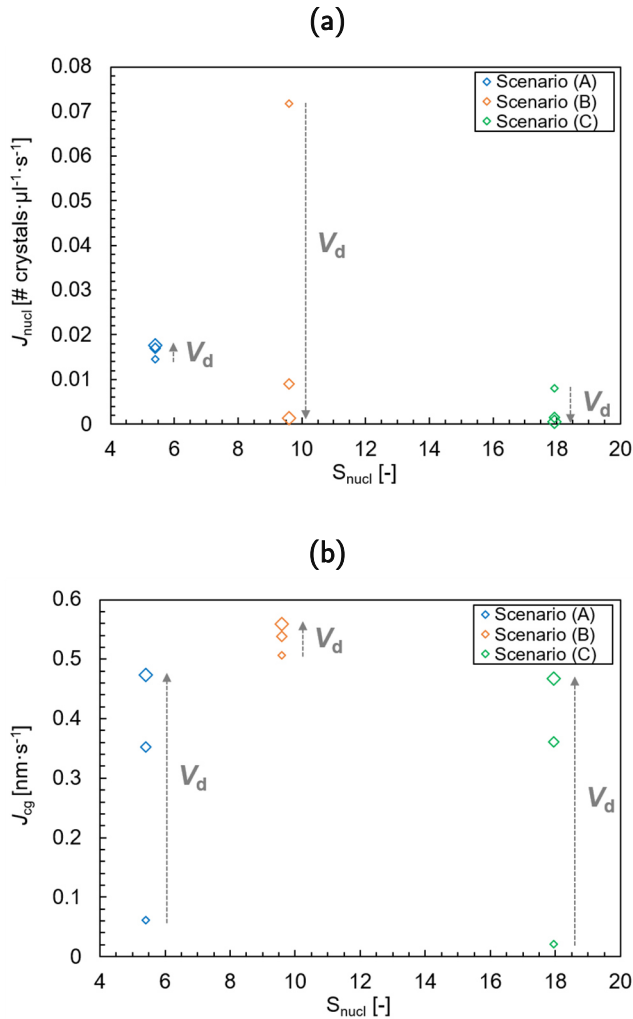
Figure 5.15. (a) Nucleation (J_{nucl}) and **(a)** Crystal growth (J_{cg}) rates as a function of the initial supersaturation ratio during the imposed nucleation time (S_{nucl}) for the studied droplet volume (V_{d}) range in Scenarios (A)–(C).

The results obtained for Scenario (A) (isothermal experiments) follow a trend of a increased nucleation rate with increasing of droplet volume [Figure 5.15-(a)]. Unexpectedly for the double-pulse temperature experiments [Scenarios (B) and (C)], the nucleation rate follows a decrease with increasing droplet volume [Figure 5.15-(a)]. This might be interpreted in light of the short-imposed nucleation time (1 h) during which the droplets are exposed to a higher supersaturation ratio. Finally, larger

crystals are obtained under a lower crystal growth rate [Figures 5.14-(a) and 5.15-(b)] since the final supersaturation ratio is lower. This might show that the main contribution for protein consumption comes from the crystal formation. McPherson & Cudney (2014) [211] reported that for higher supersaturation ratios, slower and more controlled crystal growth occurs, which seems to validate the overall results [Figures 5.12 and 5.15-(b)]. Furthermore, Ferreira *et al.* (2016) [212] highlighted that the succession of heating/cooling cycles contributes to a gradually slower crystal growth. Additionally, the crystal growth is slower for smaller droplet volumes, which follows a similar trend compared to the studied cases [Figure 9-(a.2)] [212]. The results reported by Ferreira *et al.* (2017) [27] can be explained based on a competition between crystal growth and cluster growth. Monomers are the preferred form during the nuclei generation, while the oligomers presence inhibits nucleation. Thus, oligomers might lead to the formation of a few large crystals at higher supersaturation ratios [27]. This observation emphasizes the lysozyme complex behaviour in solution and might explain the formation of larger crystals in Scenario (C).

Typically, for an equivalent growth rate and a similar number of crystals, larger crystals require more solute to grow compared to smaller crystals. Therefore, for a high number of nucleation events, the final concentration (C_p^b/C_p^0) after a long enough time for promoting crystal growth will be higher in the droplets with a larger volume [Figure 5.13-(a)].

Besides the supersaturation ratio contribution, the droplet volume also plays an important role in the protein crystallization process. The results displayed in Figure 5.15-(b) seem to indicate that independently of the estimated achieved supersaturation ratio through the different scenarios, the crystal growth rate for the largest droplet volume presents a similar value. This is possibly due to the presence of many small crystals (Figure 5.12). Furthermore, the nucleation rate seems to display different tendencies for isothermal and double-pulse temperature experiments [Figure 5.15-(a)]. While the nucleation rate decreases with the droplet volume for the double-pulse temperature experiments, the opposite takes place for the isothermal experiments. During an isothermal experiment, the decay on the initial supersaturation ratio ($S_0 = S_{nucl} = 5.4$) is gradual, until it reaches the metastable region. This might indicate a linear relationship between the number of crystals and the droplet volume [Figure 5.14-(b)]. In contrast, for the double-pulse temperature

experiments, the initial supersaturation ratios are higher [S_{nucl} = 9.6 for Scenario (B) and S_{nucl} = 17.9 for Scenario (C)], and there is a competition between nucleation and crystal growth, especially for the smallest droplet volume (Figure 5.15). The comparative difference between nucleation and crystal growth rates for the larger volumes is higher for Scenario (B), which might be related to the lower supersaturation ratios achieved at the end of the experiment [Figure 5.15-(a)].

Normally, within the labile zone, any nucleation event is spontaneous [204]. Temperature oscillations allow the formation of a critical nucleus at a lower energetic barrier [203], [204]. This might result in an earlier nucleation event, which seems to indicate slower and more ordered crystal growth [203]. However, for a similar droplet volume, Dimitrov (2019) [213] reported that slower nucleation results in larger crystal size. Despite identical temperature difference and imposed nucleation time for both Scenarios (B) and (C), the distinct estimated supersaturation ratios achieved due to the double-pulse temperature result in larger crystal size for Scenario (C) [Figure 5.14-(a)].

The droplet volume effect on the crystal number becomes more important for lower supersaturation ratios [Scenario (A)] [Figure 5.14-(b)]. For Scenario (C), the enhanced nucleation in smaller droplets results in high lysozyme concentration decay [Figure 5.13-(a)] and, consequently, slower crystal growth [Figure 5.15-(b)]. However, for Scenario (A), this is not the case as the nucleation events take place at a constant temperature. For the experiments conducted in smaller droplet volumes, the possibility for the occurrence of heterogeneous nucleation cannot be neglected. As these cases are characterized by a higher interfacial area-to-volume ratio, the probability of any heterogeneous nucleation event is higher. This can be explained based on a lower energetic barrier at the droplet interface [198].

For double-pulse experiments, smaller droplet volumes result in faster nucleation rates [Figure 5.15-(a)]. Galkin & Vekilov (2000) [26] performed lysozyme crystallization experiments in a similar volume compared to V_1 (0.7 µl), but for lower supersaturation ratios. The cases studied in this work show a faster nucleation rate due to the higher supersaturation ratios. The crystallization experiments reported by Galkin and co-workers [26] and Ildefonso *et al.* (2011, 2012) [92], [97] conducted at an identical salt

concentration seem to follow a similar tendency, as a faster nucleation rate is obtained for the smaller droplet volumes.

Finally, a last case on the application of the double-pulse experiments is reported, which follows the isothermal assays described in Chapter 4 for two distinct droplet volumes (0.1 µl and 0.6 µl) at sodium chloride 2% (w/v) and pH 4.7.   As described in Chapter 4, for isothermal experiments at 25 °C ($S_0 = 2.7$), no nucleation events were observed, and the droplets were clear. By imposing a nucleation temperature of 20 °C during 1 h ($S_{nucl} = 3.9$), crystals are produced as shown in Figure 5.16.
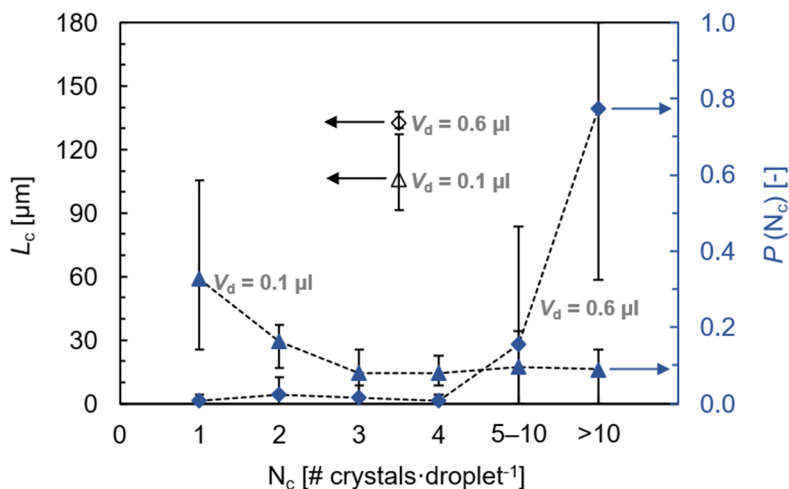
Figure 5.16. Crystal size (L_c) and number of crystals per droplet (N_c) and respective probability [$P(N_c)$] for two different droplet volumes (V_d) (0.1 µl and 0.6 µl) at lysozyme 93.3 mg·ml^{-1}, sodium chloride 2% (w/v), and pH 4.7.

Unexpectedly, larger crystals are produced in the larger droplets. This might be related to the stochastic nature of nucleation and possibly heterogeneous nucleation due to the high surface-to-volume ratio. However, it is still possible to observe the dominant effect of the droplet volume as the larger droplet volume has mainly, on average, more than 10 crystals. For smaller droplet volumes, the higher probability corresponds to generation of a single crystal (Figure 5.16).

5.4   Conclusions

Ultrasonic crystallization promotes nuclei generation during the lysozyme crystallization process in droplets. This contributes to a significant reduction of the induction time and crystal size. Besides the increase of the nucleation rate, the crystal size under ultrasound irradiation is uniform without the indication of protein precipitation. The initial supersaturation ratio has a crucial contribution to the crystal size for silent experiments, while there is a threshold for induction time under ultrasonic crystallization. This is noticed on the small number of larger crystals obtained for all the conditions under lower initial supersaturation ratio ($S_0 = 4.2$), while many small crystals are produced for the higher supersaturation ratio ($S_0 = 7.2$).

The higher nucleation probability by increasing the initial supersaturation ratio results in an increase of the nucleation rate, roughly two orders of magnitude for silent conditions, and three orders of magnitude for a sonication pulse time of 3 s·cycle^{-1}. The sonication pulse time increase from 3 s·cycle^{-1} to 10 s·cycle^{-1} results in a threefold nucleation rate increase. Finally, this study provides further perspectives for its extension to hard-to-crystallize biological macromolecules by promoting nucleation using ultrasound without compromising the control of the crystal properties.

High supersaturation ratios in small droplet volumes lead to enhanced lysozyme nucleation control in microreactors. The analysis of the protein concentration decay in the studied droplet volume range is carried out through isothermal and double-pulse temperature experiments. The droplet volume effect on the crystal size becomes more important at lower nucleation supersaturation ratios. However, fast supersaturation changes based on double-pulse temperature experiments result in larger crystals due to a faster protein concentration decay. As soon as the first nucleus is formed, the supersaturation ratio surrounding the crystal decreases due to the crystal growth. For a slower nucleation rate, typically happening in larger droplets, the growing crystal does not consume the available protein concentration in the bulk phase, and another nucleation event might take place [193]. This scenario is more probable to happen in larger droplets, since there are more active spots for nucleation. For the smallest droplet volume there is a competition between nucleation and crystal growth, where the crystal growth suppresses further nucleation events, which might lead to a lower final protein concentration in the bulk phase.

6. Insulin crystallization

"I used to say the evening that I developed the first X-ray photograph I took of insulin in 1935 was the most exciting moment of my life. But the Saturday afternoon in late July 1969, when we realized that the electron density map was interpretable, runs that moment very close."

– Dorothy Crowfoot Hodgkin, *X-rays and the structure of insulin*, *British Medical Journal*, **4**(449), 1971.

The design and characterization of droplet-based microfluidic devices for crystallization applications are introduced in Chapters 2 and 3, respectively. Towards a more detailed study on the protein phase behaviour and nucleation, lysozyme crystallization experiments are conducted in Chapters 4 and 5. Finally, the current chapter aims to close the storyline by the extension of the crystallization study from a model protein (*i.e.* lysozyme) to a complex globular protein – insulin –, and hopes to provide insights into the nucleation of protein crystals by proposing a possible insulin nucleation pathway from pre-nucleated state until a nucleus has formed. Besides all the efforts from the scientific community to study insulin, including *in vitro* studies, the reported works might be limited in terms of the fundamental and structural understanding of the insulin crystallization process. In particular, early stages of insulin nucleation require better understanding, which might be extremely relevant for further *in vivo* crystallization.

6.1   Historical perspective

While Marie Curie dominates any discussion about the importance of women in scientific research, there have been many others dedicating their life to science. One of them is Dorothy Crowfoot Hodgkin – a Prize Nobel Laureate –, who had an enormous contribution to the improvement of X-

ray crystallography techniques and, consequently, the study of biological macromolecules [214]. Among Hodgkin's longest-lasting accomplishments is the mapping of insulin structure, which involved 35 years of work. This study was concluded in 1969, but the importance of this polypeptide hormone to the medical use for diabetes treatment still highlights the importance of this protein [215]. Overall, the deficiency or resistance to insulin causes profound deregulation of metabolic processes (*i.e.* control of blood glucose) [216], which might result in disorders such as diabetes mellitus and obesity [217]. Over the last 50 years, long-acting crystalline insulin formulations have been applied [218]. However, the search for new drug formulations for replacing the frequent injections is still an unsolved question [219].

Nowadays, crystallizing target proteins to enable rational drug design has been extended to proteins related to cancer, HIV, heart disease, among others [220]. Furthermore, crystallization is an industrially relevant process [221] in the pharmaceutical manufacturing since 90% of the active pharmaceutical ingredients are produced in the crystalline form. Additionally, crystalline forms with carefully tailored properties often have longer storage lifetimes and higher purity than the dissolved form [222]. Finally, the slow dissolution rate of protein crystals allows the achievement of sustained release of medication [218], where crystal size and shape uniformity is required [217]. Crystal monodispersity ensures a sustainable and adjustable release of the therapeutic agent [223]. This can be achieved by crystal nucleation events taking place at similar time [224]. In this context, insulin crystallization opens new perspectives for further protein crystallization insights as a therapeutic hormone. Along the years, a multiplicity of research groups from biochemistry to engineering are gathering efforts to crystallize insulin under different operating conditions (*e.g.* crystallizing agent and buffer solutions, pH, among others) (see Appendix C – C1), usually in the presence of *e.g.* citrate, phosphate or ammonium acetate buffer, and a few additives (*e.g.* phenol, acetone) [225].

6.2   Introduction

Insulin is the only protein produced in a healthy human body in crystalline form, which highlights its importance for crystallization studies [226]. Bergeron *et al.* (2003) [216]   explored   the   thermodynamics   of   the

hydrophobicity of insulin molecules, where the influence of temperature on solubility was investigated. Mühlig *et al.* (2001) [227] performed microbatch crystallization experiments for the observation of the early crystallization stages and determination of crystal growth kinetics using CLSM (confocal laser scanning microscopy). The initial droplet volume was 20 μl, while it decreased over time due to solvent evaporation. This study reported that precipitation occurred after the buffer addition, which resulted in a cloudy solution at higher initial insulin concentrations. This incomplete dissolution allowed sub-microscopic insulin particles within the solution, which might correspond to insulin clusters. Anisotropic growth of monoclinic crystals was observed [227]. The crystal size reached values around 30 μm. Schlichtkrull (1957) [228] applied seeding as a crystallization technique to generate monodisperse insulin crystals. In other contributions from the same research group, an extended study of the crystallization kinetics for different crystallization mixtures was conducted [229] .

Nanev *et al.* (2011) [226] reported nucleation rate values for batch insulin crystallization experiments under different surfaces through DLS (dynamic light scattering). Nanev and co-workers made an important contribution to the nucleation study, including the energy barrier for insulin crystal nucleation and correspondent critical nucleus size. For this, the double-pulse technique was used to separate nucleation and crystal growth stages. The authors concluded that, besides homogeneous, heterogeneous (surface) insulin nucleation is still taking place in the bulk solution. Rhombohedral insulin crystals in the range 0.4–0.6 mm were produced [226]. Nanev *et al.* (2013) [223] described experimental strategies for growing equally-sized insulin crystals using batch crystallization methods (volume around 350 μl). This was done following the nucleation-growth separation principle (NGSP), where a constant number density of nucleated crystals grows further to produce insulin crystals. However, with a different growth temperature, crystals of variable sizes were produced, which possibly indicates the occurrence of secondary nucleation. MZW (metastable zone width) was deduced to belong to the temperature range [22–26] °C [223]. Nanev *et al.* (2017) [230] extended the applicability of NGSP by choosing short nucleation periods for reducing crystal polydispersity, which resulted in a uniform size distribution [230].

Once again, Penkova *et al.* (2004) [224] used the NGSP, but a supersaturation gradient along a glass capillary was applied during the

insulin crystallization experiments. Finally, Parambil *et al.* (2011) [231] explored insulin crystallization under oscillatory flow to increase the overall yield, by enhancing nucleation due to shear rate. Parambil and co-workers reported that insulin hexamers or high density liquid clusters of insulin forms resulted in ordered arrangements under shear flow [231]. Contrarily to the previous cases, Bromberg *et al.* (2005) [232] produced insulin microspheres by gradually applying cooling and using aqueous solutions of PEG (additive), avoiding the need for zinc salts addition. The kinetic measurements were conducted by DLS, and it was concluded that the nucleation rates of proteins are typically enhanced in the presence of polymers [232].

During the early stages of crystallization, Kadima *et al.* (1991) [233] explored the capabilities of DLS and concluded that the processes leading to crystallization can be distinguished from those leading to precipitation. Furthermore, is was suggested that the bonding between Zn ions and the subunits of the insulin hexamer limit aggregation in solution [233]. Chatani *et al.* (2015) [234], Dolui *et al.* (2018) [235] and Pease *et al.* (2010) [236] studied the nucleation event during the fibrillation process of insulin. After the formation of early prefibrillar aggregates, their coalescence results in larger clusters until mature amyloid fibrils. The gradual formation of assembled particles with semicrystalline nanostructures was observed for the higher insulin concentrations [234]. Protein aggregation and formation of the oligomeric state and fibrillar structure are linked to several pathologies (*i.e.* type II diabetes) [235]. Contrarily to the previous conclusions, Pease and co-workers suggested that fibrillogenesis may occur directly from assembly of denaturing insulin monomers, without passing through a series of intermediates [236].

The existing crystal forms of insulin include rhombohedral, cubic, monoclinic, and orthorhombic [237]. Typically, only porcine and human insulins are known to exhibit rhombohedral shapes, while bovine insulin is a twinned appearance (*e.g.* star and needle shape). However, the bovine insulin zinc-free crystals produced by Chen *et al.* (2017) [225] appear to be rhombohedral. A polymorphic study conducted by Fili *et al.* (2015) [238] revealed four different crystalline polymorphs of human insulin, two of those with monoclinic symmetry. Yip & Ward (1996) [239] conducted experiments with bovine insulin and three different polymorphs. While the molecules tend to form dimers (active form), in the presence of Zn^{2+} ions, they form hexamers (non-active form) [238]. In particular, hexamer is the

only significant species formed prior to crystallization, while crystal growth occurs by hexamer addition [233]. Typically, a Zn-insulin nucleus volume is 10^{-19} cm^3, which encompasses one to two hexamers (each 5 nm in size [223]) building the crystal lattice [230]. Norrman & Schluckebier (2007) [219] showed that orthorhombic crystals contain three insulin hexamers in the asymmetric unit whilst monoclinic only one [219], while Nettleton *et al.* (2000) [240] reported that insulin crystals contain predominantly two hexamers, but up to four in the presence of zinc ions. In their absence, dimers and tetramers are observed. The type, size and morphology of the crystals affect the insulin releasing speed, which is one of the reasons for the extensive study dedicated to this protein. The charge state of the insulin solution (*i.e.* pH) also has an important contribution to the crystal morphology [219]. As discussed above, there are still plenty of open questions about insulin crystallization, where one of the main issues to overcome is the polydispersity of insulin crystals. With the purpose of gaining a better control over the insulin crystallization process, assays are conducted in confined microdroplet volumes, where multiple parametric studies (*e.g.* temperature, protein and precipitating agent concentration, dynamic viscosity, and interfacial tension) are performed. This study constitutes the first attempt towards insulin crystallization trials in multiphase microsystems with a better understanding of the protein crystallization mechanisms.

6.3   Insulin crystallization experiments

As described above and indicated in Table C1, Appendix C, several studies with insulin have been conducted by applying a wide range of crystallization techniques, such as (micro/nano)batch (including salting-out), hanging-drop vapour diffusion, seeding, among others. Additionally, this includes an extensive list of insulin types, precipitant solutions, buffer solutions and additives, and pH and temperature ranges.

Solutions preparation

Recombinant human insulin (*Sigma-Aldrich*, 5.808,00 g·mol^{-1}, CAS-No. 11061-68-0) is used during the entire crystallization study without

further purification. Despite the different strategies reported in the literature for the solutions preparation (Table C1, Appendix C – C1), the protocol proposed by Bergeron *et al.* (2003) [216] is followed. The solution composition includes 0.02 M hydrochloric acid (HCl, solvent) (Chem-Lab Analytical, CAS-No. 7647-01-0), 0.10 M zinc chloride, anhydrous power (ZnCl$_2$, buffer) (*Sigma-Aldrich*, CAS-No. 7646-85-7), 0.2 M trisodium citrate, dihydrate (TC, precipitating agent) (*Sigma-Aldrich*, CAS-No. 6132-04-3), and neat acetone (co-solvent) (*VWR International*, CAS-No. 67-64-1). The acid solution is prepared with ultrapure water (MiliQ water, resistivity of 18.3 MΩ·cm^{-1} at 20 °C).

Initially, insulin is dissolved in highly diluted HCl at different concentrations. Afterwards, ZnCl$_2$, TC, and acetone are added, consecutively. Thus, the final concentrations of the components in the crystallizing solution are 0.005 M ZnCl$_2$, 0.05 M TC, and acetone 20% (v/v) acetone. The solutions preparation occurs at room temperature without any pre-heating or centrifugation steps. Before their use, all the solutions are filtered using syringe filters (Puradisc FP 30 mm, cellulose acetate, 0.2 μm) (*Sigma-Aldrich*, *Whatman*). These filters are used to remove any irregularly shaped aggregate that might reach dimensions around 1 μm [227].

Hanging-drop vapour diffusion experiments

The initial crystallization experiments are carried out using 24-well VDX plates (*Hampton Research*^{TM}) and 22 mm siliconized coverslips (*Hampton Research*^{TM}) sealed with high vacuum grease (Dow Corning). Hanging-drop vapour diffusion is the technique used for the screening of the crystallization conditions. Each drop (8 μl) is composed of a mixture of insulin solution and reservoir (precipitating agent, buffer and co-solvent) solution. The reservoir concentration is kept constant, while the ratio between the protein and reservoir concentrations is varied, by changing the drop volume. This drop is placed in vapour equilibration with the reservoir (1 ml) solution. To achieve equilibrium, as typically the drop contains a lower precipitating agent concentration (TC) than the reservoir, water vapour leaves the drop, and the insulin undergoes an increase in relative supersaturation, due to both increase of the protein and precipitating agent concentration. Equilibrium is reached when the precipitating agent

concentration in the drop is approximately the same as that in the reservoir. A schematic representation of the experimental set-up can be found in Figure C1, Appendix C.

Insulin crystallization experiments are either conducted at room temperature or at 4 °C, using an incubator for this last case. The crystallization plates are placed under a microscope (*Nikon SMZ-25*), equipped with a *Nikon DS-Fi3* digital camera, where time-lapse picture capturing and video recording are performed. All the crystallization plates are periodically checked for the presence of crystals and their size. Afterwards, the analysis is conducted using *NIS-Elements Advanced Research* [190] and *ImageJ software* [191]. The success of a crystallization experiment is defined by the factor of success, which represents the fraction of drops producing crystals. The initial insulin concentrations are 5.0 and 15.0 mg·ml^{-1}, and the initial salt ($ZnCl_2$) concentration is 0.005 M.

Protein solubility and phase behaviour constitute the basis for the determination of crystallization conditions [241]. Insulin's solubility is temperature dependent [242] as with the temperature increase, solubility increases [223], [226], [230], [243]. Figure 6.1 displays insulin solubility over a certain temperature range at acetone, 20% (v/v) and $ZnCl_2$, 0.005 M.
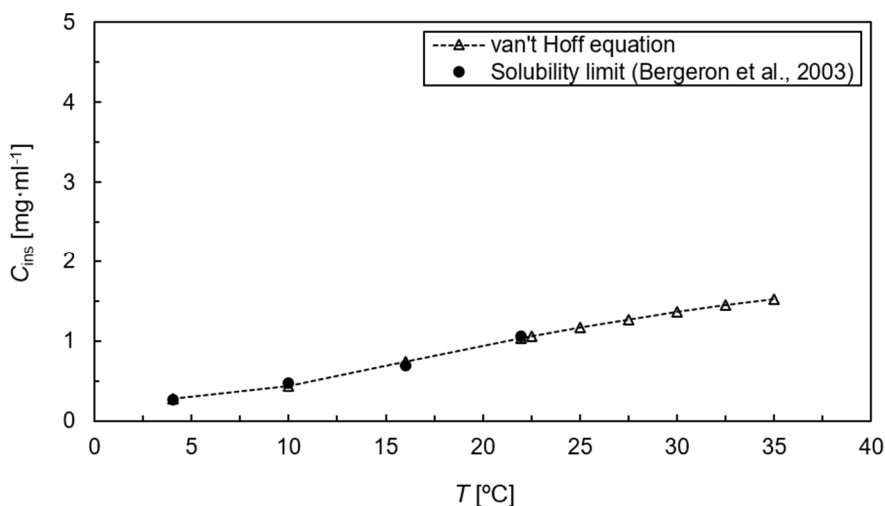
Figure 6.1. Temperature (T) dependence of the solubility of insulin (C_{ins}) at acetone, 20% (v/v) and $ZnCl_2$, 0.005 M [216].

The crystallization screening is conducted by adopting the hanging-drop as the crystallization technique and following the crystallization conditions reported by Bergeron *et al.* (2003) [216]. The crystallization conditions are further optimized to reduce the insulin consumption (Table 6.1). Afterwards, these and additional conditions are replicated in a microfluidic reactor. The initial screening of insulin crystallization conditions is carried out by hanging-drop vapour diffusion as the crystallization technique and the main results and respective discussion are reported in Appendix C – C2.

Microfluidics experiments

The experimental setup (Figure 2.3) and the analysis methodology to perform crystallization experiments in a droplet-based microreactor are mainly described in Chapter 2. Microbatch insulin crystallization experiments are conducted in microdroplets with a volume close to 1 µl, generated in a microchannel with a diameter of 1 mm, and flow rates of the continuous [Fluorinert^{TM} FC-70 (*Sigma-Aldrich*, CAS-No. 338-84-1)] and dispersed (crystallization solutions premixed before the addition of the carrier fluid) phases equal to 1.0 ml·min^{-1} and 0.5 ml·min^{-1}, respectively. These flow rate values are kept constant, except the ratio between the protein solution (insulin) and crystallization solution (ZnCl$_2$, TC, and acetone), but always maintaining the total flow rate of the dispersed phase. The initial insulin concentrations are 2.5, 5.0 and 15.0 mg·ml^{-1}.

Table 6.1. Solution concentrations of the performed experiments with hanging-drop and microfluidics experiments. [$C_{ins,0}$ defines the initial insulin concentration; C_{ins} and C_{PS} represent the insulin and salt ($ZnCl_2$) solution concentration, respectively, after the mixture].

Crystallization experiments	Solution concentrations		
	$C_{ins,0}$ [mg·ml⁻¹]	C_{ins} [mg·ml⁻¹]	C_{PS} [M]
Hanging-drop vapour diffusion	15	7.5	0.0025
		5	0.00333
		3.75	0.00375
		3	0.004
		2.5	0.00417
	5	1.67	0.00333
		1.25	0.00375
		1	0.004
		0.83	0.00417
Microfluidics	15	5	0.00333
	5	3.33	0.00167
		2.5	0.0025
		1.67	0.00333
		1	0.004
	2.5	1.25	0.0025
		0.83	0.00333

During these experiments, the insulin crystal size in confined microdroplets is measured. Typically, the size of a rhombohedral insulin crystal is defined as the greatest diagonal in the projection of the crystal on a plane through a face [225], [228]. On average, 150 droplets are analysed and, at least, 500 crystals measured per experiment. Based on the previous results from the crystallization screening, experiments are performed at different insulin and salt solution concentration. These results are presented in Figures 6.2 and 6.3. Further experiments are performed for an insulin concentration of 5 mg·ml⁻¹ at different temperatures (Figure 6.4), which resulted in the largest insulin crystal size among the studied concentrations range.
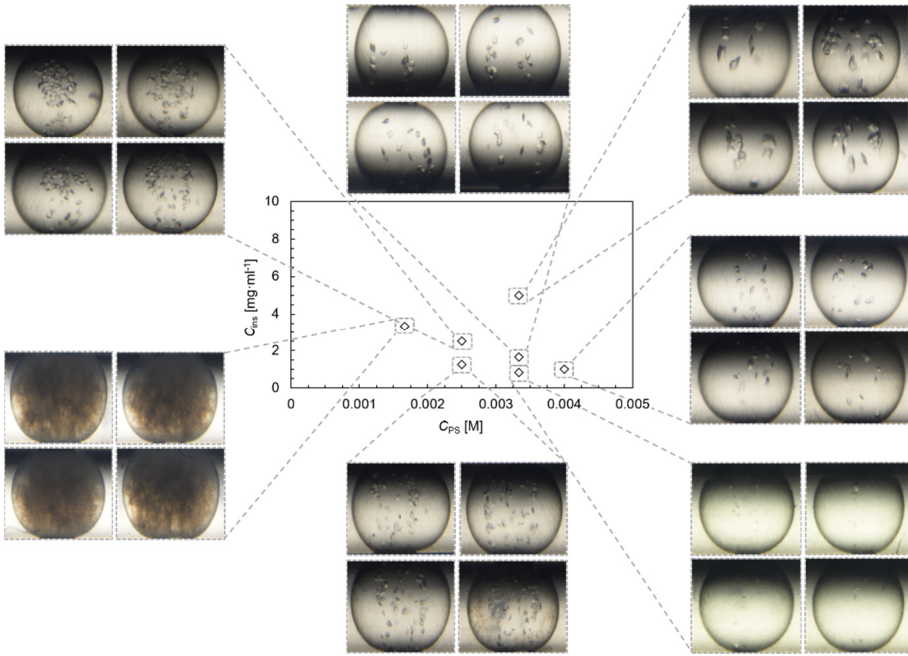
Figure 6.2. Insulin crystals produced in microdroplets at different insulin (C_{ins}) and salt (ZnCl$_2$) (C_{PS}) concentration (see Table 6.1) at 20 °C collected after 1 day.
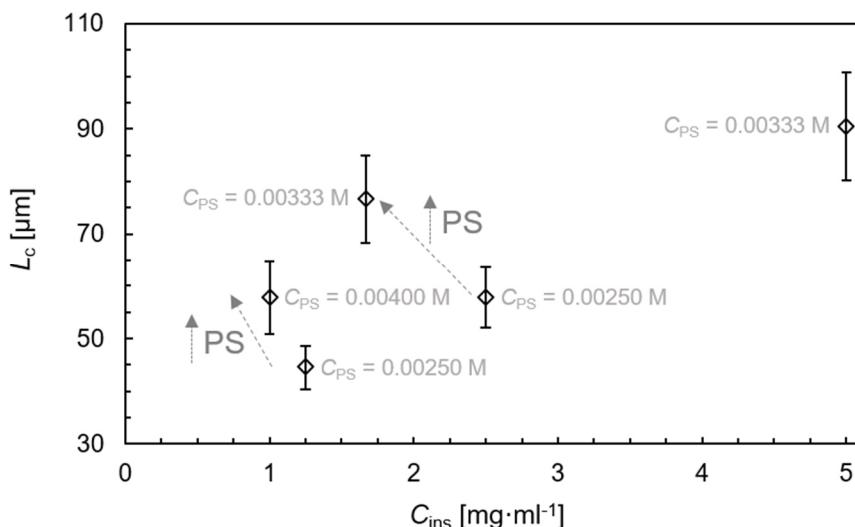
Figure 6.3. Insulin crystal size (L_c) for the experiments conducted in microdroplets at 20 °C in function of insulin concentration (C_{ins}) (see Table 6.1 and Figure 6.2 for droplets with measurable crystals) [C_{PS} defines the salt ($ZnCl_2$) solution concentration]. [The scale bars are standard deviations from, at least, three independent experiments; salt indicates zinc chloride solution].

Overall, larger insulin crystals are produced at higher insulin concentrations (Figure 6.3), and lower salt ($ZnCl_2$) concentrations tend to form agglomerates and/or aggregates (Figure 6.2). A clear formation of aggregates occurs at the lowest salt solution concentration (0.00167 M), and a few aggregates after 1 day are also observed at the second lowest salt solution concentration, 0.0025 M (and insulin concentration of 1.25 mg·ml^{-1}, Figure 6.2). An opposite behaviour is observed during the hanging-drop experiments as higher insulin concentrations tend to form more agglomerates and/or aggregates (Appendix C – C2). For the lowest insulin concentrations, 0.83 and 1.0 mg·ml^{-1}, the drops from the hanging-drop experiments do not seem to present crystals (Table C3, Appendix C), while crystals in the droplet-based microreactor at identical solution concentrations are produced. At an identical salt solution concentration, larger crystals are produced at higher insulin concentrations, which might suggest that the insulin concentration is the dominant variable (Figure 6.2).

In most of the reported works, the crystal size distribution is not presented to possibly compare the average crystal size, only a few pictures of the

crystals are available. Bergeron *et al.* (2003) [216], Parambil *et al.* (2011) [231], and Penkova *et al.* (2004) [224] observed narrower size distributions. From the available pictures, the crystals were measured following a similar procedure compared to the one adopted for the cases under study. The average crystal size obtained by Begeron and co-workers is 25.4 $\pm$ 2.0 µm after several days within a crystallization volume of 200 µl at 4 °C. Parambil and co-workers studied the effect of shear rate on the nucleation mechanism. Under stationary conditions, the achieved average crystal size range is 300–450 µm after 2 days within a glass capillary with 2 mm internal diameter at 10 °C. Penkova and co-workers also conducted experiments through a supersaturation gradient along a glass capillary and the reported crystal size is around 1 mm after 2 days at 23 °C. Nanev & Hodzhaoglu (2012) [242] obtained an average crystal size of 500 µm in customized glass cells at nucleation and crystal growth temperatures of 4 °C and 18–29 °C, respectively. More similar to the presented results, Chen *et al.* (2017) obtained an average size around 43.3 $\pm$ 2.0 µm using a PDMS chip with a microwell diameter of 100 µm at room temperature [225].
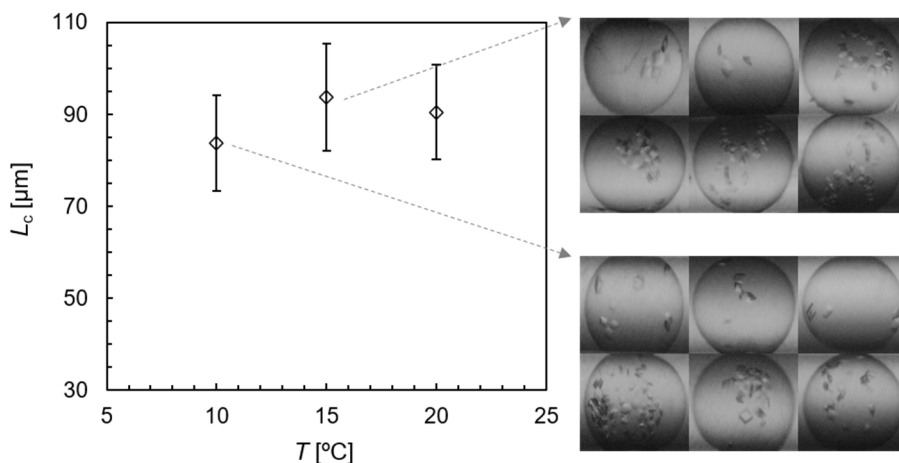
Figure 6.4. Insulin crystal size (L_c) for the experiments conducted in microdroplets at insulin (C_{ins}) and salt solutions concentration of 5 mg·ml^{-1} and 0.00333 M, respectively, for three different temperature values (T) and a few droplets with crystals collected after 1 day. [The scale bars are standard deviations from, at least, three independent experiments].

From the current experiments, no clear effect of the temperature on the crystal size for a temperature range from 10 °C to 20 °C is observed

(Figure 6.4). This follows the observations by Nanev *et al.* (2013) [223]. The authors reported identical number density of nucleated insulin crystals at different initial supersaturation values and a temperature range around 5 °C.

6.4   Rheology study

A rheology study is conducted to evaluate the protein behaviour and stability in solution, and the respective consequences based on the crystallization outcome. This analysis becomes especially important for the possible implications on the protein formulation development [244] and handling [245]. The main findings are shown in Figures 6.5–6.8 and discussed afterwards.

Shear viscosity measurements

These measurements are done using a rotational rheometer (Physica MCR301, Anton Paar) with a Peltier temperature control system set at 20 °C and cone and plate geometry. In this arrangement, the cone (diameter of 75 mm) is truncated at the centre so as not to touch the plate and this ensures that the shear rate remains constant throughout the sample [Equation (6.1)]. The fluid sample is placed in the gap (0.041 mm) between the rotating cone and the fixed place. A small cone angle (1°) allows accurate and precise normal stress measurements [246]. The constant shear rate is given by [247]

$$\dot{\gamma} = \frac{\Omega}{\sin\phi} \, , \qquad (6.1)$$

where $\dot{\gamma}$ [s^{-1}] is the shear rate, Ω [rad·s^{-1}] the angular velocity of the rotating cone, and ϕ [rad] the cone angle. The shear stress (τ_{xy}) [Pa] can be calculated from the applied torque on the cone by [247]

$$\tau_{xy} = \eta(\dot{\gamma})\dot{\gamma} = \frac{3M}{2\pi r_{\mathrm{cone}}^3} \, , \qquad (6.2)$$

where η [Pa·s] is the shear viscosity, M [N·m] the torque, and r_{cone} [m] the cone radius. For all curves measured, the lower and upper limits should be considered for accurate measurements of the shear viscosity. The lower boundary of the shear viscosity is determined using Equation (6.3) and considering 5 times the minimum resolvable torque specifications of the shear rheometer.

$$\eta_{\text{min}} = \frac{3\phi(5M_{\text{min}})}{2\pi r_{\text{cone}}^3 \sin\phi} \frac{1}{\dot{\gamma}} \; , \qquad\qquad (6.3)$$

where M_{min} is the rheometer minimum resolvable torque, which is 0.1 µN·m for the shear rheometer used in the measurements. The laminar flow of a Newtonian fluid between a rotating cone and a fixed plate is a purely steady shear flow when the criterion $\Omega\phi^2\rho r_{\text{cone}}^2/(12\eta) < 0.5$ is observed. Therefore, the upper value of the measurable shear viscosity, based on the onset of inertial instabilities (Taylor vortices) is determined by [248]

$$\eta_{\text{max}} = \frac{\Omega\phi^2\rho r_{\text{cone}}^2}{6} \; . \qquad\qquad (6.4)$$

Surface and interfacial tension measurements

The surface tension measurements (air and aqueous solutions as the light and heavy phases, respectively) are carried out using an optical tensiometer (Biolin Scientific Theta Lite 100). At least, three independent drops are measured during a time interval of 10 s. The drop images are captured, and the shape is analysed over time using the Young-Laplace equation. The interfacial tension measurements between the continuous phase (heavy phase, fluorinert FC-70) and the aqueous solutions (light phase) are performed at 20 °C in a Du Nuöy ring tensiometer (*Biolin Scientific Sigma 701*) with a platinum ring, where, at least, three repetitions are done. The maximum value of the force at the detachment of the ring from the interface determines the interfacial tension value. The main physical properties of the fluids (dispersed and continuous phases) are indicated in Table 6.2.

Table 6.2. Physical properties of the fluids at $T = 20$ °C.

Fluid	Density, ρ [kg·m^{-3}]	Dynamic viscosity, μ [mPa·s]	Interfacial tension, σ [mN·m^{-1}]
Water (dispersed phase)	1000	1.0	
Fluorinert FC-70 (continuous phase)	1945	32.8	40.7

(a)

(b)
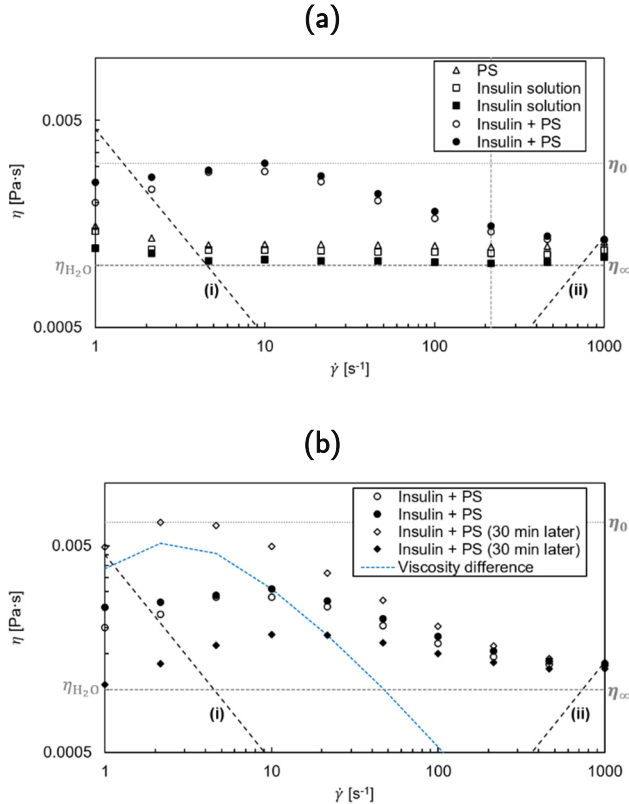
Figure 6.5. Steady-shear viscosity (η) as a function of the shear rate ($\dot{\gamma}$) measured at 20 °C: **(a)** Salt solution ($C_{PS} = 0.005$ M), insulin solutions – (□) $C_{ins} = 15$ mg·ml^{-1} and (■) $C_{ins} = 3.75$ mg·ml^{-1}, and insulin + salt solutions – (○) 3.75 mg·ml^{-1} ($C_{PS} = 0.00375$ M) and (●) 1.25 mg·ml^{-1} ($C_{PS} = 0.00333$ M). **(b)** Insulin + salt solution after 30 min [(◊) 3.75 mg·ml^{-1} and (◆) 1.25 mg·ml^{-1}] and the respective viscosity difference. η_0 represents the zero-shear rate (low shear rates) and η_∞ the infinite shear viscosity plateau (high shear rates). The dashed lines represent the minimum measurable shear viscosity based on 5x the minimum resolvable torque (i) and the onset of secondary flow due to Taylor instabilities (ii).

The viscosity of protein solutions arises from different types of interactions between protein molecules, which includes electrostatic (charge-charge) and exclude volume effect (steric) repulsions, charge-dipole and charge-charge attractions, van der Waals interactions, hydrogen bonds, and hydrophobic contact. However, the interactions between proteins are mainly explained by the long-range repulsive electrostatic interactions [245]. The inter-protein structures in solution depend on the protein-protein interactions, which determine the viscosity of proteins in solution [244]. Protein-protein interactions are directional and only some protein orientations result in favourable interactions. These orientational preferences disfavour the formation of compact clusters [249]. From the steady-shear viscosity results (Figure 6.5), it is possible to conclude that the protein and salt solutions exhibit a Newtonian behaviour since within the region between (i) and (ii) [Figure 6.5-(a)], the shear viscosity is constant over the shear rate, with an average viscosity slightly higher than the reported value for water. This tendency seems to be more evident at higher initial insulin concentrations. This outcome follows the trend of shear viscosity increase with protein volume fraction (for highly concentrated protein solutions) reported by Bülow *et al.* (2019). This might indicate that the short-range attractive interactions between the proteins cannot be ignored [249].

Following the results reported by Dharmaraj *et al.* (2016) [250] for lysozyme solutions, the shear thinning behaviour is exhibited at high concentrated solutions (140 mg·ml^{-1}) and low temperature (5 °C). When the protein concentration increases, the intermolecular attraction slows the mobility of protein molecules. The reduced concentration of protein can decrease the solution viscosity by lowering the probability of the steric repulsion between solutes. The addition of small amounts of salt (*e.g.* zinc chloride) creates an electrostatic shield between protein molecules, which leads to a decrease in the electrostatic repulsion or attraction [245]. However, as soon as these solutions are mixed, a non-Newtonian behaviour of the fluid is observed whose shear viscosity decreases under shear rate. At sufficiently high shear rates, the shear viscosity value reaches an infinite shear viscosity plateau at η_∞. The shear stress in function of the shear rate is described by a power law equation, where the linear region corresponds to a shear thinning regime [251].

$$\tau = K'\dot{\gamma}^n, \tag{6.5}$$

where τ [Pa] is the shear stress, $\dot{\gamma}$ [s^{-1}] the shear rate, K' [Pa·s^n] the fluid consistency index, and n [-] the power law index. The values of K' and n are indicated in Table 6.3 for the measured crystallization solutions, using a least squares regression analysis. This effectively indicates the pseudoplastic behaviour of the crystallization solutions ($n \leq 1$).

Table 6.3. Values of K and n for the different crystallization solutions (see Figure 6.5) [PS – salt (ZnCl$_2$) solution].

Crystallization solution	K' [Pa·s^n]	n [-]
Insulin + PS, 3.75 mg·ml^{-1}	0.002	0.93
Insulin + PS, 1.25 mg·ml^{-1}	0.003	0.90
Insulin + PS, 3.75 mg·ml^{-1} (30 min later)	1.0	1.0
Insulin + PS, 1.25 mg·ml^{-1} (30 min later)	0.002	0.96

The shear thinning regime seems to be due to the resistance generated by the dense protein film formed at the interface. This has been observed in different protein systems [244]. The dynamic cluster formation changes the solution viscosity and its stabilization occurs by the balance between short-range attraction and long-range repulsion [245]. This typical polymeric behaviour shows the importance of micromixing, which is mostly governed by convection. At higher shear rates, due to complete micromixing, the viscosity difference between the crystallization solutions (with distinct insulin concentration) is almost negligible [Figure 6.5-(b)]. This might indicate that, at the studied conditions, the tested solutions are purely viscous. However, at lower shear rates, the shear viscosity for different insulin concentrations becomes clear, where the distinct elastic contribution might explain this difference [252]. Furthermore, the solutions analysed after 30 min present a different behaviour, where the one with a large insulin concentration gradient exhibits a high viscosity in the shearing zone [Figure 6.5-(b)]. Besides the solution viscosity, the interplay between short- and long-range forces governs clustering and phase behaviour. Short-ranged attraction drives clustering, while long-ranged repulsion limits the local range of association. This produces supramolecular strands of intermediates, *i.e.* local concentrations of protein molecules clustered together, which contributes to the viscosity increase [250].

Dasari *et al.* (1995) [251] reported that bovine amniotic fluid behaves as a shear thinning fluid as the results exhibit a decrease of viscosity with increasing shear rate. Additionally, at low shear rates, the apparent increase of the shear viscosity might be associated with polymer network formation or the migration of charged proteins towards the surfaces of the cone and plate. This can result in the formation of concentration gradients in the shearing zone and, consequently, an apparent increase in viscosity [251]. Pan *et al.* (2009) [252] conducted a rheology study with lysozyme solutions. Similarly, the shear viscosity tends to be higher at higher initial concentrations of protein. The authors attribute this viscoelasticity to a dense network of weakly-bound chains of protein molecules [252].

(a)

(b)
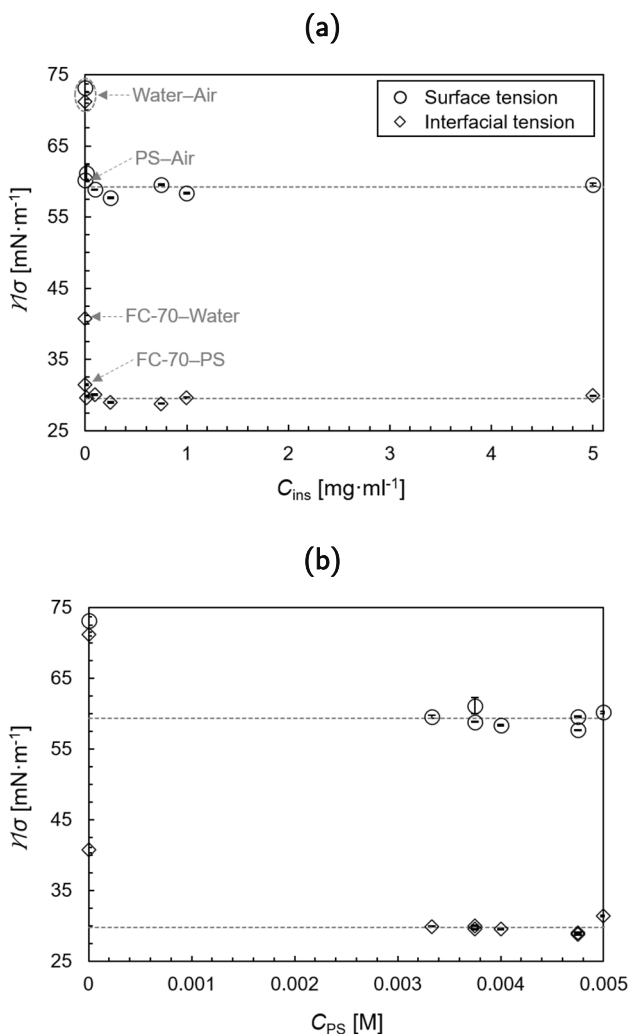
Figure 6.6. Surface (Υ) and interfacial tension (σ) values at 20 °C for different: **(a)** Insulin (C_{ins}) and **(b)** Salt (ZnCl$_2$) (C_{PS}) solution concentration. The dashed lines represent the average value of the surface/interfacial tension values for non-zero concentrations. [The scale bars are standard deviations from, at least, three independent drops].

Even though the light and heavy phases differ for surface and interfacial tensions and it is only reported that proteins tend to adsorb at the air-liquid interface, a similar trend over the indicated insulin and salt solution concentration range is observed [253] [Figure 6.6-(a)]. Due to the adsorption of the protein molecules at the interface, organised unimolecular layers might appear and, consequently, a thin monolayer of adsorbed protein onto a low energy surface [254]. Additionally, this adsorption

causes reversible or irreversible reorientation [253], which might result in an increase of the interfacial tension over time. The monolayer is saturated at higher protein concentrations, where the protein molecules form multilayers beneath the primary monolayer. However, these structures do not contribute significantly to the surface tension [255]. For the experimental condition corresponding to an insulin concentration of 5 mg·ml^{-1} (Figures 6.2 and 6.6), the interfacial tension is measured over time until reaching a long enough time to ensure crystal formation. After 5 min, the value has increased from 29.9 ± 0.06 mN·m^{-1} (Figure 6.6) to 30.2 ± 0.03 mN·m^{-1}, while after 35 min the value 31.2 ± 0.01 mN·m^{-1}.

The static interfacial tension measurements require larger fluid volumes compared to the surface tension measurements. Therefore, an extensive study through the influence of the insulin and salt solution concentration on the surface tension is carried out at three distinct initial protein concentrations and for the concentration ranges previously defined in Figure 6.6. The main results are displayed in Figure 6.7.

(a)

(b)

(c)
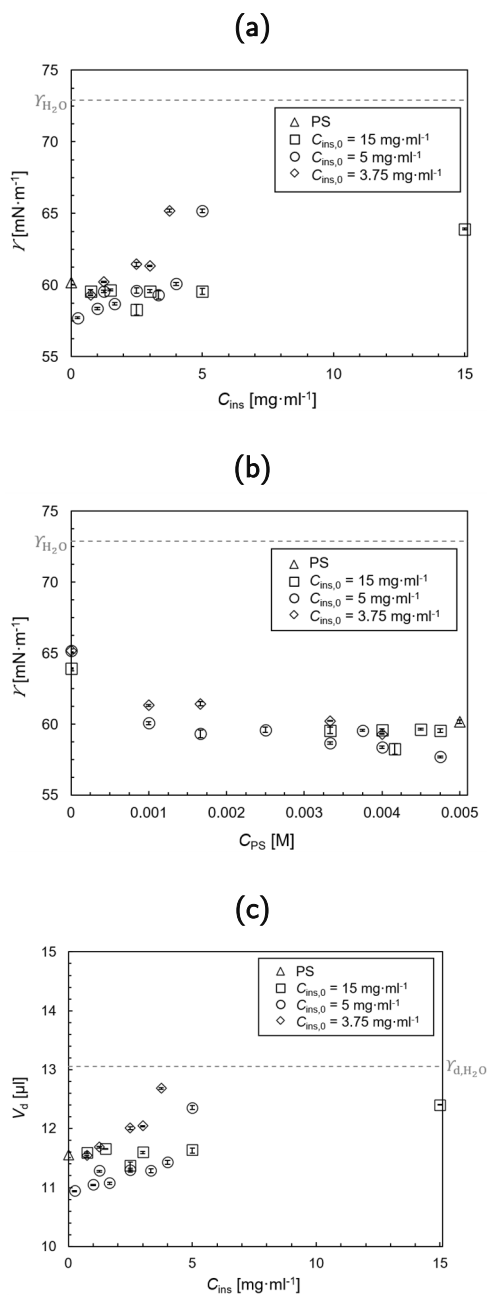
Figure 6.7. Experimental results obtained with the hanging-drop technique at different initial insulin concentrations ($C_{ins,0}$) and 20 °C: **(a)** Surface tension (Υ) as a function of the insulin concentration (C_{ins}), and **(b)** of the salt (ZnCl$_2$) solution concentration (C_{PS}), and **(c)** Hanging-drop volume (V_d) in function of the insulin concentration. [The scale bars are standard deviations from, at least, three independent drops].

The surface tension tends to increase in function of the insulin concentration. Johnston (1927) [254] also reported a decrease of the surface tension values of caseinogen and egg-albumin solutions, at low protein concentrations, with rising protein concentration, followed by an increase at high protein concentrations. Absolom *et al.* (1981) [253] performed several surface tension experiments with human serum albumin and observed a significant decrease of the surface tension after a protein-air interface is formed. Lower interfacial tension values reveal an orientation or an alteration of the secondary and/or tertiary protein configuration [256] at the protein-air interface [253]. Tomczyńska-Mleko *et al.* (2014) [257] reported a decrease of the surface tension with the whey protein concentration up to 5 mg·ml^{-1}. At a certain concentration, proteins occupy the entire interface, and further increase in their concentration does no longer influence the surface tension [257]. The results shown in Figure 6.7-(b) seem to highlight this behaviour, since a clear decrease on the surface tension with the salt solution concentration is observed at low concentrations and followed by similar surface tension values (at different initial protein concentrations) at high concentrations. On the one hand, the decrease in surface tension represents an increase in hydrophobic content of the structure, where partial unfolding and exposure of hydrophobic protein surfaces can result in intermolecular interactions between denatured protein molecules and, consequently, their aggregation. On the other hand, the increase in surface tension implies reduced hydrophobic protein surfaces which are replaced with hydrophilic ones, which results in a more stable structure of insulin with lower energy state [258].

Gibson & Murphy (2006) [259] highlighted that a reduction in surface tension can accelerate the onset of insulin aggregation. Kachooei *et al.* (2012) [258] attributed the surface tension differences to the hydrophobic changes in insulin structure. The hydrophobicity is enhanced by the formation of oligomeric forms of insulin. Furthermore, any change in physicochemical properties of insulin such as conformational changes might result in alteration of surface tension properties. Ybert & Meglio (1998) [260] described that the hydrophobic groups of the proteins tend to escape the bulk to spread at the interface and destroy the original folding, which can result in the loss of the biological activity of the protein.

Insulin monomer has large hydrophobic areas on its surface [216]. However, it exhibits a pronounced hydrophilicity characteristic of its hydrated state [253], which after exposed at the air-liquid interface exhibits a more hydrophobic tertiary configuration [257]. Typically, the bulk nucleated crystals form on some nucleants in the solution bulk, due to a similar adhesion nature of the protein molecules. Insulin's isoelectric point is around pH 5.6, which denotes insulin molecules negatively charged. PFA tubing (positive charges) will attract these molecules [226]. The maximum surface tension occurs at the isoelectric point value, which corresponds to the initial protein solutions without adding the salt solution. Additionally, at fixed protein concentrations [Figure 6.7-(a)], the higher surface tension values correspond to the lowest initial concentration (3.75 mg·ml^{-1}). This is possibly due to a higher solubility at lower insulin concentrations [254]. Therefore, Figure 6.7-(b) might give an indication of the supersaturation ratio as higher values should correspond to lower surface tension values [254].

Finally, time is an important variable for the surface tension measurement of colloidal solutions, mostly due to the slow rate of adsorption of molecules or even particles at the interface [254]. For this reason, some of the surface tension measurements previously carried out are extended up to 10 min as shown in Figure 6.8.

(a)

(b)
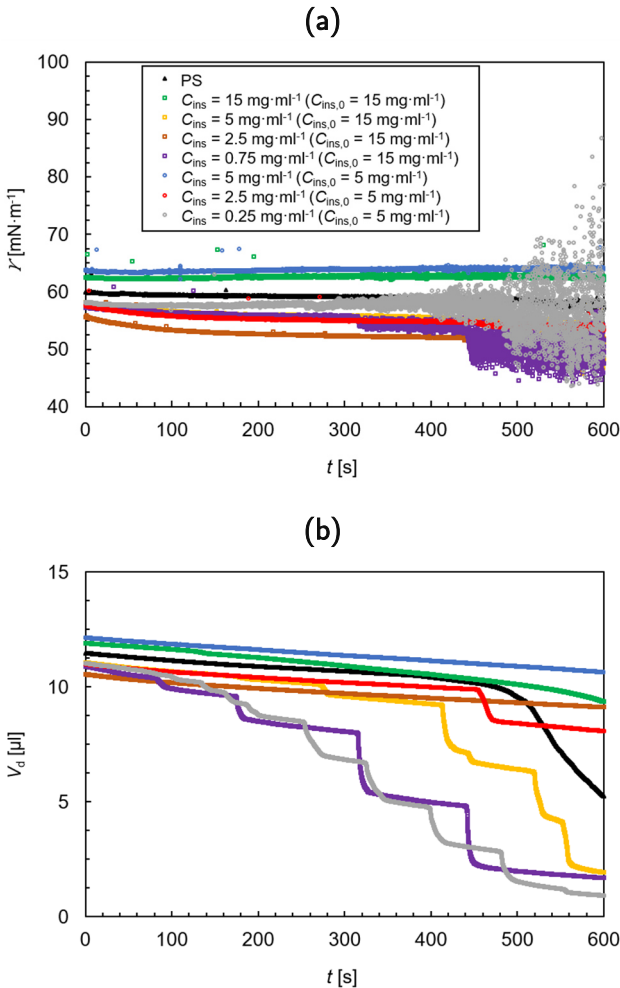
Figure 6.8. Experimental results obtained with the hanging-drop technique over time (t) at different insulin concentration (C_{ins}) [salt ($ZnCl_2$) solution concentration (C_{PS}) are indicated in Figure 6.8-(b)] and 20 °C: **(a)** Surface tension (Υ) and **(b)** Hanging-drop volume (V_d).

No considerable changes of the surface tension occurred for the insulin and salt solutions, while a slight decrease is observed for the combined crystallization solutions, especially during the first minutes [Figure 6.8-(a)]. For longer time intervals [$t > 400$ s, Figure 6.8-(a)], a clear data scatter is observed, which might be related to viscoelastic behaviour (elastic contribution) of the solutions. The long exposition to the air-liquid interface is also visible on the drop volume [Figure 6.8-(b)]. Johnston (1927) [254] also reported a fall of the surface tension values of caseinogen and egg-albumin solutions over time, as well as

166

Burgess & Sahin (1997) [256] using bovine serum albumin and human immunoglobulin G. The reduction in surface tension over time is a result of protein adsorption and the ability of adsorbed protein to interact with both phases [256]. The adsorption is higher at higher insulin concentrations. Besides this physical chemistry analysis, the surface tension measurements also give a general indication of the viscoelastic behaviour of the solutions. The initial insulin solutions behave as Newtonian fluids (Figure 6.5). Only a slight variance of the drop volume over time occurs, while for the crystallization solutions exhibiting a shear thinning behaviour, the drop volume change over time is significant.

6.5   Nucleation mechanism – Proposal and analysis

Classical Nucleation Theory (CNT) introduced in 1926 is a well-established theory to explain the protein nucleation mechanism [21]. One of the suppositions of this classical approach is that all the clusters exhibit the same degree of crystallinity regardless of their size [22]. However, recent theoretical, computational and experimental evidences revealed that some of the assumptions from CNT are poorly justified and can drastically contradict each other [23]–[25]. Alternative approaches have considered nucleation from solution as a multistep process, where metastable intermediate states (*i.e.* pre-critical clusters) are involved in a multistep nucleation theory [23]. One of these theories was proposed by Galkin and Vekilov in 2000, which conceives the protein nucleation phenomenon as a two-step mechanism [26]. Sleutel & Van Driessche (2014) [23] showed evidence that clusters are liquid-like and metastable with respect to the emerging crystalline phase, and their existence significantly increases the nucleation rate [23].

The multistep nucleation theory might justify our observations during the hanging-drop experiments because the crystal appearance seems to require the presence of the initially formed aggregates (Figures C2–C5, Appendix C – C2). However, as soon as the first crystals are formed, the cloudy aggregates tend to disappear over time (Figure 6.9). On the one hand, this suggests that nuclei might be formed within the mesoscopic protein clusters. On the other hand, these clusters might act as heterogeneous nucleation sites. These observations might support the theory defining nucleation from solution by a multistep process due to the

existence of metastable intermediate states [23]. Their existence might be justified based on the distinct values of shear viscosity (Figure 6.5) and surface and interfacial tensions (Figures 6.6–6.8) at different insulin concentrations.

Even though it has only been reported for highly concentrated protein solutions (100 mg·ml^{-1} and higher), a dynamic cluster model constitutes one of the first attempts to explain the repercussions of the viscosity increase with protein volume fraction on the protein behaviour in solution. This model hypothesises that protein molecules might diffuse not as isolated particles, but as members of transient clusters between which they constantly exchange. Due to this increase in cluster size, a slowdown of protein rotation compared with translation is observed, which might have an impact on the protein stability. The direct protein interactions are the dominant contribution to the slowdown of rotational diffusivity, whereas hydrodynamics plays only a minor contribution. However, at low protein concentrations, the motion of proteins is more effectively coupled to hydrodynamic and electrostatic forces [249]. The relationship between molecular conformation, intermolecular interaction, clustering (reversible and irreversible aggregation), and viscosity are complex [250]. The structure of globular proteins (*e.g.* insulin) is partially unfolded in aqueous media, which might result in an irreversible aggregation and, consequently, an increase in solution viscosity [249].

At low insulin concentrations (below 3 mg·ml^{-1}) for the hanging-drop experiments (Tables C2 and C3 – Appendix C – C2) and low salt solution concentrations (below 0.00167 M) for the microfluidics experiments (Figure 6.2), the aggregates formation is dominant, and no crystals are produced. This might suggest that the nucleation of the mesoscopic clusters (Figure 6.9) is only triggered when a critical protein concentration is reached [23]. However, the gradual disappearance of the aggregates due to the slow mixing between the protein and salt solution with the subsequent appearance of the intermediate mesoscopic clusters might suggest that these aggregates have a microcrystalline nature rather than amorphous. However, the experimental evidence is not enough for making a well-supported claim. Additionally, one of the key concepts of CNT is that each cluster has a critical size. Below this value, they are likely to shrink and dissolve (low insulin concentrations), while for large sizes, clusters are likely to grow until mesoscopic sizes by molecular attachment [22]. This last scenario is highlighted in Figure 6.9.
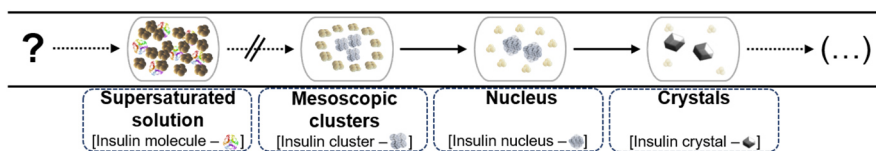
Figure 6.9. Schematic representation of the proposed multistep nucleation mechanism based on experimental evidence from the bulk liquid until the crystalline phase with the aggregate (from very cloudy/dark aggregates until light aggregates. The cloudy aggregates tend to disappear over time) dissolution over time. ['?' indicates the unknown initial stage and '(…)' the unfinished pathway.].

Nonetheless, the clusters might act as heterogeneous nucleation sites [23]. For answering this question, an analysis of the insulin crystallization during the initial stages of the experiment is carried out for the microfluidics experiments. For that purpose, the reactor device is placed under the microscope, a few images are recorded over time and time-lapse pictures are captured. These captions are displayed in Figures 6.10–6.12 and the discussion conducted afterwards.
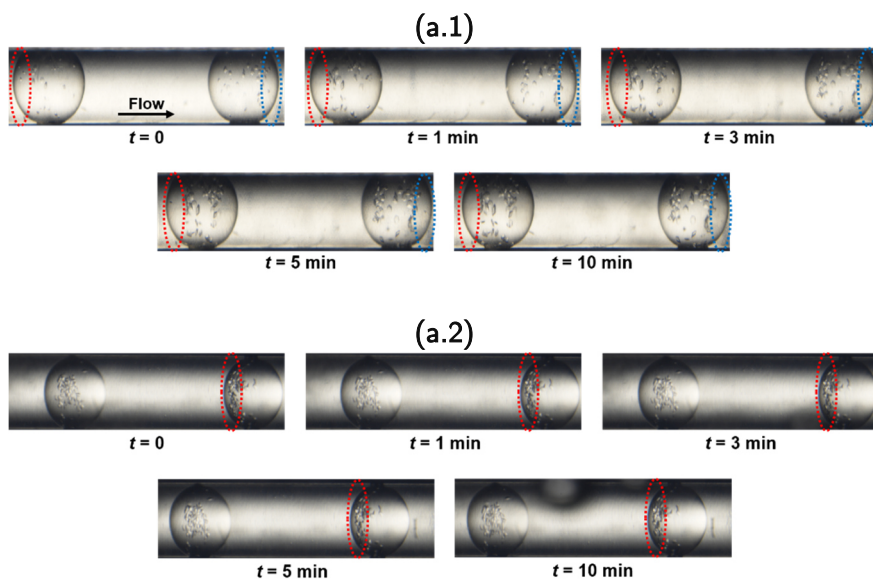
Figure 6.10. Droplets highlighting crystal appearance over time (t) for insulin and salt solution concentrations of 5 mg·ml^{-1} and 0.00333 M, respectively at 20 °C: **(a.1)** Crystals moving away from the interface and **(a.2)** Crystals staying at the interface. [Red and blue dashed contours highlight droplet tail and front, respectively].
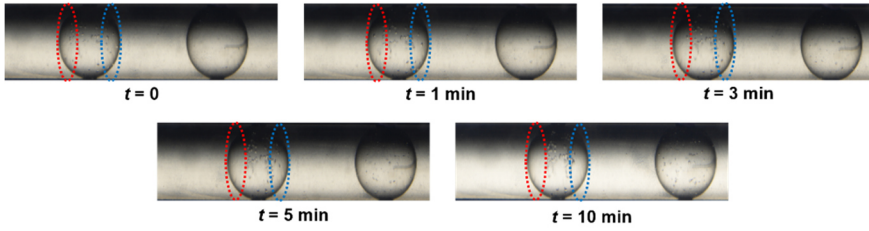
Figure 6.11. Droplets with crystal appearance over time (t) for insulin and salt solution concentration of 2.5 mg·ml^{-1} and 0.0025 M, respectively at 20 °C. [Red and blue dashed contours highlight droplet tail and front, respectively].
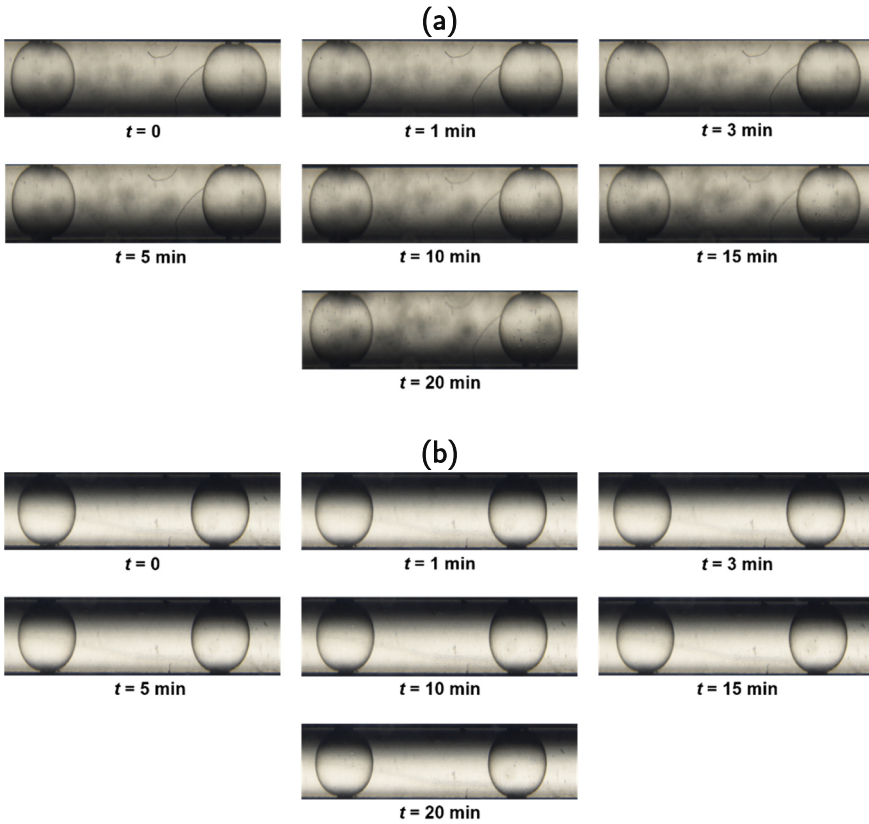
Figure 6.12. Droplets with crystal appearance over time (t) for insulin and salt solution concentration of: **(a)** 1.67 mg·ml^{-1} and 0.00333 M, respectively and **(b)** 1 mg·ml^{-1} and 0.004 M, respectively at 20 °C.

Although nucleation is a highly stochastic process, it seems to be evident that, at high insulin concentrations, the crystal appearance at the droplet interface is spontaneous. Nonetheless, two distinct scenarios over time can

occur. On the one hand, when only a few crystals emerge at the droplet interface, they tend to move away in direction to the bulk phase. As the droplets are under static conditions, this occurs for both the crystals located at the tail and front of the droplet [Figures 6.10-(a.1) and 6.12]. On the other hand, the fast generation of a lot of crystals tends to avoid the crystals dislocation from the interface, which seems to result in a slower crystal growth rate [Figures 6.10-(a.2)]. Both scenarios suggest the occurrence of heterogeneous nucleation possibly due to a lower energetic barrier at the interface, which might result in faster nucleation events compared to the cases at lower insulin concentrations [198]. At low insulin concentrations, the crystal appearance requires long time, and only small crystals are visible after a time interval of 20 min (Figure 6.12), while at high concentrations (Figures 6.10 and 6.11), crystals are already observed at the initial time and, after a time period of 10 min, a clear crystal size increase occurs. This might be related to earlier nucleation events (*i.e.* heterogeneous nucleation). Slower nucleation seems to result in smaller crystals (Figure 6.12). Due to the small size of the crystals at low insulin concentrations, it is not clear if any crystal appears at the droplet interface and start moving towards the bulk phase. However, after a time interval of 20 min, the few small crystals are observed in the bulk phase and not close to the droplet interface (Figure 6.12).

It is hypothesised that the crystal dislocation from the interface (Figure 6.13) without flow is due to Stokes' drag. *Stokes' law* derivation assumes a particle with spherical shape. By combining this law with *Newton's 2nd law of motion*, the final position of each crystal (z) is estimated by

$$z_{\mathrm{c,f}} = \frac{\pi \mu r_{\mathrm{c}} r_{\mathrm{d}} \Delta t}{m_{\mathrm{c}}} + \frac{r_{\mathrm{d}}}{3}, \tag{6.6}$$

where r_{c} [m] is the crystal (sphere) radius, r_{d} [m] the droplet radius, Δt [s] the time interval, and m_{c} [kg] the crystal mass [$m_{\mathrm{c}} = \rho_c k_{\mathrm{v}} L_{\mathrm{c}}^3$, where ρ_c [kg·m^{-3}] is the crystal density and k_{v} [-] the volumetric (sphere) shape factor]. The derivation of Equation (6.6) can be found in Appendix A – A1. This initial estimation seems to overestimate the final position of the crystals and this might be related to the uncertainties during the measurement of the crystal radius or even the assumption from *Stokes' law* (spherical particles).
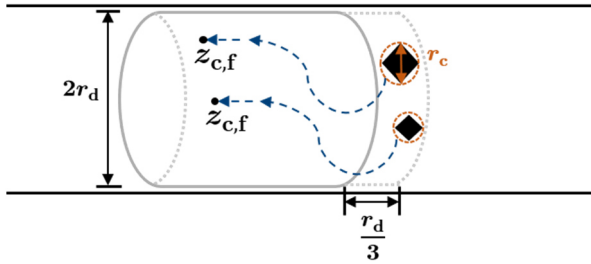
Figure 6.13. Schematic representation of the crystal dislocation from the interface to the bulk explained by the combination between *Stokes' law* and *Newton's 2nd law* of motion [see Equation (6.6)].

6.6 Conclusions

Initially, through a crystallization screening strategy, crystals are formed using hanging-drop vapor diffusion as the crystallization technique. Further on, based on this initial screening of insulin crystallization conditions, crystallization experiments in microdroplets are performed. At low protein concentrations, aggregates formation is observed during the hanging-drop experiments, while crystals with variable size are produced in the droplet-based microreactor. For this last approach, aggregates tend to appear at low salt solution concentrations. This distinct behaviour might reveal the importance of the crystallization volume and the dominant effect of the convection contribution (during the droplet formation along the experiments in the droplet-based microreactor) over the diffusion contribution (hanging-drop experiments).
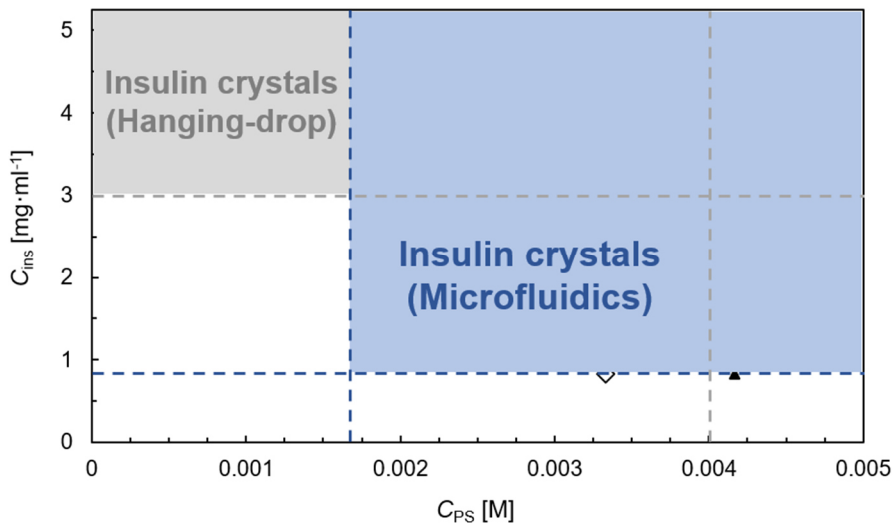
Figure 6.14. Insulin (C_{ins}) and salt (ZnCl$_2$) (C_{salt}) concentration in solution for the experiments performed at 20 °C: Operating regimes to produce insulin crystals by hanging-drop vapor diffusion (region highlighted in grey) and microfluidics (region highlighted in blue).

The crystal crystal size seems to present a higher uniformity when produced in smaller volume droplets with the suppression of agglomerates and/or aggregates formation. Contrarily to what has been reported for other proteins (*e.g.* lysozyme), the temperature effect on crystal size is not observed for insulin. Another way to define the concentration ranges for future insulin crystallization studies is done by considering the surface/interfacial tension measurements and correlating this with possible aggregation events.

7. Conclusions

"I would rather have questions that can't be answered than answers that can't be questioned."

– Richard Feynman (n.d.).

7.1   General conclusions

The general aim of this dissertation was to extend the current understanding of protein crystallization in droplet microfluidic devices, with a special focus on the nucleation process. This goal was achieved by (i) designing and characterizing a droplet-based microreactor by combining experimental and numerical approaches, (ii) studying the phase behaviour of a model protein (*i.e.* lysozyme), (iii) combining existing crystallization strategies to simultaneously promote and control protein nucleation, and (iv) providing a preliminary fundamental and structural understanding of another protein nucleation process (*i.e.* insulin).

The design and characterization of a droplet-based microfluidic device is conducted by combining experimental, numerical and empirical approaches. Although protein crystallization constitutes the main application, the methodology can be extended to a broader range of research fields, such as chemical synthesis and analytical biology. This microfluidic device allows the generation of uniform and stable droplets within the squeezing flow regime (characterized by very low Capillary numbers), and a large flexibility on the generated droplet volume. The VOF numerical approach coupled with the smoothing procedure based on a Laplacian function accurately predicts the droplet curvature and complex flow topology effects inside the droplets, with a significant suppression of the artificial spurious velocities at the interface. Therefore, transport phenomena are characterized through the integration of scalar transport equations, concentration and temperature. Although the droplet volume exhibits a minor effect on the heat transfer distribution in the

microchannel, the capabilities of the conjugate heat transfer solver are explored.

The analysis of the protein phase behaviour is accomplished using phase diagrams as a design of experiments tool to perform crystallization experiments. A multiparametric study is conducted for a broad supersaturation range, and the involved variables are lysozyme and salt concentration, temperature, and droplet volume. This enabled to acquire thermodynamic and kinetic data for further comparisons with reported cases in literature. Droplet volume has a decisive contribution to the nucleation probability, where a lower nucleation probability is predicted and, consequently, the formation of a lower number of crystals. However, this is not always observed due to the complex behaviour of lysozyme in solution at higher concentrations, and possibly the formation of aggregates that might not give rise to protein crystals.

The difficulty to simultaneously promote and control nucleation, and still avoid the occurrence of precipitation, is a relevant topic to address. By combining microbatch crystallization experiments and external stimuli, the microdroplets are subjected to three different scenarios: Low-frequency pulsed irradiation, double-pulse temperatures during nucleation and crystal growth steps, and distinct range of droplet volume. During the lysozyme crystallization assays, ultrasonic irradiation promotes nuclei generation, which contributes to a significant reduction of the induction time (and crystal size). Besides the clear increase on the nucleation rate, there are no evidence of protein precipitation. By increasing the initial supersaturation ratio, a higher nucleation probability in sonicated droplets is observed, but a threshold for induction time is reached.

High supersaturation ratios are achieved by cooling the droplets during the imposed nucleation time, followed by a considerably lower supersaturation ratio due to heating to promote crystal growth inside the metastable region. This experimental manipulation of the supersaturation ratio allows an enhanced lysozyme nucleation control in microdroplets. On the one hand, for smaller droplet volumes, a competition between nucleation and crystal growth arises. The crystal growth suppresses further nucleation events. On the other hand, for larger droplet volumes, where slower nucleation rates were obtained, the growing crystals do not consume the available protein concentration in the bulk phase and, consequently, another nucleation event might take place. Nevertheless, the droplet

volume effect on the crystal size becomes more important at lower nucleation supersaturation ratios.

Over a screening of the insulin crystallization conditions using vapour diffusion as the crystallization technique, the experimental crystallization conditions are further optimized and microbatch experiments in confined microdroplets surrounded by a carrier place are performed. The hydrodynamic mechanisms involved during the droplet generation allow the generation of small droplet volumes, where the transport phenomena are enhanced. Therefore, at low protein concentrations, aggregates and/or agglomerates formation occurs during the vapour diffusion experiments (larger droplet volumes), while crystals with a variable size and number are produced in the droplet-based microreactor. Contrarily to what has been reported for different temperatures (*e.g.* lysozyme), larger crystals at higher crystallization temperatures, the temperature effect on crystal size is not observed during the insulin crystallization assays.

A preliminary rheology study combining shear viscosity and interfacial tension measurements might reveal some insights towards a better understanding of the fundamental mechanisms involved in insulin nucleation. On the one hand, the shear thinning behaviour (exhibited when the protein and salt solutions are mixed) might be explained based on the formation of supramolecular strands of intermediates, *i.e.* dense network of weakly-bound chains of protein molecules. On the other hand, the lower interfacial tension values (at lower insulin concentrations) might reveal partial unfolding or even an orientation of the secondary/tertiary configuration of the protein and accelerate the onset of insulin aggregation. Higher interfacial tension values (at higher insulin concentrations) might contribute to a more stable insulin structure with a lower energy state. Moreover, the observations carried out during the insulin crystallization trials might support the reported non-classical nucleation hypothesis (*i.e.* nucleation as a multistep process). The presence of cloudy aggregates is observed before the formation of insulin crystals. This suggests that nuclei might be formed within the mesoscopic protein clusters (*i.e.* existence of metastable intermediates states) or that the clusters act as heterogeneous nucleation sites. The nature of these intermediate clusters and how they influence the nucleation mechanism is still an open question.

7.2 Outlook

Although a relevant contribution towards the understanding of protein crystallization in droplet microfluidic devices was achieved, still many open questions remain from both experimental and numerical approaches. Along with the following paragraphs, further research paths are suggested, each corresponding to Chapters 2 to 6.

During the hydrodynamics study performed in Chapter 2, the numerical approach demonstrated a good agreement with the experimental results. This was mainly attributed to the conservative nature of the Volume-of-Fluid method and its capability to deal with topological changes of the interface. Nevertheless, a high order of accuracy (*i.e.* no advection schemes higher than two) is difficult to achieve because of the discrete nature of the indicator function. Despite the lack of mass conservation, typically attributed to the Level-Set approach, this numerical approach offers high-order accuracy [81]. Therefore, a coupling VOF-LS could potentially lead to improved numerical results in Chapter 3 as it might benefit from the advantages of each of these approaches [33]. Additionally, a selectable interpolation for interface capturing (PLIC) has been added to the new released OpenFOAM version 8. This scheme might allow the suppression of artificial velocities. Thus, the current modified solvers should be adapted to OpenFOAM version 8.

The surface tension force is modelled as a volumetric force by the Continuum Surface Force method [116]. However, for interfacial tension dependent on *e.g.* temperature, the Continuum Surface Stress approach [112] could lead to improved calculations. This numerical method avoids explicit calculation of the droplet curvature, and could be represented as an anisotropic variant of modeling capillary forces based on the balance of tangential shear stresses around the droplet interface [132]. Finally, another important aspect to be considered for future research perspectives is the effectiveness of the current discretization strategy and, consequently, the mesh refinement. The current numerical mesh was generated with the *snappyHexMesh* utility. However, this utility involves a high number of degrees of freedom (*e.g.* refinement gradients, boundary layers) and uniformity of the mesh refinement is difficult to reach. This was a clear concern during the heat transfer simulations (Chapter 3). It is, therefore, recommendable the investment in new efficient methodologies for mesh generation (*e.g. cfMesh* or *Pointwise*®).

Bearing in mind the main application of this work, protein crystallization in droplet microfluidics, the hydrodynamics study was limited to squeezing flow regime as stable and uniform droplets are easily produced for close to unitary viscosity ratios between the dispersed and continuous phases (Chapters 2 and 3). By a conscientious selection of the fluid properties (*e.g.* dynamic viscosity and interfacial tension), considerably smaller droplets can be produced in a faster way. Exploratory experiments involving the use of dye solutions to quantify the mixing efficiency were performed. Nevertheless, these trials were too preliminary to be included in this manuscript. Moreover, this study could be complemented with micro-Particle Image Velocimetry and micro-Laser Induced Fluorescence. From both theoretical and applied science points-of-view, this integrative strategy could effectively contribute to a deeper understanding of the mechanisms during the droplet breakup, effect of the film (carrier fluid surrounding the droplet) thickness on the recirculation flow inside the droplets, and quantification of the mixing efficiency. Another perspective could be the inclusion of a bifurcation hydrodynamic strategy downstream of the current flow-focusing [261]. This proposal could be of extreme importance for the crystallization experiments (Chapters 4–6) as the initial droplet breaks in two similar droplets and, consequently, the nucleation centres are divided over these two new droplets. Additional independent microbatch crystallization experiments could be conducted, and larger crystals could be produced. Despite the valuable scientific input of this perspective, modifications to the current design would be required.

The significative reduction of the induction time during the ultrasonic crystallization of lysozyme (Chapter 5) could be further explored through a parametric study involving the influence of frequency on lysozyme crystallization outcome at similar forward powers. This study was intended to be a proof-of-concept and the first attempt for further experiments on ultrasonic crystallization in confined microdroplets. Therefore, this strategy provides perspectives for other biological macromolecules (*e.g.* insulin) by promoting nucleation with external stimuli (*e.g.* ultrasound radiation). Although not presented in this dissertation, a preliminary crystallization model was integrated into the coupled numerical solver to validate the crystallization experiments in Chapter 4. Besides the early stage, by introducing a population balance and experimental input, the mathematical model is capable to predict crystal size and number, nucleation rate, protein concentration decay over time, among others. Although very promising,

the model is still not capable to accurately predict growth rates, which still requires future work. The system of equations to be solved is

$$
\begin{cases}
\text{Crystal number: } N_{\mathrm{c}}(t) = \int_0^t J_{\mathrm{nucl}}(t) V_{\mathrm{d}} dt \\[2mm]
\text{Crystal size: } L_{\mathrm{c}}(t) = \int_0^t N_{\mathrm{c}}(t) J_{\mathrm{cg}}(t) dt \\[2mm]
\text{Protein concentration decay: } C_{\mathrm{p}}(t) = \dfrac{V_{\mathrm{d}} C_{\mathrm{p}}^0 - \rho_{\mathrm{c}} k_{\mathrm{v}} L_{\mathrm{c}}^3(t) \mathrm{N_c}(t)}{V_{\mathrm{d}}} \\[3mm]
\text{Supersaturation ratio: } \mathrm{S}(t) = \dfrac{C_{\mathrm{p}}(t)}{C_{\mathrm{s}}(t)} \\[3mm]
\text{Nucleation rate: } J_{\mathrm{nucl}}(t) = V_{\mathrm{d}} A_0 \exp\left(-\dfrac{16\pi}{3} \dfrac{V_{\mathrm{m}}^2 \sigma^3}{(k_B T)^3 \ln^2 \mathrm{S}(t)}\right) \\[3mm]
\text{Growth rate: } J_{\mathrm{cg}}(t) = k_{\mathrm{cg}}[\mathrm{S}(t) - 1]^2.
\end{cases}
\tag{7.1}
$$

Finally, additional experimental work is necessary for Chapter 6 to translate the current speculative hypothesis on firmer footing. The crystallization screening revealed the appearance of the first nuclei after a few minutes. With this conclusion arises the perspective for continuous crystallization experiments, which by its own constitutes another challenge to tackle. A possible strategy is through the application of emulsion-based microfluidics. Nevertheless, insulin is available in low amounts and crystal growth requires high residence times. Preliminary dynamic light scattering and circular dichroism measurements were performed, but the outcome is still not robust enough to draw conclusive theories. This is mainly due to the limited experimental data and protein concentration range at which the measurements can be performed. These techniques or even additional ones (*e.g.* Fourier-transform infrared spectroscopy, transmission electron microscopy, and liquid-phase electron microscopy to characterize the cloudy aggregates) could bring new insights on the early stages of crystallization and possible conformational and configurational changes before nucleation. Admittedly, most of these techniques and involved theoretical concepts are outside my field of competence, which is characterized by a very limited biochemistry background. Also, the initial rheology study could still be extended. Among the range of options, large amplitude oscillatory shear measurements experiments could be performed to characterize the viscoelastic behaviour of the insulin solutions [262]. As a step further, current open-source numerical models could be tested (*e.g. Rheotool* [263]).

Appendix A

A1 Droplet curvature change due to the temperature effect

For the studied droplet volume range along Chapter 5 (see subsection 5.3), any effect of the droplet length on the surface tension is not expected [264], while the temperature effect due to Marangoni effects needs further discussion [265]. This effect can be correlated to a buoyancy force, opposed by viscous drag and by heat diffusion, and, consequently, flow [266]. The successive cooling and heating steps result in a thermal gradient effect [267] responsible for the thermocapillary motion [268], [269] within a radial surface tension gradient [270] (from the highest to the lowest surface energy) [271]. This is observed during the experiments since the droplets contact the channel wall due to the film drainage, where the film disappears in less than 60 ms. This value comes from a calculation assuming isothermal conditions and spherical droplets, and even neglecting van der Waals forces (see Table A1). The drainage time (t_{drain}) [s] is calculated by

$$t_{\mathrm{drain}} = 20 \; d_{\mathrm{d}} \sqrt{\frac{\mu_{\mathrm{c}}}{u_{\mathrm{d}}\sigma}}, \qquad\qquad \text{(A1)}$$

where d_{d} [m] is the droplet diameter, μ_{c} [Pa·s] the dynamic viscosity of the continuous phase, u_{d} [m·s^{-1}] the superficial velocity of the dispersed phase, and σ [N·m^{-1}] the interfacial tension.

Finally, the hypothesis of immobile interface is also assumed since the condition $t_{\mathrm{drop}} \ll t_{\mathrm{film}}$ is not satisfied for the cases under study [272] (Table A1). The values for the diffusive time scale (t_{drop}) [s] and the film time scale (t_{film}) [s] are indicated in Table A1, which can be calculated by

$$t_{\mathrm{drop}} = \frac{L_{\mathrm{d}}}{u_{\mathrm{d}}}, \qquad\qquad \text{(A2.1)}$$

and

$$t_{\text{film}} = \frac{\varepsilon}{u_{\text{d}}}, \qquad (A2.2)$$

respectively; where L_{d} [m] is the droplet length, and ε [m] the film thickness calculated using *Bretherton's law* and described by [121]

$$\varepsilon = 1.34 \frac{d_{\text{d}}}{2} \left(\frac{u_{\text{d}}\mu_{\text{c}}}{\sigma}\right)^{2/3}. \qquad (A2.3)$$

During the cooling step, from *e.g.* 25 °C to 15 °C, the tail curvature changes, and the front remains unchanged. During the heating step, from *e.g.* 15 °C to 25 °C, the tail curvature slowly recovers and the front changes its curvature. As soon as the final temperature is reached, the receding and advancing contact angles recover their initial values [268]. This is generated from a non-uniform surface gradient along the flow direction [267]. Since the carrier film disappears in less than 60 ms and the droplet generation occurs within the metastable region, the hypothesis of promoting nucleation by increasing the channel wall wettability and droplet curvature changes can be excluded. For the crystallization points belonging to the nucleation zone, this hypothesis might also be excluded as the crystals do not preferentially appear at the droplet interface. Finally, an extensive revision on the thermocapillary motion in several microfluidics' applications can be found in [273].

Table A1. Overview of the hydrodynamic points from Chapter 5 (see subsection 5.3).

Hydrodynamic condition	#1	#2	#3
Q_c [ml·min^{-1}]	0.6	0.6	0.4
Q_d [ml·min^{-1}]	0.2	0.7	1
α_c [-]	0.75	0.5	0.3
L_d [mm]	1.1	2.1	4.0
V_d [µl]	0.7	3.2	12.1
t_{drop} [s]	0.26	0.14	0.18
ε [µm]	1.5	3.4	4.3
t_{film} [ms]	0.35	0.23	0.20
t_{drain} [ms]	48	26	22

[**Note**: Q_c – Flow rate of the continuous phase, Q_d – flow rate of the dispersed phase, α_c – volume fraction of the continuous phase ($\alpha_c = Q_c/(Q_c + Q_d)$), V_d – droplet volume].

In the absence of flow, the slight increase in the droplet length can be explained by the change of the droplet tail to maintain a similar volume (Figure A1). The volumes of the cap and the cylinder (with height, h) can be calculated by

$$\begin{cases} V_{\text{cap}} = \pi r^3 - \dfrac{2}{3}\pi r^3 \\ \quad V_{\text{cyl}} = \pi r^2 h \end{cases}. \tag{A3.1}$$

(a)   (b)
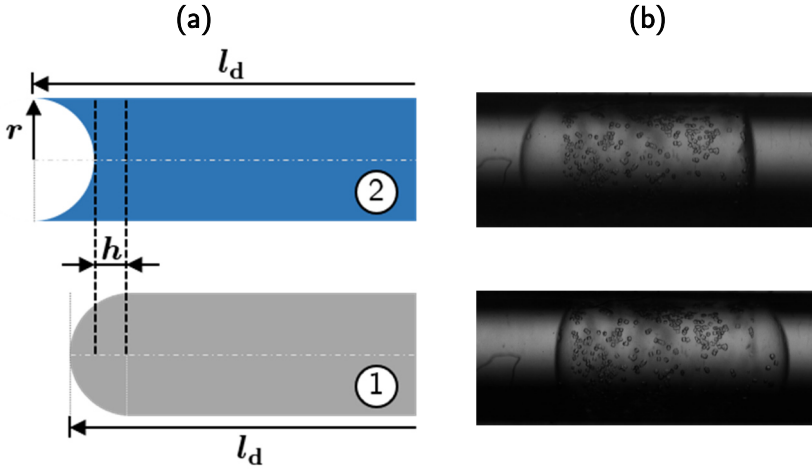
Figure A1. (a) Schematic representation of the droplet tail at the initial stage **(1)** and in the absence of flow **(2)** (where the droplet curvature changes, which is compensated by a slight increase in the droplet length) with the involved variables. **(b)** Experimental images of a single droplet with lysozyme crystals with a time frame difference of 10 min.

Firstly, by equalling these volumes [Equation (A3)], it is obtained that $h = r/3$, which corresponds to the length increase. Therefore, the droplet velocity corresponds to $u_f = r/(3\Delta t)$.

By applying *Stokes's law* (and assuming a crystal with spherical shape), the drag force (F_c) can be estimated by

$$F_c = 6\pi\mu r_c (u_f - u_c). \qquad (A3.2)$$

At this stage, it is assumed that the crystal does not move.

So,

$$F_c = \frac{6\pi\mu r_c r}{3\Delta t}. \qquad (A3.3)$$

Secondly, by applying the *Newton's 2nd law of motion*, the final position of the droplet (and droplet velocity) can be estimated by

$$m_{\rm c}\frac{d^2 z_{\rm f}}{dt^2} = \frac{6\pi\mu r_{\rm c}r}{3\Delta t} \implies u_{\rm f} = \frac{6\pi\mu r_{\rm c}r}{3m_{\rm c}} \implies z_{\rm f} = \frac{6\pi\mu r_{\rm c}r}{3m_{\rm c}}\frac{\Delta t}{2}. \qquad \text{(A3.4)}$$

Analogously to the previous derivation, a similar procedure can be applied to the crystal

$$m_{\rm c}\frac{d^2 z_{\rm c}}{dt^2} = 6\pi\mu r_{\rm c}(u_{\rm c} - u_{\rm f}). \qquad \text{(A3.5)}$$

At this stage, it is assumed that the droplet does not move.

Therefore,

$$m_{\rm c}\frac{du_{\rm c}}{dt} = -6\pi\mu r_{\rm c}u_{\rm f} \implies u_{\rm c} = u_{\rm f}\,\exp\left(-\frac{6\pi\mu r_{\rm c}t}{m_{\rm c}}\right)$$

$$\implies z_{\rm c} = u_{\rm f}\int_0^\infty \exp\left(-\frac{6\pi\mu r_{\rm c}t}{m_{\rm c}}\right)dt \qquad \text{(A3.6)}$$

$$\implies z_{\rm c} = \frac{u_{\rm f}m_{\rm c}}{6\pi\mu r_{\rm c}}.$$

The droplet velocity ($u_{\rm f}$) has been obtained before, so $z_{\rm c} = r/3$.

Finally, the final position of a certain crystal corresponds to

$$z_{\rm c,f} = z_{\rm f} + z_{\rm c} \implies z_{\rm c,f} = \frac{\pi\mu r_{\rm c}r\Delta t}{m_{\rm c}} + \frac{r}{3}. \qquad \text{(A3.7)}$$

Lastly, the crystal dislocation from the interface is explained not only based on the *Stokes's law* but also on the energetic barrier. However, this last contribution is not predicted.

Appendix B

B1   Protein self-assembly theory

Different authors have been reporting experimental approaches to measure concentration changes in a protein solution over time during the crystallization steps, nucleation and crystal growth. This includes the works reported by Ataka & Asai (1988) [274], Vekilov & Vorontsova (2014) [163], Ferreira *et al.* (2017) [27], Yang *et al.* (2018) [275], and Yang *et al.* (2019) [276]. Ataka & Asai (1988) tracked the experiments using optical microscopy (OM) and UV absorption, while Vekilov & Vorontsova (2014) reported different techniques to experimentally understand the two-steps nucleation mechanism, with Atomic Force Microscopy (AFM), Dynamic Light Scattering (DLS) and Brownian Microscopy (BM). Ferreira *et al.* (2017) used DLS and OM to explain the influence of protein oligomerization and metastable clusters during the nucleation step. Finally, Yang and co-workers measured UV absorbance in both batch and continuous oscillatory flow crystallization processes.

The studied cases in Chapters 4 and 5 involve an additional level of complexity since the crystallization takes place inside confined droplets surrounded by an immiscible carrier fluid. Therefore, this makes any online analysis technique difficult to implement. In this context, the protein concentration in the bulk phase over time is estimated using the analytical solution derived from the protein self-assembly theory.

General theory

This theory explains protein crystallization following an analogy with polymerization from a thermodynamic and kinetic point-of-view [277], [278]. Nucleation and crystal growth kinetics are represented by Equations (B1.1) and (B1.2), respectively [278], [279]. In a simplified way, nuclei are formed as a result of the interaction between 3 or 4 monomers and the crystal, while growth proceeds via attachment of monomers. The

initial-conditions, expressed by Equation (B1.3), imply that at the initial time, nucleus formation is spontaneous, without adding seeds [278], [279].

$$\frac{\mathrm{d}C_{\mathrm{n}}}{\mathrm{d}t} = k_1 C_{\mathrm{m}}^{i_0}, \tag{B1.1}$$

$$-\frac{\mathrm{d}C_{\mathrm{m}}}{\mathrm{d}t} = k_2 C_{\mathrm{n}} C_{\mathrm{m}}, \tag{B1.2}$$

and

$$\text{I.C.: } t = 0 \rightarrow \begin{cases} C_{\mathrm{n}} = 0 \\ C_{\mathrm{m}} = C_0 \end{cases}, \tag{B1.3}$$

where C_{n} [mol·m^{-3}] is the nuclei concentration, C_{m} [mol·m^{-3}] the monomer concentration, i_0 [-] the unit cells number (number of monomer molecules that constitute the nucleus) (usually $i_0 = 2$ for tetragonal and $i_0 = 4$ for orthorhombic crystals) [280], k_1 and k_2 the rate constants for nucleation and crystal growth, respectively, and C_0 [mol·m^{-3}] the initial protein concentration. With some algebraic manipulation to eliminate C_{m}, a single first-order ordinary differential equation is obtained, which is in fact a *Riccati equation* [278], [279]

$$\frac{\mathrm{d}C_{\mathrm{n}}}{\mathrm{d}t} = -\frac{1}{2} k_2 i_0 C_{\mathrm{n}}^2 + k_1 C_0^{i_0}. \tag{B2}$$

Integrating Equation (B2) and attending to the initial-conditions of the problem [Equation (B1.3)], nuclei concentration over time is expressed by [278], [279]

$$\ln \left(\frac{1 + C_{\mathrm{n}}(t) \sqrt{\frac{1}{2} \frac{k_2}{k_1} \frac{i_0}{C_0^{i_0}}}}{1 - C_{\mathrm{n}}(t) \sqrt{\frac{1}{2} \frac{k_2}{k_1} \frac{i_0}{C_0^{i_0}}}} \right) = \sqrt{k_1 k_2} \sqrt{2 i_0 C_0^{i_0}} \, t. \tag{B3}$$

Simplifying Equation (B3) by using the equality expressed in Equation (B1.1), a dependence of nuclei concentration over time can be

obtained using Equation (B4.1) [278], [279]. Following a similar approach, the monomeric concentration over time can also be calculated as the concentration over time expressed by Equation (B4.2) [280].

$$C_{\mathrm{n}}(t) = \sqrt{2\frac{k_1}{k_2}\frac{1}{\mathrm{i}_0}\left(C_0^{\mathrm{i}_0} - C_{\mathrm{m}}^{\mathrm{i}_0}\right)}, \tag{B4.1}$$

and

$$C_{\mathrm{m}}(t) = C_0 \operatorname{sech}^{2/\mathrm{i}_0}\left(\sqrt{k_1 k_2}\,\sqrt{\frac{1}{2}\mathrm{i}_0 C_0^{\mathrm{i}_0}}\,t\right). \tag{B4.2}$$

Theory validation

The derived equations were validated using data reported in the literature, both in batch and continuous microreactors [275], [276], [279]–[281]. The obtained data and the model fitting and parameters are presented in Figures B1–B4 and Table B1 for both tetragonal ($\mathrm{i}_0 = 2$) and orthorhombic ($\mathrm{i}_0 = 4$) crystals by applying Equation (B4.2). Furthermore, the resulting conclusions will contribute to a generic modeling framework for the analysis and design of crystallization experiments. The results are displayed in Figures B1–B4. Although the derived equations constitute an expeditious way to estimate the nuclei and monomer concentration over time, there are some limitations. This includes the inadequacy of the theory to express the dependency of the crystallization volume and temperature as well as the formation of crystal polymorphs besides tetragonal and orthorhombic shapes.

(a.1)

(a.2)

(a.3)
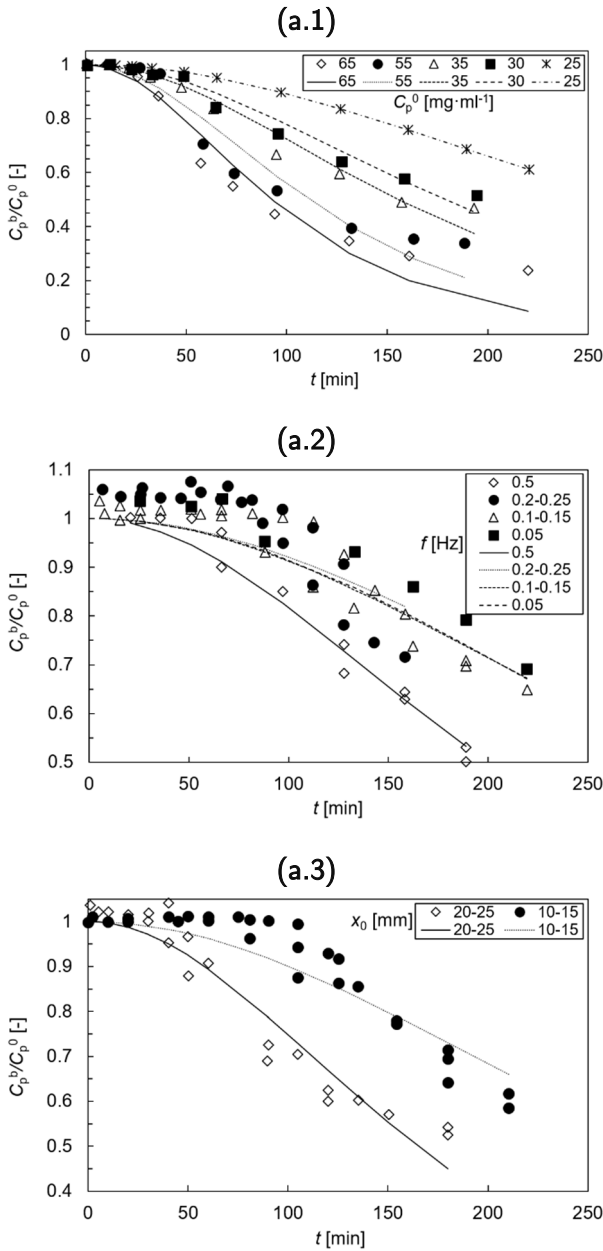
Figure B1. Protein concentration remaining in the bulk phase (C_p^b) normalized with the initial protein concentration (C_p^0) over time (t) for different: **(a.1)** Initial protein concentrations (C_p^0), **(a.2)** Oscillation frequencies (f), and **(a.3)** Oscillation amplitudes (x_0) reported by Yang *et al.* (2018) [275] for a batch oscillatory flow crystallizer [Markers represent experimental points and lines the fitting model].
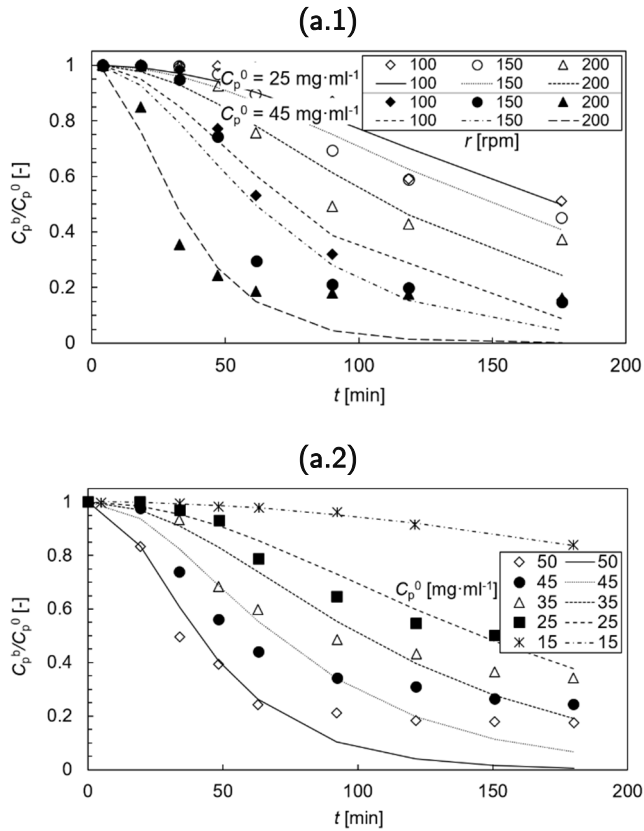
Figure B2. Protein concentration remaining in the bulk phase (C_p^b) normalized with the initial protein concentration (C_p^0) over time (t) for different: **(a.1)** Shaking rates (r), and **(a.2)** Initial protein concentrations (C_p^0) reported by Yang *et al.* (2019) [276] for a batch shaking crystallizer [Markers represent experimental points and lines the fitting model].
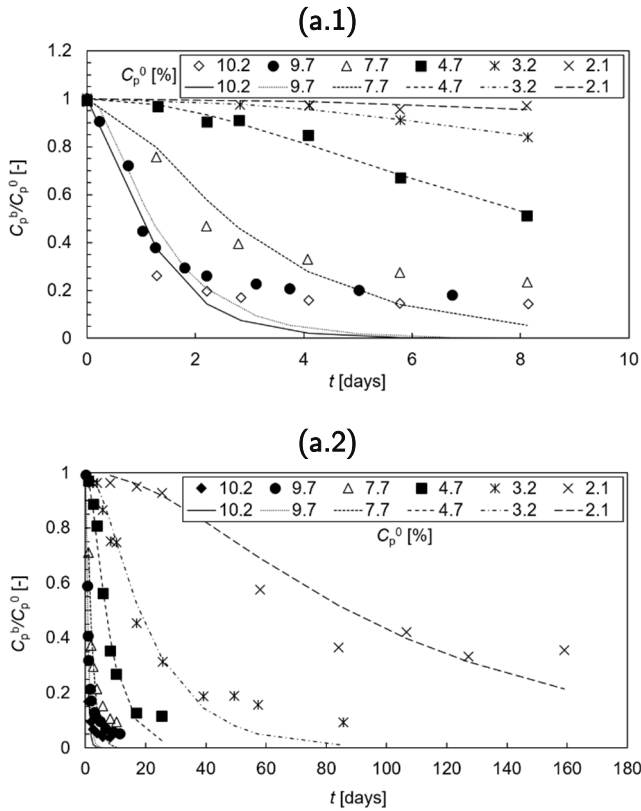
Figure B3. Protein concentration remaining in the bulk phase ($C_p{}^b$) normalized with the initial protein concentration ($C_p{}^0$) over time (t) for: **(a.1)** Shorter time periods, and **(a.2)** Longer time periods reported by Ataka and co-workers (1988, 1986) [279], [280] for a batch crystallizer [Markers represent experimental points and lines the fitting model].

(a.1)

(a.2)

(a.3)
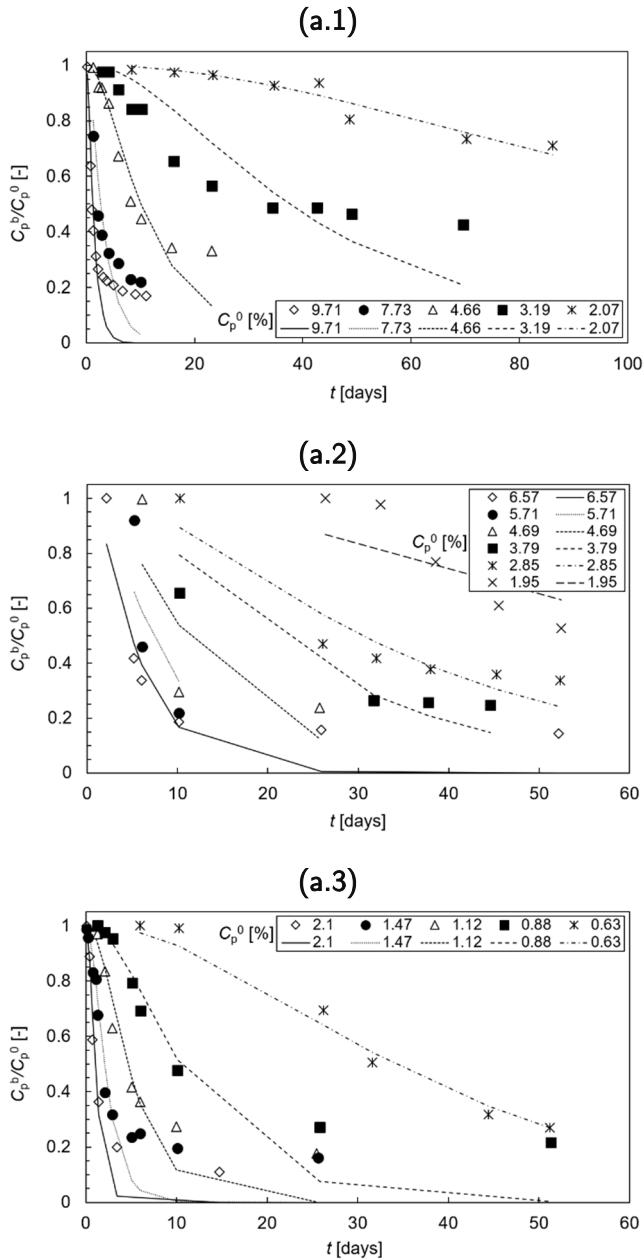
Figure B4. Protein concentration remaining in the bulk phase (C_p^b) normalized with the initial protein concentration (C_p^0) over time (t) for: **(a.1)** Orthorhombic crystals at pH = 4.6 (T = 35 °C), **(a.2)** Orthorhombic crystals at pH = 6.0 (T = 35 °C), and **(a.3)** Tetragonal crystals at pH = 6.0 (T = 5 °C) reported by Bessho *et al.* (1994) [281] for a batch crystallizer [Markers represent experimental points and lines the fitting model].

The fitting parameters are determined through the minimization of the sum of quadratic errors between the theoretically calculated [Equation (B4.2)] and experimentally obtained concentrations $[\sum (C_{\mathrm{p,exp}}^{\mathrm{b}} - C_{\mathrm{p,analyt}}^{\mathrm{b}})^2]$, where the kinetic constant value $(k_1 k_2)$ is a single calculated parameter.

Table B1. Kinetic constant values for the different studies reported in the literature (i_0 is fixed a priori) (continues).

Case study	C_p^0	i_0	$k_1 k_2$	Additional conditions
Yang *et al.* (2018) [275] Batch oscillatory flow crystallizer	65 mg·ml^{-1}		4.8×10^{-8} (mg·ml^{-1})$^{-4}$·min^{-2}	$T = 20$ °C | pH = 4.9 $x_0 = 20$ mm | $f = 0.1$ Hz
	55 mg·ml^{-1}		4.7×10^{-8} (mg·ml^{-1})$^{-4}$·min^{-2}	
	35 mg·ml^{-1}	2	5.9×10^{-8} (mg·ml^{-1})$^{-4}$·min^{-2}	
	30 mg·ml^{-1}		6.1×10^{-8} (mg·ml^{-1})$^{-4}$·min^{-2}	
	25 mg·ml^{-1}		3.8×10^{-8} (mg·ml^{-1})$^{-4}$·min^{-2}	
	25 mg·ml^{-1}	2	3.5×10^{-6} (mg·ml^{-1})$^{-4}$·min^{-2}	$x_0 = 20$ mm | $f = 0.5$ Hz
			2.7×10^{-8} (mg·ml^{-1})$^{-4}$·min^{-2}	$x_0 = 20$ mm | $f = 0.2$-0.25 Hz
			3.0×10^{-8} (mg·ml^{-1})$^{-4}$·min^{-2}	$x_0 = 20$ mm | $f = 0.1$-0.15 Hz
			7.1×10^{-7} (mg·ml^{-1})$^{-4}$·min^{-2}	$x_0 = 20$ mm | $f = 0.05$ Hz
	25 mg·ml^{-1}	2	1.0×10^{-7} (mg·ml^{-1})$^{-4}$·min^{-2}	$f = 0.15$ Hz | $x_0 = 20$-25 mm
			3.4×10^{-8} (mg·ml^{-1})$^{-4}$·min^{-2}	$f = 0.15$ Hz | $x_0 = 10$-15 mm
Yang *et al.* (2019) [276] Batch shaking crystallizer	25 mg·ml^{-1}	2	9.0×10^{-8} (mg·ml^{-1})$^{-4}$·min^{-2}	$T = 20$ °C | pH = 4.8 $r = 100$ rpm
			1.2×10^{-7} (mg·ml^{-1})$^{-4}$·min^{-2}	$r = 150$ rpm
			2.3×10^{-7} (mg·ml^{-1})$^{-4}$·min^{-2}	$r = 200$ rpm
	45 mg·ml^{-1}	2	1.6×10^{-7} (mg·ml^{-1})$^{-4}$·min^{-2}	$r = 100$ rpm
			2.3×10^{-7} (mg·ml^{-1})$^{-4}$·min^{-2}	$r = 150$ rpm
			8.7×10^{-7} (mg·ml^{-1})$^{-4}$·min^{-2}	$r = 200$ rpm
Yang *et al.* (2019) [276] Batch oscillatory flow crystallizer	50 mg·ml^{-1}		4.1×10^{-7} (mg·ml^{-1})$^{-4}$·min^{-2}	$T = 20$ °C | pH = 4.8 $x_0 = 20$ mm | $f = 0.5$ Hz
	45 mg·ml^{-1}		1.8×10^{-7} (mg·ml^{-1})$^{-4}$·min^{-2}	
	35 mg·ml^{-1}	2	1.4×10^{-7} (mg·ml^{-1})$^{-4}$·min^{-2}	
	25 mg·ml^{-1}		8.2×10^{-5} (mg·ml^{-1})$^{-4}$·min^{-2}	
	15 mg·ml^{-1}		5.1×10^{-8} (mg·ml^{-1})$^{-4}$·min^{-2}	
Ataka & Asai (1990) [279] & Ataka (1995) [280] Batch crystallizer	10.2%		2.0×10^{-4} %$^{-4}$·days^{-2}	$T = 35$ °C | pH = 4.6 $C_{NaCl} = 3\%$
	9.7%		1.7×10^{-4} %$^{-4}$·days^{-2}	
	7.7%		9.0×10^{-5} %$^{-4}$·days^{-2}	
	4.7%	4	6.0×10^{-5} %$^{-4}$·days^{-2}	
	3.2%		5.5×10^{-5} %$^{-4}$·days^{-2}	
	2.1%		7.5×10^{-5} %$^{-4}$·days^{-2}	
Ataka & Asai (1990) [279] & Ataka (1995) [280] Batch crystallizer	10.2%		6.2×10^{-4} %$^{-4}$·days^{-2}	$T = 35$ °C | pH = 4.6 $C_{NaCl} = 3\%$
	9.7%		4.1×10^{-4} %$^{-4}$·days^{-2}	
	7.7%		2.0×10^{-4} %$^{-4}$·days^{-2}	
	4.7%	4	1.4×10^{-5} %$^{-4}$·days^{-2}	
	3.2%		6.4×10^{-5} %$^{-4}$·days^{-2}	
	2.1%		1.4×10^{-5} %$^{-4}$·days^{-2}	

Table B1. Kinetic constant values for the different studies reported in the literature (i_0 is fixed a priori) (continued).

Case study	C_P^0	i_0	$h_1 h_2$	Additional conditions
	9.71%		$1.6 \times 10^{-4} \%^{-4} \cdot days^{-2}$	
	7.73%	4	$3.3 \times 10^{-5} \%^{-4} \cdot days^{-2}$	
	4.66%		$2.4 \times 10^{-6} \%^{-4} \cdot days^{-2}$	$T = 35\ °C \mid pH = 4.6$
	3.19%		$1.7 \times 10^{-7} \%^{-4} \cdot days^{-2}$	$C_{NaCl} = 3\%$
	2.07%		$1.5 \times 10^{-8} \%^{-4} \cdot days^{-2}$	
Bessho *et al.*	6.57%		$1.0 \times 10^{-5} \%^{-4} \cdot days^{-2}$	
(1994)	5.71%		$4.6 \times 10^{-6} \%^{-4} \cdot days^{-2}$	
[281]	4.69%	4	$2.0 \times 10^{-6} \%^{-4} \cdot days^{-2}$	$T = 35\ °C \mid pH = 6.0$
Batch crystallizer	3.79%		$5.8 \times 10^{-7} \%^{-4} \cdot days^{-2}$	$C_{NaCl} = 3\%$
	2.85%		$2.6 \times 10^{-7} \%^{-4} \cdot days^{-2}$	
	1.95%		$5.0 \times 10^{-8} \%^{-4} \cdot days^{-2}$	
	2.10%		$1.8 \times 10^{-2} \%^{-4} \cdot days^{-2}$	
	1.47%		$4.3 \times 10^{-3} \%^{-4} \cdot days^{-2}$	
	1.12%	2	$8.4 \times 10^{-4} \%^{-4} \cdot days^{-2}$	$T = 5\ °C \mid pH = 6.0$
	0.88%		$1.7 \times 10^{-4} \%^{-4} \cdot days^{-2}$	$C_{NaCl} = 3\%$
	0.63%		$1.6 \times 10^{-5} \%^{-4} \cdot days^{-2}$	

From the data in Chapter 5, it seems reasonable to assume a value for the kinetic constant based on the works reported by Yang and co-workers [275], [276]. The theory cannot be used to draw any conclusion about the double-pulse temperature experiments, it only can be used to give a rough estimation of the protein concentration in the bulk phase over time. The temperature, pH, and protein and precipitating agent concentration are among the range reported in those studies, besides the fact that the crystal morphology is identical (tetragonal crystals, $i_0 = 2$). The values do not seem to indicate a clear tendency for the effect of the oscillation and amplitude frequencies on the kinetic constant values. However, higher shaking rates seem to contribute to higher kinetic constant values. Thereby, it is necessary to investigate the results obtained with batch crystallizers for observing an effect of the initial protein concentration on the kinetic constant. Based on the previous points, it will be assumed a kinetic constant value of 1.0×10^{-9} $(mg \cdot ml^{-1})^{-4} \cdot min^{-2}$. This results in a protein concentration in the bulk phase of 39.9 mg·ml^{-1} and 16.7 mg·ml^{-1} after 1 h and 20 h, respectively ($T = 20\ °C$, $S_0 = 5.4$). The last value explains the reason for the appearance of large crystals during the isothermal experiments. While the experiment starts inside the nucleation zone, due to the protein consumption, the crystals will start growing after roughly 12 h, which corresponds to the moment at which the metastability concentration is reached (27.5 mg·ml^{-1}). Even though the available data at different temperature values is limited, it is possible to

induce from the results in Table B1 that higher supersaturations contribute to higher kinetic constant values, which results in steeper protein concentration decays. This can explain the reason for the crystal growing during the double-pulse temperature experiments. For the experiments conducted at 10 °C (nucleation temperature, $S_0 = 17.9$) and 20 °C (crystal growth temperature, $S_0 = 5.4$), even though these supersaturation values belong to the nucleation zone, the concentration decay will make the protein solution to surpass the metastability limit and promote the crystal growth inside the metastable zone. However, for the experiments conducted at 15 °C (nucleation temperature, $S_0 = 9.6$) and 25 °C (crystal growth temperature, $S_0 = 3.4$), the concentration decay during the nucleation time (1 h) seems to not be enough to generate crystals with a detectable size.

Appendix C

C1   Insulin crystallization studies reported in the literature

Table C1. Summary of the studies conducted with insulin and corresponding crystallization conditions (continues).

Author(s)	Insulin type & concentration	Buffer solutions & Precipitating agent	Additive(s)	pH	T [°C]	Crystallization technique & Outcome
Mühlig *et al.* (2001) [227]	**Human insulin** (in HCl) [2–5] mg·ml⁻¹	Trisodium citrate	Phenol	6.5	Room temperature	Microbatch Monoclinic crystals
Parambil *et al.* (2011) [231]	**Human insulin** (in trisodium citrate) 2.5 mg·ml⁻¹	Zinc sulphate Trisodium citrate	Acetone	6	10	Oscillatory flow in capillaries Several crystal shapes
Bergeron *et al.* (2003) [216]	**Porcine insulin** (in HCl) [0.75–5] mg·ml⁻¹	Zinc chloride Trisodium citrate	Acetone	–	4	Microbatch Rhombohedral crystals
Nanev *et al.* (2011, 2013, 2017) [223], [224], [226], [230]	**Porcine insulin** (in HCl) 5 mg·ml⁻¹ 7 mg·ml⁻¹	Zinc chloride Trisodium citrate	Acetone	7	4	Microbatch Rhombohedral crystals

Table C1. Summary of the studies conducted with insulin and corresponding crystallization conditions (continues).

Author(s)	Insulin type & concentration	Buffer solutions & Precipitating agent	Additive(s)	pH	T [°C]	Crystallization technique & Outcome
Chatani *et al.* (2015) [234]	Bovine insulin (in HCl) 5 mg·ml⁻¹	Sodium chloride Deuterium chloride	–	8.5	25	– Amyloid fibrils
Dolui *et al.* (2015) [235]	Human insulin (in HCl) 1.5 mg·ml⁻¹	Sodium chloride	–	–	24	– Amyloid fibrils
Pease *et al.* (2010) [236]	Human insulin (in HCl) 2 mg·ml⁻¹	Sodium chloride	–	–	Room temperature	– Amyloid fibrils
Nettleton *et al.* (2000) [240]	Bovine & human insulin (in HCl or ammonia) 10 mg·ml⁻¹	Zinc phosphate Deuterium oxide Deuterium chloride	–	4	20	Dialysis Amyloid fibrils
Bromberg *et al.* (2005) [232]	Human insulin (Zn content 0.4 wt%)	Sodium chloride PEG	–	5.65	[15–45]	Microbatch in capillaries Insulin microspheres (no crystallization)
Govardhan *et al.* (2005) [282]	Human insulin (in Tris) 15 mg·ml⁻¹	Sodium citrate PEG	2-propanol Ethanol DDM	7.5 8.6	25 33	Hanging-drop vapour diffusion & Batch Needle-shaped crystals
	Human insulin (in phosphate) 6 mg·ml⁻¹	Zinc acetate	Acetone	6.1	15	Monoclinic crystals

Table C1. Summary of the studies conducted with insulin and corresponding crystallization conditions (continues).

Author(s)	Insulin type & concentration	Buffer solutions & Precipitating agent	Additive(s)	pH	T [°C]	Crystallization technique & Outcome
Chen *et al.* (2017) [225]	Bovine insulin (in HCl) 2 mg·ml⁻¹	Sodium bicarbonate Citrate	–	6.6	Room temperature	Microbatch in microwells Rhombohedral (rhombic dodecahedra) crystals
Fili *et al.* (2015) [238]	Human insulin (in water) 13.11 mg·ml⁻¹	Zinc acetate Sodium phosphate Monopotassium phosphate	Sodium thiocyanate 4-ethylresorcinol Dimethyl sulfoxide	[4–8.5]	25	Batch salting-out –
Norrman & Schluckebier (2007) [219]	Human insulin (certain Zn content) 6.9 mg·ml⁻¹	Sodium chloride Resorcinol Phosphate	Urea Sodium thiocyanate Ethanol	6.5 7.0	18	Hanging-drop vapour diffusion Orthorhombic crystals Monoclinic crystals
Li *et al.* (2019) [283]	Bovine insulin (in HCl) 1.25 mg·ml⁻¹	Zinc chloride Citrate	–	8		Nanobatch Rhombohedral crystals
Kadima *et al.* (1991) [233]	Porcine insulin (in HCl) [2–10] mg·ml⁻¹	Zinc sulphate Trisodium citrate	Acetone	–	–	Batch Rhombohedral crystals
Hodzhaoglu *et al.* (2016) [284]	Porcine & human insulin (in HCl) [0.85–7.6] mg·ml⁻¹	Zinc chloride Trisodium citrate	Acetone	6.98	24	Microbatch Cubic crystals

Table **C1**. Summary of the studies conducted with insulin and corresponding crystallization conditions (continues).

Author(s)	Insulin type & concentration	Buffer solutions & Precipitating agent	Additive(s)	pH	T [°C]	Crystallization technique & Outcome
Maeda *et al.* (2004) [241]	Porcine insulin (in deuterium oxide) [5–25] mg·ml^{-1}	Disodium hydrogen phosphate	Trisodium acetate	6.3	Room temperature	Batch & Dialysis Cubic crystals
Yip & Ward (1996) [239]	**Bovine insulin** (in HCl)	Zinc acetate Trisodium citrate Sodium chloride	Phenol	8.5	Room temperature	Microbatch Rhombohedral crystals
Reviakine *et al.* (2003) [285]	**Bovine insulin** (in HCl) [0.75–5] mg·ml^{-1}	Zinc chloride Trisodium citrate	Acetone	–	[26.8–27.3]	Microbatch in capillaries Rhombohedral crystals
Nanev & Hodzhaoglu (2012) [242]	**Porcine insulin** (in HCl) 5 mg·ml^{-1} 7 mg·ml^{-1}	Zinc chloride Trisodium citrate	Acetone	7	4 [18–29]	Microbatch Rhombohedral crystals
Abel (1926) [286]	**Insulin** (in acetic acid) –	Disodium hydrogen phosphate Pyridine	Brucine	[4.7–5]	–	– Rhombohedral crystals

Table C1. Summary of the studies conducted with insulin and corresponding crystallization conditions (continued).

Author(s)	Insulin type & concentration	Buffer solutions & Precipitating agent	Additive(s)	pH	T [°C]	Crystallization technique & Outcome
Schlichtkrull (1957) [228], [229], [287]–[289]	Bovine & porcine insulin (in HCl) 2.42 mg·ml^{-1} 17 mg·ml^{-1}	Zinc chloride Sodium chloride Sodium acetate	Acetone	[5.45–5.55]		Batch Rhombohedral crystals
	Bovine & porcine insulin (in HCl) 2.42 mg·ml^{-1} 10 mg·ml^{-1}	Zinc chloride Citrate	Citric acid Methylparaben	[6.2–6.5]	25	Seeding Rhombohedral crystals
	Porcine insulin (in HCl) 5 mg·ml^{-1}	Zinc chloride Trisodium citrate	Acetone	6.3		Batch Rhombohedral crystals
Dimitrov et al. (2013) [290]	Porcine insulin [1.9–9] mg·ml^{-1} [16.7-18.1] mg·ml^{-1}	Zinc chloride Trisodium citrate	Phenol	6.89	[15–20] 36	Batch Monoclinic crystals
	[4.5–11] mg·ml^{-1}	Sodium chloride Sodium acetate	Methylparaben	7.92	[10–36]	Cubic crystals
	(in HCl) 5 mg·ml^{-1}	Sodium acetate	Acetone	4.51	36	Tetragonal crystals

C2 Screening of insulin crystallization conditions

The screening of insulin crystallization conditions is carried out by using hanging-drop vapour diffusion as the crystallization technique. As proposed by Bergeron *et al.* (2003) [216], the first crystallization trials are conducted at 4 °C with an initial insulin concentration of 15 mg·ml⁻¹. A schematic representation of the hanging-drop experimental set-up is presented in Figure C1.
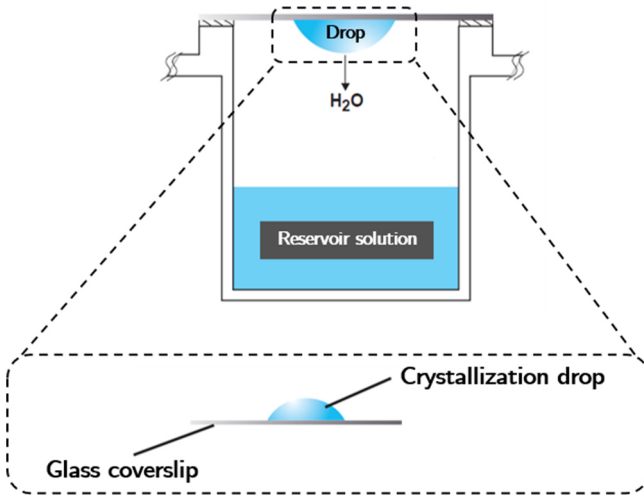
Figure C1. Schematic representation of the hanging-drop experimental set-up: Drop of 8 µl (containing the protein solution) and reservoir solution of 1 ml ([PS] defines the precipitating agent solution concentration).

During the reservoir solution preparation, the crystallization solution becomes cloudy after adding the precipitating agent (TC). When acetone is added, the solution becomes clear. However, due to the very slow diffusion and convection mechanisms within the hanging drop, after combining the drops of insulin and reservoir solutions, the drop is slightly turbid. This turbidity, possibly related to the formation of insulin aggregates, tends to disappear over time. This has been reported before by Mühlig *et al.* (2001) [227] and observed by Hodzhaoglu *et al.* (2016) [284].

As described along Chapter 6, Mühlig and co-workers reported the occurrence of precipitation after the buffer addition, which resulted in a cloudy solution at higher initial insulin concentrations [227]. Hodzhaoglu

and co-workers also conducted insulin crystallization experiments using the hanging-drop vapour diffusion technique, while no hypothesis for explaining the cloudy solution was addressed, the precipitation occurrence is visible under certain crystallization conditions. Finally, Sauter *et al.* (2015) [291] studied the crystallization process of bovine β-lactoglobulin and observed that, after adding the salt solution, protein aggregates are formed and, consequently, the solution becomes turbid. The turbid solution becomes gradually clearer, which might indicate that the aggregates are consumed. The authors also highlight that by removing the aggregates, as observed with other proteins, results in a reduction on the number of crystals [291]. The main findings resulting from the initial screening of crystallization conditions are displayed in Figures C2–C5.
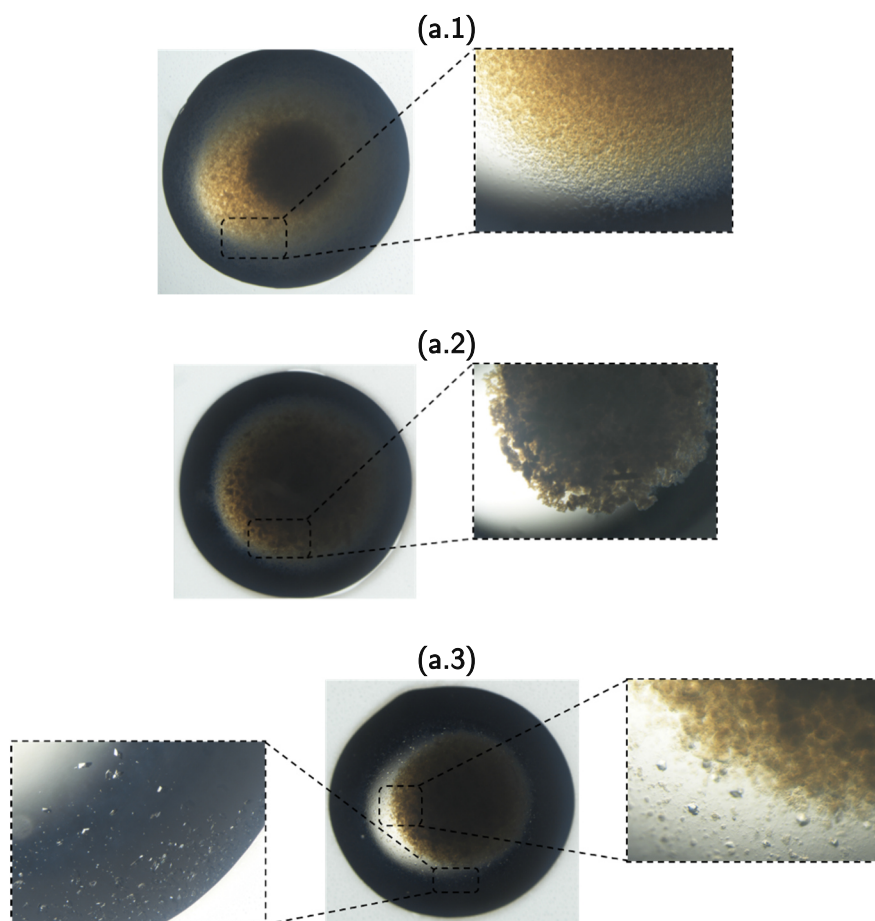
Figure C2. Hanging-drop crystallization outcome for an insulin concentration of 7.5 mg·ml^{-1} and salt solution concentration of 0.0025 M after 1 day at 4 °C: **(a.1)** to **(a.3)** represent different drops and close-ups.

(a)

(b)
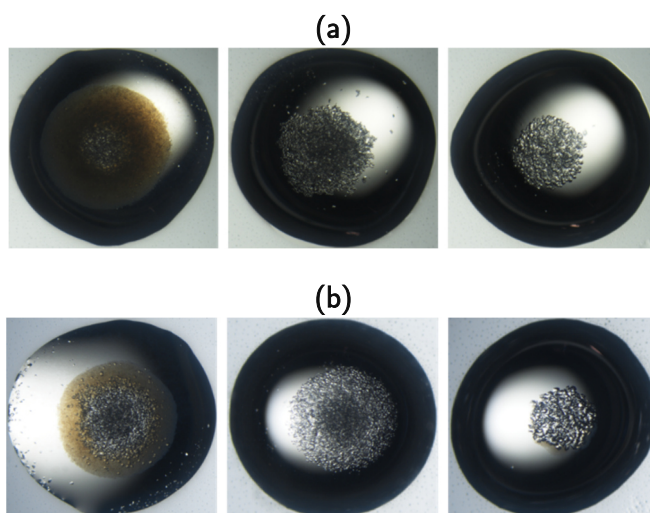
Figure C3. Hanging-drop crystallization outcome for an insulin concentration of 7.5 mg·ml^{-1} and salt solution concentration of 0.0025 M after: **(a)** 5 days and **(b)** 15 days at 4 °C for different drops (see Figure C2).
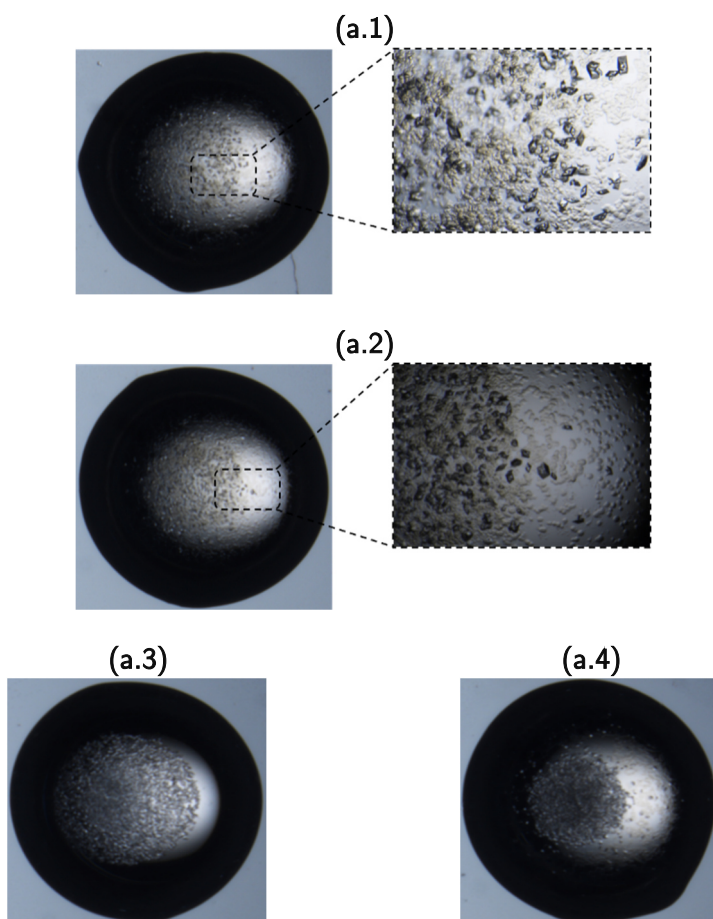
Figure C4. Hanging-drop crystallization outcome for an insulin concentration of 5 mg·ml^{-1} and salt solution concentration of 0.00333 M after 4 h at 4 °C: **(a.1)** to **(a.4)** represent different drops and close-ups.

(a.1)

(b.1)

(b.2)

(b.3)
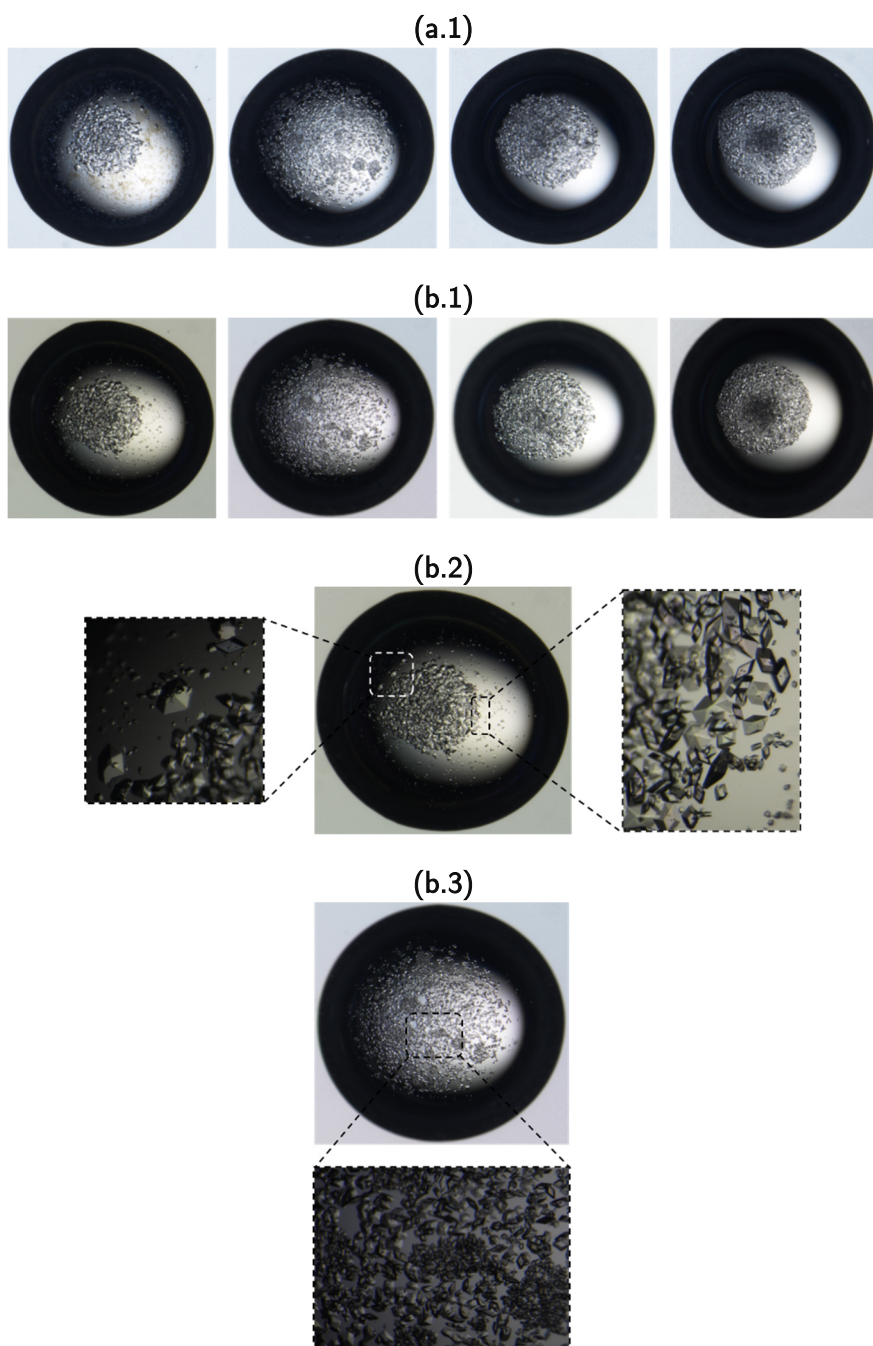
Figure C5. Hanging-drop crystallization outcome for an insulin concentration of 5 mg·ml^{-1} and salt solution concentration of 0.00333 M after **(a)** 5 days, and **(b)** 15 days at 4 °C: **(1)** Different droplets, and **(2)** and **(3)** close-ups.

From the current results, it becomes evident that the insulin concentration in solution plays an important contribution to the formation of insulin aggregates (Figures C2–C5). It appears to be prominent that a lower insulin concentration leads to a suppression of insulin agglomerates and/or aggregates formation (Figures C4 and C5). However, for the studied range of insulin concentration, the formation of insulin aggregates and/or agglomerates occurs with a distinct time interval to disappear. Afterwards, insulin rhombohedral crystals start to appear in the bulk phase. Although crystal formation is observed, excessive nucleation takes place, which results in the formation of many small crystals (Figure C5). For counteracting the appearance in parallel of many crystals and insulin agglomerates and/or aggregates (Figures C2 and C4), hanging-drop experiments are performed at different initial insulin concentrations: 15 mg·ml^{-1} and 5 mg·ml^{-1}. These results are displayed in Tables C2 and C3.

Table C2. Hanging-drop crystallization outcome for an initial insulin concentration of 15 mg·ml^{-1} at different time frames in drops of 10 µl. [The indicated insulin and salt solution concentration result from the mixing].
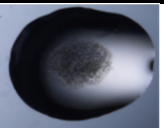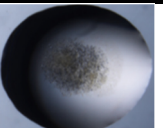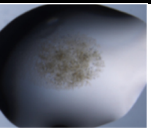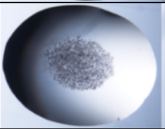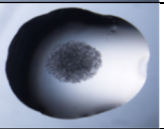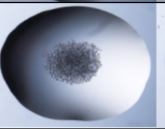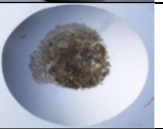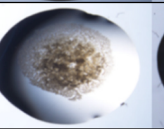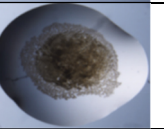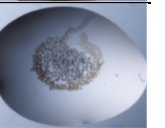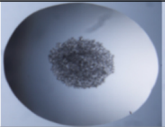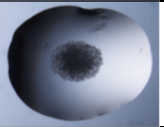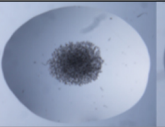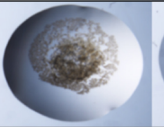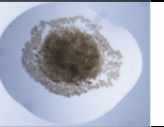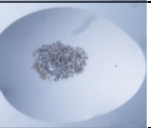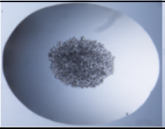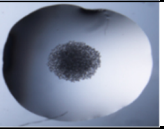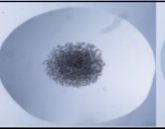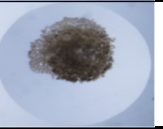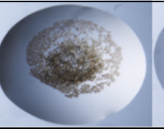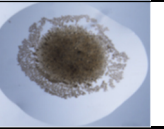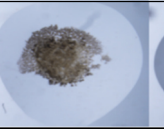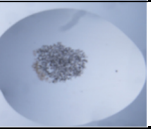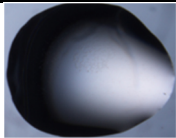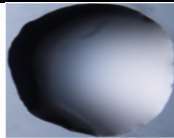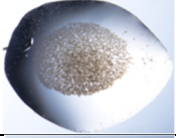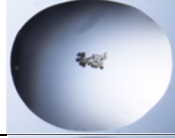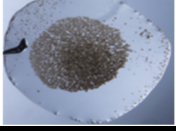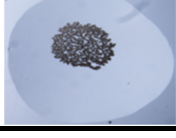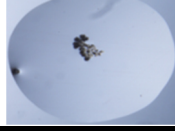
Time frame	Insulin concentration [mg·ml^{-1}]			
	5.0	3.75	3.0	2.5
	Salt solution concentration [M]			
	0.00333	0.00375	0.004	0.00417
Initially				
After 1 day				
After 3 days				
After 1 week				

Table C3. Hanging-drop crystallization outcome for an initial insulin concentration of 5 mg·ml⁻¹ at different time frames in drops of 10 µl. [The indicated insulin and salt solution concentration result from the mixing].

Time frame	Insulin concentration [mg·ml^{-1}]			
	1.7	1.25	1.0	0.83
	Salt solution concentration [M]			
	0.00333	0.00375	0.004	0.00417
Initially				
After 1 day				
After 3 days				
After 1 week				

Attending to the outcome of this initial screening of insulin crystallization conditions, it is possible to draw an operating regime to define the insulin and salt solution concentration. This is shown in Figure C6, where it is observed that the formation of insulin crystals required insulin concentrations higher than 3 mg·ml^{-1} and salt solution concentrations up to 0.004 M.
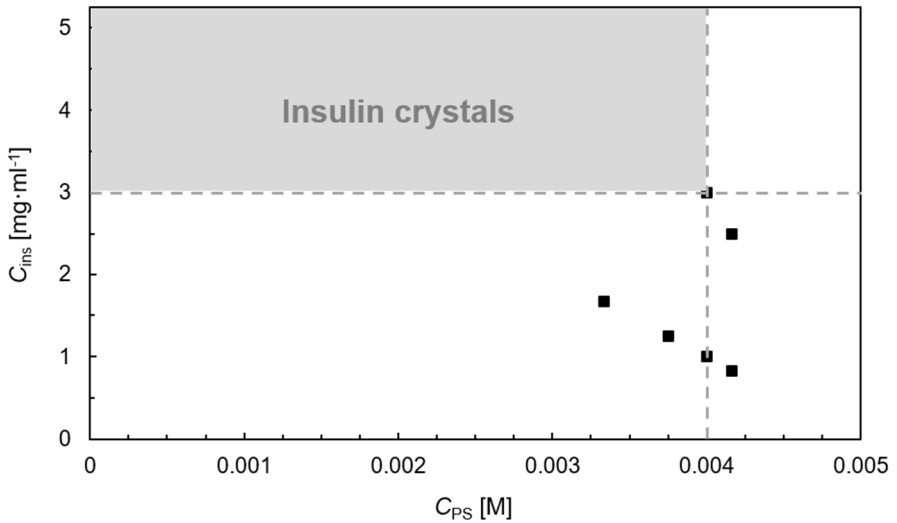
Figure C6. Insulin (ins) and salt (ZnCl$_2$) (PS) concentration in solution for the experiments performed at 20 °C: Operating regime to produce insulin crystals (region highlighted in grey) with hanging-drop vapor diffusion experiments.

Bibliography

[1]   J. C. Brooks-bartlett, E. F. Garman, J. C. Brooks-bartlett, and E.
        F. Garman, "The Nobel Science: One Hundred Years of
        Crystallography," *Interdisciplinary Science Reviews*, vol. 40, no. 3,
        pp. 244–264, 2015.

[2]   Y. Lin, "What's happened over the last five years with high-
        throughput protein crystallization screening?," *Expert Opinion on
        Drug Discovery*, vol. 13, no. 8, pp. 691–695, 2018.

[3]   B. K. Jap *et al.*, "2D crystallization: from art to science,"
        Ultramicroscopy, vol. 46, no. 1–4, pp. 45–84, 1992.

[4]   N. E. Chayen, "Turning protein crystallisation from an art into a
        science," *Current Opinion in Structural Biology*, vol. 14, no. 5,
        pp. 577–583, 2004.

[5]   D. J. Watkin, "Chemical crystallography – Science , technology or
        a black art," *Crystallography Reviews*, vol. 16, no. 3, pp. 197–230,
        2010.

[6]   G. Walsh, *Proteins: Biochemistry and Biotechnology*, 2nd Edition.
        Wiley, 2015.

[7]   R. Giegé, "A historical perspective on protein crystallization from
        1840 to the present day," *FEBS Journal*, vol. 280, no. 24,
        pp. 6456–6497, 2013.

[8]   A. Ducruix and R. Giegé, *Crystallization of Nucleic Acids and
        Proteins: A Practical Approach*, 2nd Edition. Oxford University
        Press, 1999.

[9]   A. McPherson and J. A. Gavira, "Introduction to protein
        crystallization," *Acta Crystallographica Section F: Structural
        Biology Communications*, vol. 70, no. 1, pp. 2–20, 2014.

[10]   J. W. Mullin, *Crystallization*, 4th Edition. Oxford, 2001.

[11]   R. Giegé and A. McPherson, "Chapter: Crystallization – General
        Methods," in *International Tables of Crystallography, Vol. F,
        Crystallography of Biological Macromolecules*, 2nd Edition., E.
        Arnold, D. M. Himmel, and M. G. Rossmann, Eds. John
        Wiley & Sons, 2006, pp. 81–93.

[12]   N. E. Chayen and E. Saridakis, "Protein crystallization: from purified protein to diffraction-quality crystal," *Nature - Methods*, vol. 5, pp. 147–153, 2008.

[13]   M. A. Vorontsova, D. Maes, and P. G. Vekilov, "Recent advances in the understanding of two-step nucleation of protein crystals," *Faraday Discussions*, vol. 179, no. 27, pp. 27–40, 2015.

[14]   J. Leng and J.-B. Salmon, "Microfluidic crystallization," *Lab on a Chip*, vol. 9, no. 1, pp. 24–34, 2009.

[15]   S. Haeberle and R. Zengerle, "Microfluidic platforms for lab-on-a-chip applications," *Lab on a Chip*, vol. 7, pp. 1094–1110, 2007.

[16]   M. Maeki, H. Yamaguchi, M. Tokeshi, and M. Miyazaki, "Microfluidic Approaches for Protein Crystal Structure Analysis," *Analytical Sciences*, vol. 32, pp. 3–9, 2016.

[17]   C.-G. Yang, Z.-R. Xu, and J.-H. Wang, "Manipulation of droplets in microfluidic systems," *Trends in Analytical Chemistry*, vol. 29, no. 2, pp. 141–157, 2010.

[18]   L. Shui, J. C. T. Eijkel, and A. van den Berg, "Multiphase flow in microfluidic systems - Control and applications of droplets and interfaces," *Advances in Colloid & Interface Science*, vol. 133, pp. 35–49, 2007.

[19]   S.-Y. Teh, R. Lin, L.-H. Hung, and A. P. Lee, "Droplet microfluidics," *Lab on a Chip*, vol. 8, no. 2, pp. 198–220, 2008.

[20]   O. Galkin and P. G. Vekilov, "Direct Determination of the Nucleation Rates of Protein Crystals," *The Journal of Physical: Chemistry B*, vol. 103, no. 49, pp. 10965–10971, 1999.

[21]   J. M. García-Ruiz, "Nucleation of protein crystals," *Journal of Structural Biology*, vol. 142, no. 1, pp. 22–31, 2003.

[22]   M. Sleutel and A. E. S. Van Driessche, "Nucleation of protein crystals-a nanoscopic perspective," *Nanoscale*, vol. 10, no. 26, pp. 12256–12267, 2018.

[23]   M. Sleutel and A. E. S. Van Driessche, "Role of clusters in nonclassical nucleation and growth of protein crystals," *Proceedings of the National Academy of Sciences*, vol. 111, no. 5, pp. E546–E553, 2014.

[24]   P. G. Vekilov, "Dense liquid precursor for the nucleation of ordered solid phases from solution," *Crystal Growth and Design*, vol. 4, no. 4, pp. 671–685, 2004.

[25] G. Nicolis and D. Maes, *Advances in Chemical Physics, Kinetics and Thermody- namics of Multistep Nucleation and Self-Assembly in Nanoscale Materials*, Vol. 151. Hoboken, New Jersey, United States: John Wiley & Sons, Inc., 2012.

[26] O. Galkin and P. G. Vekilov, "Are nucleation kinetics of protein crystals similar to those of liquid droplets?," *Journal of the American Chemical Society*, vol. 122, no. 1, pp. 156–163, 2000.

[27] C. Ferreira, S. Barbos, P. Taboada, F. A. Rocha, A. M. Damas, and P. M. Martins, "The nucleation of protein crystals as a race against time with on- and off-pathways," *Journal of Applied Crystallography*, vol. 50, pp. 1056–1065, 2017.

[28] G. M. Whitesides, "The origins and the future of microfluidics," *Nature*, vol. 442, no. 7101, pp. 368–373, Jul. 2006.

[29] S. Hardt and F. Schönfeld, "Microfluidic Technologies for Miniaturized Analysis Systems," in *Springer*, Hannover and Mainz, 2007, pp. 1–58.

[30] J. X. J. Zhang and K. Hoshino, "Molecular Sensors and Nanodevices," in *Molecular Sensors and Nanodevices*, 2014, pp. 103–168.

[31] R. Khalil, *The MEMS Handbook*. CRC Press, 2002.

[32] R. Raj, N. Mathur, and V. V Buwa, "Numerical Simulations of Liquid - Liquid Flows in Microchannels," *Industrial & Engineering Chemistry Research*, vol. 49, no. 21, pp. 10606–10614, 2010.

[33] M. Wörner, "Numerical modeling of multiphase flows in microfluidics and micro process engineering: A review of methods and applications," *Microfluidics & Nanofluidics*, vol. 12, no. 6, pp. 841–886, 2012.

[34] L. Capretto, W. Cheng, M. Hill, and X. Zhang, "Micromixing Within Microfluidic Devices," *Topics in Current Chemistry*, vol. 304, pp. 27–68, 2011.

[35] T. M. Squires and S. R. Quake, "Microfluidics: Fluid physics at the nanoliter scale," *Reviews of Modern Physics*, vol. 77, no. 3, pp. 977–1026, 2005.

[36] L. Shui, J. C. T. Eijkel, and A. van den Berg, "Multiphase flow in micro- and nanochannels," *Sensors and Actuators, B: Chemical*, vol. 121, no. 1, pp. 263–276, 2007.

[37] L. Peng, M. Yang, S. Guo, W. Liu, and X.-Z. Zhao, "The effect of interfacial tension on droplet formation in flow-focusing microfluidic devices," *Biomedical Microdevices*, vol. 13, pp. 559–564, 2011.

[38] H. Song, D. L. Chen, and R. F. Ismagilov, "Reactions in droplets in microfluidic channels," *Angewandte Chemie - International Edition*, vol. 45, no. 44, pp. 7336–7356, 2006.

[39] S. Bashir, J. M. Rees, and W. B. Zimmerman, "Simulations of microfluidic droplet formation using the two-phase level set method," *Chemical Engineering Science*, vol. 66, pp. 4733–4741, 2011.

[40] S. Zhao, W. Wang, M. Zhang, T. Shao, Y. Jin, and Y. Cheng, "Three-dimensional simulation of mixing performance inside droplets in micro-channels by Lattice Boltzmann method," *Chemical Engineering Journal*, vol. 207–208, pp. 267–277, 2012.

[41] J. Castillo-León and W. E. Svendsen, *Lab-on-a-Chip Devices and Micro-Total Analysis Systems - A Practical Guide*. London, 2015.

[42] C. Y. Lee, C. L. Chang, Y. N. Wang, and L. M. Fu, "Microfluidic mixing: A review," *International Journal of Molecular Sciences*, vol. 12, no. 5, pp. 3263–3287, 2011.

[43] D. Mark, S. Haeberle, G. Roth, F. von Stetten, and R. Zengerle, "Microfluidic lab-on-a-chip platforms: requirements, characteristics and applications," *Chemical Society Reviews*, vol. 39, no. 3, pp. 1153–1182, 2010.

[44] Y. Li, M. Jain, Y. Ma, and K. Nandakumar, "Control of the breakup process of viscous droplets by an external electric field inside a microfluidic device," *Soft Matter*, vol. 11, pp. 3884–3899, 2015.

[45] D. F. Rivas and S. Kuhn, "Synergy of Microfluidics and Ultrasound," *Topics in Current Chemistry*, vol. 340, no. 70, pp. 1–30, 2016.

[46] A. Günther and M. T. Kreutzer, "Multiphase Flow," in *Micro Process Engineering*, 2009, pp. 1–40.

[47] G. S. Jeong, S. Chung, C.-B. Kim, and S.-H. Lee, "Applications of micromixing technology," *The Analyst*, vol. 135, no. 3, pp. 460–473, 2010.

[48] A. M. C. van Dinther, C. G. P. H. Schroën, F. J. Vergeldt, R. G. M. van der Sman, and R. M. Boom, "Suspension flow in microfluidic devices - A review of experimental techniques focussing on concentration and velocity gradients," *Advances in Colloid & Interface Science*, vol. 173, pp. 23–34, 2012.

[49] A. Belkadi, D. Tarlet, A. Montillet, J. Bellettre, and P. Massoli, "Water-in-oil emulsification in a microfluidic impinging flow at high capillary numbers," *International Journal of Multiphase Flow*, vol. 72, pp. 11–23, 2015.

[50]   H. Huang and X. He, "Fluid displacement during droplet formation at microfluidic flow-focusing junctions," *Lab on a Chip*, vol. 15, no. 21, pp. 4197–205, 2015.

[51]   F. H. Kakavandi, M. Rahimi, O. Jafari, and N. Azimi, "Liquid − liquid two-phase mass transfer in T-type micromixers with different junctions and cylindrical pits," *Chemical Engineering & Processing: Process Intensification*, vol. 107, pp. 58–67, 2016.

[52]   X. Yao, Y. Zhang, L. Du, J. Liu, and J. Yao, "Review of the applications of microreactors," *Renewable and Sustainable Energy Reviews*, vol. 47, pp. 519–539, 2015.

[53]   S. Kuhn and K. F. Jensen, "A pH Sensitive Laser-Induced Fluorescence Technique to Monitor Mass Transfer in Multiphase Flows in Microfluidic Devices," *Industrial & Engineering Chemistry Research*, vol. 51, pp. 8999–9006, 2012.

[54]   Z. Chen, R. Zhang, and X. Wang, "CFD study of flow-diffusion process in Y-shape micromixer," *Journal of Central South University*, vol. 23, no. 4, pp. 969–974, 2016.

[55]   J. E. Prest *et al.*, "Miniaturised free flow isotachophoresis of bacteria using an injection moulded separation device," *Journal of Chromatography B: Analytical Technologies in the Biomedical and Life Sciences*, vol. 903, pp. 53–59, 2012.

[56]   J. Nilsson, M. Evander, B. Hammarström, and T. Laurell, "Review of cell and particle trapping in microfluidic systems," *Analytica Chimica Acta*, vol. 649, no. 2, pp. 141–157, 2009.

[57]   R. Seemann, M. Brinkmann, T. Pfohl, and S. Herminghaus, "Droplet based microfluidics," *Reports on Progress in Physics*, vol. 75, pp. 1–41, 2012.

[58]   T. A. Prileszky, B. A. Ogunnaike, and E. M. Furst, "Statistics of droplet sizes generated by a microfluidic device," *American Institute of Chemical Engineers Journal*, vol. 62, no. 8, pp. 1–20, 2016.

[59]   P. Occhetta, M. Licini, A. Redaelli, and M. Rasponi, "Design of a microfluidic strategy for trapping and screening single cells," *Medical Engineering & Physics*, vol. 38, pp. 1–8, 2015.

[60]   Z. Wu, B. Willing, J. Bjerketorp, J. K. Jansson, and K. Hjort, "Soft inertial microfluidics for high throughput separation of bacteria from human blood cells," *Lab on a Chip*, vol. 9, pp. 1193–1199, 2009.

[61]   Y. Ai, S. W. Joo, Y. Jiang, X. Xuan, and S. Qian, "Pressure-driven transport of particles through a converging-diverging microchannel," *Biomicrofluidics*, vol. 3, no. 2, pp. 1–14, 2009.

[62]   J. Tan, J. H. Xu, S. W. Li, and G. S. Luo, "Drop dispenser in a cross-junction microfluidic device: Scaling and mechanism of break-up," *Chemical Engineering Journal*, vol. 136, no. 2–3, pp. 306–311, 2008.

[63]   T. Bayraktar and S. B. Pidugu, "Characterization of liquid flows in microfluidic systems," *International Journal of Heat and Mass Transfer*, vol. 49, no. 5–6, pp. 815–824, 2006.

[64]   C. Westerwalbesloh *et al.*, "Modeling and CFD simulation of nutrient distribution in picoliter bioreactors for bacterial growth studies on single-cell level," *Lab on a Chip*, vol. 15, pp. 4177–4186, 2015.

[65]   A. Günther and K. F. Jensen, "Multiphase microfluidics: from flow characteristics to chemical and materials synthesis," *Lab on a Chip*, vol. 6, no. 12, pp. 1487–1503, 2006.

[66]   T. Cubaud, B. M. Jose, S. Darvishi, and R. Sun, "Droplet breakup and viscosity-stratified flows in microchannels," *International Journal of Multiphase Flow*, vol. 39, pp. 29–36, 2012.

[67]   C. Jiu-Sheng and J. Jia-Huan, "Droplet Microfluidic Technology: Mirodroplets Formation and Manipulation," *Chinese Journal of Analytical Chemistry*, vol. 40, no. 8, pp. 1293–1300, 2012.

[68]   R. B. Bird, W. E. Stewart, and E. N. Lightfoot, *Transport Phenomena*, 2nd Edition. John Wiley & Sons, Inc., 2007.

[69]   B. J. Kirby, *Micro- and Nanoscale Fluid Mechanics: Transport in Microfluidic Devices*, First. Cambridge: Cambridge University Press, 2010.

[70]   W. Lan, C. Wang, X. Guo, S. Li, and G. Luo, "Study on the Transient Interfacial Tension in a Microfluidic Droplet Formation Coupling Interphase Mass Transfer Process," *American Institute of Chemical Engineers Journal*, vol. 62, no. 7, pp. 2542–2549, 2016.

[71]   J. Carneiro, E. Doutel, J. B. L. M. Campos, and J. M. Miranda, "PDMS droplet formation and characterization by hydrodynamic flow focusing technique in a PDMS square microchannel," *Journal of Micromechanics & Microengineering*, vol. 26, no. 10, pp. 1–8, 2016.

[72] A. Pradeep, J. Raveendran, T. Ramachandran, B. G. Nair, and S. B. T. G, "Computational simulation and fabrication of smooth edged passive micromixers with alternately varying diameter for ef fi cient mixing," *Microelectronic Engineering*, vol. 165, pp. 32–40, 2016.

[73] C. Yao, Y. Liu, S. Zhao, Z. Dong, and G. Chen, "Bubble/droplet formation and mass transfer during gas-liquid-liquid segmented," *American Institute of Chemical Engineers Journal*, pp. 1–46, 2016.

[74] Z. Dong, S. Zhao, Y. Zhang, C. Yao, G. Chen, and Q. Yuan, "Mixing and residence time distribution in ultrasonic microreactors," *American Institute of Chemical Engineers Journal*, pp. 1–47, 2016.

[75] D. Gobby, P. Angeli, and A. Gavriilidis, "Mixing characteristics of T-type microfluidic mixers," *Journal of Micromechanics & Microengineering*, vol. 11, pp. 126–132, 2001.

[76] A. Woitalka, S. Kuhn, and K. F. Jensen, "Scalability of mass transfer in liquid-liquid flow," *Chemical Engineering Science*, vol. 116, pp. 1–8, 2014.

[77] M. Maeki *et al.*, "An Approach for Single Crystallization of Protein By Using Droplet Based Microfluidics," in *16th International Conference on Miniaturized Systems for Chemistry and Life Sciences*, 2012, pp. 1219–1221.

[78] B. Rupp, "Origin and use of crystallization phase diagrams," *Acta Crystallographica Section F: Structural Biology Communications*, vol. 71, pp. 247–260, 2015.

[79] C. N. Baroud, F. Gallaire, and R. Dangla, "Dynamics of microfluidic droplets," *Lab on a Chip*, vol. 10, no. 16, p. 2032, 2010.

[80] L. Li and R. F. Ismagilov, "Protein Crystallization Using Microfluidic Technologies Based on Valves, Droplets, and SlipChip," in *Annual Review of Biophysics*, Buffalo., vol. 39, New York, 2010, pp. 139–158.

[81] E. Olsson and G. Kreiss, "A conservative level set method for two phase flow," *Journal of Computational Physics*, vol. 210, no. 1, pp. 225–246, 2005.

[82] Autodesk Inc., "Autodesk AutoCAD," 2018. [Online]. Available: https://www.autodesk.com/products/autocad/overview. [Accessed: 01-Dec-2018].

[83] Websters, "Antleron Engineering Life," 2019. [Online]. Available: https://www.antleron.com/. [Accessed: 01-Feb-2019].

[84]   P. Tabeling, *Introduction to Microfluidics*, First. Paris: Oxford University Press, 2005.

[85]   "Protolabs - Rapid Prototyping & On-demand Production." [Online]. Available: https://www.protolabs.co.uk/. [Accessed: 17-Oct-2019].

[86]   B. Zheng, C. J. Gerdts, and R. F. Ismagilov, "Using nanoliter plugs in microfluidics to facilitate and understand protein crystallization," *Current Opinion in Structural Biology*, vol. 15, no. 5, pp. 548–555, 2005.

[87]   K. Dhouib *et al.*, "Microfluidic chips for the crystallization of biomacromolecules by counter-diffusion and on-chip crystal X-ray analysis," *Lab on a Chip*, vol. 9, no. 10, pp. 1412–1421, 2009.

[88]   M. Hamon and J. W. Hong, "Systematic Evaluation of the Efficiencies of Proteins and Chemicals in Pharmaceutical Applications," in *Microfluidic Technologies for Human Health*, U. Demirci, A. Khademhosseini, R. Langer, and J. Blander, Eds. 2013, pp. 21–46.

[89]   B. Zheng, J. D. Tice, L. S. Roach, and R. F. Ismagilov, "A droplet-based, composite PDMS/glass capillary microfluidic system for evaluating protein crystallization conditions by microbatch and vapor-diffusion methods with on-chip X-ray diffraction," *Angewandte Chemie - International Edition*, vol. 43, pp. 2508–2511, 2004.

[90]   C. J. Gerdts *et al.*, "Time-controlled microfluidic seeding in nL-volume droplets to separate nucleation and growth stages of protein crystallization," *Angewandte Chemie - International Edition*, vol. 45, pp. 8156–8160, 2006.

[91]   H. Shi, Y. Xiao, S. Ferguson, X. Huang, N. Wang, and H. Hao, "Progress of crystallization in microfluidic devices," *Lab on a Chip*, vol. 23, pp. 806–812, 2017.

[92]   M. Ildefonso, N. Candoni, and S. Veesler, "A cheap, Easy Microfluidic Crystallization Device Ensuring Universal Solvent Compatibility," *Organic Process Research & Development*, vol. 16, no. 4, pp. 556–560, 2012.

[93]   S. Zhang *et al.*, "Microfluidic platform for optimization of crystallization conditions," *Journal of Crystal Growth*, pp. 1–21, 2017.

[94]   S. Zhang, C. Guivier-Curien, S. Vessler, and N. Candoni, "Prediction of sizes and frequencies of nanoliter-sized droplets in cylindrical T-junction microfluidics," *Chemical Engineering Science*, vol. 138, pp. 128–139, 2015.

[95]   H. Yamaguchi, M. Maeki, K. Yamashita, H. Nakamura, M. Miyazaki, and H. Maeda, "Controlling one protein crystal growth by droplet-based microfluidic system," *Journal of Biochemistry*, vol. 153, no. 4, pp. 339–346, 2013.

[96]   M. Ildefonso, E. Revalor, P. Punniam, J. B. Salmon, N. Candoni, and S. Veesler, "Nucleation and polymorphism explored via an easy-to-use microfluidic tool," *Journal of Crystal Growth*, vol. 342, no. 1, pp. 9–12, 2012.

[97]   M. Ildefonso, N. Candoni, and S. Veesler, "Using Microfluidics for Fast, Accurate Measurement of Lysozyme Nucleation Kinetics," *Crystal Growth & Design*, vol. 11, no. 5, pp. 1527–1530, 2011.

[98]   Z. Hammadi, N. Candoni, R. Grossier, M. Ildefonso, R. Morin, and S. Veesler, "Small-volume nucleation," *Comptes Rendus Physique*, vol. 14, no. 2–3, pp. 192–198, 2013.

[99]   S. L. Anna, "Droplets and Bubbles in Microfluidic Devices," *Annual Review of Fluid Mechanics*, vol. 48, no. 1, pp. 285–309, 2016.

[100] R. Grossier, Z. Hammadi, R. Morin, and S. Veesler, "Predictive nucleation of crystals in small volumes and its consequences," *Physical Review Letters*, vol. 107, no. 2, pp. 1–4, 2011.

[101] S. Zhang, N. Ferté, N. Candoni, and S. Veesler, "Versatile Microfluidic Approach to Crystallization," *Organic Process Research & Development*, vol. 19, no. 12, pp. 1–5, 2015.

[102] M. M. Roberts, J. Y. Y. Heng, and D. R. Williams, "Protein crystallization by forced flow through glass capillaries: Enhanced lysozyme crystal growth," *Crystal Growth & Design*, vol. 10, no. 3, pp. 1074–1083, 2010.

[103] S. V. Akella, A. Mowitz, M. Heymann, and S. Fraden, "Emulsion-based technique to measure protein crystal nucleation rates of lysozyme," *Crystal Growth & Design*, vol. 14, no. 9, pp. 4487–4509, 2014.

[104] J. Zhang, K. Wang, A. R. Teixeira, K. F. Jensen, and G. Luo, "Design and Scaling Up of Microchemical Systems: A Review," *Annual Review of Chemical and Biomolecular Engineering*, vol. 8, no. 1, pp. 285–305, 2017.

[105]   "NIS Elements Basic Research - Microscope Imaging Software," 2017. [Online]. Available: https://www.nikoninstruments.com/en_EU/Products/Software/NIS-Elements-Basic-Research. [Accessed: 20-Jul-2017].

[106]   A. Ferreira, N. Faria, F. Rocha, and J. Teixeira, "Using an online image analysis technique to characterize sucrose crystal morphology during a crystallization run," *Industrial & Engineering Chemistry Research*, pp. 6990–7002, 2011.

[107]   A. Ferreira, G. Pereira, J. A. Teixeira, and F. Rocha, "Statistical tool combined with image analysis to characterize hydrodynamics and mass transfer in a bubble column," *Chemical Engineering Journal*, vol. 180, pp. 216–228, 2012.

[108]   W. Wang, T. Shao, S. Zhao, Y. Jin, and Y. Cheng, "Experimental and Numerical Study of Mixing Behavior inside Droplets in Microchannels," *American Institute of Chemical Engineers Journal*, vol. 59, no. 5, pp. 1801–1813, 2013.

[109]   T.-D. Ngo, SangWoo Joo Ich-Long Dang and C. Byon, "A numerical study on the dynamics of droplet formation in a microfluidic double T-junction," *Biomicrofluidics*, vol. 9, pp. 1–14, 2015.

[110]   Y. Li, R. K. Reddy, C. S. S. R. Kumar, and K. Nandakumar, "Computational investigations of the mixing performance inside liquid slugs generated by a microfluidic T-junction," *Biomicrofluidics*, vol. 8, no. 5, pp. 1–18, 2014.

[111]   J. Wang, J. Wang, L. Feng, and T. Lin, "Fluid mixing in droplet-based microfluidics with a serpentine microchannel," *RSC Advances*, vol. 5, pp. 104138–104144, 2015.

[112]   B. Lafaurie, C. Nardone, R. Scardovelli, S. Zaleski, and G. Zanetti, "Modelling merging and fragmentation in multiphase flows with SURFER," *Journal of Computational Physics*, vol. 113, no. 1. pp. 134–147, 1994.

[113]   H. Weller, "OpenFOAM-5.x," 2017. [Online]. Available: https://github.com/OpenFOAM/OpenFOAM-5.x. [Accessed: 20-Aug-2017].

[114]   K. van As, "OF-kva_interfaceProperties," 2017. [Online]. Available: https://github.com/floquation/OF-kva_interfaceProperties. [Accessed: 20-Aug-2017].

[115] D. A. Hoang, V. van Steijn, L. M. Portela, M. T. Kreutzer, and C. R. Kleijn, "Benchmark numerical simulations of segmented two-phase flows in microchannels using the Volume of Fluid method," *Computers & Fluids*, vol. 86, no. November 2013, pp. 28–36, 2013.

[116] J. U. Brackbill, D. B. Kothe, and C. Zemach, "A continuum method for modeling surface tension," *Journal of Computational Physics*, vol. 100, no. 2, pp. 335–354, 1992.

[117] D. A. Hoang, V. van Steijn, L. M. Portela, M. T. Kreutzer, and C. R. Kleijn, "Benchmark numerical simulations of segmented two-phase flows in microchannels using the Volume of Fluid method," *Computers and Fluids*, vol. 86, pp. 28–36, 2013.

[118] M. J. Nieves-Remacha, L. Yang, and K. F. Jensen, "OpenFOAM Computational Fluid Dynamic Simulations of Two-Phase Flow and Mass Transfer in an Advanced-Flow Reactor," *Industrial & Engineering Chemistry Research*, vol. 54, pp. 6649–6659, 2015.

[119] "SALOME - The Open Source Integration Platform for Numerical Simulation," 2018. [Online]. Available: http://www.salome-platform.org/. [Accessed: 20-Aug-2018].

[120] N. Dombrowski, E. A. Foumeny, S. Ookawara, and A. Riza, "The influence of Reynolds number on the entry length and pressure drop for laminar pipe flow," *The Canadian Journal of Chemical Engineering*, vol. 71, no. 3, pp. 472–476, 1993.

[121] F. P. Bretherton, "The motion of long bubbles in tubes," *Journal of Fluid Mechanics*, vol. 10, no. 2, pp. 166–188, 1961.

[122] G. K. Kurup and A. S. Basu, "Shape dependent Laplace vortices in deformed liquid-liquid slug flow," *Proceedings of the Annual International Conference of the IEEE Engineering in Medicine and Biology Society, EMBS*, pp. 4034–4037, 2011.

[123] P. Zhu and L. Wang, "Passive and active droplet generation with microfluidics: a review," *Lab on a Chip*, vol. 17, pp. 34–75, 2017.

[124] Z. Nie *et al.*, "Emulsification in a microfluidic flow-focusing device: Effect of the viscosities of the liquids," *Microfluidics & Nanofluidics*, vol. 5, no. 5, pp. 585–594, 2008.

[125] P. Zhu and L. Wang, "Passive and active droplet generation with microfluidics: a review," *Lab on a Chip*, vol. 17, no. 1, pp. 34–75, 2017.

[126] N. Kim, M. C. Murphy, S. A. Soper, and D. E. Nikitopoulos, "Liquid-liquid segmented flows in polycarbonate microchannels with cross-sectional expansions," *International Journal of Multiphase Flow*, vol. 58, pp. 83–96, 2014.

[127] P. Garstecki, M. J. Fuerstman, H. A. Stone, and G. M. Whitesides, "Formation of droplets and bubbles in a microfluidic T-junction-scaling and mechanism of break-up," *Lab on a Chip*, vol. 6, no. 3, pp. 437–446, 2006.

[128] D. Funfschilling, H. Debas, H. Z. Li, and T. G. Mason, "Flow-field dynamics during droplet formation by dripping in hydrodynamic-focusing microfluidics," *Physical Review E - Statistical, Nonlinear, and Soft Matter Physics*, vol. 80, no. 1, pp. 2–5, 2009.

[129] P. Urbant, A. Leshansky, and Y. Halupovich, "On the forced convective heat transport in a droplet-laden flow in microchannels," *Microfluidics and Nanofluidics*, vol. 4, no. 6, pp. 533–542, 2008.

[130] M. Fischer, D. Juric, and D. Poulikakos, "Large Convective Heat Transfer Enhancement in Microchannels With a Train of Coflowing Immiscible or Colloidal Droplets," *Journal of Heat Transfer*, vol. 132, no. 11, p. 112402, 2010.

[131] Z. Che, T. N. Wong, N.-T. Nguyen, and C. Yang, "3D features of convective heat transfer in droplet-based microchannel heat sinks," *International Journal of Heat & Mass Transfer*, vol. 86, pp. 455–464, 2015.

[132] A. Khater, M. Mohammadi, A. Mohamad, and A. S. Nezhad, "Dynamics of temperature-actuated droplets within microfluidics," *Scientific Reports*, vol. 9, no. 1, pp. 1–11, 2019.

[133] D. Brune and S. Kim, "Predicting protein diffusion coefficients," *Proceedings of the National Academy of Sciences of the United States of America*, vol. 90, no. 9, pp. 3835–3839, 1993.

[134] T. Baştuğ and S. Kuyucak, "Temperature dependence of the transport coefficients of ions from molecular dynamics simulations," *Chemical Physics Letters*, vol. 408, no. 1–3, pp. 84–88, 2005.

[135] A. V. Svanidze *et al.*, "Specific features of the temperature behavior of lysozyme diffusivity in solutions with different protein concentrations," *Journal of Molecular Liquids*, vol. 168, pp. 7–11, 2012.

[136] X. Liu, "Diffusion in Liquids - Equilibrium Molecular Simulations and Predictive Engineering Models," Delft University of Technology, 2012.

[137] P. Laval, A. Crombez, and J. B. Salmon, "Microfluidic Droplet Method for Nucleation Kinetics Measurements," *Langmuir*, vol. 25, no. 3, pp. 1836–1841, 2009.

[138] D. Kashchiev, *Nucleation: Basic Theory with Applications*. Sofia, Bulgaria: Butterworth-Heinemann, 2000.

[139] C. A. Stan, S. K. Y. Tang, and G. M. Whitesides, "Independent control of drop size and velocity in microfluidic flow-focusing generators using variable temperature and flow rate," *Analytical Chemistry*, vol. 81, no. 6, pp. 2399–2402, 2009.

[140] J. K. Lai, E. Merzari, and Y. A. Hassan, "Sensitivity analyses in a buoyancy-driven closed system with high resolution CFD using Boussinesq approximation and variable density models," *International Journal of Heat & Fluid Flow*, vol. 75, pp. 1–13, 2019.

[141] T. C. Thulasidas, M. A. Abraham, and R. L. Cerro, "Flow patterns in liquid slugs during bubble-train flow inside capillaries," *Chemical Engineering Science*, vol. 52, no. 17, pp. 2947–2962, 1997.

[142] E. L. Forsythe, R. A. Judge, and M. L. Pusey, "Tetragonal Chicken Egg White Lysozyme Solubility in Sodium Chloride Solutions," *Journal of Chemical & Engineering Data*, vol. 44, no. 3, pp. 637–640, May 1999.

[143] S. B. Howard, P. J. Twigg, J. K. Baird, and E. J. Meehan, "The Solubility of Hen Egg-Whjte Lysozyme," *Journal of Crystal Growth*, vol. 90, pp. 94–104, 1988.

[144] R. Crespo, P. M. Martins, L. Gales, F. Rocha, and A. M. Damas, "Potential use of ultrasound to promote protein crystallization," *Journal of Applied Crystallography*, vol. 43, no. 6, pp. 1419–1425, 2010.

[145] F. Castro, A. Ferreira, J. Teixeira, and F. Rocha, "Protein Crystallization as a Process Step in a Novel Meso Oscillatory Flow Reactor: Study of Lysozyme Phase Behavior," *Crystal Growth & Design*, pp. 1–8, 2016.

[146] S. Maosoongnern, V. Diaz Borbon, A. E. Flood, and J. Ulrich, "Introducing a fast method to determine the solubility and metastable zone width for proteins: Case study lysozyme," *Industrial & Engineering Chemistry Research*, vol. 51, no. 46, pp. 15251–15257, 2012.

[147] B. G. Abdallah, S. Roy-Chowdhury, R. Fromme, P. Fromme, and A. Ros, "Protein Crystallization in an Actuated Microfluidic Nanowell Device," *Crystal Growth & Design*, vol. 16, no. 4, pp. 2074–2082, 2016.

[148] E. I. Howard, J. M. Fernandez, and J. M. Garcia-Ruiz, "On the mixing of protein crystallization cocktails," *Crystal Growth & Design*, vol. 9, no. 6, pp. 2707–2712, 2009.

[149] V. Bhamidi, P. J. A. Kenis, and C. F. Zukoski, "Probability of Nucleation in a Metastable Zone: Induction Supersaturation and Implications," *Crystal Growth & Design*, vol. 17, pp. 1132–1145, 2017.

[150] S. Teychené and B. Biscans, "Microfluidic device for the crystallization of organic molecules in organic solvents," *Crystal Growth & Design*, vol. 11, no. 11, pp. 4810–4818, 2011.

[151] S. Teychené and B. Biscans, "Crystal nucleation in a droplet based microfluidic crystallizer," *Chemical Engineering Science*, vol. 77, pp. 242–248, Jul. 2012.

[152] W. S. Price, F. Tsuchiya, and Y. Arata, "Lysozyme aggregation and solution properties studied using PGSE NMR diffusion measurements," *Journal of the American Chemical Society*, vol. 121, no. 49, pp. 11503–11512, 1999.

[153] T. Vetter, M. Iggland, D. R. Ochsenbein, F. S. Hänseler, and M. Mazzotti, "Modeling nucleation, growth, and ostwald ripening in crystallization processes: A comparison between population balance and kinetic rate equation," *Crystal Growth & Design*, vol. 13, no. 11, pp. 4890–4905, 2013.

[154] A. A. Streets and S. R. Quake, "Ostwald Ripening of Clusters during Protein Crystallization," *Physical Review Letters*, vol. 104, no. 17, pp. 1–9, 2010.

[155] M. Maeki, Y. Teshima, S. Yoshizuka, H. Yamaguchi, K. Yamashita, and M. Miyazaki, "Controlling protein crystal nucleation by droplet-based microfluidics," *ChemPubSoc Europe*, vol. 20, no. 4, pp. 1049–1056, 2014.

[156] L. B. Wang, N. I. Wakayama, and W. Q. Tao, "The role of solutal convection in protein crystal growth - A new dimensionless number to evaluate the effects of convection on protein crystal growth," *Journal of Crystal Growth*, vol. 310, no. 24, pp. 5370–5374, 2008.

[157] M. E. Dolega, S. Jakiela, M. Razew, A. Rakszewska, O. Cybulski, and P. Garstecki, "Iterative operations on microdroplets and continuous monitoring of processes within them; determination of solubility diagrams of proteins.," *Lab on a Chip*, vol. 12, no. 20, pp. 4022–4025, 2012.

[158] J. S. I. Kwon, M. Nayhouse, P. D. Christofides, and G. Orkoulas, "Protein crystal shape and size control in batch crystallization: Comparing model predictive control with conventional operating policies," *Industrial & Engineering Chemistry Research*, vol. 53, no. 13, pp. 5002–5014, 2014.

[159] R. D. Dombrowski, J. D. Litster, N. J. Wagner, and Y. He, "Modeling the Crystallization of Proteins and Small Organic Molecules in Nanoliter Drops," *AIChE Journal*, vol. 56, no. 1, pp. 79–91, 2010.

[160] D. Shi, P. Mhaskar, N. H. El-Farra, and P. D. Christofides, "Predictive control of crystal size distribution in protein crystallization," *Nanotechnology*, vol. 16, no. 7, pp. S562–S574, 2005.

[161] H. Li, Y. Kawajiri, M. A. Grover, and R. W. Rousseau, "Modeling of Nucleation and Growth Kinetics for Unseeded Batch Cooling Crystallization," *Industrial & Engineering Chemistry Research*, vol. 56, no. 14, pp. 4060–4073, 2017.

[162] M. V. Saikumar, C. E. Glatz, and M. A. Larson, "Lysozyme crystal growth and nucleation kinetics," *Journal of Crystal Growth*, vol. 187, no. 2, pp. 277–288, 1998.

[163] P. G. Vekilov and M. A. Vorontsova, "Nucleation precursors in protein crystallization," *Acta Crystallographica Section F: Structural Biology Communications*, vol. 70, no. 3, pp. 271–282, 2014.

[164] E. Revalor *et al.*, "Usual and unusual crystallization from solution," *Journal of Crystal Growth*, vol. 312, no. 7, pp. 939–946, 2010.

[165] F. Li and R. Lakerveld, "Electric-Field-Assisted Protein Crystallization in Continuous Flow," *Crystal Growth & Design*, vol. 18, no. 5, pp. 2964–2971, 2018.

[166] M. Taleb, C. Didierjean, C. Jelsch, J. P. Mangeot, B. Capelle, and A. Aubry, "Crystallization of proteins under an external electric field," *Journal of Crystal Growth*, vol. 200, no. 3, pp. 575–582, 1999.

[167] L. F. Alexander and N. Radacsi, "Application of electric fields for controlling crystallization," *CrystEngComm*, vol. 21, no. 34, pp. 5014–5031, 2019.

[168] A. Rodríguez-Romero, N. E. Escofet, C. Pareja-Rivera, and A. Moreno, "Crystal Growth of High-Quality Protein Crystals under the Presence of an Alternant Electric Field in Pulse-Wave Mode, and a Strong Magnetic Field with Radio Frequency Pulses Characterized by X-ray Diffraction," *Crystals*, vol. 7, no. 179, pp. 1–13, 2017.

[169] E. K. Yan, C. Y. Zhang, J. He, and D. C. Yin, "An overview of hardware for protein crystallization in a magnetic field," *International Journal of Molecular Sciences*, vol. 17, no. 11, pp. 1–19, 2016.

[170] J. P. Astier, S. Veesler, and R. Boistelle, "Protein crystals orientation in a magnetic field," *Acta Crystallographica Section D: Biological Crystallography*, vol. 54, no. 4, pp. 703–706, 1998.

[171] D.-C. Yin, "Protein crystallization in a magnetic field," *Progress in Crystal Growth & Characterization of Materials*, vol. 61, no. 1, pp. 1–26, 2015.

[172] S. Veesler, K. Furuta, H. Horiuchi, H. Hiratsuka, N. Ferté, and T. Okutsu, "Crystals from light: Photochemically induced nucleation of hen egg-white lysozyme," *Crystal Growth & Design*, vol. 6, no. 7, pp. 1631–1635, 2006.

[173] T. Okutsu, "Photochemically-induced crystallization of protein," *Journal of Photochemistry and Photobiology C: Photochemistry Reviews*, vol. 8, no. 3, pp. 143–155, 2007.

[174] C. N. Nanev and A. Penkova, "Nucleation of lysozyme crystals under external electric and ultrasonic fields," *Journal of Crystal Growth*, vol. 232, no. 1–4, pp. 285–293, 2001.

[175] K. Kakinouchi *et al.*, "Effect of ultrasonic irradiation on protein crystallization," *Journal of Crystal Growth*, vol. 292, no. 2, pp. 437–440, 2006.

[176] H. Kitayama, Y. Yoshimura, M. So, K. Sakurai, H. Yagi, and Y. Goto, "A common mechanism underlying amyloid fibrillation and protein crystallization revealed by the effects of ultrasonication," *Biochimica & Biophysica Acta - Proteins and Proteomics*, vol. 1834, no. 12, pp. 2640–2646, 2013.

[177] Y. Mao *et al.*, "Enhancement of Lysozyme Crystallization under Ultrasound Field," *Ultrasonics Sonochemistry*, vol. 63, no. 104975, pp. 1–7, 2020.

[178] Z. Zhang, D. W. Sun, Z. Zhu, and L. Cheng, "Enhancement of Crystallization Processes by Power Ultrasound: Current State-of-the-Art and Research Advances," *Comprehensive Reviews in Food Science and Food Safety*, vol. 14, no. 4, pp. 303–316, 2015.

[179] G. Ruecroft, D. Hipkiss, T. Ly, N. Maxted, and P. W. Cains, "Sonocrystallization: The use of ultrasound for improved industrial crystallization," *Organic Process Research & Development*, vol. 9, no. 6, pp. 923–932, 2005.

[180] B. Ratsimba, B. Biscans, H. Delmas, and J. Jenck, "Sonocrystallization: The end of empiricism? A review on the fundamental investigations and the industrial developments," *KONA Powder and Particle Journal*, vol. 17, no. May, pp. 38–48, 1999.

[181] H.-L. Cao *et al.*, "Rapid crystallization from acoustically levitated droplets," *The Journal of the Acoustical Society of America*, vol. 131, no. 4, pp. 3164–3172, 2012.

[182] D. Rossi, R. Jamshidi, N. Saffari, S. Kuhn, A. Gavriilidis, and L. Mazzei, "Continuous-Flow Sonocrystallization in Droplet-Based Microfluidics," *Crystal Growth & Design*, vol. 15, no. 11, pp. 5519–5529, 2015.

[183] M. Jiang, C. D. Papageorgiou, J. Waetzig, A. Hardy, M. Langston, and R. D. Braatz, "Indirect ultrasonication in continuous slug-flow crystallization," *Crystal Growth and Design*, vol. 15, no. 5, pp. 2486–2492, 2015.

[184] R. J. P. Eder, S. Schrank, M. O. Besenhard, E. Roblegg, H. Gruber-Woelfler, and J. G. Khinast, "Continuous sonocrystallization of acetylsalicylic acid (ASA): Control of crystal size," *Crystal Growth and Design*, vol. 12, no. 10, pp. 4733–4738, 2012.

[185] Z. K. Nagy and R. D. Braatz, "Advances and New Directions in Crystallization Control," *Annual Review of Chemical & Biomolecular Engineering*, vol. 3, no. 1, pp. 55–75, 2012.

[186] J. Ferreira, F. Castro, F. Rocha, and S. Kuhn, "Protein crystallization in a droplet-based microfluidic device: Hydrodynamic analysis and study of the phase behaviour," *Chemical Engineering Science*, vol. 191, pp. 232–244, 2018.

[187] C. Delacour, C. Lutz, and S. Kuhn, "Pulsed ultrasound for temperature control and clogging prevention in micro-reactors," *Ultrasonics Sonochemistry*, vol. 55, pp. 67–74, 2019.

[188] Z. Dong, D. Fernandez Rivas, and S. Kuhn, "Acoustophoretic focusing effects on particle synthesis and clogging in microreactors," *Lab on a Chip*, vol. 19, no. 2, pp. 316–327, 2019.

[189] Z. Dong, A. P. Udepurkar, and S. Kuhn, "Synergistic effects of the alternating application of low and high frequency ultrasound for particle synthesis in microreactors," *Ultrasonics Sonochemistry*, vol. 60, pp. 104800–104809, 2020.

[190] N. I. E. B.V., "NIS-Elements Imaging Software," 2019. [Online]. Available: https://www.microscope.healthcare.nikon.com/en_EU/products/software/nis-elements/nis-elements-advanced-research. [Accessed: 01-Nov-2019].

[191] "ImageJ," *ImageJ*, 2019. [Online]. Available: https://imagej.net/ImageJ. [Accessed: 15-Nov-2019].

[192] M. A. Durán-Olivencia and F. Otálora, "A Brownian model for crystal nucleation," *Journal of Crystal Growth*, vol. 380, pp. 247–255, 2013.

[193] M. Heymann *et al.*, "Room-temperature serial crystallography using a kinetically optimized microfluidic device for protein crystallization and on-chip X-ray diffraction," *IUCrJ*, vol. 1, no. 2014, pp. 349–360, 2014.

[194] K. J. Takano, H. Harigae, Y. Kawamura, and M. Ataka, "Effect of hydrostatic pressure on the crystallization of lysozyme based on in situ observations," *Journal of Crystal Growth*, vol. 171, no. 3–4, pp. 554–558, 1997.

[195] H. N. Kim and K. S. Suslick, "The effects of ultrasound on crystals: Sonocrystallization and sonofragmentation," *Crystals*, vol. 8, no. 7, 2018.

[196] V. S. Nalajala and V. S. Moholkar, "Investigations in the physical mechanism of sonocrystallization," *Ultrasonics Sonochemistry*, vol. 18, no. 1, pp. 345–355, 2011.

[197] S. L. Hem, "The effect of ultrasonic vibrations on crystallization processes," *Ultrasonics*, vol. 5, no. 4, pp. 202–207, 1967.

[198] J. W. Gibbs, *On the equilibrium of heterogeneous substances*. 1878.

[199] G. M. Maggioni and M. Mazzotti, "Modelling the stochastic behaviour of primary nucleation," *Faraday Discussions*, vol. 179, pp. 359–382, 2015.

[200] B. Zheng, L. S. Roach, and R. F. Ismagilov, "Screening of Protein Crystallization Conditions on a Microfluidic Chip Using Nanoliter-Size Droplets," *Journal of the American Chemical Society*, vol. 125, no. 37, pp. 11170–11171, 2003.

[201] B. T. C. Lau, C. A. Baitz, X. P. Dong, and C. L. Hansen, "A Complete Microfluidic Screening Platform for Rational Protein Crystallization," *Journal of the American Chemical Society*, vol. 129, no. 3, pp. 454–455, 2007.

[202] C. Gerard *et al.*, "Crystallization via tubing microfluidics permits both in situ and ex situ X-ray diffraction," *Acta Crystallographica Section F: Structural Biology Communications*, vol. 73, no. 10, pp. 574–578, 2017.

[203] C. Ferreira, R. Crespo, P. M. Martins, L. Gales, F. Rocha, and A. M. Damas, "Small temperature oscillations promote protein crystallization," *CrystEngComm*, vol. 13, no. 8, p. 3051, 2011.

[204] R. Bin Zhou, H. L. Cao, C. Y. Zhang, and D. C. Yin, "A review on recent advances for nucleants and nucleation in protein crystallization," *CrystEngComm*, vol. 19, no. 8, pp. 1143–1155, 2017.

[205] Y. M. Liu *et al.*, "Sensitivity of lysozyme crystallization to temperature variation," *CrystEngComm*, vol. 18, no. 9, pp. 1609–1617, 2016.

[206] X. K. Wang, D. C. Yin, C. Y. Zhang, Q. Q. Lu, Y. Z. Guo, and W. H. Guo, "Effect of temperature programmes on protein crystallisation," *Crystal Research & Technology*, vol. 45, no. 5, pp. 479–489, 2010.

[207] M. Ataka and S. Tanaka, "The growth of large single crystals of lysozyme," *Biopolymers*, vol. 25, no. 2, pp. 337–350, 1986.

[208] R. A. Judge, R. S. Jacobs, T. Frazier, E. H. Snell, and M. L. Pusey, "The effect of temperature and solution pH on the nucleation of tetragonal lysozyme crystals," *Biophysical Journal*, vol. 77, no. 3, pp. 1585–1593, 1999.

[209] J. F. Lutsko and M. A. Durán-Olivencia, "Classical nucleation theory from a dynamical approach to nucleation," *Journal of Chemical Physics*, vol. 138, no. 24, pp. 1–15, 2013.

[210] M. Pusey and R. Naumann, "Growth kinetics for tetragonal lysozyme crystals," *Journal of Crystal Growth*, vol. 76, no. 3, pp. 593–599, 1986.

[211] A. McPherson and B. Cudney, "Optimization of crystallization conditions for biological macromolecules," *Acta Crystallographica Section F: Structural Biology Communications*, vol. 70, pp. 1445–1467, 2014.

[212] C. Ferreira, F. A. Rocha, A. M. Damas, and P. M. Martins, "The Finding of Nondissolving Lysozyme Crystals and Its Significance for the Study of Hard-to-Crystallize Biological Macromolecules," *Crystal Growth & Design*, vol. 16, no. 8, pp. 4285–4291, 2016.

[213] I. L. Dimitrov, "Crystal nucleation from solutions of proteins with temperature-independent solubility: a case study of apoferritin," *CrystEngComm*, vol. 21, no. 8, pp. 1279–1287, 2019.

[214] D. Crowfoot, "X-Ray Single Crystal Photographs of Insulin," *Nature*, pp. 591–592, 1935.

[215] J. A. K. Howard, "Dorothy Hodgkin and her contributions to biochemistry," *Nature Reviews: Molecular Cell Biology*, vol. 4, no. 11, pp. 891–896, 2003.

[216] L. Bergeron, L. F. Filobelo, O. Galkin, and P. G. Vekilov, "Thermodynamics of the Hydrophobicity in Crystallization of Insulin," *Biophysical Journal*, vol. 85, no. 6, pp. 3935–3942, 2003.

[217] J. Brange, *Galenics of Insulin: The Physico-chemical and Pharmaceutical Aspects of Insulin and Insulin Preparations*, 1st Edition. Berlin: Springer-Verlag Berlin Heidelberg, 1987.

[218] H. P. Merkle and A. Jen, "A crystal clear solution for insulin delivery," *Nature Biotechnology*, vol. 20, no. 8, pp. 789–790, 2002.

[219] M. Norrman and G. Schluckebier, "Crystallographic characterization of two novel crystal forms of human insulin induced by chaotropic agents and a shift in pH," *BMC Structural Biology*, vol. 7, no. 83, pp. 1–14, 2007.

[220] T. L. Blundell, "Protein crystallography and drug discovery: Recollections of knowledge exchange between academia and industry," *IUCrJ*, vol. 14, no. 82, pp. 308–321, 2017.

[221] D. Hekmat, "Large-scale crystallization of proteins for purification and formulation," *Bioprocess & Biosystems Engineering*, vol. 38, no. 7, pp. 1209–1231, 2015.

[222] E. K. Lee and W. Kim, *Isolation and Purification of Proteins*, 1st Edition. CRC Press, 2003.

[223] C. N. Nanev, V. D. Tonchev, and F. V. Hodzhaoglu, "Protocol for growing insulin crystals of uniform size," *Journal of Crystal Growth*, vol. 375, pp. 10–15, 2013.

[224] A. Penkova, I. Dimitrov, and C. Nanev, "Nucleation of insulin crystals in a wide continuous supersaturation gradient," *Annals of the New York Academy of Sciences*, vol. 1027, pp. 56–63, 2004.

[225] F. Chen *et al.*, "Crystallization of bovine insulin on a flow-free droplet-based platform," *AIP Conference Proceedings*, vol. 1820, 2017.

[226] C. N. Nanev, F. V. Hodzhaoglu, and I. L. Dimitrov, "Kinetics of insulin crystal nucleation, energy barrier, and nucleus size," *Crystal Growth & Design*, vol. 11, no. 1, pp. 196–202, 2011.

[227] P. Mühlig, T. Klupsch, U. Schell, and R. Hilgenfeld, "Observation of the early stage of insulin crystallization by confocal laser scanning microscopy," *Journal of Crystal Growth*, vol. 232, no. 1–4, pp. 93–101, 2001.

[228] J. Schlichtkrull, "Insulin Crystals - IV. The Preparation of Nuclei, Seeds and Monodisperse Insulin Crystal Suspensions," *Acta Chemica Scandinavica*, vol. 11, pp. 299–302, 1957.

[229] J. Schlichtkrull, "Insulin Crystals - V. The Nucleation and Growth of Insulin Crystals," *Acta Chemica Scandinavica*, vol. 11, pp. 439–460, 1957.

[230] C. N. Nanev and K. P. Petrov, "Steering a crystallization process to reduce crystal polydispersity; case study of insulin crystallization," *Journal of Crystal Growth*, vol. 480, pp. 164–169, 2017.

[231] J. V. Parambil, M. Schaepertoens, D. R. Williams, and J. Y. Y. Heng, "Effects of Oscillatory Flow on the Nucleation and Crystallization of Insulin," *Crystal Growth & Design*, vol. 11, no. 10, pp. 4353–4359, 2011.

[232] L. Bromberg, J. Rashba-Step, and T. Scott, "Insulin particle formation in supersaturated aqueous solutions of poly(ethylene glycol)," *Biophysical Journal*, vol. 89, no. 5, pp. 3424–3433, 2005.

[233] W. Kadima, A. McPherson, M. F. Dunn, and F. Jurnak, "Precrystallization aggregation of insulin by dynamic light scattering and comparison with canavalin," *Journal of Crystal Growth*, vol. 110, no. 1–2, pp. 188–194, 1991.

[234] E. Chatani *et al.*, "Early aggregation preceding the nucleation of insulin amyloid fibrils as monitored by small angle X-ray scattering," *Scientific Reports*, vol. 5, no. 15485, pp. 1–14, 2015.

[235] S. Dolui, A. Roy, U. Pal, A. Saha, and N. C. Maiti, "Structural Insight of Amyloidogenic Intermediates of Human Insulin," *ACS Omega*, vol. 3, no. 2, pp. 2452–2462, 2018.

[236] L. F. Pease *et al.*, "Probing the nucleus model for oligomer formation during insulin amyloid fibrillogenesis," *Biophysical Journal*, vol. 99, no. 12, pp. 3979–3985, 2010.

[237] B. W. Low and J. E. Berger, "Insulin: preliminary X-ray studies of citrate crystals," *Acta Crystallographica*, vol. 14, no. 82, p. 1, 1961.

[238] S. Fili *et al.*, "Human insulin polymorphism upon ligand binding and pH variation: The case of 4-ethylresorcinol," *IUCrJ*, vol. 2, pp. 534–544, 2015.

[239] C. M. Yip and M. D. Ward, "Atomic force microscopy of insulin single crystals: Direct visualization of molecules and crystal growth," *Biophysical Journal*, vol. 71, no. 2, pp. 1071–1078, 1996.

[240] E. J. Nettleton, P. Tito, M. Sunde, M. Bouchard, C. M. Dobson, and C. V. Robinson, "Characterization of the oligomeric states of insulin in self-assembly and amyloid fibril formation by mass spectrometry," *Biophysical Journal*, vol. 79, no. 2, pp. 1053–1065, 2000.

[241] M. Maeda, T. Chatake, I. Tanaka, A. Ostermann, and N. Niimura, "Crystallization of a large single crystal of cubic insulin for neutron protein crystallography," *Journal of Synchrotron Radiation*, vol. 11, no. 1, pp. 41–44, 2004.

[242] C. N. Nanev and F. V. Hodzhaoglu, "Temperature control of protein crystal nucleation," *Crystal Research & Technology*, vol. 47, no. 11, pp. 1195–1200, 2012.

[243] G. K. Christopher, A. G. Phipps, and R. J. Gray, "Temperature-dependent solubility of selected proteins," *Journal of Crystal Growth*, vol. 191, no. 4, pp. 820–826, 1998.

[244] Z. Zhang and Y. Liu, "Recent progresses of understanding the viscosity of concentrated protein solutions," *Current Opinion in Chemical Engineering*, vol. 16, pp. 48–55, 2017.

[245] T. Hong, K. Iwashita, and K. Shiraki, "Viscosity Control of Protein Solution by Small Solutes: A Review," *Current Protein & Peptide Science*, vol. 19, no. 8, pp. 746–758, 2017.

[246] T. A. Strivens and C. K. Schoff, "Rheometry," in *Ullmann's Encyclopedia of Industrial Chemistry*, Weinheim, Germany: Wiley-VCH, 2010, pp. 1–30.

[247] H. A. Barnes, *A Handbook of Elementary Rheology*. Aberystwyth, Wales, 2000.

[248] H. P. Sdougos, S. R. Bussolari, and C. F. Dewey, "Secondary flow and turbulence in a cone-and-plate device," *Journal of Fluid Mechanics*, vol. 138, pp. 379–404, 1984.

[249] S. von Bülow, M. Siggel, M. Linke, and G. Hummer, "Dynamic cluster formation determines viscosity and diffusion in dense protein solutions," *Proceedings of the National Academy of Sciences of the United States of America*, vol. 116, no. 20, pp. 9843–9852, 2019.

[250] V. L. Dharmaraj, P. D. Godfrin, Y. Liu, and S. D. Hudson, "Rheology of clustering protein solutions," *Biomicrofluidics*, vol. 10, no. 4, pp. 1–11, 2016.

[251] G. Dasari, I. Prince, and M. T. W. Hearn, "Investigations into the rheological characteristics of bovine amniotic fluid," *Journal of Biochemical & Biophysical Methods*, vol. 30, no. 4, pp. 217–225, 1995.

[252] W. Pan, L. Filobelo, N. D. Q. Pham, O. Galkin, V. V. Uzunova, and P. G. Vekilov, "Viscoelasticity in homogeneous protein solutions," *Physical Review Letters*, vol. 102, no. 5, pp. 1–4, 2009.

[253] D. R. Absolom, C. J. Van Oss, W. Zingg, and A. W. Neumann, "Determination of surface tensions of proteins II. Surface tension of serum albumin, altered at the protein-air interface," *Biochimica et Biophysica Acta*, vol. 670, no. 1, pp. 74–78, 1981.

[254] J. H. Johnston, "The Surface Tension of Protein Solutions. Part III," *Biochemical Journal*, vol. 21, no. 6, pp. 1314–1328, 1927.

[255] M. R. R. Niño and J. M. R. Patino, "Surface tension of protein and insoluble lipids at the air-aqueous phase interface," *Journal of the American Oil Chemists' Society*, vol. 75, no. 10, p. 1233, 1998.

[256] D. J. Burgess and N. O. Sahin, "Interfacial rheological and tension properties of protein films," *Journal of Colloid & Interface Science*, vol. 189, no. 1, pp. 74–82, 1997.

[257] M. Tomczyńska-Mleko *et al.*, "Changes of Secondary Structure and Surface Tension of Whey Protein Isolate Dispersions upon pH and Temperature," *Czech Journal of Food Sciences*, vol. 32, no. 1, pp. 82–89, 2014.

[258] E. Kachooei, A. A. Moosavi-Movahedi, F. Khodagholi, H. Ramshini, F. Shaerzadeh, and N. Sheibani, "Oligomeric forms of insulin amyloid aggregation disrupt outgrowth and complexity of neuron-like PC12 cells," *PLoS ONE*, vol. 7, no. 7, pp. 1–9, 2012.

[259] T. J. Gibson and R. M. Murphy, "Inhibition of insulin fibrillogenesis with targeted peptides," *Protein Science*, vol. 15, no. 5, pp. 1133–1141, 2006.

[260] C. Ybert and J. M. Di Meglio, "Study of protein adsorption by dynamic surface tension measurements: Diffusive regime," *Langmuir*, vol. 14, no. 2, pp. 471–475, 1998.

[261] J. Chang and J. Cai, "Dynamics of obstructed droplet breakup in microfluidic T-junction based on diffuse interface method," *Heat & Mass Transfer*, vol. 56, no. 5, pp. 1601–1611, 2020.

[262] K. Hyun *et al.*, "A review of nonlinear oscillatory shear tests: Analysis and application of large amplitude oscillatory shear (LAOS)," *Progress in Polymer Science*, vol. 36, no. 12, pp. 1697–1753, 2011.

[263] F. Pimenta and M. A. Alves, "Stabilization of an open-source finite-volume solver for viscoelastic fluid flows," *Journal of Non-Newtonian Fluid Mechanics*, vol. 239, pp. 85–104, 2017.

[264] R. C. Tolman, "The effect of droplet size on surface tension," *The Journal of Chemical Physics*, vol. 17, no. 3, pp. 333–337, 1949.

[265] S. W. Mayer, "Dependence of surface tension on temperature," *The Journal of Chemical Physics*, vol. 38, no. 8, pp. 1803–1808, 1963.

[266] J. A. Maroto, V. Pérez-Mũuzuri, and M. S. Romero-Cano, "Introductory analysis of Bénard-Marangoni convection," *European Journal of Physics*, vol. 28, no. 2, pp. 311–320, 2007.

[267] D. T. Wasan, A. D. Nikolov, and H. Brenner, "Droplets speeding on surfaces," *Science*, vol. 291, no. 5504, pp. 605–606, 2001.

[268] Y. Kita, C. Mackenzie Dover, A. Askounis, Y. Takata, and K. Sefiane, "Drop mobility on superhydrophobic microstructured surfaces with wettability contrasts," *Soft Matter*, vol. 14, no. 46, pp. 9418–9424, 2018.

[269] G. Karapetsas, N. T. Chamakos, and A. G. Papathanasiou, "Thermocapillary Droplet Actuation: Effect of Solid Structure and Wettability," *Langmuir*, vol. 33, no. 41, pp. 10838–10850, 2017.

[270] S. Daniel, M. K. Chaudhury, and J. C. Chen, "Fast drop movements resulting from the phase change on a gradient surface," *Science*, vol. 291, no. 5504, pp. 633–636, 2001.

[271] J. B. Brzoska, F. Brochard-Wyart, and F. Rondelez, "Motions of Droplets on Hydrophobic Model Surfaces Induced by Thermal Gradients," *Langmuir*, vol. 9, pp. 2220–2224, 1993.

[272] E. Klaseboer, J. P. Chevaillier, C. Gourdon, and O. Masbernat, "Film drainage between colliding drops at constant approach velocity: Experiments and modeling," *Journal of Colloid & Interface Science*, vol. 229, no. 1, pp. 274–285, 2000.

[273] A. Karbalaei, R. Kumar, and H. J. Cho, "Thermocapillarity in microfluidics - A review," *Micromachines*, vol. 7, no. 1, pp. 1–41, 2016.

[274] M. Ataka and M. Asai, "Systematic Studies on the Crystallization of Lysozyme," *Journal of Crystal Growth*, vol. 90, no. 1–3, pp. 86–93, 1988.

[275] H. Yang, P. Peczulis, P. Inguva, X. Li, and J. Y. Y. Heng, "Continuous Protein Crystallisation Platform and Process: Case of Lysozyme," *Chemical Engineering Research & Design*, vol. 136, pp. 529–535, 2018.

[276] H. Yang, W. Chen, P. Peczulis, and J. Y. Y. Heng, "Development and Workflow of a Continuous Protein Crystallization Process: A Case of Lysozyme," *Crystal Growth & Design*, vol. 19, no. 2, pp. 983–991, 2019.

[277] F. Oosawa and S. Asakura, *Thermodynamics of the Polymerization of Proteins*, Molecular. London: Academic Press Inc., 1975.

[278] F. Oosawa and M. Kasai, "A theory of linear and helical aggregations of macromolecules," *Journal of Molecular Biology*, vol. 4, no. 1, pp. 10–21, 1962.

[279] M. Ataka and M. Asai, "Analysis of the nucleation and crystal growth kinetics of lysozyme by a theory of self-assembly," *Biophysical Journal*, vol. 58, no. 3, pp. 807–811, 1990.

[280] M. Ataka, "Nucleation and growth kinetics of hen egg-white lysozyme crystals," *Progress in Crystal Growth & Characterization of Materials*, vol. 30, no. 2–3, pp. 109–128, 1995.

[281] Y. Bessho, M. Ataka, M. Asai, and T. Katsura, "Analysis of the crystallization kinetics of lysozyme using a model with polynuclear growth mechanism," *Biophysical Journal*, vol. 66, no. 2, pp. 310–313, 1994.

[282] C. Govardhan *et al.*, "Novel long-acting crystal formulation of human growth hormone," *Pharmaceutical Research*, vol. 22, no. 9, pp. 1461–1470, 2005.

[283] Y. Li, M. Kvetny, M. Bowen, W. Brown, D. Wang, and G. Wang, "Method to Directly Measure and Actively Control a Single Nucleation-Crystal Growth Process," *Crystal Growth & Design*, vol. 19, no. 4, pp. 2470–2475, 2019.

[284] F. V. Hodzhaoglu, M. Conejero-Muriel, I. L. Dimitrov, and J. A. Gavira, "Optimization of the classical method for nucleation and growth of rhombohedral insulin crystals by pH titration and screening," *Bulgarian Chemical Comunications*, vol. 48, no. Special Issue A, pp. 29–37, 2016.

[285] I. Reviakine, D. K. Georgiou, and P. G. Vekilov, "Capillarity effects on crystallization kinetics: Insulin," *Journal of the American Chemical Society*, vol. 125, no. 38, pp. 11684–11693, 2003.

[286] J. J. Abel, "Crystalline Insulin," *PNAS*, pp. 132–136, 1926.

[287] J. Schlichtkrull, "Insulin Crystals - VII. The Growth of Insulin Crystals," *Acta Chemica Scandinavica*, vol. 11, pp. 1248–1256, 1957.

[288] J. Schlichtkrull, "Insulin Crystals - VI. The Anisotropic Growth of Insulin Crystals," *Acta Chemica Scandinavica*, vol. 11, pp. 484–486, 1957.

[289] J. Schlichtkrull, "Insulin Crystals - III. Determination of the Rhombohedral Zinc-Insulin Unit-Cell by Combined Microscopical and Chemical Examinations," *Acta Chemica Scandinavica*, vol. 11, pp. 291–298, 1957.

[290] I. Dimitrov, F. Hodzhaoglu, and I. Ivanov, "Relevant to In Vivo Environment," *Dissolution Technologies*, pp. 11–16, 2013.

[291] A. Sauter, F. Roosen-Runge, F. Zhang, G. Lotze, R. M. J. Jacobs, and F. Schreiber, "Real-time observation of nonclassical protein crystallization kinetics," *Journal of the American Chemical Society*, vol. 137, no. 4, pp. 1485–1491, 2015.

List of publications

Publications in international, peer-reviewed journals

J. Ferreira, F. Castro, F. Rocha, S. Kuhn. Protein crystallization in a droplet-based microfluidic device: Hydrodynamics analysis and study of the phase behaviour. *Chemical Engineering Science*, **191**(14): 232–244. 2018.

J. Ferreira, F. Castro, S. Kuhn, F. Rocha. Controlled protein crystal nucleation in microreactors: The effect of the droplet volume *versus* high supersaturation ratios. *CrystEngComm*, **22**(28): 4692–4701. 2020.

J. Ferreira, J. Opsteyn, F. Rocha, F. Castro, S. Kuhn. Ultrasonic protein crystallization: Promoting nucleation in microdroplets through pulsed sonication. *Chemical Engineering Research & Design*, **162**: 249–257. 2020.

Conference contributions

J. Ferreira, F. Castro, F. Rocha, S. Kuhn. Lysozyme crystallization in a droplet-based microfluidic platform. *6th International School on Biological Crystallization*. Granada, Spain. 2017.

J. Ferreira, F. Castro, F. Rocha, S. Kuhn. A droplet-based microfluidic platform for protein crystallization. *2nd Doctoral School in Engineering: Symposium on Chemical, Biological and Environmental Engineering*. Porto, Portugal. 2017.

J. Ferreira, F. Castro, F. Rocha, S. Kuhn. Hydrodynamics and mixing dynamics in droplet-based microfluidics for protein crystallization. *8th World Congress on Particle Technology*, AIChE Meeting. Particle design, Crystallization II. Orlando, USA. 2018.

J. Ferreira, F. Castro, F. Rocha, S. Kuhn. Droplet microfluidic devices for protein crystallization. *17th International Conference on the Crystallization of Biological Macromolecules*. Young Scientist Short Talk. Shanghai, China. 2018.